A Thesis Submitted for the Degree of PhD at the University of Warwick

http://go.warwick.ac.uk/wrap/59753

Spin densities in $4f$ and $3d$ magnetic systems

by

Ian Maskery

Thesis

Submitted to the University of Warwick

for the degree of

Doctor of Philosophy

Department of Physics

May 2013

THE UNIVERSITY OF
WARWICK

Dedicated to

William Lister Park
(1909 - 2011)

and

Robert Robinson Armstrong
(1927 - 2006)

Contents

List of Figures

List of Tables

Acknowledgements

The order in which people are thanked in this brief section should absolutely not be taken as an indicator of the extent of my gratitude. I've had so much help and encouragement from friends, family and colleagues, that I couldn't possibly attempt to rank or quantify their respective contributions. That being said, if you're reading this you probably have a pretty good idea of how much you helped, so why not commend or admonish yourself accordingly.

First, my mam, Dianne and dad, Mark. In the acknowledgements section of many theses family are thanked last, but since my parents share the responsibility (blame?) for my actually being here, thanking them first seems to make more sense. They also encouraged me to do well at school, college, etc. and made financial contributions in times of need. As did my grandma, Maureen, who is happy that I'm soon to be at least a *type* of doctor. Thanks also to my uncle, Cliff, who inspired me to take up squash, thus ensuring that, unlike many science postgraduates, I was able to maintain something of a social life outside the department.

Sarah Cowin (soon to be Sarah Maskery) has, and always will have, all the love and gratitude I can give. This may be a good opportunity to let Sarah know, before she reads about it in a later chapter, that the squid I sometimes worked with is not quite what I let her believe. Sorry.

My friends can be categorised thus; Warwick friends, York friends, Home friends. I'd like to thank them all for... mainly just keeping me going. Over the years I've always been able to rely on them for support, advice and distractions from the mundane. My thanks to David Gillespie, James Keaveney, Peter Watt, Kirsten Cooper, Amy Milka, David Coates, Christopher Windle, Colin Baker, (H)Amy-Claire Scott, Alberto Furlan, Davina Chauhan, Lianne Scruton, Raphael Clarkson and Nathan Evans.

Moving to the friend/co-worker category, special thanks go to the most recent lineup of Magnetic Compton Scattering students; David Pickup, David Kersh and Matthew Butchers.

My thanks to fellow scatterers Jon Taylor, Sean Giblin and Steve Dugdale, and also to Chris Burrows and Mo Saghir, surface scientists extraordinaire and ever-willing collaborators of the Compton group.

My thanks go to all the academics at Warwick who supported my research with useful advice and discussions, and provided access to the equipment I needed to get the job done. Thanks to Martin Lees, Oleg Petrenko, Don Mck. Paul and Geetha Balakrishnan. Also, thanks to Tom Hase for consistently forcing me to consider statistics and for helping me to become a better lab demonstrator. Thanks too, to the academics at York who deployed their combined knowledge and teaching experience at me for four enjoyable years. Some of it actually stuck.

Finally, my great thanks go to my supervisors, Jon Duffy and Gavin Bell. They gave me the opportunity to become a better physicist, and never stopped providing the knowledge, both scientific and 'real world', that I'll no doubt be using on a daily basis for the rest of my career.

Declarations

This thesis details my own independent research, except where explicitly acknowledged in the text. It has been submitted to the University of Warwick in support of my application for the degree of Doctor of Philosophy. It has not been submitted to any other academic institution. All work took place under the supervision of Dr. J. A. Duffy and Dr. G. R. Bell between October 2009 and March 2013. A list of published work, as well as items currently awaiting submission to peer-reviewed journals, is provided below.

Ian Maskery

May 2013
(*Viva voce* examination: November 2013)
(Corrected thesis submitted: January 2014)

- **I. Maskery**, J. A. Duffy, J. W. Taylor, M. W. Butchers, D. Billington, S. R. Giblin, S. B. Dugdale, Z. Bukowski, M. Itou, and Y. Sakurai, *Fe spin moment in* $EuFe_{2-x}Co_xAs_2$ *observed with magnetic Compton scattering*, (currently in preparation), 2013

- **I. Maskery**, M. W. Butchers, D. Kersh, D. Ernsting, J. A. Duffy, J. W. Taylor, S. R. Giblin, D. O'Flynn, G. Balakrishnan, M. Itou, and Y. Sakurai, *The 4f orbital occupation and magnetic structure of* $TbMnO_3$, (currently in preparation), 2013

- C. W. Burrows, A. Dobbie, M. Myronov, T. P. A. Hase, S. B. Wilkins, M. Walker, J. J. Mudd, **I. Maskery**, M. R. Lees, C. F. McConville, D. R. Leadley and G. R. Bell *Heteroepitaxial Growth of Ferromagnetic MnSb(0001) Films on Ge/Si(111) Virtual Substrates*, Cryst. Growth Des., 2013, **13**, 4923-4929

- T. D. Haynes, **I. Maskery**, M. W. Butchers, J. A. Duffy, J. W. Taylor, S. R. Giblin, C. Utfeld, J. Laverock, S. B. Dugdale, Y. Sakurai, M. Itou, C. Pfleiderer, M. Hirschberger, A. Neubauer, W. Duncan and F. M. Grosche, *Ferrimagnetism in Fe-rich* $NbFe_2$, Phys. Rev. B, 2012, **85**, 115137

- J. D. Aldous, C. W. Burrows, A. M. Sanchez, R. Beanland, **I. Maskery**, M. K. Bradley, M. dos Santos Dias, J. B. Staunton and G. R. Bell, *Cubic MnSb: Epitaxial growth of a predicted room temperature half-metal*, Phys. Rev. B, 2012, **85**, 060403

- J. D. Aldous, C. W. Burrows, **I. Maskery**, M. S. Brewer, T. P. A. Hase, J. A. Duffy, M. R. Lees, C. Sanchez-Hanke, T. Decoster, W. Theis, A. Quesada, A. K. Schmid and G. R. Bell, *Depth-dependent magnetism in epitaxial MnSb thin films: effects of surface passivation and cleaning*, Journal of Physics: Condensed Matter, 2012, **24**, 146002

- J. D. Aldous, C. W. Burrows, **I. Maskery**, M. S. Brewer, D. Pickup, M. Walker, J. Mudd, T. P. A. Hase, J. A. Duffy, S. Wilkins, C. Sanchez-Hanke and G. R. Bell, *Growth and characterisation of NiSb(0001)/GaAs(111)B epitaxial films*, Journal of Crystal Growth, 2012, **357**, 1

Abstract

This thesis documents investigations into three novel magnetic materials: the predicted half-metal, NiMnSb; the magnetoelectric perovskite, $\mathrm{TbMnO_3}$; and the layered superconductor, $\mathrm{EuFe_{2-x}Co_xAs_2}$. The first exhibits magnetism due to its $3d$ electronic bands, whilst in the other materials the magnetism is driven primarily by the $4f$ electrons of the rare-earth ions, though the $3d$ bands play an important role.

The primary investigative technique was magnetic Compton scattering. This probes the spin momentum density of a material, allowing its spin moment to be found directly and, through comparison with theoretical work, information about its electronic structure to be deduced. Other experimental techniques included SQuID magnetometry, X-ray diffraction, energy-dispersive X-ray spectroscopy and X-ray photoelectron spectroscopy. *Ab initio* calculations were performed to complement the experimental findings.

For the study of NiMnSb, a single crystal was grown and characterised with a host of experimental techniques, before being subject to magnetic Compton scattering. Characterisation confirmed that the crystal was of high quality in terms of its chemical composition and single-phase structure. Magnetisation measurements showed that the total magnetic moment was very close to the expected 4 μ_B/f.u. and indicated a deviation from Bloch's law for magnetisation as a function of temperature, which was unexpected for this type of ferromagnet. The experimental magnetic Compton profiles yielded spin moments in relatively good agreement with conventional magnetometry, but their shapes were irreconcilable with *ab initio* calculations. Good experimental-theoretical agreement was achieved by manually adjusting the relative magnetic contributions due to the transition metal elements, resulting in smaller- and larger-than-predicted moments for the Mn and Ni, respectively. In combination with the temperature-dependent magnetometry, the magnetic Compton scattering results indicated that the studied NiMnSb crystal probably did not possess the half-metallic electronic structure predicted by theory.

An X-ray photoelectron study of NiMnSb, MnSb and NiSb surfaces was performed with the aim of finding a preparation method that removed contaminants and oxidation. HCl etching, vacuum annealing and $\mathrm{Ar^+}$ ion bombardment were the preparation methods employed. An etch-anneal cycle was found to be quite effective in removing oxides and resulted in surfaces which were *almost* restored to their ideal stoichiometries.

For $\mathrm{TbMnO_3}$, magnetic Compton scattering was performed in fields above and below a metamagnetic transition which, according to an existing model for the rare-earth moments in some perovskites, marks the flipping of half of the Tb moments to align with the applied field. *Ab initio* molecular orbital calculations yielded magnetic Compton profiles for fitting to those obtained experimentally. The fitting procedure provided evidence for a $4f^{7\uparrow+1\downarrow}$ spin structure for the Tb ions, with the doubly occupied orbital being the $4f_{z(x^2-y^2)}$. This spin configuration is consistent with the deduced spin and orbital moments, as well as previous predictions from density-functional theory. The angle the Tb moments make with the b-axis was found to be $\sim 60°$, slightly larger than the value previously put forward for this system. This is believed to be the first instance that the Ising-like model has been verified using separate spin and orbital contributions to the Tb magnetism.

Samples of $\text{EuFe}_{2-x}\text{Co}_x\text{As}_2$, with $x = 0$ and 0.3, were studied with SQuID magnetometry and magnetic Compton scattering. A range of informative parameters including the saturated moment, Curie constant and Curie-Weiss temperature were obtained from analysis of the total magnetisation as a function of applied field and temperature. These agreed with results from other authors. The spin moments from magnetic Compton scattering agreed broadly with the total moments, indicating that there is no orbital moment present in the system, though further work in this area is recommended. Fitting theoretical Compton profiles to a high statistics amalgamation of $\text{EuFe}_{2-x}\text{Co}_x\text{As}_2$ data indicated a negatively polarised Fe spin moment of size $(-4.7 \pm 0.08)\%$ of the total, that is $\sim -0.31 \pm 0.05\ \mu_{\text{B}}$/f.u., while temperature-difference magnetic Compton profiles provided no evidence for the anomalous temperature effects seen by other authors in a similar compound.

Chapter 1

Introduction

This thesis details investigations into three quite different magnetic materials; NiMnSb, $TbMnO_3$ and $EuFe_{2-x}Co_xAs_2$. The materials fall into the categories of half-metallic ferromagnets (HMFMs), magnetoelectric multiferroics and layered superconductors, thus spanning a large area of research in modern condensed matter physics.

The primary experimental technique was magnetic Compton scattering. This uses high energy circularly polarised photons to probe the spin-polarised electron momentum density of a material. In turn, and often through comparison with theoretical work, this allows the identification of orbital/band-specific contributions to the material's spin moment because of their characteristic electron momentum density distributions. In combination with conventional magnetometry, magnetic Compton scattering enables a material's spin and orbital magnetic moments to be resolved.

Aims

The main aims of this research were:

- To produce a high quality single crystal of the predicted half-metallic ferromagnetic alloy NiMnSb, and to investigate its magnetic properties with conventional magnetometry and magnetic Compton scattering. Comparison of experimental data with theoretical work will provide information about the system's spin polarisation, which is predicted to be 100% and provides the main motivation for its study.
- To investigate the magnetoelectric multiferroic compound $TbMnO_3$ with magnetic Compton scattering and *ab initio* theoretical modelling. This system includes lanthanide

and transition metal ions which possess magnetic $4f$ and $3d$ bands, respectively. Identification of the system's orbital moment, as well as the assignment of the spin to the lanthanide and transition metal ions, will aid in the understanding of the mechanisms responsible for the system's concurrent ferromagnetism and ferroelectricity.

- To investigate the Fe-As layered superconductor $\mathrm{EuFe}_{2-x}\mathrm{Co}_x\mathrm{As}_2$ with conventional magnetometry and magnetic Compton scattering. The largest unresolved issue regarding this system is that of the Fe spin moment - is a net Fe moment induced with an applied field, or is the magnetism solely due to the Eu ion? Another issue is the origin of the Eu spin moment - is it entirely of $4f$ orbital character, or are there contributions from $5d$ electrons also, as in pure Gd? Magnetic Compton scattering is the ideal experimental tool to address these issues.

1.1 Magnetic Compton scattering - brief overview

A brief overview of the primary experimental technique of this thesis is given here. A more detailed description is to be found in Chapter 3.

The Compton effect, discovered by Arthur Holly Compton in 1923[1] is the inelastic scattering of a photon by an electron. The scattering process is illustrated in figure 1.1 and described by equation 1.1, which is valid for a stationary target electron only. We have that

$$E_2 = \frac{E_1}{1 + \left(\frac{E_1}{m_e c^2} (1 - \cos\phi) \right)}, \tag{1.1}$$

where E_1 and E_2 are the energies of the incident and scattered photons, respectively, ϕ is the scattering angle, m_e is the electron rest mass and c is the velocity of light. Significantly, when the initial momentum, $\boldsymbol{p}$, of the scattering electron is considered, the energy shift is given by

$$E_2 - E_1 = \frac{\hbar^2 \boldsymbol{q}^2}{2m_e} + \frac{\hbar \boldsymbol{q} \cdot \boldsymbol{p}}{m_e}, \tag{1.2}$$

where $\boldsymbol{q}$ is the scattering vector (equal to the difference between incident and scattered photon wavevectors, $\boldsymbol{k}_1 - \boldsymbol{k}_2$) and $\hbar$ is the reduced Planck constant. The second term in this equation acts to Doppler-broaden the measured photon energy peak at E_2 and provides the sensitivity

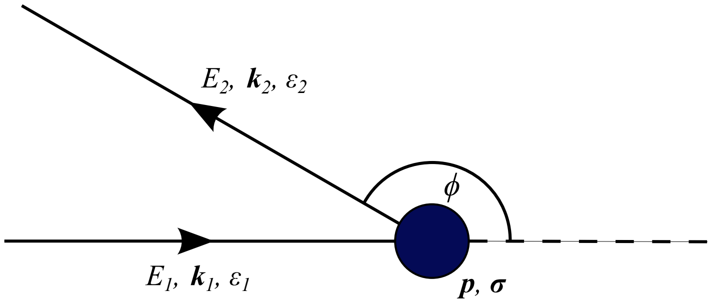

Figure 1.1: An incident photon with energy E_1, wave vector $\boldsymbol{k}_1$, and polarisation ε_1 is scattered by an electron of momentum $\boldsymbol{p}$ and spin σ. The scattered photon leaves with E_2, $\boldsymbol{k}_2$ and ε_2. The scattering angle is ϕ.

to the momentum of the electron. When a system of many electrons is considered, the energy distribution of the scattered photons represents the electron momentum density distribution of all of the electrons in a material.

Magnetic Compton scattering follows the same process as described above, but involves circularly polarised photons which couple to the electron spins. The scattered photon spectrum yields a magnetic Compton profile (MCP), from which a material's spin moment can be deduced directly. The extent of the spatial localisation or itinerancy of the system's spins is reflected in the shape of the MCP; this serves as a useful tool for separating magnetic contributions in a system with both lanthanide and transition metal ions, for example, where the spins of the former are localised and the latter have a larger spatial distribution.

1.2 Chapter synopsis

Chapter 2 of this thesis provides an overview of the behaviour of electrons in solids, with emphasis on those properties which are relevant for the materials examined in later chapters. The concepts of atomic orbitals and electronic bands in solids are introduced, as well as the forms of magnetic order and the mechanisms responsible for them. Also discussed are the phenomena of the magnetoelectric effect and superconductivity, both intimately linked to magnetism.

In Chapter 3, the primary experimental method of this thesis, magnetic Compton scattering, is outlined in some detail. The equations which describe Compton and magnetic Compton scattering are introduced, as is the MCP, the analysis of which constitutes a significant part of the experimental analysis in later chapters.

Chapter 4 describes the numerous experimental techniques deployed throughout this thesis, beginning with the production and use of high energy, polarised photons at synchrotron facilities, and continuing with the characterisation methods deployed at Warwick. Theoretical techniques, namely molecular orbital calculations and density-functional theory, are discussed in Chapter 5.

Chapters 6, 7 and 8 deal with the investigations into NiMnSb, $TbMnO_3$ and $EuFe_{2-x}Co_xAs_2$, respectively. In each of these chapters, the system is introduced along with the current state of the research into its magnetic properties. Experimental and theoretical results are provided and discussed with respect to current theories and other experimental evidence. The conclusions of the work in this thesis are given in Chapter 9, along with suggestions for future work.

Chapter 2

Electrons in solids

This chapter provides a short introduction to the behaviour of electrons in solids. The Schrödinger equation, which is of central importance in the quantum mechanical description of solids, is introduced and some key results regarding atomic orbitals and electronic bands are provided. In addition, the physical mechanisms that lie behind magnetism, superconductivity and the magnetoelectric effect are discussed.

2.1 Atomic orbitals and band theory

The Schrödinger equation

The best place to start an overview of atomic orbitals and bands may be with the Schrödinger equation, as given in equation 2.1 (which is the time-*independent* part only). Put forward nearly ninety years ago, it provided physicists with one of their most powerful and frequently used tools for understanding the behaviour of quantum mechanical systems. Prior to this, only classical or semi-classical descriptions of atoms and metals were available. Bohr's atomic model was an improvement on prior attempts and was successful in predicting the energy levels of hydrogen-like atoms. Likewise, Drude's 'free electron gas' description of metals was sufficient to explain DC and AC conductivity, as well as the Hall effect. However, both models failed in some regard to predict experimental phenomena. The Schrödinger equation not only offered verifiable predictions and was consistent with established physics, it also gave tremendous insight into the nature of particles. We have that

$$\widehat{\mathrm{H}}\psi(\boldsymbol{r}) = \left(-\frac{\hbar^2}{2m_e}\nabla^2 \; + \; V(\boldsymbol{r})\right)\psi(\boldsymbol{r}) = E\psi(\boldsymbol{r}). \tag{2.1}$$

The Hamiltonian, $\widehat{\mathrm{H}}$, operating on a wavefunction, $\psi(\boldsymbol{r})$, is intrinsically modifiable. In its simplest form it describes a system with kinetic energy only (with the quantum mechanical operator $\widehat{T} = -\hbar^2/2m_e\nabla^2$), but any potential, $V(\boldsymbol{r})$, may be added. Typical $V(\boldsymbol{r})$ terms include the potential from atomic nuclei and periodic crystals, as well as electron exchange and correlation, which provide solutions for magnetic and strongly-correlated systems.

Free electron solution

The solution for the case of a single free electron is obtained using a trial wavefunction of the form $A\mathrm{e}^{(\boldsymbol{b}\cdot\boldsymbol{r})}$. Applying the kinetic energy operator and the normalisation condition $\int_{-\infty}^{\infty} |\psi(\boldsymbol{r})|^2 \,\mathrm{d}\Omega = 1$ (the electron must be found in some volume Ω) then provides

$$\psi(\boldsymbol{r}) = \frac{1}{\sqrt{\Omega}}\,\mathrm{e}^{i(\boldsymbol{k}\cdot\boldsymbol{r})}, \tag{2.2}$$

$$E(\boldsymbol{k}) = \frac{\hbar^2\boldsymbol{k}^2}{2m_e}, \tag{2.3}$$

where equation 2.3 is the free electron dispersion relation, analogous to the classical quadratic increase in kinetic energy due to momentum, that is $E(\boldsymbol{p}) = \boldsymbol{p}^2/2m$.

Solution for H-like ions

After the free electron solution, we can introduce a nuclear potential, $V_{\mathrm{n}}(r) = -Ze^2/(4\pi\epsilon_0 r)$, into the Schrödinger equation to find solutions for H-like atoms, i.e. those with effectively one electron. The solutions are the atomic orbitals:

$$\psi(r,\theta,\phi) = R(r)Y(\theta,\phi), \tag{2.4}$$

$$\psi_{n,l,m}(r,\theta,\phi) = NR_{n,l}(r)P_l^{m_l}(\cos\theta)\mathrm{e}^{im_l\phi}. \tag{2.5}$$

In equation 2.5, N is a constant for normalisation and $R_{n,l}(r)$ is a general solution for the radial part of the wavefunction. It has a dependence on the associated Laguerre polynomials which exist only for $n \geq l$, with integer n and l. $P_l^{m_l}$ are the solutions to the polar part; they are the Legendre functions. For the azimuthal part, the general solution is $F(\phi) = Ae^{c\phi}$, but the condition $F(\phi) = F(\phi + 2\pi)$, that the wavefunction should be the same at $\phi = 0°$ and 360°, means that the solution $F(\phi) = A\mathrm{e}^{im_l\phi}$ is needed. The m_l values range from -l

to l. These solutions provide the shell-like ordering of electrons around nuclei and describe the shapes of their l-dependent orbits. We also obtain the result that the orbital angular momentum in an atom is quantised with $L = m_e v r = n\hbar$ (with n as a positive integer), which is exactly that proposed by Bohr[2].

The periodic potential of a crystal

Finally, and rather importantly for the purposes of solid state physics, the case of a periodic potential from a crystal is considered. Bloch's theorem states that the resulting wavefunctions can be expressed as

$$\psi_{n,\boldsymbol{k}}(\boldsymbol{r}) = \mathrm{e}^{i(\boldsymbol{k}\cdot\boldsymbol{r})} u_{n,\boldsymbol{k}}(\boldsymbol{r}), \tag{2.6}$$

where $e^{i(\boldsymbol{k}\cdot\boldsymbol{r})}$ are simple plane waves and $u_{n,\boldsymbol{k}}(\boldsymbol{r})$ are functions with the same periodicity as the crystal potential. The corresponding energies follow

$$E_n(\boldsymbol{k}) = E_n(\boldsymbol{k} + \boldsymbol{G}), \tag{2.7}$$

and are therefore periodic in any particular direction in $\boldsymbol{k}$-space. The periodicity is determined by $\boldsymbol{G}$, which is given by

$$\boldsymbol{G} = c_1\boldsymbol{b}_1 + c_2\boldsymbol{b}_2 + c_3\boldsymbol{b}_3, \tag{2.8}$$

where $c_{1,2,3}$ are integers and $\boldsymbol{b}_{1,2,3}$ are the primitive vectors of the reciprocal-space lattice. The latter vectors are determined by a set of vector products of the real-space lattice vectors.

Equations 2.6, 2.7 and 2.8 ultimately provide the band description of electrons in solids, what might be considered the 'large-scale limit' of molecular orbital theory. When many atoms are brought together, their wavefunctions overlap and form molecular orbitals with distinct energies due to the Pauli exclusion principle. When the number of atoms is sufficiently large, of the order 10^{20} or more, the energy levels are so numerous and closely spaced that they form continuous bands in $\boldsymbol{k}$-space. $\boldsymbol{k}$-space, which is interchangeable with momentum space due to de Broglie's $\boldsymbol{p} = \hbar\boldsymbol{k}$, provides an often superior way of representing the electronic structure of periodic solids compared to the simpler case of the potential from a single atomic nucleus.

Generally, when a material's electronic structure is analysed, it is only within a small section

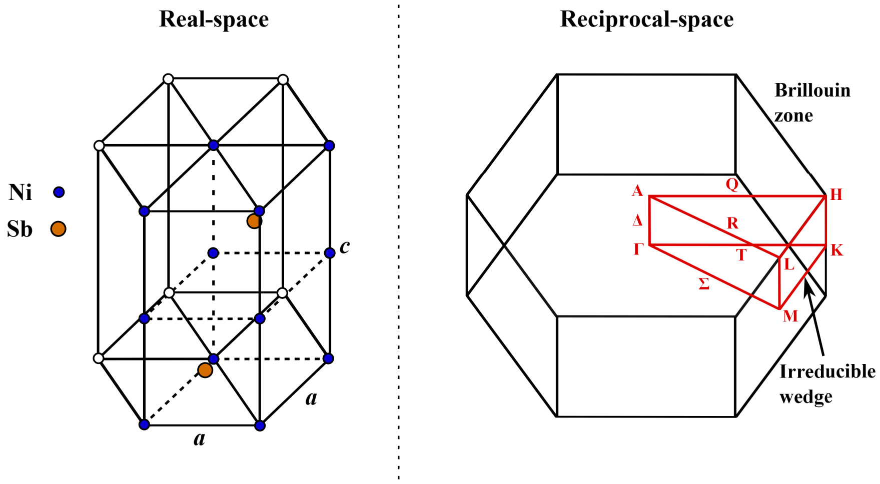

Figure 2.1: The real-space NiSb crystal structure (left) and corresponding first Brillouin zone and irreducible wedge (right). Blue and orange spheres represent Ni and Sb atoms, respectively, and, on the right, a selection of special $\boldsymbol{k}$ vectors are shown. These relate to the notation in figure 2.2 - the NiSb electronic band structure.

of all available $\boldsymbol{k}$-space - the first Brillouin zone (BZ). Further still, information from a part of the BZ refererd to as the irreducible Brillouin zone (IBZ) or irreducible wedge, is sufficient to describe the entire system. The BZ is a primitive cell in reciprocal space; its size and shape are determined by the real-space positions of the atoms in the crystal. Figure 2.1 shows the real-space crystal structure and reciprocal-space first BZ for a hexagonal system, chosen for its relevance to the material NiSb, which is employed below to exemplify an electronic band structure diagram and density-of-states (DoS). For a more involved discussion of reciprocal-space, $\boldsymbol{k}$-space and the Brillouin zone, and their significance in solid state physics, the interested reader is directed to Kittel's *Introduction to Solid State Physics* (page 37)[3].

Band structure and density-of-states

Figure 2.2 shows the relationship between a material's electronic band structure and its DoS. The material in question is the paramagnetic alloy NiSb. This is closely related to MnSb, which is of great interest as a potential half-metal, and both materials are discussed further in section 6.6, which provides the results of an X-ray photoelectron spectroscopy (XPS) study on their surfaces. The features most readily identified in the NiSb DoS are the parabolic s states of Sb, lying between -12 and -9 eV, and the flatter, almost dispersionless, d-like bands of Ni, from -6 to -1 eV. Figure 2.2's main purpose here is to illustrate that the DoS of a particular system may be thought of as a summation of electronic bands over all $\boldsymbol{k}$-space. When the

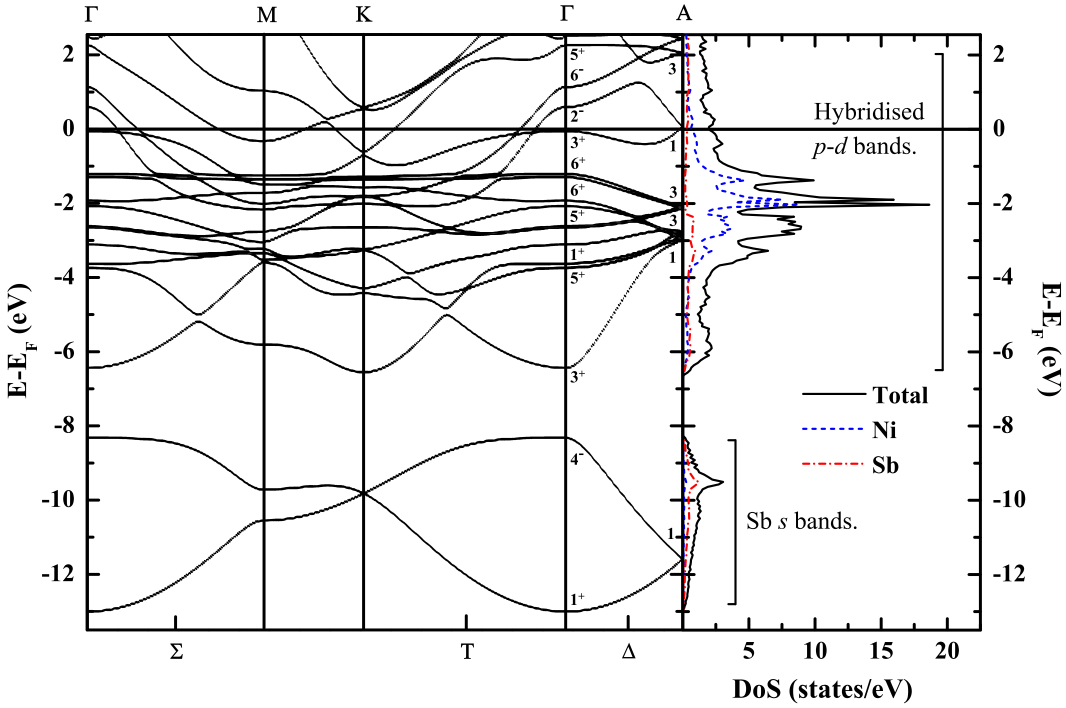

Figure 2.2: Band structure and density-of-states of NiSb, calculated with the SPR-KKR DFT package (see section 5.3). The band labelling scheme ($1^+, 4^-, 3^+$, etc.) is that used by Coehoon, Haas and de Groot in their theoretical work on MnSb[4]; those authors denoted the MnSb bands according to a basis set of s, p and d wavefunctions. (This work saw publication in the *Journal of Crystal Growth*[5] and, at the time of writing, represents the only known theoretical band structure for NiSb in the literature. The corresponding Fermi surface for this calculation exhibited the electron and hole features seen by Motizuki *et al.* with de Haas-van Alphen measurements and full-potential DFT[6].)

position of the Fermi energy is noted, the DoS indicates which bands are occupied and neatly signifies some of the bulk properties of the system, specifically the metallicity and magnetism. In the example of NiSb, there is a continuum of populated states (of hybridised p-d type) across the Fermi level, indicating that this material is a conductor.

2.2 Magnetism

Direct exchange

Every material exhibits diamagnetism and paramagnetism. Diamagnetism is simply the tendency for the motion of electrons to create an internal magnetic field which opposes that applied externally. Paramagnetism is the alignment of a material's spins with a field large enough to overcome the diamagnetic effect. This provides the paramagnetic material a net magnetic moment, which is lost when the external field is removed. Within metals or strongly-correlated systems, interactions between electron spins may lead to some form of spontaneous alignment below a characteristic temperature; the Curie temperature, T_{C}, for ferromagnets and the Néel temperature, T_{N}, for antiferromagnets. The direct exchange interaction is a consequence of the Pauli exclusion principle; specifically, the insistence that the total wavefunction for a pair of overlapping electrons remains antisymmetric when their positions and spins are exchanged. The total energy associated with the interaction was defined by Heisenberg as

$$\widehat{\mathrm{H}} = -\sum_{ij} J_{ij}\ \boldsymbol{S}_i \cdot \boldsymbol{S}_j, \tag{2.9}$$

where the summation is performed over all pairs of spins, $\boldsymbol{S}_i$ and $\boldsymbol{S}_j$, in the crystal. J_{ij}, the

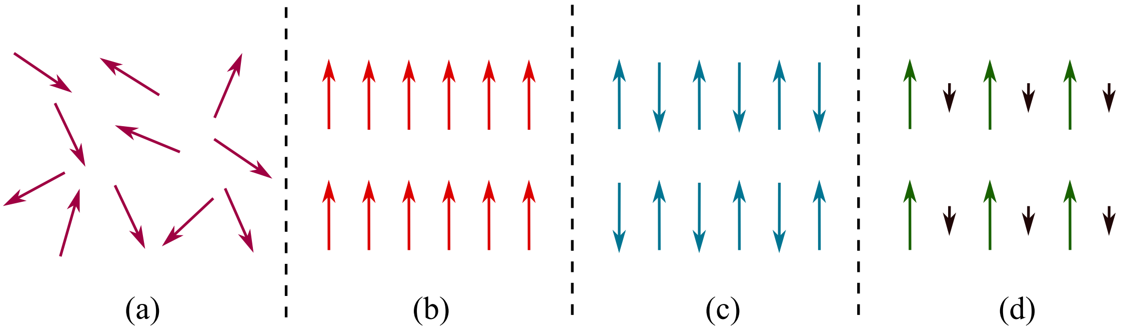

Figure 2.3: (a) Paramagnetism, (b) ferromagnetism, (c) G-type antiferromagnetism (where the inter- and intra-plane coupling is antiferromagnetic) and (d) ferrimagnetism.

exchange constant, is a function of the separation between the spins. It can be positive or negative, resulting in a reduced energy when the alignment is ferromagnetic (parallel) or antiferromagnetic (antiparallel), respectively. A fourth type of magnetic order, known as ferrimagnetism, exists when the magnetic moments of different sublattices are opposed, but the moments are of different magnitudes, so a net magnetisation remains. Paramagnetism, ferromagnetism, antiferromagnetism and ferrimagnetism are illustrated in figure 2.3.

Indirect exchange

As well as by direct overlap of their wavefunctions, electrons may be coupled through some *indirect* exchange mechanism. There are various kinds, with varying degrees of complexity, but the two most commonly encountered are superexchange and the Ruderman-Kittel-Kasuya-Yosida (RKKY) interaction[7]. In the former, the exchange between two magnetic ions is conveyed by a non-magnetic intermediary; it is often seen for TM-O-TM chains, where TM is a transition metal and O is oxygen. An illustration of superexchange is given in figure 2.4, which shows the case for σ-type bonding between the e_g orbitals of two magnetic ions. The oxygen ion has two electrons in its p orbital and, because of the Pauli exclusion principle, their spatial freedom is increased if they are of opposite spin to each other *and* the neighbouring, and overlapping, TM d orbitals. Having a large spatial extent minimises their energy, making the anti-alignment of the magnetic ions preferable.

The RKKY interaction occurs when the exchange between magnetic ions is mediated by the conduction electrons, which are said to become magnetically 'polarised'. As in direct exchange,

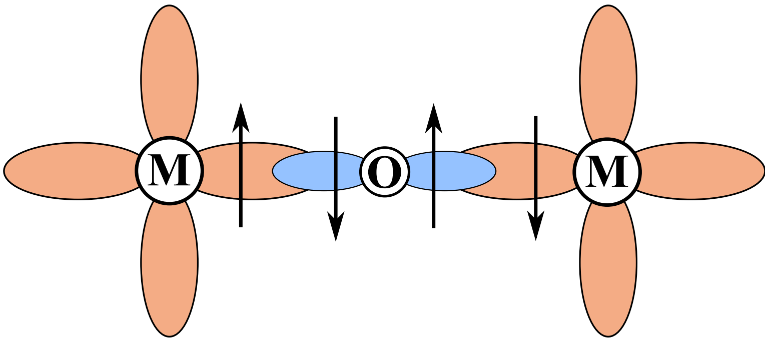

Figure 2.4: The superexchange mechanism. The exchange interaction is mediated by a non-magnetic ion - in this case, oxygen. Antiferromagnetic alignment of the magnetic ions (M) is favoured when the oxygen (O) spins are antiparallel.

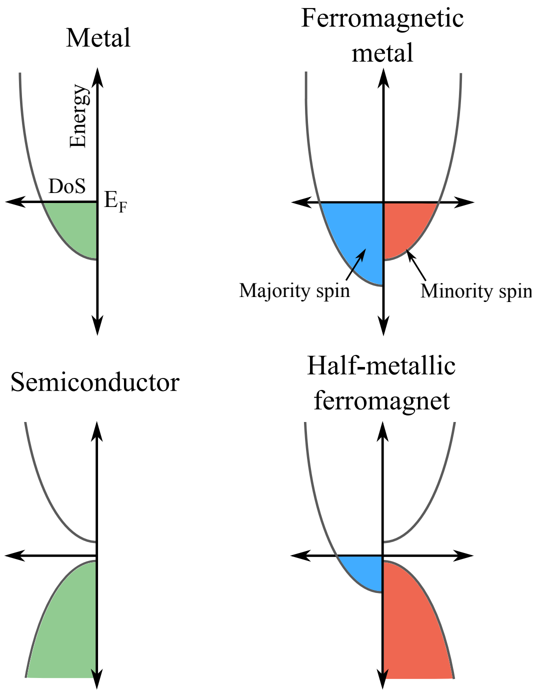

Figure 2.5: Simplistic densities-of-states illustrating the electronic structure around the Fermi energy of several classes of material.

the exchange constant is determined by the separation between spins, but in the RKKY interaction, J_{ij} also varies sinusoidally with distance. The coupling between any two magnetic ions may therefore be ferromagnetic or antiferromagnetic, depending on their separation. This can lead to quite complex magnetic structures in metallic systems and may also provide a degree of magnetic frustration, a phenomenon which attracts a large amount of research in condensed matter physics.

Figure 2.5 shows simplistic DoS diagrams for several classes of material; a metal, a semiconductor, a ferromagnetic metal and a half-metallic ferromagnet. The ferromagnet exhibits an imbalance of populated majority and minority spins, giving rise to a net spin moment. The ideal half-metal has a semiconducting band gap in one of its spin channels, usually given as the minority channel. This provides the material with a net spin moment which is an integer number of Bohr magnetons, μ_B, where 1 μ_B is the intrinsic spin carried by a single electron.

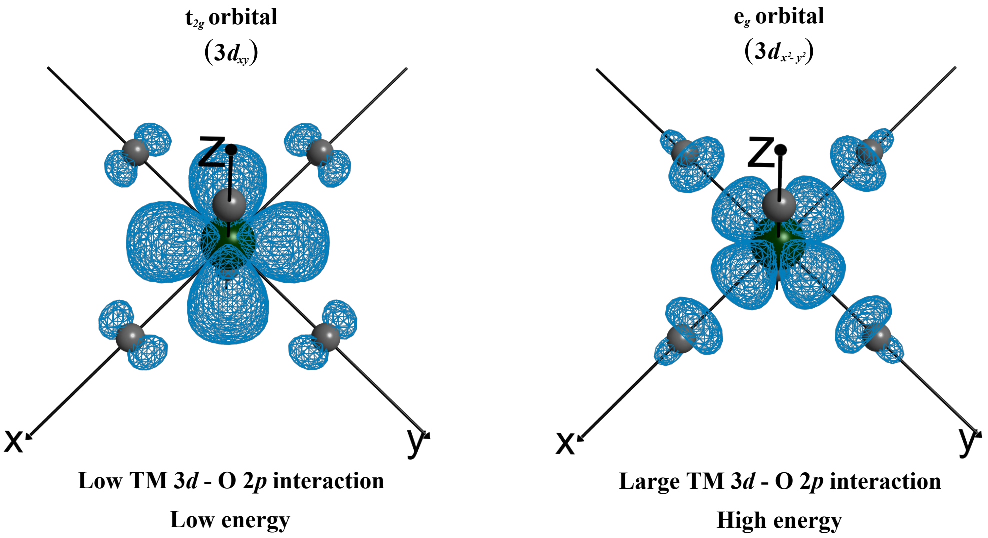

Figure 2.6: The crystal field splitting mechanism for TM-O_6 octahedra. This example is that of an e_g ($3d_{xy}$ type) and a t_{2g} ($d_{x^2-y^2}$ type) orbital of a MnO_6 octahedra, as found in $TbMnO_3$ and similar perovskite systems. In each case, the central fourfold-symmetric orbital is that of the Mn ion (dark green sphere), while the others are the p orbitals of the oxygen ions (grey spheres). The energy of the t_{2g} orbital is higher than the e_g orbital because of the larger interaction with the O $2p$ charge distribution.

2.3 Crystal field splitting and the Jahn-Teller distortion

This section is relevant mainly for the work on $TbMnO_3$, as discussed in Chapter 7, which possesses MnO_6 octahedra with the kind of orbital splitting and distortion discussed here.

Transition metal and oxygen ions generally have ‘active’ $3d$ and $2p$ atomic orbitals, respectively. These are the orbitals which primarily interact with other atoms, giving rise to the bonding and, often, the electronic and magnetic properties of the solid. For a free TM ion, the $3d$ orbitals are energy-degenerate, but once surrounded by oxygen ions, interaction with their $2p$ orbitals lifts the degeneracy and sub-levels are formed. For the specific case of octahedral coordination (a central TM ion with equally spaced oxygen ions along the x-, y- and z-axes), the $3d$ band splits into t_{2g} and e_g sub-levels. The p_x, p_y and p_z orbitals of oxygen point along the axes and interact repulsively with the TM e_g orbitals, raising their energy compared to the t_{2g}, which mainly lie between the axes. This mechanism and resultant energy splitting are illustrated in figures 2.6 and 2.7, respectively.

Another reduction in the total energy of a TM-O_6 octahedron may be achieved by means of a

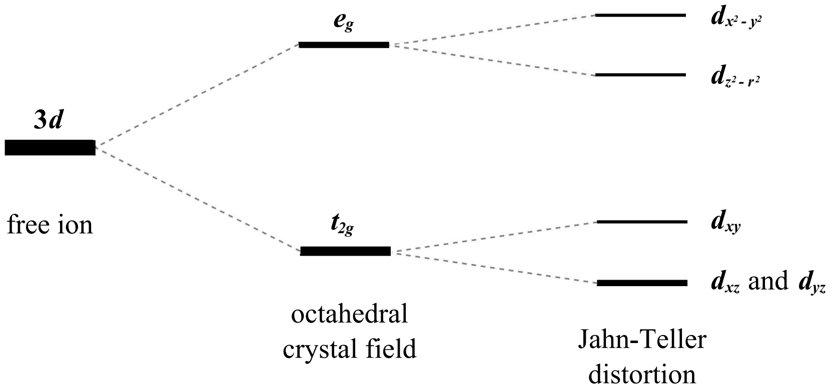

Figure 2.7: The effect of the crystal field and the Jahn-Teller distortion on $3d$ energy levels.

Jahn-Teller distortion. This is essentially a stretching of the octahedron along some direction, usually, but not always, the z-axis. The effect is to split the t_{2g} and e_g sub-levels further, into the constituent d_{xy}, d_{xz}, d_{yz}, $d_{z^2-r^2}$ and $d_{x^2-y^2}$ orbitals. Because of the Jahn-Teller distortion, the z-axis TM-O separation is larger, while the separation along x and y is smaller. This reduces the energy of the $d_{z^2-r^2}$ orbital and raises the energy for $d_{x^2-y^2}$. Again, figure 2.7 provides the resulting energy level arrangement. For a Mn^{3+} ion (with 4 electrons in its $3d$ shell) the final spin state, providing Hund's rules apply, becomes $3d$ t_{2g}^3 e_g^1, with the occupied e_g orbital being the low energy $d_{z^2-r^2}$.

Note that for $3d$ systems, crystal field effects like those described above tend to be much larger than the spin-orbit interaction that would otherwise determine their electron energy levels. For $4f$ systems the opposite is true; the spin-orbit coupling is the dominant term. This means that, even in a crystalline environment, $4f$ ions generally possess a simple Hund's rule spin configuration, with all 7 m_l levels being filled with one spin type before the other.

2.4 Quenching of orbital moments

Orbital quenching, that is the reduction of the angular component of the magnetic moment to zero, is another consequence of crystal field effects. It arises principally because, in a non-spherically-symmetric potential (i.e. a crystalline environment), the relatively itinerent d electrons of the transition metals react strongly to external influences (other electrons) and do not maintain the orbital shapes, or current loops, which give them their classical magnetic moments. The effect is especially pronounced in situations where the crystal field is much stronger than the spin-orbit interaction of the unpaired electrons; this condition is true of most transition metals, though Co^{2+} and Ni^{2+} are examples where the $\boldsymbol{L} \cdot \boldsymbol{S}$ coupling and crystal field are of similar magnitude, resulting in a *partially*-quenched orbital moment only. From a theoretical standpoint, and more generally, it can be shown that the expectation value for an angular momentum operator, $\langle L_z \rangle$ for example, applied to an electronic orbital in a crystal environment must be both imaginary and, because it is an obervable, real. This condition can only be met if it is zero[8].

2.5 The magnetoelectric effect

Magnetoelectric materials, of which $\mathrm{TbMnO_3}$ is an example, have the unusual property of exhibiting electric polarisation in an applied magnetic field *and* spontaneous magnetisation in an applied electric field. They are quite rare, and a discussion of the magnetoelectric mechanism explains why this is the case.

There exist terms relating a material's electric polarisation, $\boldsymbol{P}$, and magnetisation, $\boldsymbol{M}$, to applied magnetic and electric fields, respectively. These might be thought of as higher order terms in the traditional Maxwell equations. They have the form

$$\boldsymbol{P}(\boldsymbol{H}) = \alpha \boldsymbol{H}, \tag{2.10a}$$

$$\boldsymbol{M}(\boldsymbol{E}) = \alpha \boldsymbol{E}, \tag{2.10b}$$

where α is the magnetoelectric susceptibility tensor. For most materials $\alpha = 0$; this is because most materials possess spatial and/or temporal inversion symmetry. To demonstrate: if $\boldsymbol{M} = \alpha \boldsymbol{E}$ then, under time reversal, we must have $-\boldsymbol{M} = \alpha \boldsymbol{E}$, because the magnetisation, which is classically due to a current loop, changes direction if time is reversed, while the electric field does not. For this to be true, α must be zero. Only materials which lack both spatial and temporal inversion symmetry can have a non-zero α and exhibit magnetoelectricity[9]. Indeed, Brown *et al.*[10] provided the inequality

$$\alpha_{\eta\xi} < 4\pi(\chi_\eta \, \kappa_\xi)^{1/2}, \tag{2.11}$$

suggesting large magnetoelectric coupling only for materials with large magnetic, χ_η, and/or, electric, κ_ξ, susceptibilities, i.e. good ferromagnets or ferroelectrics.

2.6 Superconductivity

$EuFe_{2-x}Co_xAs_2$, the material examined in Chapter 8, is a high temperature superconductor. The aim of developing superconducting materials with high transition temperatures, T_{SC}, drives a lot of the ongoing research into superconductivity, and crucial to this is the understanding of the physical mechanisms responsible for the phenomenon. The interested reader is directed to Kittel's *Introduction to Solid State Physics* (page 333)[3] and Annett's *Superconductivity, Superfluids and Condensates* (page 47)[11], both of which offer an account of Bardeen, Cooper and Schrieffer's BCS theory[12,13] for conventional superconductors. For a detailed account of unconventional superconductivity in particular, refer to Ketterson and Song's *Superconductivity*[14].

Unconventional superconductivity

Superconducting materials that can not be described by BCS theory are referred to as 'unconventional'. Their ground states possess a different form of symmetry to the conventional superconductors, where the superconducting gap has a constant value under the available symmetry operations of the Brillouin zone. The usual isotropy of the gap is due to the Cooper pairs, which are s-wave spin-singlet states. However, unconventional superconductors have anisotropic, or *nodal*, superconducting gaps that are increasingly believed to have highly two-dimensional $d_{x^2-y^2}$ symmetry in the Brillouin zone, though the determination of the exact pairing mechanism responsible represents a large fraction of the ongoing research.

Cuprates and FeAs superconductors

The unconventional superconductors tend to have T_{SC} higher than the theoretical maximum predicted by BCS theory, which is around 30 K. Though assignment of a particular material into the group of unconventional superconductors is somewhat controversial, since the superconducting mechanism is not yet fully understood, examples are generally accepted to include the highly-studied cuprate systems such as $YBa_2Cu_3O_7$ (YBCO) with $T_{\mathrm{SC}} = 93$ K[15], $BiSrCaCu_2O_x$ (BSCCO) with $T_{\mathrm{SC}} = 105$ K[16] and $HgBa_2Ca_2Cu_3O_{8+\delta}$ with $T_{\mathrm{SC}} = 135$ K[17] that contain nearly two-dimensional layers of copper and oxygen. Strong supporting evidence for the classification of YBCO as unconventional came from the temperature dependence of its London penetration depth (the depth inside a material at which an external magnetic field is screened to zero). This was seen to have a linear T dependence in accordance with the d-wave model for its superconductivity[18].

The more recently discovered iron arsenide superconductors, such as $EuFe_{2-x}Co_xAs_2$, possess FeAs layers that are similar to the CuO layers of the cuprates. However, for the FeAs systems there is a great deal of ongoing debate regarding the nature of the superconducting pairing mechanism, with s-wave (nodeless gap) and d-wave (nodal gaps) theories currently existing. There is evidence from various types of experiment for both kinds of pairing symmetry[19–26]. Maitai *et al.* and Hirschfeld *et al.* recently suggested that both s-wave and d-wave superconductivity was possible in the FeAs materials, and that the mechanisms compete depending on the level of electron or hole doping[27,28].

Chapter 3

Magnetic Compton scattering

This chapter provides an overview of Compton scattering and its magnetic counterpart. These experimental techniques directly probe the electron and spin densities of a given material. When analysed within the context of other experimental and theoretical results, Compton and magnetic Compton scattering allow a great deal of information about a system's electronic and magnetic structures to be found.

With respect to the theory of Compton scattering, emphasis here is placed on those aspects which are of most relevance to the experimenter. More advanced discussions of scattering theory, cross sections, and momentum density transformations can be found in a number of sources, though the book *X-ray Compton Scattering* by Cooper *et al.*[29] is regarded as one of the best; Chapter 2 focuses on theoretical issues and the derivation of key formulae.

3.1 The history of Compton scattering

A short history of Compton scattering is given below; for a full account, the interested reader is directed to the work of Stuewer[30].

Compton's experiments

Between 1921 and 1922, A. H. Compton undertook X-ray scattering experiments which exhibited a previously unseen effect and provided strong evidence for a quantum mechanical description of the X-ray scattering process. In May 1923, the culmination of his experimental and theoretical work was published in *The Physical Review*[1]. The discovery would soon be known as the 'Compton effect'.

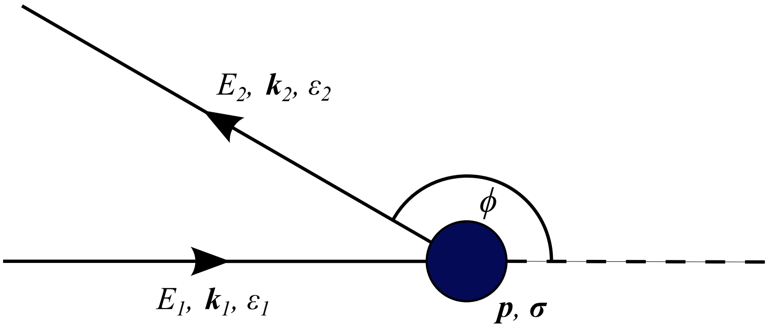

Figure 3.1: An incident photon with energy, E_1, wave vector, $\boldsymbol{k}_1$, and polarisation, ε_1, is scattered by an electron of momentum, $\boldsymbol{p}$, and spin, σ. The scattering angle is ϕ.

Compton had sent Mo K_α X-rays ($\lambda = 0.708$ Å) into samples of pyrex and graphite, observing that the scattered X-rays experienced a wavelength shift proportional to $\sin^2(\phi/2)$, where ϕ is the scattering angle. He was able to describe the scattering properly by considering the conservation of energy and momentum throughout the photon-electron interaction. His vector diagram, reproduced here in figure 3.1, and now-famous equation (equation 3.1) are synonymous with this elegant and important discovery.

Broadening of the scattered X-ray peak

An important artefact of Compton scattering, which was apparent to its discoverer but remained relatively unexploited for some time, is the broadening in energy of the scattered X-ray peak. This broadening is essentially a Doppler effect and originates from the momentum distribution of the scattering electrons. J. W. M. DuMond was one of the first to recognise this aspect of Compton scattering as a valuable probe of electron momentum densities. He demonstrated the technique in his 1929 study of electrons in beryllium, showing that the classical Maxwell-Boltzmann and Bohr-Sommerfeld models were insufficient to describe experimental results[31]. He showed that Fermi-Dirac statistics, making use of Pauli's exclusion principle, were required to replicate the width of the measured Compton profile. Though findings of this significance are understandably rare, Compton scattering has been employed in many studies in the decades since its discovery and has contributed in a range of scientific disciplines including condensed matter physics, astrophysics and biophysics. With advances in synchrotron and detector technology, it is now becoming a staple probe of electron and spin momentum densities.

3.2 The Compton scattering process

The Compton scattering process is illustrated in figure 3.1, which includes notation used in the following discussion and formulae. An incident photon with energy, E_1, wave vector, $\boldsymbol{k}_1$, and polarisation, ε_1, is scattered through an angle, ϕ, by an electron of momentum, $\boldsymbol{p}$, and spin, σ. The scattered photon leaves with E_2, $\boldsymbol{k}_2$ and ε_2.

The impulse approximation

Before continuing with a physical description of Compton scattering, it is crucial that an approximation is established and understood. For high energy photons, where the momentum and energy transfered to an electron are large, the impulse approximation (IA) is applicable[32]. This states that the photon-electron interaction is entirely impulsive. We can picture an interaction over a short timescale, where the scattered photon moves on before experiencing the target electron in its final state. In this way the scattered photon carries information about the initial electronic state only, the property of interest to the investigator. This semi-classical picture of the scattering brings us to another important consequence of the IA; magnetic Compton scattering is insensitive to the orbital moment of the electron. This is due to the fact that, in order to probe the orbital moment, the interaction time should be of the order, preferably greater than, the orbital period. In the limit of the infinitesimally short interaction time, no orbital moment is experienced by the scattered photon.

Another benefit of employing the high energy incident photons needed to satisfy the impulse approximation is the absence of absorption from the range of possible interactions. This allows us to consider somewhat simpler versions of the scattering cross sections, which retain their validity in the high energy regime. Note that photon energies up to 220 keV are used in this work, whereas absorption edges or ‘resonances’ are typically just several keV in metals.

Compton scattering equations

For the case of a stationary target electron, we can describe Compton scattering in terms of the photon wavelength shift, $\Delta\lambda$, and the scattering angle, ϕ. However, it is more useful to consider the process in terms of the incident and scattered photon energies, E_1 and E_2. We

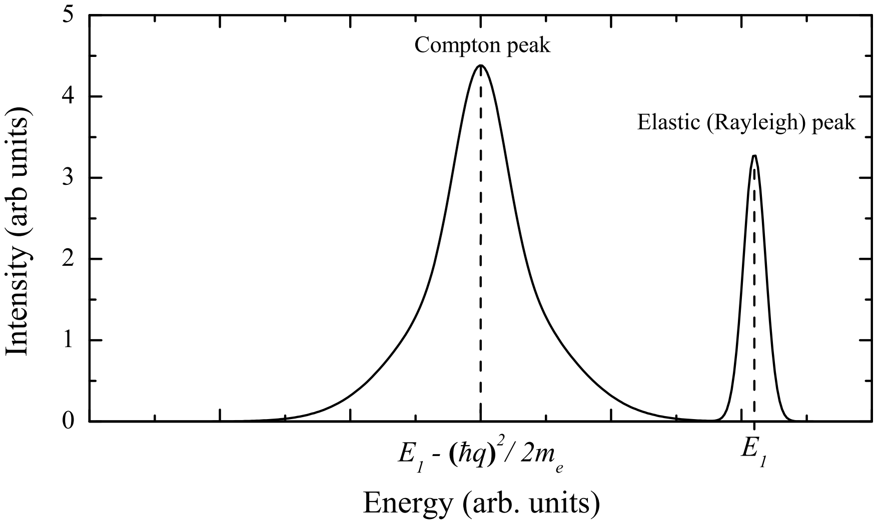

Figure 3.2: A scattered photon energy spectrum highlights the effects of both terms, the Compton shift and the broadening, in equation 3.3b. The horizontal axis displays photon energy, as opposed to the energy carried away by target electrons. Note that the relative sizes of the Compton and elastic peaks have been adjusted to better illustrate the effect of broadening due to the scattering electrons. In experimental spectra the elastic peak is generally far smaller than this.

have that

$$\Delta\lambda = \frac{2h}{m_e c}\sin^2\frac{\phi}{2} = \frac{h}{m_e c}\,(1-\cos\phi), \tag{3.1}$$

$$E_2 = \frac{E_1}{1+\left(\frac{E_1}{m_e c^2}(1-\cos\phi)\right)}. \tag{3.2}$$

Upon considering the motion of the scattering electron, we can, utilising conservation of energy and momentum, arrive at an expression for the energy lost by the photon;

$$E_2 - E_1 = \frac{(\boldsymbol{p}+\hbar(\boldsymbol{k}_1-\boldsymbol{k}_2))^2}{2m_e} - \frac{|\boldsymbol{p}|^2}{2m_e} \tag{3.3a}$$

$$= \frac{\hbar^2\boldsymbol{q}^2}{2m_e} + \frac{\hbar\boldsymbol{q}\cdot\boldsymbol{p}}{m_e}, \tag{3.3b}$$

where $\boldsymbol{q}$ is equal to $\boldsymbol{k}_1 - \boldsymbol{k}_2$, the difference between incident and scattered photon wavevectors.

Equation 3.3b reveals the photon energy loss to be made of two terms; the first is the Compton shift, dependent only on the scattering angle; the second is a Doppler broadening term, directly proportional to the component of electron momentum lying along the scattering direction. Thus, the greatest broadening of the Compton peak occurs when the scattering electron has a large momentum in the direction of $\boldsymbol{q}$. Figure 3.2 illustrates the effects of both terms.

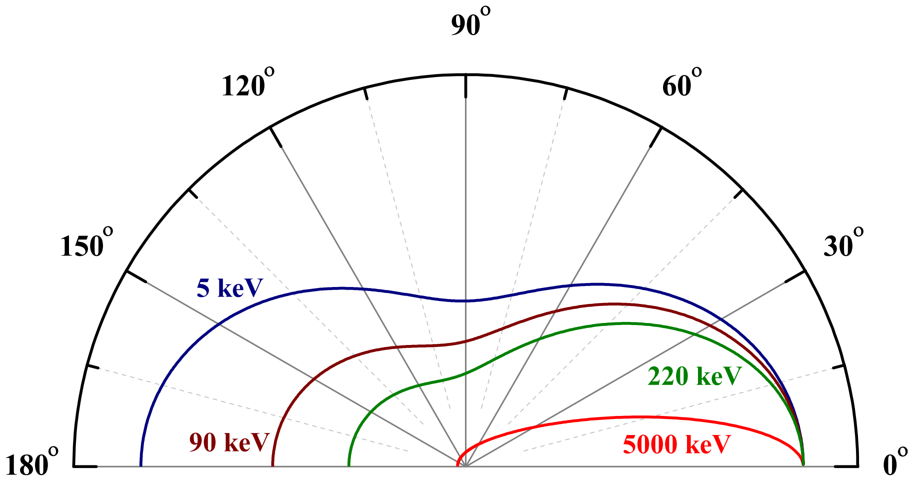

Figure 3.3: The angular-dependent scattering for a range of incident photon energies according to the Klein-Nishina cross section. Reproduced from the Ph.D. thesis of Matthew Butchers[34].

3.3 Scattering cross sections and the Compton profile

Total scattering - Klein-Nishina

Klein and Nishina put forward a general form of the photon-electron scattering cross section, capable of describing the angular- and energy-dependent scattering from a single stationary electron even when the energy of the photon approaches $m_e c^2$, which is where the classical Thomson approximation fails to provide accurate results. The cross section is given by[33]

$$\left(\frac{d\sigma(\phi)}{d\Omega}\right)_{\mathrm{KN}} = \frac{{r_e}^2}{2}\left(\frac{E_2}{E_1}\right)^2\left(\frac{E_1}{E_2}+\frac{E_2}{E_1}-\sin^2\phi\right), \tag{3.4}$$

where r_e is the classical radius of the electron;

$$r_e = \frac{e^2}{4\pi\epsilon_0 m_e c^2} = 2.81794\times10^{-15}\ \mathrm{m}. \tag{3.5}$$

The resulting scattering is shown in figure 3.3 for a range of incident photon energies. It can be seen that the amount of backscattering decreases significantly with increasing energy; on this basis alone it might be assumed that forward scattering would provide the best experimental arrangement at higher photon energies. However, once consideration is paid to the separate charge- and spin-dependent scattering cross sections, it becomes clear that backscattering is required for optimum magnetic Compton scattering. This will now be shown.

Charge and magnetic scattering

Lipps and Tolhoek examined the work of Klein and Nishina from the perspective of Compton scattering. They provided the charge- and spin-dependent scattering cross sections[35]

$$\left(\frac{\mathrm{d}\sigma(\phi)}{\mathrm{d}\Omega}\right)_{\text{charge}} = \frac{{r_e}^2}{4}\left(\frac{\boldsymbol{k}_2}{\boldsymbol{k}_1}\right)^2\left(1+\cos^2\phi+(\boldsymbol{k}_1-\boldsymbol{k}_2)\,(1-\cos\phi)+\xi_1\sin^2\phi\right) \tag{3.6a}$$

$$\left(\frac{\mathrm{d}\sigma(\phi)}{\mathrm{d}\Omega}\right)_{\text{mag}} = -\frac{{r_e}^2}{4}\left(\frac{\boldsymbol{k}_2}{\boldsymbol{k}_1}\right)^2\xi_3\,(1-\cos\phi)\,\widehat{\boldsymbol{s}}\cdot(\boldsymbol{k}_1\cos\phi+\boldsymbol{k}_2)\,, \tag{3.6b}$$

where ξ_1 and ξ_3 are the Stokes parameters for linearly and circularly polarised photons, respectively, and $\widehat{\boldsymbol{s}}$ is a unit vector in the direction of the electron spin.

Focussing on the magnetic scattering cross section, it can be seen that in order to probe the spin of the electron, circularly polarised light must be used. This cross section can be made to change sign by flipping either the photon helicity, ξ_3, or the spin magnetisation direction, $\widehat{\boldsymbol{s}}$. This property allows for an experimental procedure which selects the magnetic scattering only, providing the tool by which magnetic Compton profiles are obtained. Additionally, the $(1-\cos\phi)$ and $\widehat{\boldsymbol{s}}\cdot(\boldsymbol{k}_1\cos\phi+\boldsymbol{k}_2)$ terms dictate that the magnetic scattering is maximised when $\phi = 180°$ (complete backscattering) and when the spin moment is parallel or antiparallel to $(\boldsymbol{k}_1\cos\phi+\boldsymbol{k}_2)$. This last criteria, when backscattering is imposed and $\boldsymbol{k}_1 \parallel \boldsymbol{k}_2$, tells us that the spin moment should lie in the direction of the incident beam. Therefore, that is the direction in which the external magnetic field is applied during experiments.

Dividing equation 3.6b by 3.6a provides the ratio of spin-dependent scattering to charge-dependent scattering. This is shown in figure 3.4 for a range of incident photon energies, demonstrating the necessity of employing high energy photons and backscattering geometry for spin-dependent measurements.

Double differential cross section

The cross sections provided above are independent of the target electron; they relate to the scattering geometry and other experimental parameters only. Together, they form part of the double differential cross section (DDCS), which describes the scattering from a material more completely by considering all of the electrons and the distribution of their momenta. The

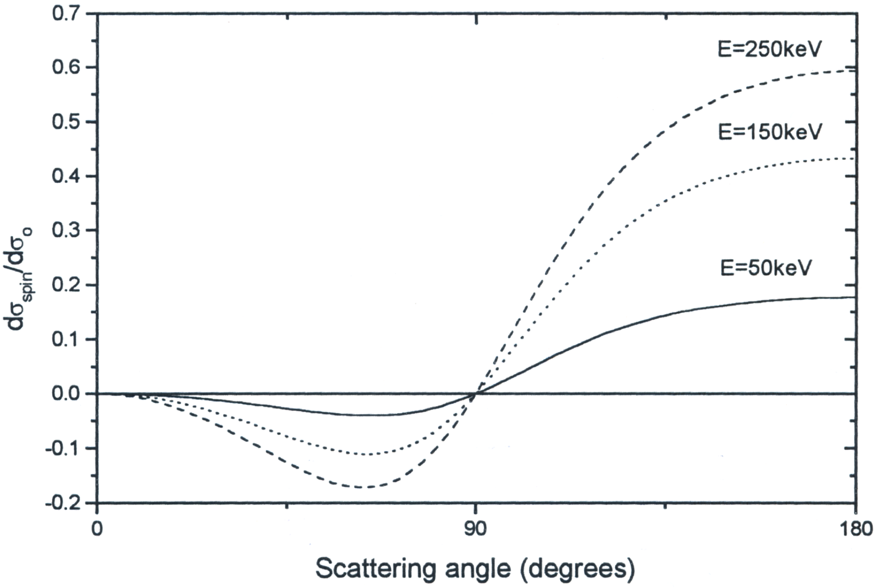

Figure 3.4: The ratio of spin-dependent scattering to charge-dependent scattering as a function of incident angle and photon energy. Reproduced from the Ph.D. thesis of Mark Dixon[36].

DDCS, as given by Żukowski, is defined as[29]

$$\frac{\mathrm{d}^2\sigma(\phi)}{\mathrm{d}\Omega\ \mathrm{d}E_2} = \left(\frac{\mathrm{d}\sigma(\phi)}{\mathrm{d}\Omega}\right)_{\mathrm{charge}} J(\boldsymbol{p}_z) + \left(\frac{\mathrm{d}\sigma(\phi)}{\mathrm{d}\Omega}\right)_{\mathrm{mag}} J_{\mathrm{mag}}(\boldsymbol{p}_z). \tag{3.7}$$

Compton profiles

$J(\boldsymbol{p}_z)$ and $J_{\mathrm{mag}}(\boldsymbol{p}_z)$ are properties of the scattering electrons. These are the Compton and *magnetic* Compton profiles. They are defined as the one-dimensional projections of the electron and spin momentum density distributions, respectively. By including the normalising prefactors $1/N$ and $1/\mu$, where N and μ represent the total number of electrons and the spin-unpaired electrons only, we choose the integrated profile areas to be equal to the total charge and spin of the system. Thus,

$$J(\boldsymbol{p}_z) = \frac{1}{N} \iint_{-\infty}^{\infty} n(\boldsymbol{p})\ \mathrm{d}\boldsymbol{p}_x\ \mathrm{d}\boldsymbol{p}_y \tag{3.8a}$$

$$J_{\mathrm{mag}}(\boldsymbol{p}_z) = \frac{1}{\mu} \iint_{-\infty}^{\infty} \left(n^{\uparrow}(\boldsymbol{p}) - n^{\downarrow}(\boldsymbol{p})\right)\ \mathrm{d}\boldsymbol{p}_x\ \mathrm{d}\boldsymbol{p}_y, \tag{3.8b}$$

where $n(\boldsymbol{p})$, $n^{\uparrow}(\boldsymbol{p})$ and $n^{\downarrow}(\boldsymbol{p})$ are the three-dimensional electron momentum distributions for all, majority-spin (↑) and minority-spin (↓) electrons, respectively. With equation 3.8b in mind, it can now be seen that a magnetic Compton profile can obtained simply from the

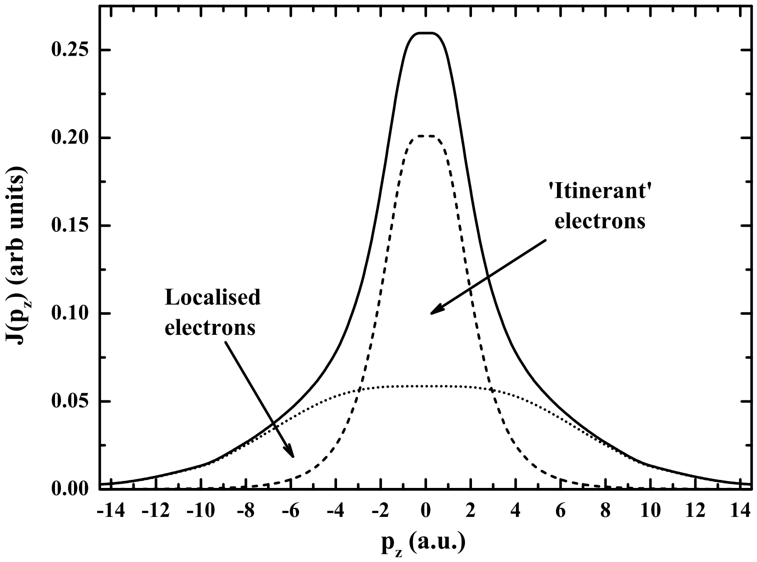

Figure 3.5: Contributions from spatially localised electrons are characteristically broad in momentum space, and therefore in the Compton profile. Conversely, the more itinerant electrons are represented by narrow Compton profiles. In later chapters, the Compton profiles for various atomic/molecular orbitals and electronic bands are shown which illustrate this principle effectively and with relevance to the specific materials in question.

difference of two Compton profiles, each with the sample magnetisation direction parallel or antiparallel to the scattering direction. More information about the experimental procedure is provided in section 4.2.

Real- and momentum-space electron densities

If we consider the three-dimensional Fourier transform of a real-space electron density distribution into momentum-space, we can begin to see how various atomic/molecular orbitals and electronic bands might be represented in a Compton profile. We have that $\psi(\boldsymbol{r})$ is the real-space single electron wavefunction and $\chi(\boldsymbol{p})$ is its Fourier transform. The momentum density distribution, $n(\boldsymbol{p})$, is then given by

$$n(\boldsymbol{p}) = |\chi(\boldsymbol{p})|^2, \tag{3.9a}$$

$$= \frac{1}{(2\pi\hbar)^3} \left| \int_{-\infty}^{\infty} \psi(\boldsymbol{r}) \mathrm{e}^{-i\boldsymbol{p}\cdot\boldsymbol{r}} \, \mathrm{d}\boldsymbol{r} \right|^2, \tag{3.9b}$$

which relates to the Compton profile as defined above. This Fourier transform relationship, along with several others applicable and useful to the study of electron momentum densities, was summarised in the work of Saenz *et al.*[37], who provide the reversible and irreversible

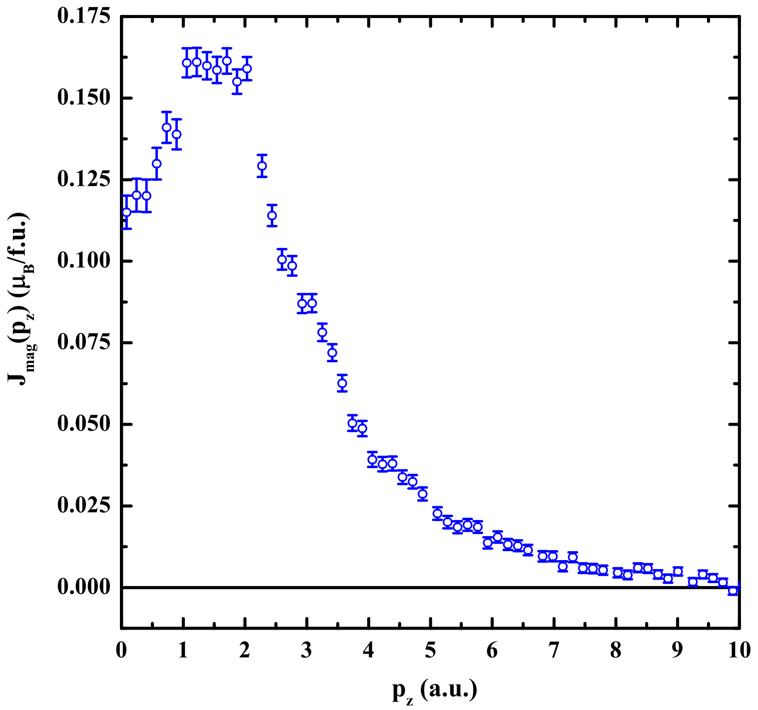

Figure 3.6: Experimental Ni magnetic Compton profile along the [110] direction. This data was collected on the same experimental run that yielded the $EuFe_{2-x}Co_xAs_2$ data provided in Chapter 8.

mathematical operations linking various real- and momentum-space properties. An illustration of these relations, adapted from that of Saenz *et al.*, is provided in Chapter 5, which deals with the theoretical methods employed in this work.

The Fourier transform of $\psi(\boldsymbol{r})$ into momentum space has an important consequence; those electrons which are spatially well-localised will possess a broad range of momentum, while the more delocalised, or itinerant, electrons will be represented by relatively narrow distributions in momentum-space. When the Compton profiles of the resulting momentum-space distributions are obtained, it is the width of the Compton peaks which carry this information - see figure 3.5. This principle is employed throughout this thesis when discussing the origins of magnetic Compton profile features.

Figure 3.5 also serves to highlight an important aspect of the Compton profile as usually presented; the horizontal axis represents the momentum, $\boldsymbol{p}_z$, of the scattering electrons. The units are atomic units ($c = 137$, $e = \hbar = m_e = 1$), where 1 a.u. $= 1.99 \times 10^{-24}$ kg m s^{-1}. The momentum scale is determined from the incident and scattered energies, as well as the scattering angle, ϕ[38]:

$$\boldsymbol{p}_z = m_e c \, \frac{E_2 - E_1 + \frac{E_1 E_2}{m_e c^2}(1 - \cos\ \phi)}{(E_1^2 + E_2^2 - 2E_1 E_2 \cos\phi)^{\frac{1}{2}}}. \tag{3.10}$$

The final feature of note for the investigator of Compton profiles is that an experimentally recorded Compton profile is usually 'folded' about the momentum axis at $\boldsymbol{p}_z = 0$ a.u., as shown in figure 3.6 for an MCP along the [110] direction of a Ni single crystal sample. The folding process improves the statistical quality of the MCP by essentially doubling the count rate at each data point, thereby reducing the size of its associated error by a factor of around $\sqrt{2}$. No information is lost with this approach because the Compton, or *magnetic* Compton, profile is necessarily symmetric about 0 a.u.

3.4 The spin moment

The flipping ratio, R, is used to deduce the spin moment from the Compton and magnetic Compton profiles. It is defined as the ratio of magnetic to charge scattering,

$$R = \frac{\int J_{\mathrm{mag}}(\boldsymbol{p}_z)\ \mathrm{d}\boldsymbol{p}_z}{\int J(\boldsymbol{p}_z)\ \mathrm{d}\boldsymbol{p}_z}, \tag{3.11}$$

and is obtained experimentally through the relationship

$$R = \frac{I^{\uparrow} - I^{\downarrow}}{I^{\uparrow} + I^{\downarrow}}, \tag{3.12}$$

where $I^{\uparrow}$ and $I^{\downarrow}$ are the integrated Compton profile intensities with the sample's magnetisation parallel and antiparallel to the scattering direction. The spin moment of the sample of interest is then found by comparison with a calibration sample; Ni is usually used. Consideration is paid, not only to the ratio of their R values, but also to their total number of electrons, N. We have that

$$\mu_{\mathrm{sample}} = \frac{R_{\mathrm{sample}}}{R_{\mathrm{Ni}}} \frac{N_{\mathrm{sample}}}{N_{\mathrm{Ni}}} \mu_{\mathrm{Ni}}, \tag{3.13a}$$

$$= \frac{R_{\mathrm{sample}}}{R_{\mathrm{Ni}}} \frac{N_{\mathrm{sample}}}{28} 0.56\ \mu_{\mathrm{B}}, \tag{3.13b}$$

where 0.56 μ_B is the known spin moment of Ni. The Bohr magneton, μ_B, is the intrinsic spin moment carried by a single electron, equal to $e\hbar/2m_e$, or 9.274×10^{-24} J T^{-1} in S.I. units.

Other calibration samples beside Ni could be used (Fe, Co, etc.), but owing to the relatively small size of its magnetic effect Ni, provides an experimental sensitivity of which materials with larger spin moments are incapable. In practice, the shape of the measured Ni magnetic Compton profile and the size of its moment, which are now quite familiar to the Compton Scattering group, are checked against previous results and any discrepancies are identified and addressed.

3.5 Magnetic Compton scattering and other techniques

There are a host of experimental techniques available to probe a material's electronic and magnetic structures. Some of the more uncomplicated and commonly used, though still highly valuable, are electrical transport and magnetisation measurements. Other techniques include X-ray photoelectron spectroscopy (XPS) (and its often more informative high energy (HAXPES), angle-resolved (ARPES) and spin-polarised (SPARPES) varieties), X-ray absorption spectroscopy (XAS), X-ray magnetic circular dichroism (XMCD), magnetic X-ray diffraction, neutron scattering and two-dimensional angular correlation of annihilation radiation (2D-ACAR), a positron annihilation technique. Many of these techniques are discussed where relevant throughout this thesis, chiefly in terms of the varied and complementary information they provide in the study of condensed matter systems. The forms of information that each of these techniques yield are too numerous to detail, but combinations of these techniques, as well as theoretical modelling methods (density-functional theory, etc.), often provide the means to obtain a deep understanding of the particular system under investigation.

The main features that set magnetic Compton scattering apart from many of the above techniques are these:

- It solely samples, and can provide a value for, the spin moment of a system. Comparison with conventional magnetometry can then be used to identify the system's total, spin and orbital magnetic moments.

- It is a direct probe of the spin momentum density distribution. It is possible, generally in conjunction with theoretical modelling, to uniquely identify the electronic orbitals/bands that contribute to a system's magnetism through analysis of a recorded magnetic Compton profile. This can help to clarify the system's entire electronic structure and indicate the extent of electronic hybridisation.

- Unlike some of the techniques listed above, it is a *bulk* probe (it is not affected by the quality of the sample's surface) and the measurements do not require ultra-high vacuum (UHV) conditions, defined by pressures below $\sim 10^{-9}$ mbar, or very low temperatures, such as those only achievable with the use of liquid ^{3}He.

Chapter 4

Experimental techniques

As discussed in the previous chapter, magnetic Compton scattering requires high energy, circularly polarised photons. For this reason, magnetic Compton scattering data are collected at synchrotron radiation facilities. A wide range of experimental techniques are used to produce and characterise each material, and there are many complementary techniques capable of adding to our understanding of a material's electronic and magnetic properties. In this chapter, information is provided about the production and use of high energy polarised X-rays at synchrotron radiation facilities, as well as some of the complementary 'in-house' techniques that were used in this work.

Note that some of the details in first section relate specifically to the arrangement at the SPring-8 synchrotron in Hyōgo Prefecture, Japan, where most of the magnetic Compton scattering data presented in this thesis were obtained. In general, these processes are the same for other synchrotron facilities and vary according to exact specifications.

4.1 Synchrotron radiation

Synchrotron radiation is that which occurs when a charged particle, usually moving relativistically, is accelerated tangentially to its velocity. At SPring-8, after being emitted from an electron gun, electron bunches are accelerated in a linear accelerator (LINAC), reaching energies from 0.9 to 1.15 GeV. They are then transferred to a circularly accelerating section known as a booster synchrotron, where they can reach up to 8 GeV. Finally, the electrons enter the storage ring, where they are steered from one straight section to another by bending-magnets, producing synchrotron radiation when they pass through specialised insertion devices. These

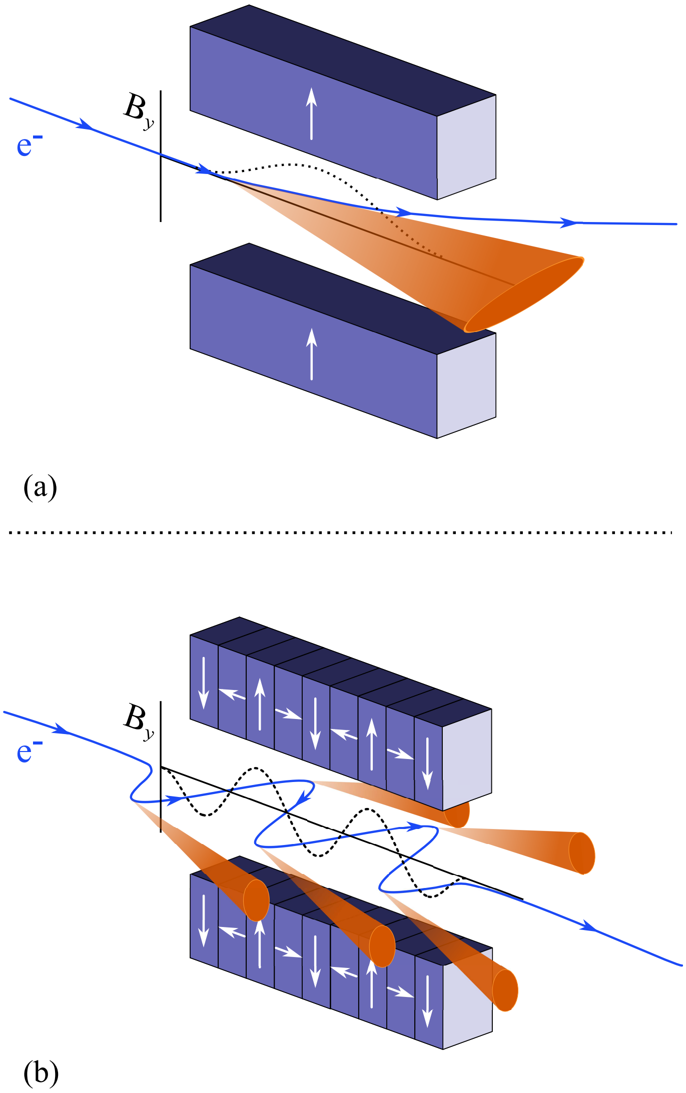

Figure 4.1: Synchrotron radiation produced by (a) a bending-magnet, and (b) a wiggler or undulator.

are made of a series of magnets, the configuration of which determines the properties of the resulting radiation, specifically the energy spectrum and polarisation. Only a brief overview of synchrotron insertion devices is given here; more information can be found in the work of Clarke[39] and Duke[40].

Insertion devices

The simplest insertion device is the bending-magnet, illustrated in figure 4.1(a). In modern synchrotrons, these are used primarily for electron beam steering purposes, while the radiation used for most experiments comes from more sophisticated device designs. The bending-magnet uses a single pair of magnets to create a static vertical field, B_y, which turns the electron beam with a Lorentz force, $\boldsymbol{F} = q(\boldsymbol{v} \times \boldsymbol{B})$. The electron beam continues in its horizontal orbit within the storage ring, while producing a conical dispersion of broad-spectrum synchrotron radiation which, as $v \to c$, is mainly directed in the original direction of electron travel.

Undulators and wigglers offer several advantages over the simple bending-magnet. They can produce highly brilliant, tunable and strongly polarised light for a variety of experimental requirements. Both devices employ a large number of magnets with an intricate field structure, which cause the electron beam to oscillate horizontally along its path, ultimately returning to its original trajectory - see figure 4.1(b). Synchrotron radiation is produced at each of the turning points in the oscillating beam's path. In essence, undulators and wigglers function in the same way; only the extent to which they deflect the electron beam is different. In an undulator, the deflections are relatively small, and interference effects result in the emission of radiation of only a few wavelengths. This radiation is usually of very high intensity, making the undulator highly desirable for a range of experimental techniques where only one or several wavelengths are required. Wigglers use larger fields to deflect the electron beam to a much larger degree, producing broad-spectrum radiation with higher energies than achievable with the other designs, making them suitable for magnetic Compton scattering where high energy X-rays are a necessity.

Insertion devices on the BL08W and ID15A beamlines

Finally, we have the types of insertion device used for magnetic Compton scattering experiments on the ID15A beamline, at the ESRF, and the BL08W beamline, at SPring-8. ID15A uses an asymmetric multipole wiggler (AMPW), which has a field structure similar to that shown in figure 4.1(b), but with the difference that the positive and negative field strengths are no longer symmetric - a large positive field exists for a short distance, followed by a smaller negative field for a long distance. The AMPW produces linearly polarised X-rays in the plane of the electron beam's orbit, but there exists an increasing degree of circular polarisation with increasing angular deviation from the plane. Thus, on the ID15A beamline, and others which employ the same method to obtain circularly polarised light, radiation is taken 'off-axis'. The increase in circular polarisation, which benefits magnetically-sensitive techniques such as magnetic Compton scattering, must be weighed against the

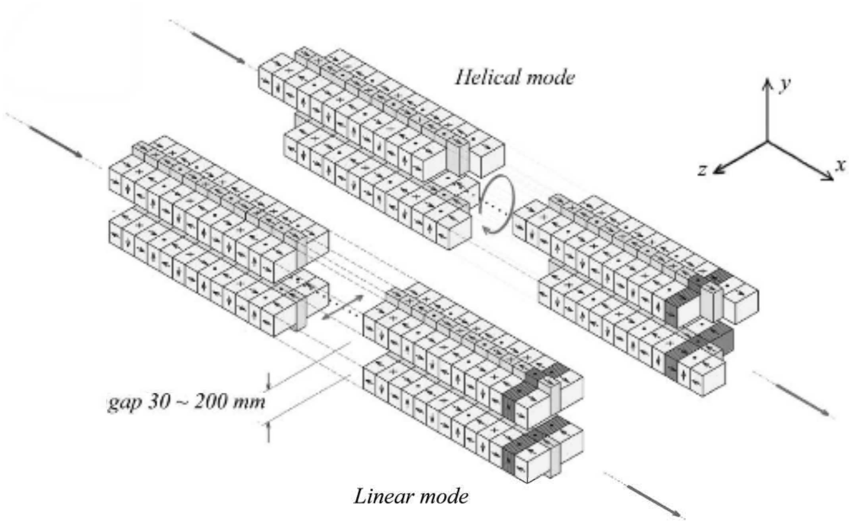

Figure 4.2: The elliptical multipole wiggler (EMPW) uses horizontal and vertical magnetic fields to steer the electron beam along a helical path, producing circularly polarised X-rays in the plane of the storage ring. Figure adapted from the work of Rybalchenko *et al.*[41].

drop-off in photon flux that accompanies going off-axis. A figure of merit may be used to find the optimum geometrical condition that maximises both photon flux and circular polarisation, an example of which is given in Cooper *et al.*'s *X-ray Compton Scattering* (chapter 3)[29].

The BL08W beamline of SPring-8 uses another type of insertion device, the elliptical multipole wiggler (EMPW), as illustrated in figure 4.2. In this device, additional magnets arranged horizontally along the electron beam's path produce a field B_x. This causes the electron beam to experience a vertical deflection as well as the horizontal deflection seen in the undulator and wiggler. The beam's path becomes helical, with the result that circularly polarised light is produced on-axis, alleviating the need to compromise on photon flux by employing a figure of merit. The spectral brilliance and degree of circular polarisation for the radiation of the EMPW at SPring-8 are provided in figure 4.3.

4.2 The SPring-8 BL08W beamline

Most of the magnetic Compton profiles presented in this work were collected on the BL08W beamline of the SPring-8 synchrotron. The main components and operating procedures of the beamline are described here. An illustrative schematic of the optics hutch and experimental hutch of BL08W is given in figure 4.4.

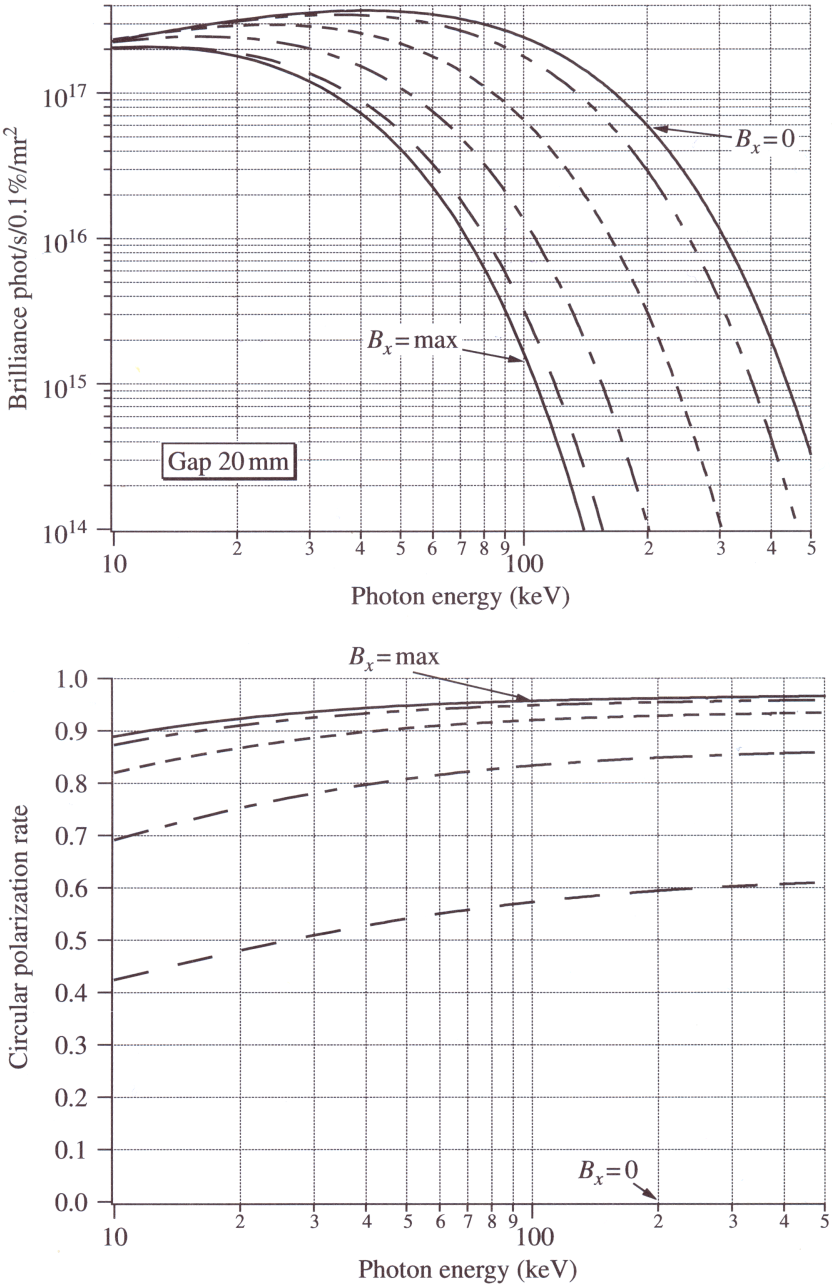

Figure 4.3: The spectral brilliance and degree of circular polarisation of radiation from the BL08W EMPW. The values are determined for six values of B_x, the horizontal field component which results in on-axis circular polarisation. The B_x values are 100%, 95%, 81%, 59%, 31% and 0% of maximum. Reproduced from Cooper *et al.*[29], which originally cited permission from Marèchal *et al.*[42].

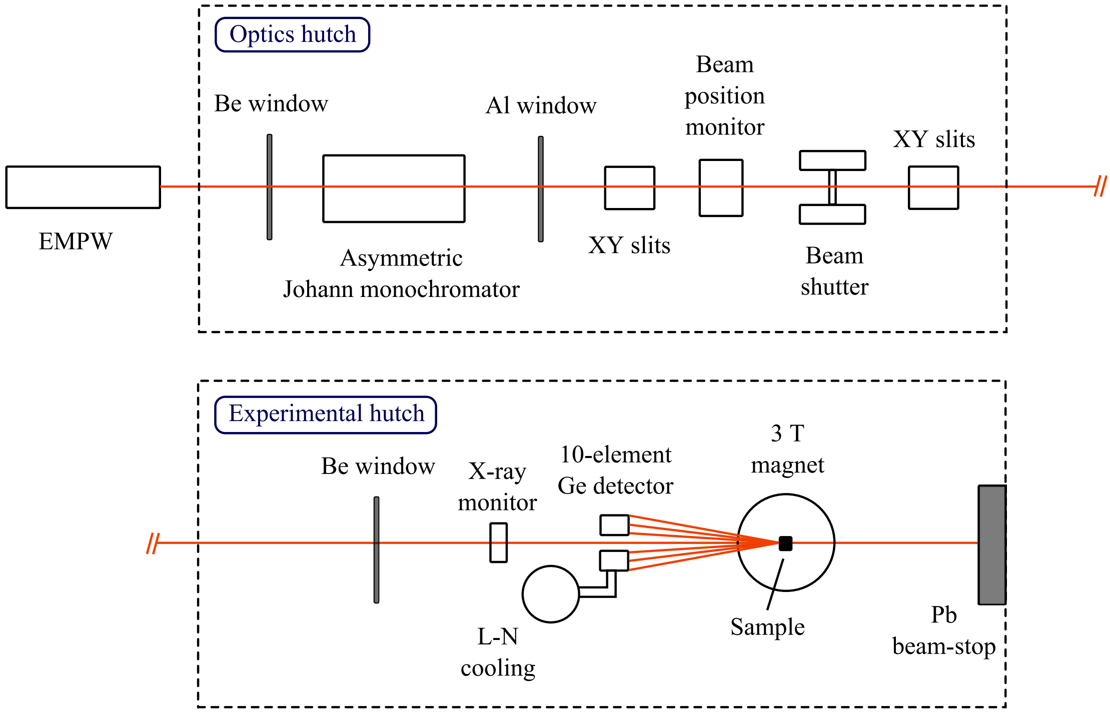

Figure 4.4: Schematic of the BL08W beamline at SPring-8, including the optics and experimental hutches. The path of the X-ray beam is denoted in orange. This schematic is illustrative only; it is not to scale.

Circularly polarised X-rays

Circularly polarised X-rays of energy up to 300 keV are produced by an EMPW. These enter the optics hutch and are monochromated and focussed by a water-cooled asymmetric Johann monochromator. This uses reflection from Si (771) crystallographic planes to provide a final energy, incident on the sample, of 175 keV. The photon flux is then around 10^{10} s^{-1} and the beam profile has been focussed to a 'letterbox' shape, around 10 μm high and 50 μm wide, though this is varied in each experiment in order to obtain a reasonable count rate. This should be not so low that the experiment takes unnecessarily long to achieve good statistics, but not so high as to introduce a large dead-time in the solid-state Ge detectors. Around 3×10^4 s^{-1}, over the full energy range collected by the detectors, is a reasonable count rate.

The superconducting magnet

The superconducting magnet used on the BL08W beamline is capable of producing fields up to ±3 T and flipping fields approximately every 60 seconds, depending on the required field.

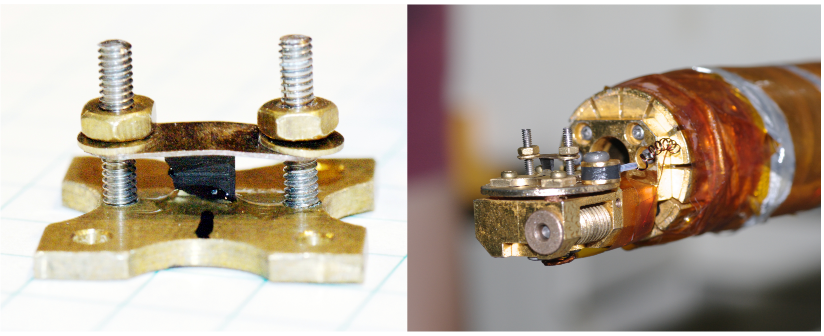

Figure 4.5: (Left) The sample plate used on the BL08W beamline. In this case, because the moment of the sample, $TbMnO_3$, is large, a copper bridge is used, in addition to epoxy resin, to secure the sample whilst in the magnet. (Right) The sample plate is positioned at the end of a helium-cooled cold-finger, which then slides into the magnet.

The sample, which is mounted securely on a non-magnetic sample plate, is positioned at the end of a cold-finger and inserted into the magnet - see figure 4.5. At one end, the cold-finger can be actively cooled by a closed-cycle liquid-helium cryostat. When the cryostat is activated, the sample temperature may reach as low as 7 K, while a small heater, mounted close to the sample, provides access to higher temperatures. If room temperature measurements are required, the cryostat is not used, and even higher temperatures, up to $\sim$ 500 K, can be achieved with the use of a high temperature insert that was recently developed at Warwick.

X-ray detectors

A series of 10 solid-state Ge detectors are arranged circularly around the path of the incoming X-ray beam. In this way, the scattering angle for each detector is the same 173°. This makes the data analysis, specifically the conversion of scattered photon energy into electron momentum, simpler than say, ID15A, where the detectors have a range of scattering geometries. In cases where a large amount of X-ray fluorescence is exhibited by the sample, usually true only if it contains some heavy elements (i.e. post La), scattered X-rays enter the detectors through a set of Sn windows. These absorb a lot of the low-energy fluorescence which might otherwise contribute significantly to the total count rate and introduce undesirable detector dead-time.

The Ge detector crystals are cooled with liquid-nitrogen and have a negative bias of 1000 V. When a scattered X-ray is absorbed, electron-hole pairs are created in the Ge, resulting in a charge pulse. The pulse passes to a pre-amplifier and a multi-channel analyser (MCA), where the integrated charge pulse is converted to a voltage pulse and recorded in terms of channel number, 0 to 8190. This linearly corresponds to the energy of the absorbed X-ray. The conversion of channel number to photon energy is achieved by comparison with standard fluorescence peaks of known energy. As mentioned previously, the incident count rate must be adjusted so that the detector dead-time is minimised. Dead-time occurs because, due to electronic processing, for a short time after a current pulse is collected the system is unable to record another. Any photon arriving in this time is essentially disregarded, resulting in a count rate which may be significantly less than optimum. The energy resolution with this detector-MCA setup is around 1.5 keV and is the main constituent of the final resolution.

The experimental procedure

When performing a magnetic Compton scattering experiment, scattered X-ray spectra are recorded over 60 seconds with positive, A, and negative, B, fields in the sequence ABBABAAB. This was devised as a means of counteracting a non-linear drop-off in the measured count rate due to the decaying synchrotron beam current and the resulting decrease in detector dead-time. The 60 second count time provides a compromise between longer count times, in which the magnet is flipping for a smaller percentage of the time, and shorter counting times, which give better normalisation (but bigger data files). A single ABBABAAB set is referred to as a cycle and takes $\sim$ 10 minutes to collect (including time spent flipping the magnetic field). Depending on the flipping ratio of the sample (see section 3.4) and the desired statistical accuracy, the number of cycles needed per measurement might be as low as 2 or 3, or might be considerably higher. The collected X-ray spectra are normalised using a gas-based X-ray monitor positioned before the sample.

Experimental resolution

The final experimental resolution, in terms of the momentum of the scattering electrons, is around 0.4 a.u. There are three main contributors to this; the energy resolution of the synchrotron radiation (which includes broadening introduced by the asymmetric monochromator), the detector energy resolution, and a term determined by the scattering geometry; the accuracy with which all the detectors are aligned with the same scattering angle. It is the solid-state detector resolution which contributes the most to the final value. Charge-coupled devices (CCDs) perform better in this regard, and for this reason are used in high resolution charge Compton experiments, but they are incapable of collecting the large number of X-rays required for magnetic Compton scattering experiments in a reasonable time frame.

4.3 The ESRF ID15A beamline

Some of the data presented in this thesis were collected on the ID15A beamline of the European Synchrotron Radiation Facility (ESRF), in Grenoble, France. X-rays produced by an AMPW are monochromated and focussed by a bent Ge crystal monochromator. The X-rays incident on the sample are of energy 220 keV. The ID15A beamline has seen extensive use by the Compton scattering group, due in part to the presence there of a group-owned cryomagnet. This is an Oxford Instruments Spectromag cryomagnet, which can produce fields up to ±9 T and has a variable temperature insert that can control the sample temperature from 1.3 to 300 K. Sample temperatures of up to 700 K can be achieved with a special furnace insert designed and built at Warwick.

The detector setup on ID15A is similar to that of BL08W. It comprises a bank of 13 liquid-nitrogen cooled Ge crystals held at a bias of 3000 V. As above, the charge pulses that result from X-ray absorption are converted into voltage pulses and assigned a channel number by a pre-amplifier and MCA. The channel number is linearly proportional to the energy of the absorbed X-ray. Normalisation of the scattered spectra is achieved by means of an X-ray diode positioned in the X-ray beam before the sample.

At the time of writing, the Oxford Instruments Spectromag magnet has been transported to Japan and installed temporarily on the BL08W beamline. This is part of a long term research program aiming to combine the high field, low temperature capabilities of the Oxford Instruments Spectromag magnet with the high photon flux and beam stability of SPring-8.

4.4 Tri-arc polycrystal production

Attention is now paid to the ‘in-house’, or at least non-synchrotron, techniques that were deployed in the work for this thesis. The first technique relates to the production of the polycrystalline samples studied in Chapter 6.

A bench-mounted tri-arc furnace was used to produce polycrystalline samples of NiSb, MnSb and NiMnSb. The starting materials were granules Ni, Mn and Sb of at least 99.99% purity. The furnace includes a water-cooled copper crucible sealed within a cylindrical pyrex case. The crucible serves as the anode. Three cathodes provide arcs to melt the elemental constituents; these are housed in a copper lid section which is clamped over the pyrex case. The cathodes are manoeuvrable by hand so that the user can position them close to the sample, allowing all regions of the sample to get the same treatment. Prior to heating and melting, the furnace is purged and flushed with Ar gas several times in order to reduce the levels of moisture and oxygen. During the melting procedure, a constant overpressure of Ar gas is maintained so that the molten sample is exposed to as chemically inert an atmosphere as possible. Standard procedure is to invert and remelt the sample several times. This eliminates the possibility that some parts of the sample have stayed in contact with water-cooled crucible base throughtout the melt, thereby improving its homogeneity. All arc-melted samples were subsequently sealed under vacuum in a quartz tube and annealed in a conventional, oven-like furnace where the heat is provided by heating elements. During a typical annealing treatment the samples spent 150 hours at 850 °C. Again, the purpose of this final stage is to improve sample homogeneity.

Elemental mixing ratio

To produce a sample of composition B_xC_y, the constituents B and C must be mixed in a ratio which accounts for the difference in their atomic masses. The ratio is given simply by

$$A_B \times x \ : \ A_C \times y, \tag{4.1}$$

where A_B and A_C are the atomic masses of elements A and B.

Elemental losses during melting

Before an effort can be made to produce a good stoichiometric sample, it is important to investigate the effects of arc-melting on the different elemental constituents. If one material has a melting temperature which is much lower than another, it may be preferentially lost to vapourisation during melting. Likewise if one material has a higher vapour pressure than another. To counteract this, a good starting procedure is to successively melt and weigh small amounts of the elements to be used, recording the fraction lost each time. In this way it should be possible to predict what fraction of each constituent will be lost after each melt once they are mixed. Even with this precautionary measure it is often difficult to predict how the elemental differences will manifest in the production of a certain alloy. For example, considering that Sb melts at around 600 °C less than Mn and 800 °C less than Ni[43], it is assumed that a starting mixture of equal parts Mn:Sb or Ni:Sb would produce a Sb-deficient sample after melting. Indeed, this is what was observed. EDX results showed that MnSb and NiSb alloys prepared in this way had an average composition around $\mathrm{TM}_{0.55}\mathrm{Sb}_{0.45}$, where TM is the transition metal element, which can be accounted for by adding more Sb in the initial mix. The same was expected for the ternary alloy NiMnSb, but in practice it exhibited entirely different behaviour. Starting mixtures of equal parts Ni:Mn:Sb resulted in polycrystals which were Mn-deficient by as much as 5%. The ideal starting mix was found to be 1:1.05:1 for NiMnSb. More details are given in section 6.2.

4.5 Energy-dispersive X-ray spectroscopy - EDX

Energy-dispersive X-ray spectroscopy (EDX) is used to determine the chemical composition of a sample by analysis of an emitted X-ray spectrum. At Warwick, EDX measurements were performed with an EDAX Genesis analytical system, using a nitrogen-cooled Si(Li) X-ray detector. Inside a vacuum chamber, an electron beam of variable energy (0.1 to 30 keV) is produced by a thermal field emission gun and is incident upon the sample. The incident beam excites core-level electrons in the sample, leaving behind electron-holes. These are then filled by electrons from higher energy levels, resulting in the emission of X-rays of characteristic energies. These X-ray emission lines are well documented and easily identified, assuming sufficiently long counting times. After the X-ray spectra are collected, the quantitative analysis which yields the chemical composition is performed. This is essentially a three step process. First, a background due to Bremsstrahlung radiation is removed from the spectrum and Gaussian profiles are fitted to the X-ray peaks. Second, a ZAF correction is applied to each peak area to account for differing backscatter coefficients (which are atomic number, Z, dependent), absorption edges (A) and fluorescence effects (F). Finally, the corrected peak areas are compared to those of a standard sample and the relative elemental concentrations

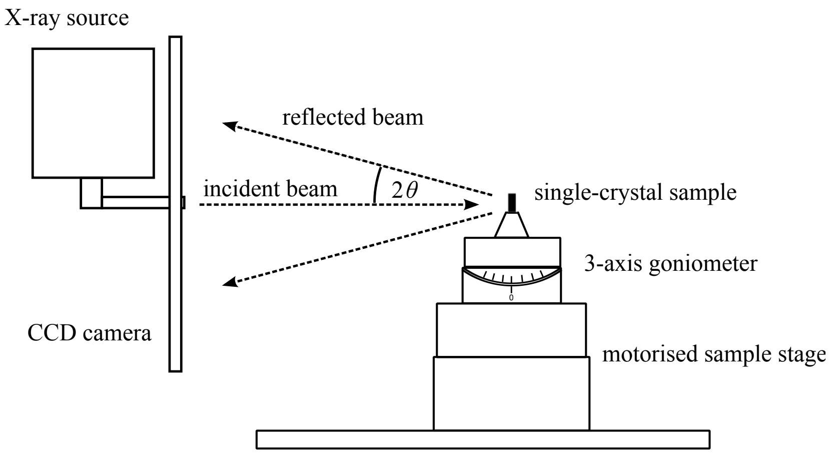

Figure 4.6: The experimental setup for sample alignment using Laue backscattering.

are provided. For polished bulk target samples of the kind used in this work, the accuracy of the final elemental composition is around ±1%[44]. The depth sensitivity of EDX varies with the energy of the electron beam and the properties of the sample being probed; in this work, it is estimated at around 2 μm.

4.6 The back-reflection Laue method

The back-reflection Laue method was used primarily to align crystalline samples for use in Compton scattering experiments. The Laue setup is illustrated in figure 4.6. Initially, the sample is fastened loosely on top of a motorised goniometer, allowing rotation around three axis as well as translation in x, y and z. A white beam of X-rays is produced by a W source and passes through the centre of a charge-coupled device (CCD). The X-rays are incident upon the sample and undergo elastic scattering. After reflection, the X-rays interfere constructively if Bragg's condition is met: $n\lambda = 2d\sin\theta$, where n is an integer, λ is the X-ray wavelength, d is the planar spacing in the sample and θ is the angle of incidence (see figure 4.7).

Laue patterns were recorded using a computer-controlled CCD and compared to theoretical patterns generated by the OrientExpress software package[45]. Once the samples were aligned satisfactorily they were glued, using a hard-setting epoxy resin, to a sample plate specific to either the BL08W or ID15A beamline. After gluing, more Laue patterns were collected in order to confirm that the crystallographic directions were oriented correctly.

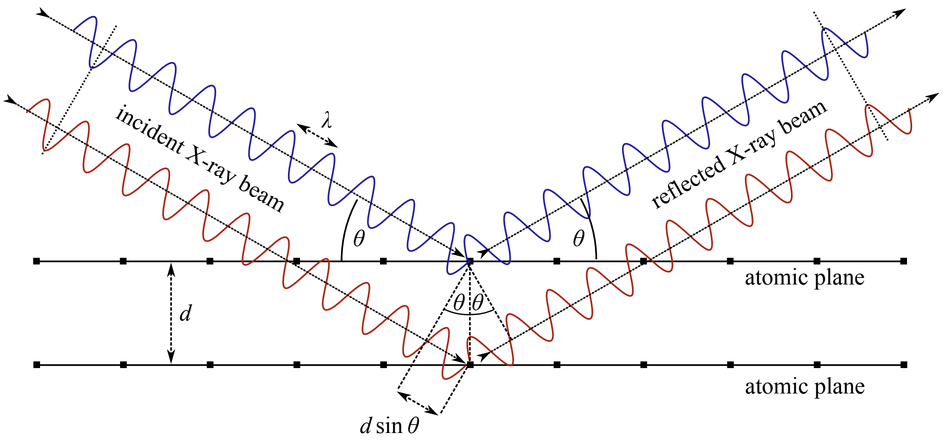

Figure 4.7: Elastic scattering of X-rays from atomic planes leads to constructive interference if the Bragg condition is met: $n\lambda = 2d\sin\theta$.

4.7 Powder X-ray diffraction

During the characterisation of the NiMnSb single crystal, a powder X-ray diffraction measurement was performed. The purpose was to determine the crystallographic phases present in the sample, and to find the associated lattice parameters. Powder diffraction is very similar to Laue diffraction, and relies on the same process of scattering from lattice planes as is illustrated in figure 4.7. Again, the Bragg condition dictates the position of X-ray peaks due to constructive interference after scattering. We assume the $n = 1$ case (the principle Bragg condition) and we vary the incident angle, θ. A range of d values will satisfy the Bragg condition and provide diffraction peaks at angles of 2θ. In this work, a Panalytical X-Pert Pro powder diffraction system was used. The sample was ground to a powder and packed into a small cylindrical holder. Cu Kα_1 X-rays ($\lambda = 1.5406$ Å) were diffracted by the powdered sample and collected by a PiXcel point detector. To maximise the number of powdered crystallites contributing to scattered X-ray peaks, the sample was rotated at a rate of 1/4 rotations per second during the measurement. After data collection, an online database of previously reported spectra was consulted to find an accepted crystal structure (if it exists) and determine the possible phases present in the sample. The lattice parameter was then found through a Rietveld refinement process, a non-linear, least-squares method that compares the measured pattern with a calculated pattern based on the known phases.

Good overviews of Laue back-reflection and powder X-ray diffraction, along with other

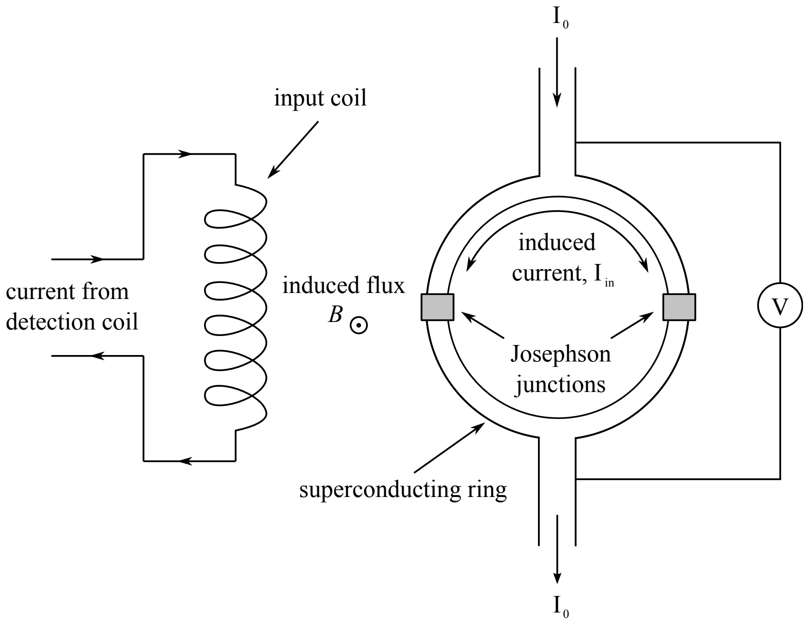

Figure 4.8: Illustration of the superconducting quantum interference device (SQuID).

crystallographic X-ray methods and accompanying theory, are provided in *Crystallographic Instrumentation* by Aslanov *et al.*[46] and *Theory of X-ray Diffraction in Crystals* by Zachariasen[47].

4.8 SQuID magnetometer

A superconducting quantum interference device (SQuID) magnetometer was used to perform magnetisation versus temperature, $M\text{v}T$, and magnetisation versus applied field, $M\text{v}H$, measurements for various samples.

During SQuID magnetometer measurements, the sample is attached to a non-magnetic holder and moved slowly through a superconducting detection coil. An external field is applied by a superconducting solenoidal magnet. The magnetic response of the sample induces a current in the detection coil, which then passes to the SQuID input coil, producing a flux through the SQuID ring - see figure 4.8. The flux induces a current, I_{in}, in the SQuID which flows with or against the applied current, I_0, depending on the magnitude of the flux. I_{in} changes direction every time the flux produced by the input coil is increased by $\Phi_0/2$, where Φ_0 is the magnetic flux quantum, equal to 2.0678×10^{-15} Wb. Thus, the voltage measured across the SQuID varies periodically with increasing flux. Analysis of the recorded SQuID voltage, performed automatically by the magnet control software, then yields the magnetisation of the sample. The SQuID magnetometer used at Warwick is a Quantum Design MPMS-5S, capable of applying fields of ±5 T, with a temperature range of 1.8 to 400 K. The Quantum Design MPMS manual[48] provides a good overview of SQuID magnetometer theory and operation.

4.9 X-ray photoelectron spectroscopy - XPS

X-ray photoelectron spectroscopy is a surface-sensitive technique allowing the chemical composition of a sample to be determined. In addition, a thorough analysis of XPS data can provide information about the bonding environments of specific chemical species, which is particularly useful when attempting to assess the extent of oxidation in a sample.

The XPS process

In XPS measurements, a sample is exposed to a monochromatic beam of X-rays with energy $\hbar\omega$. The X-rays cause the photoemission of electrons from core levels and/or the valence band, depending on the X-ray energy. In the simplest view, the photoelectrons have kinetic energy $\hbar\omega - E_b - \phi_w$, where E_b is the electron binding energy and ϕ_w is the work function. In reality, the energy of the photoelectrons is modified by a host of extra terms, including an intra-atomic shift due to the relaxation of the ion after photoionisation, and an inter-atomic shift due to the screening of the resulting electron-hole by itinerant electrons.

The basic XPS setup is illustrated in figure 4.9. The ejected photoelectrons move into an energy analyser. This consists of two concentric hemispherical plates held at high potentials. Altering the velocity of the photoelectrons with the input lenses allows only those with a certain range of energies to pass through to the detector. The resulting spectra may encompass the whole range of binding energies allowed (E_b from 0 eV up to $\hbar\omega$) - this is referred to as a survey scan. Alternatively, as used in this work, regions of a few tens of eV can be scanned with some precision to obtain clear core level peak shapes for analysis.

Features of XPS spectra

To illustrate the general shape and features of a core-level XPS spectrum, figure 4.10 shows the Sb 4d region from a NiSb sample (more NiSb, MnSb and NiMnSb XPS can be found

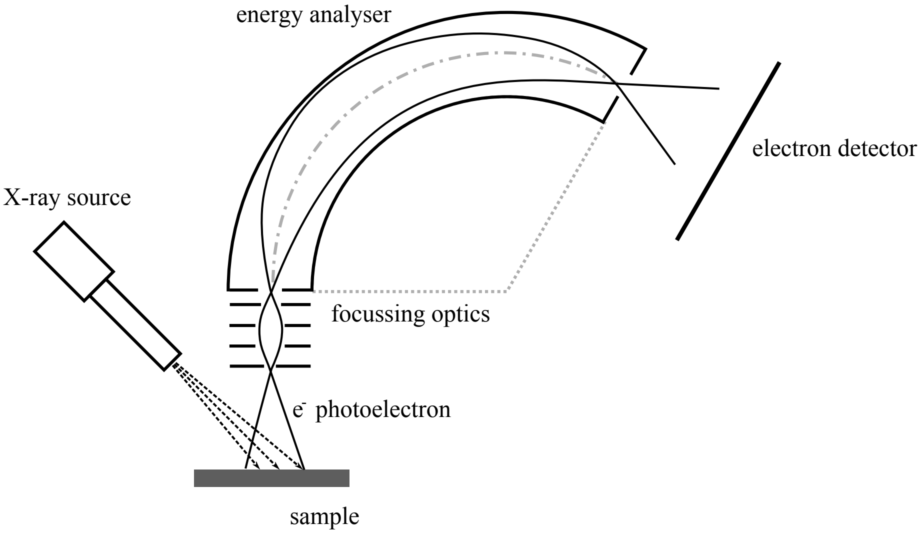

Figure 4.9: Schematic illustration of X-ray photoelectron spectroscopy (XPS). Note that this process takes place inside a vacuum chamber.

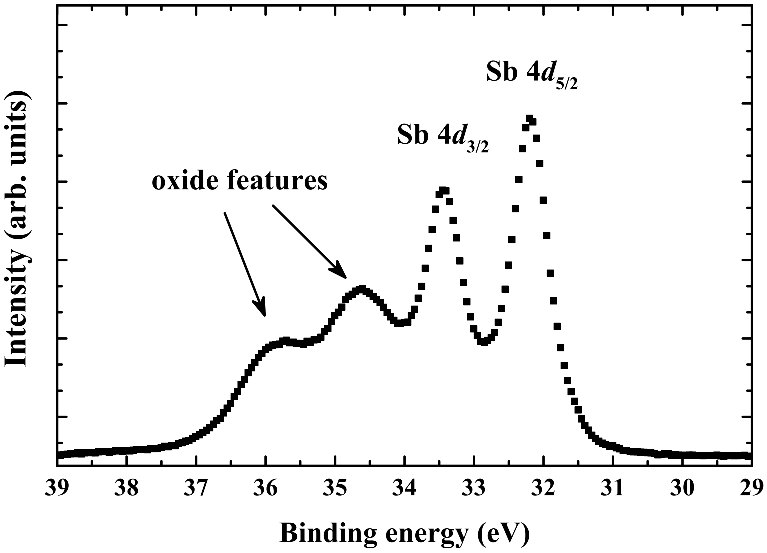

Figure 4.10: The Sb $4d$ core level region of a NiSb XPS. See the text for an explanation of its shape and features.

in section 6.6). We see two ‘elemental’ peaks, labelled $4d_{5/2}$ and $4d_{3/2}$, at lower binding energies. These peaks are those with no chemical shift (mentioned below). They possess the elemental binding energies of pure Sb. The 5/2 and 3/2 subscripts describe the total angular momentum of the state. This quantity, denoted j, is equal to $l \pm 1/2$, where l is the orbital angular momentum (0 for s-states, 1 for p-states, 2 for d-states, etc.). The $\pm 1/2$ term is due to the intrinsic spin of the electrons. The degeneracy of these states is given by $2j + 1$, meaning that d orbitals contain 6 electrons in $d_{5/2}$ states and 4 electrons in $d_{3/2}$ states. Thus, XPS spectra of core level d regions have two peaks with intensities in a ratio of 3:2.

Looking again at figure 4.10, at higher binding energies we see features due to antimony oxides (Sb_2O_3, Sb_2O_4 and Sb_2O_5 are known to exist[49]). The electronegativity of oxygen tends to draw electrons from whatever it is bonded to, reducing that atom’s ability to screen its nuclear charge. As more nuclear charge is felt by the bound electrons, their binding energy increases.

XPS instruments used in this work

XPS spectra were collected at the National Centre for Electron Spectroscopy and Surface Analysis (NCESS), part of Daresbury Laboratory, and at Warwick. The XPS systems at both facilities use monochromatic Al K_α X-ray sources ($\hbar\omega = 1486.7$ eV) and have a maximum energy resolution of 0.3 to 0.7 eV. The depth sensitivity of XPS is determined by the inelastic mean free path (IMFP) of the excited photoelectrons. In turn, the IMFP depends on the photoelectron energy and some properties of the material, specifically the density and the Z-dependent cross sections for various kinds of inelastic scattering. Most of the photoelectrons, around 95%, which escape from the sample with their characteristic emission energy intact, come from within 3 IMFPs of the surface. For metals, this corresponds to a depth of approximately 3 to 10 nm for a wide range of photoelectron energies.

Chapter 5

Theoretical techniques

This chapter introduces the three main theoretical methods used to provide information about the materials that were examined experimentally. These are Hartree-Fock theory, a molecular orbital wavefunction method and density-functional theory.

Hartree-Fock theory is the simplest of these methods; it provides wavefunctions for many-electron systems, such as atoms, which are composed of combinations of single-electron wavefunctions, i.e. the atomic orbitals. In recent decades, Hartee-Fock theory has been used extensively in Compton and magnetic Compton scattering studies and has provided the tool for determining the origin of the magnetism in several materials. A good example is the work of McCarthy *et al.*[50], in which the authors use Compton profiles from Hartree-Fock theory to determine the Sm $4f$ and Mn $3d$ spin contributions in $SmMn_2Ge_2$.

Molecular wavefunction methods build up a description of an entire molecule or cluster of atoms from a basis set of atomic orbitals. The Compton scattering group at Warwick have only recently started working with this method, but it is already beginning to develop into a powerful tool for analysing magnetic Compton profiles, supporting and complementing the use of atomic Hartree-Fock theory.

Density-functional theory offers a more complete description of the electrons in a material than atomic or molecular wavefunction methods, generally providing detailed information about the electronic structure that can be used to interpret magnetic Compton scattering data.

5.1 Hartree-Fock Compton profiles

In sections 6.4, 7.3 and 8.4 use is made of the Hartree-Fock (HF) and relativistic Dirac-Hartree-Fock (RDHF) Compton profiles provided by Biggs *et al.*[51]. These are spherically-averaged free-atom profiles, and their main use is usually as a means of checking the high momentum regions of experimental Compton profiles to ensure agreement with atomic theory. This short section will show the origin of these profiles.

Hartree-Fock theory attempts to solve the general time-independent Schrödinger equation, $\widehat{\mathrm{H}}\Psi = E\Psi$, using a multi-electron wavefunction. For a system of N non-interacting electrons bound to an atom, $\Psi_{n,l,m}(\boldsymbol{r},\theta,\phi)$ is described with a Slater determinant of the form

$$\Psi_{n,l,m}(\boldsymbol{r},\theta,\phi) = \frac{1}{\sqrt{N!}} \begin{vmatrix} \psi_1(\boldsymbol{r}_1,\theta_1,\phi_1) & \psi_2(\boldsymbol{r}_1,\theta_1,\phi_1) & \dots & \psi_N(\boldsymbol{r}_1,\theta_1,\phi_1) \\ \psi_1(\boldsymbol{r}_2,\theta_2,\phi_2) & \psi_2(\boldsymbol{r}_2,\theta_2,\phi_2) & \dots & \psi_N(\boldsymbol{r}_2,\theta_2,\phi_2) \\ \vdots & \vdots & \ddots & \vdots \\ \psi_1(\boldsymbol{r}_N,\theta_N,\phi_N) & \psi_2(\boldsymbol{r}_N,\theta_N,\phi_N) & \dots & \psi_N(\boldsymbol{r}_N,\theta_N,\phi_N) \end{vmatrix}, \quad (5.1)$$

where $\psi_1(\boldsymbol{r}_1,\theta_1,\phi_1)$, etc. are the single-electron atomic wavefunctions (the atomic orbitals) as given previously in equation 2.5. $\Psi_{n,l,m}(\boldsymbol{r},\theta,\phi)$ is an antisymmetric product of these wavefunctions, thus complying with the Pauli exclusion principle regarding the interchange of coordinates, $\boldsymbol{r}$. To obtain the Hartree-Fock wavefunction, the iterative Hartree-Fock-Roothan computational approach is used, minimising the total energy by varying the coefficients in the Slater determinant[52,53].

Obtaining Compton profiles from Hartree-Fock wavefunctions

Biggs *et al.* break the total wavefunction into radial and angular parts, such that

$$\Psi_{n,l,m}(\boldsymbol{r},\theta,\phi) = R_{n,l}(\boldsymbol{r})Y_l^m(\theta,\phi), \quad (5.2)$$

which is essentially the same as the result provided in equation 2.5. The Fourier transform, $\chi_{n,l}(\boldsymbol{p})$, is then given as

$$\chi_{n,l}(\boldsymbol{p}) = \left(\frac{2}{\pi}\right)^{1/2} \int_0^\infty R_{n,l}(\boldsymbol{r}) j_l(\boldsymbol{p}\boldsymbol{r}) \boldsymbol{r}^2 \, \mathrm{d}\boldsymbol{r}, \quad (5.3)$$

where $j_l(\boldsymbol{pr})$ is a spherical Bessel function of the first kind, containing information about the angular part of the wavefunction. Biggs *et al.* finally give the Compton profile as

$$J_{n,l}(\boldsymbol{p}) \quad = \quad \frac{1}{2}\int_p^\infty \quad |\chi_{n,l}(\boldsymbol{p})|^2\, \boldsymbol{p}\ \mathrm{d}\boldsymbol{p}, \tag{5.4}$$

which we can see conveys the same information as the previously provided equations 3.8a and 3.9a combined, differing only in the normalising prefactor.

Extending into the relativistic case, another quantum number, $j = l \pm \frac{1}{2}$, is introduced to deal with the spin splitting of atomic orbitals. The result is that equation 5.4 becomes slightly more complicated;

$$J_{n,l,j}(\boldsymbol{p}) \quad = \quad \frac{1}{2}\int_p^\infty \quad \left(\chi^G_{n,l,j}(\boldsymbol{p})^2 + \chi^F_{n,l,j}(\boldsymbol{p})^2\right)\ \mathrm{d}\boldsymbol{p}, \tag{5.5}$$

where $\chi^G_{n,l,j}(\boldsymbol{p})$ and $\chi^F_{n,l,j}(\boldsymbol{p})$ are the Fourier transforms of new radial wavefunctions $G_{n,l,j}(\boldsymbol{r})$ and $F_{n,l,j}(\boldsymbol{r})$. The former is the larger component and appears very much like the nonrelativistic version. The latter contains the dependence on $l \pm \frac{1}{2}$. Thus, in the nonrelativistic limit, equation 5.5 reverts to 5.4. Biggs *et al.* employ the non-relativistic equation 5.4 for elements in the region $1 \leq Z \leq 36$, and the relativistic version, equation 5.5, for $36 \leq Z \leq 102$.

5.2 The GAMESS approach to theoretical Compton profiles

The General Atomic and Molecular Electronic Structure System (GAMESS)[54] is a computational code which has shown itself to be useful in the study of spin momentum densities. Koizumi *et al.* published extensively on the $La_{2-2x}Sr_{1+2x}Mn_2O_7$ system, combining experimental magnetic Compton scattering data with GAMESS calculations to better understand the electronic structure of this ferromagnetic perovskite[55–58]. Qureshi *et al.* used the same approach in their work on $Co_3V_2O_8$[59]. In both cases, the authors were able to determine which of the TM 3d t_{2g} and e_g orbitals were populated and reconstruct the two-dimensional spin momentum densities (2-D SMD). Recently, the Compton Scattering group at Warwick has obtained the GAMESS-US code (a freely available variant) and applied its capabilities in the study of $Ca_3Co_2O_6$, $Sr_3Ru_2O_7$, $La_{0.74}Sr_{0.26}CoO_3$ and $TbMnO_3$, with work on some of these systems already yielding interesting results.

GAMESS theory and operation

GAMESS is an *ab initio* quantum chemistry package. For a given molecule or cluster of atoms, limited in number only by computational considerations, the GAMESS code can produce a set of self-consistent molecular wavefunctions by combining atomic orbitals (AOs). Each molecular wavefunction, $\Psi(\boldsymbol{r}, \theta, \phi)$, is given by

$$\Psi(\boldsymbol{r}, \theta, \phi) = \sum_k c_k \psi_k(\boldsymbol{r}, \theta, \phi), \tag{5.6}$$

where $\psi_k(\boldsymbol{r}, \theta, \phi)$ are the AOs of the atoms involved in the calculation and c_k are their respective weighting factors. The primary aim of a linear combination of orbitals (LCAO) package like GAMESS is the determination of the set c_k, enabling the full molecular orbitals to be constructed. This is achieved with iterative computation, reducing the total system energy while considering the changes in energy and density - as in DFT methods, these changes are reduced to some predefined threshold when self-consistency is reached.

The basis set

The AOs are specified by the choice of basis set, of which there are many types available, suited to different types of atoms (transition metals, rare-earths, actinides, etc.). In this work, the basis sets were obtained from the online EMSL Basis Set Exchange[60]. Commonly used basis sets are those of triple-zeta-valence (TZV) type, which go beyond the simplest approximations by allowing polarisation and some expansion/contraction of the AOs. A TZV basis set was used by Koizumi *et al.* in their work, mentioned above, and so was employed in the $TbMnO_3$ work detailed here in section 7.3. This aside, all AOs possess a similar form to that given in equation 2.5, the atomic solution of the Schrödinger equation.

Sampling the 3-D atomic/molecular wavefunctions

The molecular wavefunctions of GAMESS were interpreted by a program called MACMOLPLT[61], a graphics package developed for plotting 3-D molecular structures, as well as 2-D and 3-D wavefunctions and electron densities. Using the functionality of MACMOLPLT, the real-space wavefunctions of each molecular orbital were sampled using a $n \times n \times n$ box centred on the

$$\begin{tikzcd}
\psi(\boldsymbol{r}) \arrow[rr, leftrightarrow, "\text{3-D FT}"] \arrow[d, "\text{AC}"'] & & \chi(\boldsymbol{p}) \arrow[d, "|\,|^2"] \\
B(\boldsymbol{s}) \arrow[r, leftrightarrow, "\text{1-D FT}"'] \arrow[d, "\langle\,\rangle\Omega_s"] & J(\boldsymbol{q}) \arrow[d, "\langle\,\rangle\Omega_q"] & n(\boldsymbol{p}) \arrow[l, "\text{Proj.}"'] \arrow[d, "\langle\,\rangle\Omega_p"] \arrow[ll, leftrightarrow, bend right, "\text{3-D FT}"'] \\
B(s) \arrow[r, leftrightarrow, "\text{1-D FT}"'] \arrow[rr, leftrightarrow, bend right, "\text{HT}"'] & J(q) \arrow[r, shift left, "\text{Int.}"] & n(p) \arrow[l, shift left, "\text{Diff.}"]
\end{tikzcd}$$

Figure 5.1: Reversible (blue) and irreversible (red) mathematical operations for various real-space and momentum-space expressions relating to Compton scattering. FT is a Fourier transformation, HT is a Hankel transformation and AC is autocorrelation. $|\;|^2$ is the square modulus, Proj. is the projection into a single dimension, and Int. and Diff. are single-dimension integration and differentiation, respectively. The $\langle\;\rangle\,\Omega$ operations represent obtaining spherical averages through double integration. Reproduced from the work of Saenz *et al.*[37] - for more information, refer to the original text.

atom or atomic cluster of interest, where n is simply an integer. It was essential at this stage to ensure that the wavefunctions were effectively zero at the edges of the box; if electron density was cut off, the corresponding Compton profiles would be unrepresentative of the simulated molecular orbitals. For this reason, an investigation was performed to find the optimum box size, and subsequently a $99 \times 99 \times 99$ box of size 9 Å was used to sample all of the relevant wavefunctions. The most spatially delocalised electron densities examined in this work, those of the hybridised $3d/2sp$ orbitals of TbMnO$_3$, were seen to diminish to zero within $\sim 2/3$ of the sampling volume. This molecular orbital sampling strategy provided real-space, and ultimately momentum-space, resolution sufficient to obtain theoretical profiles comparable with experimental data.

Obtaining the Compton profiles

Manipulation of the molecular wavefunctions was performed using MATLAB. Once a real-space wavefunction was obtained, its Fourier transform was taken in order to obtain $\chi(\boldsymbol{p})$, its momentum-space equivalent. The modulus of this was squared, giving $n(\boldsymbol{p})$, the 3-D electron momentum density (3-D EMD). Finally, $n(\boldsymbol{p})$ was projected into a single dimension by integrating along the directions perpendicular to the scattering direction. Thus, the end-stage

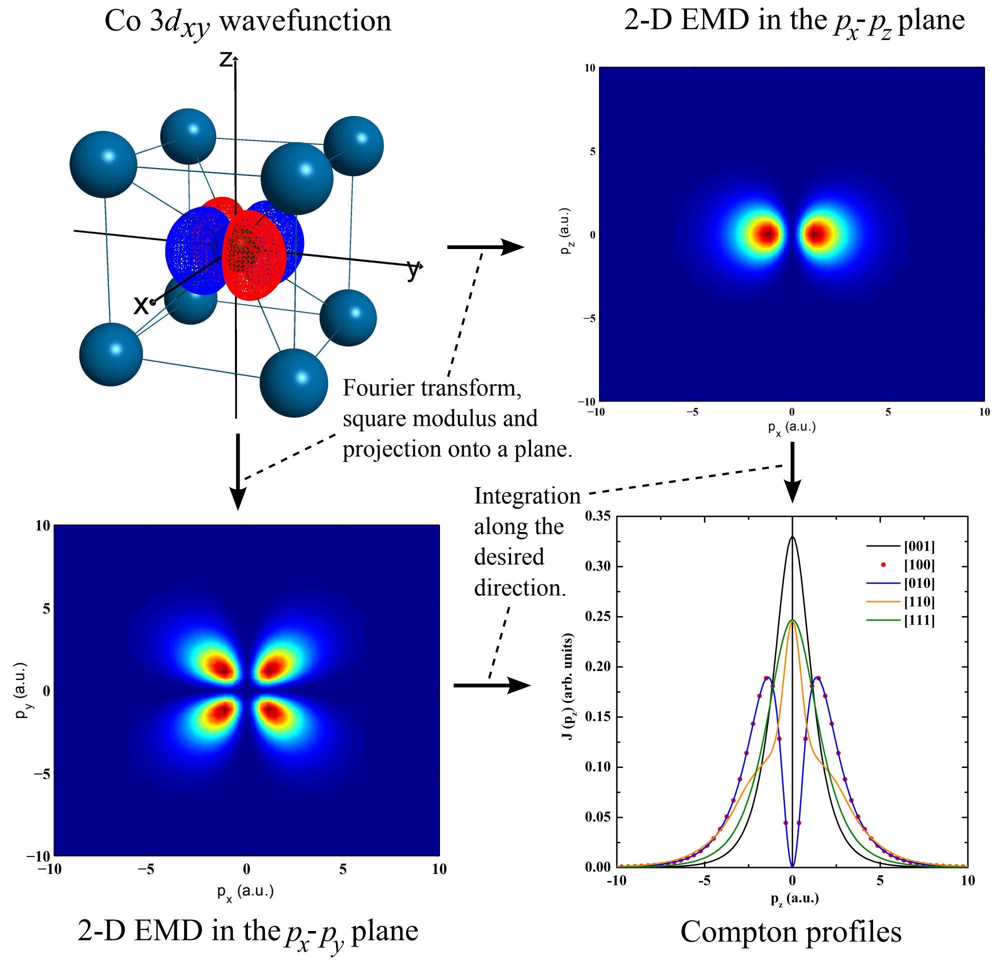

Co $3d_{xy}$ wavefunction

2-D EMD in the p_x-p_z plane

Fourier transform, square modulus and projection onto a plane.

Integration along the desired direction.

2-D EMD in the p_x-p_y plane

Compton profiles

Figure 5.2: Obtaining electron densities and Compton profiles from the result of a GAMESS calculation. The example here is the $3d_{xy}$ orbital of a Co atom surrounded by an arrangement of La atoms, as in the cubic perovskite system $LaCoO_3$.

for each molecular wavefunction was a two-column dataset of momentum and projected electron density, the Compton profile. These mathematical processes are defined concisely in equations 3.8a, 3.8b, 3.9a and 3.9b, as well as being illustrated in figure 5.1. The Compton profiles of the molecular orbitals possessed arbitrary momentum scales, and so were convoluted with a resolution function of 0.4 a.u. (see section 4.2) and interpolated onto experimental momentum scales to allow realistic comparison, and fitting, to data. Figure 5.2 illustrates the process of obtaining Compton profiles from the result of a GAMESS calculation - the example given is the $3d_{xy}$ orbital of a Co atom surrounded by La atoms, as in the cubic perovskite system $\mathrm{LaCoO_3}$, a system previously studied by the Compton Scattering group.

5.3 Density-functional theory

Density-functional theory (DFT) was developed by Hohenberg and Kohn to deal with inhomogeneous systems of interacting electrons[62]. They stated that the energy, E, of a system is a universal functional of its density, $n(\boldsymbol{r})$, and that it is minimised when it is equal to the ground-state energy. We have that

$$E\left[n(\boldsymbol{r})\right] = \int V(\boldsymbol{r})n(\boldsymbol{r})\ \mathrm{d}\boldsymbol{r} + F\left[n(\boldsymbol{r})\right], \tag{5.7}$$

where the first term deals with any external potential, $V(\boldsymbol{r})$, and might include, for example, the potential due to an atomic nucleus. The second term, $F\left[n(\boldsymbol{r})\right]$, is a functional of the density.

Inclusion of exchange and correlation

The initial work was expanded upon by Kohn and Sham, who included the crucial exchange and correlation energies in their description of the ground-state[63]. Equation 5.7 then becomes

$$E\left[n(\boldsymbol{r})\right] = \int V(\boldsymbol{r})n(\boldsymbol{r})\ \mathrm{d}\boldsymbol{r} + \frac{1}{2}\iint \frac{n(\boldsymbol{r})n(\boldsymbol{r}')}{|\boldsymbol{r}-\boldsymbol{r}'|}\ \mathrm{d}\boldsymbol{r}\ \mathrm{d}\boldsymbol{r}' + G\left[n(\boldsymbol{r})\right]. \tag{5.8}$$

The second term is the electron-electron Coulomb interaction, and the functional, $G\left[n(\boldsymbol{r})\right]$, is given by

$$G\left[n(\boldsymbol{r})\right] \equiv T\left[n(\boldsymbol{r})\right] + E_{\mathrm{xc}}\left[n(\boldsymbol{r})\right], \tag{5.9}$$

where $T\left[n(\boldsymbol{r})\right]$ is the kinetic energy of the system and $E_{\mathrm{xc}}\left[n(\boldsymbol{r})\right]$, the exchange-correlation energy, is defined as

$$E_{\mathrm{xc}}\left[n(\boldsymbol{r})\right] = \int n(\boldsymbol{r})\varepsilon_{\mathrm{xc}}\left(n(\boldsymbol{r})\right)\,\mathrm{d}\boldsymbol{r}. \tag{5.10}$$

This last equation represents the only aspect of DFT which is not exact; it must be approximated. In the work of Kohn and Sham, E_{xc} is solely a function of the electron density - this came to be known as the local density approximation (LDA). There exist other approximations which include the spin densities, a necessity for studying magnetic systems, and consider the density gradients, improving the description of exchange and correlation effects.

Exchange and correlation terms

In equation 5.10, $\varepsilon_{\mathrm{xc}}$ is the exchange and correlation energy per particle, itself made of ε_{x} and ε_{c} terms. For as long as exchange and correlation have been discussed, many contributors have offered different forms of ε_{x} and ε_{c}, with a simple and commonly-used version of ε_{x} being given by Dirac as early as 1930[64]. With only a few exceptions, approximations for these parameters fall into two categories; local spin density approximations (LSDA) and generalised gradient approximations (GGA). The first type are determined only by the spin densities - commonly used LSDA functionals are those of Vosko, Wilk and Nusair[65], as well as many from Perdew *et al.*[66–68]. GGA functionals, such as those from Becke[69]; Perdew, Burke and Wang[70]; and Perdew, Burke and Ernzerhof[71], can be expressed as

$$E_{\mathrm{xc}}^{\mathrm{GGA}}\left[n_{\uparrow}(\boldsymbol{r}), n_{\downarrow}(\boldsymbol{r})\right] = \int n(\boldsymbol{r})\varepsilon_{\mathrm{xc}}\left(n_{\uparrow}(\boldsymbol{r}), n_{\downarrow}(\boldsymbol{r}), \nabla n_{\uparrow}(\boldsymbol{r}), \nabla n_{\downarrow}(\boldsymbol{r})\right)\,\mathrm{d}\boldsymbol{r}, \tag{5.11}$$

where the consideration of the spin density gradients, $\nabla n_{\uparrow}(\boldsymbol{r})$ and $\nabla n_{\downarrow}(\boldsymbol{r})$, generally leads to improved bond angles, bond lengths and total energies[72].

5.4 SPR-KKR

The Munich spin polarised relativistic - Korringa-Kohn-Rostocker package (SPR-KKR)[73,74] was used in this thesis to obtain information primarily about NiMnSb. KKR methods use Green's function formalism to solve the Kohn-Sham-Dirac equation and tend to provide the usual gamut of DFT necessities; self-consistent fields (SCF), densities-of-states (DoS) and site-specific spin moments. In addition, SPR-KKR has an emphasis on calculating spectroscopic properties, such as X-ray absorption spectra (XAS), X-ray magnetic circular dichroism (XMCD), X-ray photoelectron spectroscopy (XPS) and, most usefully for those studying spin densities, magnetic Compton profiles (MCPs). These too are available for each site in the system. A useful overview of the application of the KKR method to the study of electron densities and Compton profiles is provided by Bansil *et al.*[75].

Like various other types of DFT, SPR-KKR attempts to solve the Kohn-Sham-Dirac equation;

$$\left(\frac{\hbar}{i}c\alpha \cdot \nabla^2 + \beta mc^2 + V(\boldsymbol{r})\right)\psi(\boldsymbol{r}, E) = E\psi(\boldsymbol{r}, E). \tag{5.12}$$

The form given here is theoretically identical to the Schrödinger equation provided previously in equation 2.1, but includes a relativistic energy term, βmc^2, and the notation is slightly different. A full description of the system is achieved when the Green's function, $G(\boldsymbol{r}, \boldsymbol{r}', E)$, is determined, where

$$\left(\frac{\hbar}{i}c\alpha \cdot \nabla^2 + \beta mc^2 + V(\boldsymbol{r}) - E\right)G(\boldsymbol{r}, \boldsymbol{r}', E) = \delta(\boldsymbol{r} - \boldsymbol{r}'). \tag{5.13}$$

As a side note, the necessity of the Dirac equation to be relativistically covariant means that the parameters α and β must be matrices - it is this feature which leads the Dirac equation to predict the existence of electron spin.

Regarding the potential term, we have

$$V(\boldsymbol{r}) = V_{\mathrm{n}} + V_{\mathrm{e}} + V_{\mathrm{xc}} + \beta\sigma \cdot \boldsymbol{B}_{\mathrm{eff}}. \tag{5.14}$$

$V(\boldsymbol{r})$ includes the Coulomb potentials from nuclei, V_{n} ($\propto -Ze^2/r$), and other electrons, V_{e} (as given in equation 5.8), as well as exchange and correlation. The latter part is split into a spin-averaged term, V_{xc}, and a spin-dependent term, $\beta\sigma \cdot \boldsymbol{B}_{\mathrm{eff}}$, which is determined by E_{xc}. Within SPR-KKR several approximations for E_{xc} are available, including VWN[65] and PBE[71].

SPR-KKR utilises the muffin-tin approximation (MTA), in which the nuclear potentials are described as being spherically symmetric within a given region around each nucleus known as the muffin-tin. The muffin-tins are non-overlapping spheres which vary in size according to the atoms they represent; generally muffin-tin radii are in the region 1 to 2 Å. Outside of these spheres, in the interstitial region, the potential is represented by a constant. The wavefunctions inside and outside of the muffin-tins are made of linear combinations of spherical harmonics and plane waves, respectively. These, like the corresponding potentials, are constrained to be continuous at the muffin-tin/interstitial boundaries.

Useful features of the KKR method

A number of DFT packages are used within the physical sciences for a wide variety of purposes. For the magnetic Compton scattering group, the advantageous features offered by KKR over some other DFT methods are these:

- The KKR method is generally thought to provide good descriptions of metallic and magnetic systems.

- The calculation times are relatively short. This is due in part to the fact that the atomic spherical harmonics, which sum to provide part of the wavefunctions within the muffin-tins, are already well known. The total basis set is also much smaller than is typically used in entirely plane wave DFT methods.

- The charge and spin distributions, density-of-states, band structure, Fermi surface and, importantly, the magnetic Compton profile, can all be readily extracted for the system of interest. These are obtained through straightforward mathematical operations on the computed Green's function, $G(\boldsymbol{r}, \boldsymbol{r}', E)$.

- Owing to the use of atom-centred muffin-tin potentials, quantities for charge, spin moment and orbital moment are attributed to specific sites and atomic orbital types (s, p, d, etc.) in the system. This contrasts with some DFT methods where only band-specific contributions are directly available.

- Atomic disorder can be simulated with the use of the coherent potential approximation (CPA)[76], in which the effective potential of a certain site is composed of the potentials from several chemical species, representing a random interchange of atoms throughout the entire system. This contrasts with other methods where large supercells are often required to deal with disorder.

Chapter 6

NiMnSb - theory, production and characterisation

NiMnSb is a half-Heusler alloy and one of the most widely studied materials in the field of *spintronics* (or *spin electronics*). This is because NiMnSb, along with only a handful of other magnetic materials, is predicted to be 100% spin-polarised at the Fermi level[77]. This makes it ideal for the injection of a highly spin-polarised current into devices such spin-LEDs, spin-FETs and magnetic tunnel junctions (MTJs), with one application being magnetic random-access memory (MRAM) elements with improved sensitivity and processing speed[78–80]. These spintronic devices provide the advantages of decreased power consumption, miniturisation and nonvolatility in a field where continuous improvement of performance is a requirement.

Motivation

Since the work of de Groot *et al.* in 1983[77], half-Heusler alloys have been considered amongst the strongest candidates for the production of spintronic devices. de Groot *et al.* performed band structure calculations on several half-Heuslers, showing that they belonged to a new class of material: the half-metallic ferromagnet (HMFM). This is a ferromagnet which possesses zero density-of-states at the Fermi level in one of its spin channels, but conducts normally in the other, providing a spin polarisation of 100%. NiMnSb was exhibited as an archetype of this new class of material and has since been the focus of a wide range of theoretical and experimental work. In addition to its appealing electronic properties, NiMnSb is epitaxially compatible with several commercially available semiconductor surfaces; InP (001)[81], CdS[82] and GaAs[83–85], reinforcing its suitability for the development of spintronic devices.

Several attempts have been made to confirm the predicted spin polarisation of NiMnSb in thin films[86–91] and in bulk samples[89,92]. The experimental results have generally been around 50%[87,90–92], with the exception of a report of nearly 100% from Ristoiu *et al.* in 2000[86]. The theoretical 100% spin-polarised band structure of NiMnSb is based on a perfectly ordered crystal in its ground state, i.e. at a temperature of '0 K', but in reality, reduced spin polarisation in the bulk may be caused by non-stoichiometry, atomic disorder, the existence of other phases and non-zero temperature effects such as reduced magnetisation. At surfaces and interfaces, these issues are still important, but nanostructuring and the general surface/interface quality, may also play a large role[93–95].

Reduced magnetisation, in particular, has recently been shown to have a significant effect on the spin polarisation of predicted HMFMs. Fully *ab initio* disordered local moment DFT (DLM-DFT) calculations were presented by Aldous *et al.* showing that the spin polarisation for NiMnSb and zincblende-MnSb (also a predicted HMFM) diminished rapidly above a temperature, T^*, that was much less than T_C[94]. The calculations simulated the effects of thermally induced spin fluctuations on the electronic structure of NiMnSb, specifically the positions of states around the Fermi energy, and predicted a vastly reduced spin polarisation at a T^* of 100 or 180 K, depending on whether the experimental or theoretical value of T_C was chosen. This demonstrates the importance of non-zero temperature effects in the predicted HMFMs and provides a possible explanation for the reduced spin-polarisation values of NiMnSb mentioned previously. The calculations also provide motivation for this and future studies of NiMnSb's electronic and magnetic properties as a function of temperature.

As mentioned above, Ristoiu *et al.* examined a thin film sample of NiMnSb and reported a spin polarisation of nearly 100%[86]. They used inverse photoemission and attributed their value to the quality and near-ideal stoichiometry of their prepared NiMnSb surface. The usual techniques used to measure spin polarisation are point-contact Andreev reflection (PCAR) and spin-polarised photoemission, both of which are surface sensitive. If the composition or structure of a sample's surface deviates from the ideal, the electronic structure being probed with these methods will be modified and, most likely, the spin polarisation will be reduced.

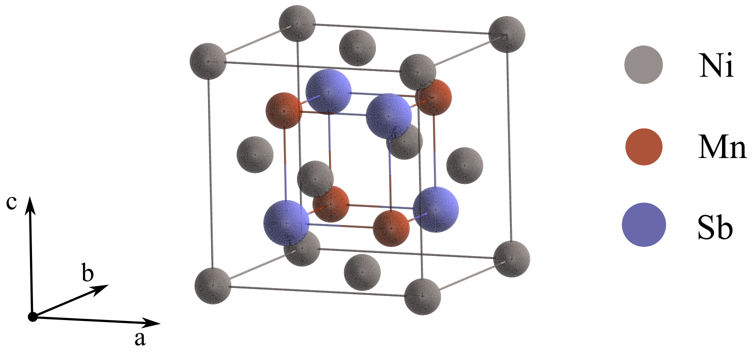

Figure 6.1: The $C1_b$ crystal structure of NiMnSb (space group $F\bar{4}3m$).

Magnetic Compton scattering offers the possibility of measuring only the bulk electronic structure of NiMnSb. The high energy of the X-rays used, typically around 200 keV, means that scattering from a sample's surface is negligible.

Chapter overview

This chapter primarily describes the production and study of a NiMnSb single crystal. Details of the crystal production method, along with results from various characterisation techniques, is provided, as well as theoretical results from DFT. The MCPs are given and discussed in relation to the other work. Finally, the results of an XPS study involving NiSb, MnSb and NiMnSb surfaces are given. The motivation for this stems from the experimental desire to perform more informative measurements on clean stoichiometric surfaces of these materials. A more extensive introduction to this work is provided in the relevant section, 6.6.

6.1 Introduction

Crystal structure

NiMnSb has the $C1_b$ structure (space group $F\bar{4}3m$), which consists of four interpenetrating face centred cubic (f.c.c.) lattices - see figure 6.1. The Wyckoff positions for the atoms are: Ni at (0, 0, 0), Mn at (1/4, 1/4, 1/4) and Sb at (3/4, 3/4, 3/4). The (1/2, 1/2, 1/2) site is vacant. The experimental lattice parameter is 5.903 Å according to Castelliz[96], 5.92(2) Å according to Endo[97] and 5.921 Å according to Gardelis *et al.*[98]. These values come from room temperature X-ray diffraction studies of annealed polycrystal samples.

Spin polarisation

Like all magnetic systems, HMFMs possess distinct band structures for majority- and minority-spin electrons. In ideal HMFMs one spin channel possesses zero density-of-states (DoS) at the Fermi level, thus yielding an integer spin moment, in μ_B, and 100% spin polarisation.

The spin polarisation of a material may be reported to be 100% solely on the basis of theoretical work, usually when a DoS calculation shows there to be a band gap for one spin channel only. It is important to note, however, that for comparison with experimental results, the spin polarisation, P_n, may need to be weighted by the Fermi velocity, v_F, to account for different transport properties. As derived by Mazin, we have[99]

$$P_n = \frac{N_\uparrow v^n_{\mathrm{F},\uparrow} - N_\downarrow v^n_{\mathrm{F},\downarrow}}{N_\uparrow v^n_{\mathrm{F},\uparrow} + N_\downarrow v^n_{\mathrm{F},\downarrow}}, \tag{6.1}$$

where n can take values 0, 1 or 2. With $n = 0$, P_0 is defined entirely by the DoS at the Fermi energy. Having $n = 1$ or 2 represents the ballistic and diffusive transport regimes, respectively. Different experimental techniques may therefore yield different values for P_n, depending on the type of electrical transport being exploited. As has been previously demonstrated for $\mathrm{Co}_{1-x}\mathrm{Fe}_x\mathrm{S}_2$[100], magnetic Compton scattering is sensitive to the spin-dependent DoS *without* modification by v_F (i.e. the $n = 0$ case). Therefore, deduction of NiMnSb's spin polarisation should be possible by direct comparison of the MCPs with theoretical calculations. It is worth noting that spin-polarised photoemission measurements are also of $n = 0$ type.

Electronic structure

The electronic properties of NiMnSb are essentially determined by hybridisation of two types[101]; (a) *d*-*d* hybridisation between the lower energy $3d$ states of Ni and the higher energy $3d$ states of Mn, and (b) *sp*-*d* hybridisation between the $5s$ and $5p$ states of Sb and the $3d$ states of the transition metals. The former leads to the creation of bonding and antibonding bands in the minority channel which, much like the situation in many elemental and compound semiconductors, are separated by an energy gap. The implications are twofold. First, electrons tend to migrate from Mn sites, where the antibonding states are mainly located, to the Ni sites which possess the bonding states. Accordingly, a DoS diagram for NiMnSb (provided later in figure 6.12) reveals more unpopulated states above the Fermi level for Mn than for Ni. The second result of *d*-*d* hybridisation is the formation of a band gap in the minority-spin channel that straddles the Fermi level.

The *sp*-*d* hybridisation is crucial to the development of half-metallicity in NiMnSb. Sb 5*s* and 5*p* states are capable of holding 8 electrons per formula unit, but Sb alone has only 5. Charge originating on the transition metals is subsumed into these low energy *s* and *p* bands. In this way we are left with the '18 electron rule' for half-Heusler alloys[101,102], stating that if a particular system has 18 valence electrons in total, 8 will be accommodated by the Sb *sp* band and 10 will fill the bonding *d* band. An 18 electron system, such as CoTiSb or NiTiSn, would then be a semiconductor in the majority *and* minority-spin channels, because no electrons are available to populate the higher energy antibonding states[103]. If more than 18 valence electrons are present in the system, they begin to fill up the antibonding states of the majority channel, contributing to the conductivity as in a normal metal. This is seen for NiMnSb, which has 22 valence electrons. The spin moment of the system, which is simply the number of spin-unpaired electrons, is given by $M = Z_v - 18$, where Z_v is the number of valence electrons. Thus, NiMnSb is predicted to have a spin moment of 4 μ_{B}/f.u.

6.2 Crystal production and characterisation

Crystal production

A polycrystalline sample of stoichiometric NiMnSb was produced using a small tri-arc furnace - see section 4.4 for details. Precursory investigations were performed to determine the fractional losses of Ni, Mn and Sb over several melts. In these tests it was seen that Sb experienced the largest loss per melt, so first attempts at a stoichiometric polycrystal included between 3 and 5% more Sb than specified by the proper mixing ratio. These first polycrystals, upon investigation with EDX, were actually deficient in Mn, but had approximately the correct ratio of Ni:Sb. The next batch of polycrystals was produced with varying excesses of Mn.

After production, annealing (850 °C for 150 hours) and analysis with EDX, a sample with composition Ni:Mn:Sb $\sim$ 1:1:1 was chosen and subject to a second growth technique. This involved a larger four-arc furnace, specifically designed to produce single crystals from ingots

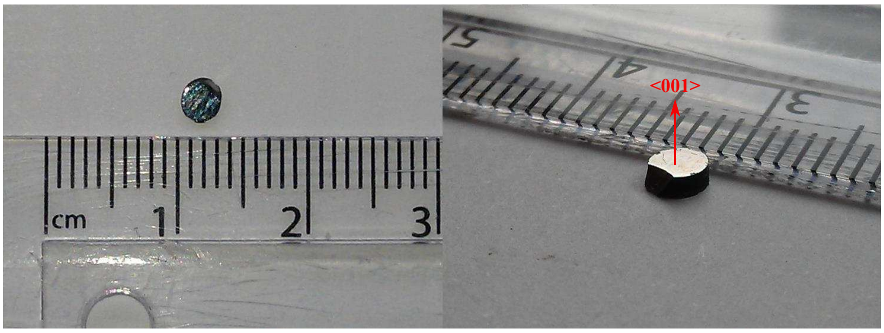

Figure 6.2: The NiMnSb crystal disc, as used in Laue imaging, magnetic Compton scattering and XPS. The approximate ⟨001⟩ crystallographic direction is indicated.

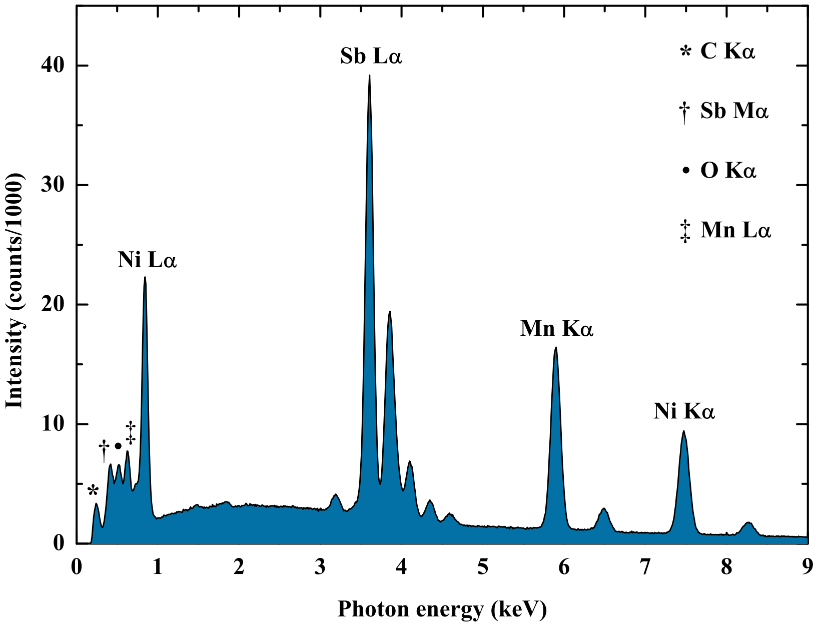

Figure 6.3: Energy dispersive X-ray spectrum from a NiMnSb crystal. After ZAF corrections, the composition of the crystal was found to be: Ni 35.2%, Mn 32.3%, Sb 32.5%.

of polycrystal material. Following the Czochralski method, under 1 atm of Ar gas, the sample was melted by the arcs and a tungsten seed crystal was introduced. The NiMnSb crystal formed around the seed and was pulled, at a rate of a few mm/hour, from the molten boule, being slowly rotated at the same time. This part of the NiMnSb single crystal production was performed by Ravi Singh of the Superconductivity and Magnetism group.

Energy-dispersive X-ray spectroscopy

The NiMnSb single crystal was cylindrical in shape, around 20 mm long and 3 mm in diameter. The material at the centre of the cylinder was cut into five discs around 2 mm in thickness

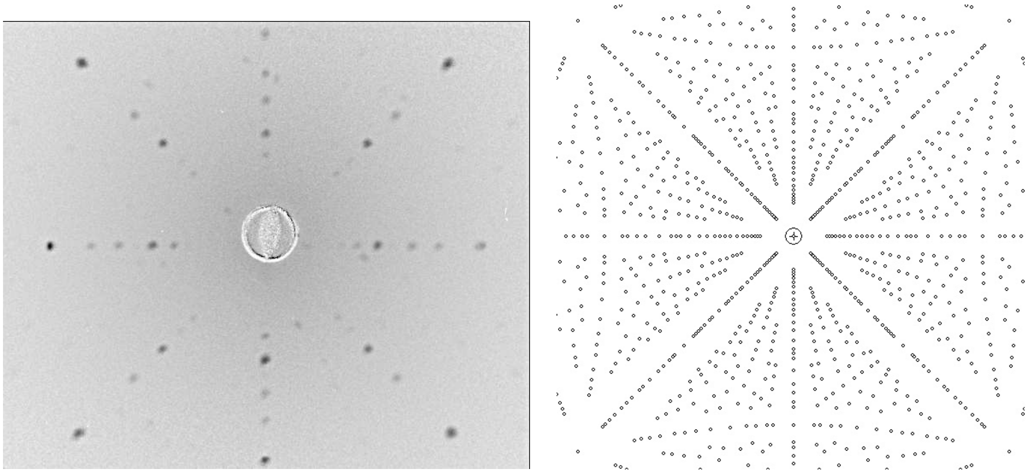

Figure 6.4: (Left) The Laue image from a NiMnSb crystal with the X-ray beam directed along a ⟨001⟩ direction - see figure figure 6.2. (Right) A theoretical Laue pattern obtained from the OrientExpress software package. OrientExpress is not capable of reproducing the intensity variation in experimental Laue spots due to atom- and lattice-specific structure factors.

in order to achieve access to the interior for characterisation. Figure 6.2 shows the size and shape of the crystal samples. First, EDX measurements were performed on the five discs to determine the chemical composition. The EDX spectrum from one disc is shown in figure 6.3, where the relevant peaks are identified. The quantitative analyses of all five samples, performed by the EDX spectrum collection software, were consistent to within $\sim 0.5\%$. The composition of the crystal was found to be: Ni 35.2%, Mn 32.3%, Sb 32.5%, which conforms reasonably well to the expected values of 1/3 per species.

Laue reflection

The back-reflection Laue method was used to investigate the NiMnSb sample and align it for magnetic Compton scattering and SQuID magnetometry. The Laue patterns had clear single spots at the high-symmetry reflections, indicating that the sample was a single crystal - blurry spots or 'twinning' (several misaligned copies of the same Laue pattern) would suggest otherwise. Comparison with patterns obtained from the Orient Express software package[45] showed that the sample's crystal structure was consistent with the cubic symmetry expected for NiMnSb. Figure 6.4 shows an experimental NiMnSb Laue pattern along a ⟨001⟩-type crystallographic direction alongside theory from Orient Express. The ⟨001⟩-type direction lies approximately perpendicular to the polished face of crystal disc, as illustrated in figure 6.2.

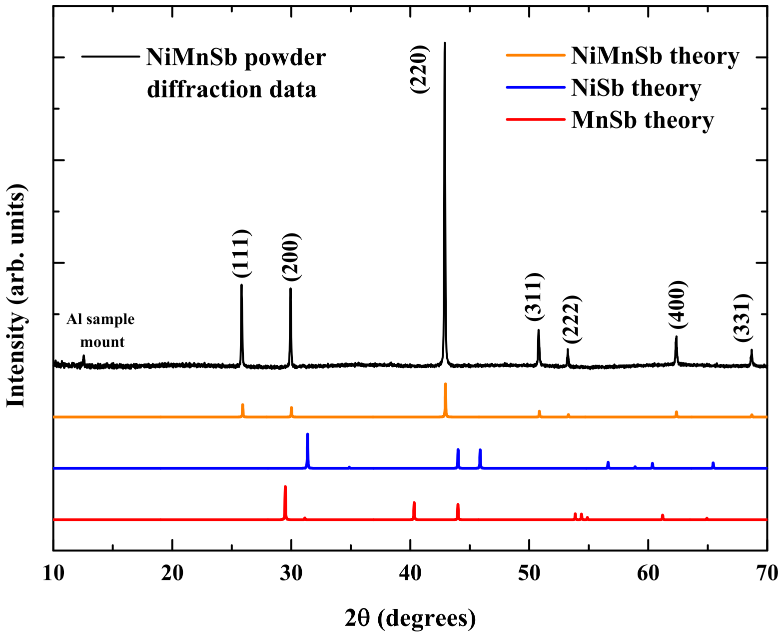

Figure 6.5: NiMnSb powder X-ray diffraction data. For comparison, theoretical 2θ plots from the PowderCell software package are also shown. To a high level of confidence, the sample appears to be single-phase crystalline NiMnSb, with lattice parameter 5.945 ± 0.001 Å.

Powder X-ray diffraction

To further check the crystallinity and quality of the NiMnSb sample, a powder X-ray diffraction experiment was performed using powder from two of the NiMnSb discs. A high statistical quality 2θ scan was performed over 15 hours. The 2θ plot is shown in figure 6.5, along with theoretical plots from the PowderCell software package[104] for NiMnSb, NiSb and MnSb. NiSb, in particular, has been identified as an impurity phase in NiMnSb bulk crystals[98].

With the exception of a small peak at 13° associated with the Al sample holder, the 2θ scan contains no peaks other than those of NiMnSb. The peak positions and relative sizes are in good agreement with those of the predicted 2θ spectrum from PowderCell. In addition to the EDX and Laue reflection results, this is a good indicator that the sample was a high quality single crystal. Structural refinement of the powder diffraction data resulted in a lattice parameter of 5.945 ± 0.001 Å, which is between 0.4 and 0.7% larger than previously reported values for bulk samples; 5.92(2) Å from Endo[97] and 5.903 Å from Castelliz[96]. These measurements and structural refinement were performed with the help of David Walker of the Ferroelectrics and Crystallography group.

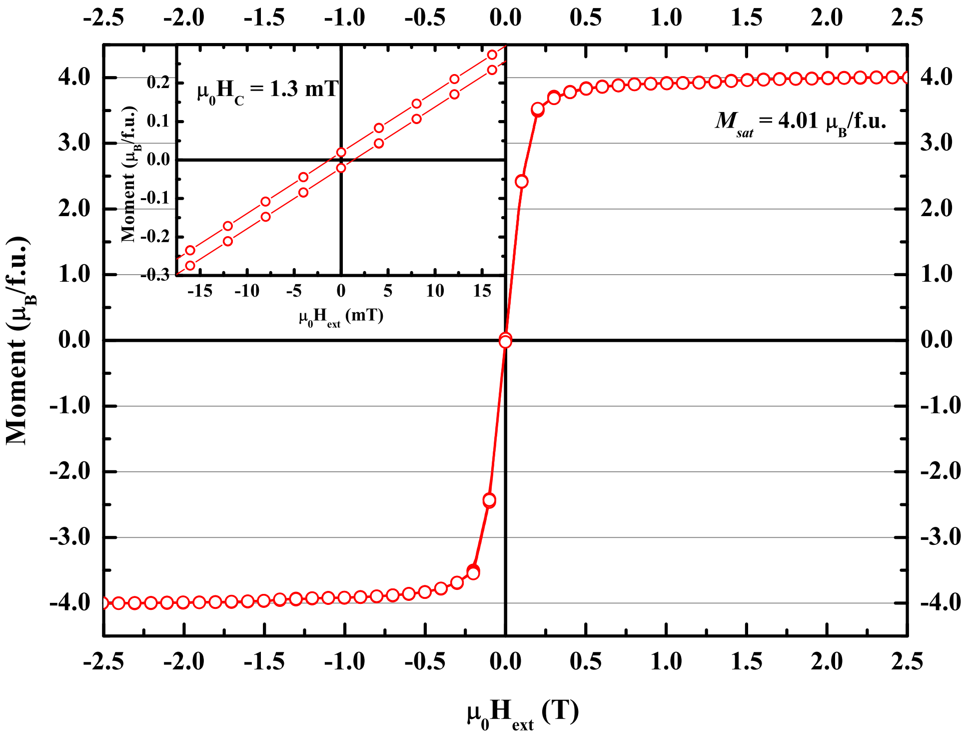

Figure 6.6: SQuID magnetometry of NiMnSb recorded at 2 K from -2.5 T to +2.5 T. The saturated moment is close to the expected 4 μ_B per formula unit. The inset shows the low field response, confirming the hysteretic behaviour of a ferromagnet.

6.3 Magnetometry

SQuID magnetometry was performed on small fragments of one of the discs cut from the crystal. Magnetisation vs applied field, MvH, and magnetisation vs temperature, MvT, measurements were performed. The results are given in figures 6.6 and 6.7.

During the magnetisation measurements, the magnetic field was applied approximately along the ⟨001⟩ direction. The magnetic anisotropy of NiMnSb is known to be small[105], so the saturated moment and saturating field are not greatly affected by the misalignment, estimated at 5 to 10°, of the crystallographic axis with the direction of the applied field. Indeed, Hordequin *et al.*[105] showed that the saturated moments in NiMnSb differed only slightly, ~0.4%, along the crystallographic directions ⟨001⟩, ⟨110⟩ and ⟨111⟩.

MvH measurements

The MvH measurements were performed at a temperature of 2 K. The coercive field was

1.3 mT. The NiMnSb moment saturated at ∼0.25 T, in agreement with work on by Clowes *et al.*[89] and Gardelis *et al.*[98]. The saturated moment, after extrapolating the data over 2 T back to $H = 0$, was 3.98 ± 0.01 μ_B/f.u., again in good agreement with previous reports and theory.

MvT measurements

MvT measurements were performed in fields of 0.75 and 2.5 T. Initially, 200 data points were collected for each field, employing the relatively slow temperature sweep rate of 0.5 K/min. These data, though statistically very good, were seen to suffer from some sinusoidal variation to the measured moment - possibly relating to the way the temperature in the SQuID sample space is controlled. This complicated the power law fitting and made the derivatives $\mathrm{d}M/\mathrm{d}T$ and $\mathrm{d}M^2/\mathrm{d}T^2$ impossible to interpret meaningfully. Repeating the experiment with a smaller sample (0.12 *cf.* 0.24 e.m.u. total moment), a slower sweep rate of 0.33 K/min and a higher data point density, resulted in the MvT data presented here.

MvT analysis - Bloch's power law

Bloch's $T^{3/2}$ law, given in equation 6.2, has previously been applied to various 'low temperature' regions, up to 70 K, 200 K and 300 K, of NiMnSb MvT data[98,105,106]. For a classical ferromagnet with localised moments and long-range order, Bloch's law describes the reduction in spontaneous magnetisation due to excited spin-waves, or magnons, well below the Curie temperature, T_C. T_C for NiMnSb is ∼ 730 K[98]. Spin-waves impair the effective ordering of magnetic moments. Correspondence between MvT data and Bloch's $T^{3/2}$ law is often taken as an indicator of localised, Heisenberg-like ferromagnetism. Bloch's law states that[3]

$$M(T) = M_0(1 - AT^{3/2}), \tag{6.2}$$

where M_0 is the '0 K' magnetisation (i.e. all spins aligned) and the $T^{3/2}$ dependence stems from a derivation of the total number of spin-waves in a system with temperature, T - see Kittel's *Introduction to Solid State Physics* (page 455)[3]. The parameter A relates to the spin-wave stiffness, D, which is the coefficient in the classical spin-wave dispersion relation, $E(\boldsymbol{q}) = D\boldsymbol{q}^2$, on which Bloch's law depends.

It is worth noting that Hordequin *et al.*[105] predicted the existence of a small energy gap, β,

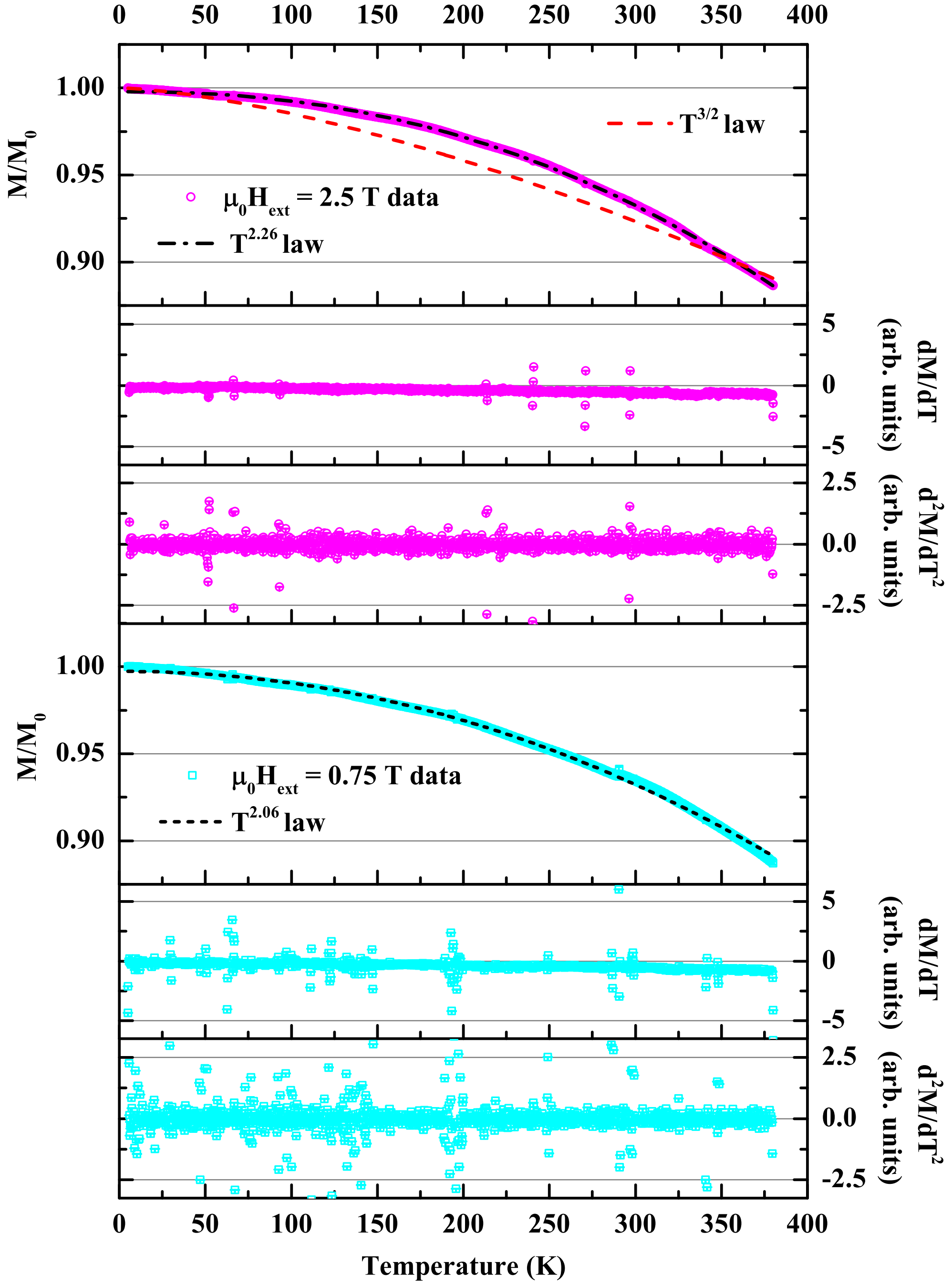

Figure 6.7: SQuID magnetometry of NiMnSb recorded at fields of 0.75 and 2.5 T from 5 to 380 K. The derivatives $\mathrm{d}M/\mathrm{d}T$ and $\mathrm{d}M^2/\mathrm{d}T^2$ are also shown, highlighting the lack of transitions in this temperature range. Dashed black lines represent the T^n fitting laws applicable for each field while the dashed red line is a Bloch's law $T^{3/2}$ fit to the 2.5 T data. The error bars are smaller than the data points.

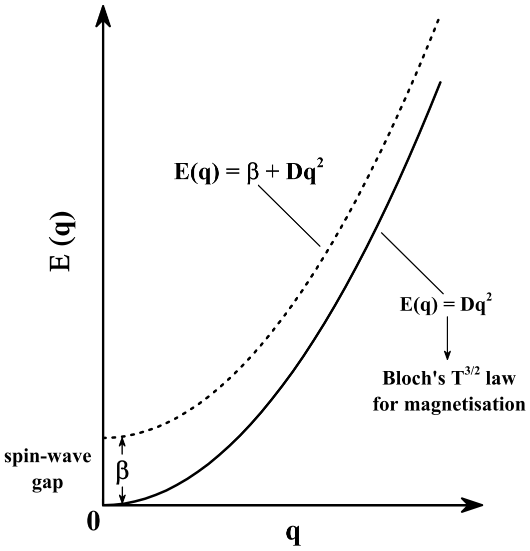

Figure 6.8: The low wavevector, long wavelength, dispersion relation for spin-waves, or magnons, in a ferromagnet. The solid line depicts the ideal Heisenberg case where no spin-wave gap exists - this leads to Bloch's $T^{3/2}$ law for magnetisation in classical ferromagnets. If magnetic anisotropy is present, a gap, β, appears at $\boldsymbol{q} = 0$, modifying the dispersion relation and the magnetisation power law. This second case is depicted with a dashed line.

in the spin-wave excitation spectrum of NiMnSb based on inelastic neutron scattering[105]. They gave the value of β as 1.0 ± 0.2 meV at 25 K and at room temperature. Illustrative low wavevector spin-wave dispersions are shown in figure 6.8.

Bloch's $T^{3/2}$ law was applied here, but was incapable of describing well any region of the NiMnSb $M\text{v}T$ plots, for fields of 0.75 or 2.5 T. Next, instead of being constrained to 3/2, the T power exponent, n, was allowed to vary freely. Good descriptions of the data (reduced-$\chi^2_{0.75} = 1.90$ and reduced-$\chi^2_{2.5} = 0.43$) were obtained for values of $n_{0.75} = 2.063 \pm 0.005$ and $n_{2.5} = 2.258 \pm 0.003$. Both values deviate from that predicted by Bloch's law, but another interesting result is that they do not agree with *each other*. Possible reasons for these features are discussed shortly.

Interpretations of previous NiMnSb $M\text{v}T$ data

Otto *et al.* discovered a similar deviation from Bloch's law for NiMnSb[106]. They observed an n of 1.9 and ascribed this to a strongly temperature-dependent spin-wave stiffness of the form $D(T) = D_0 - D_1T^2$. In other work, Gardelis *et al.*, whose measurements were performed in a field of 2 T, saw a T^2 dependence above 200 K, and interpreted this as evidence of itinerant, or

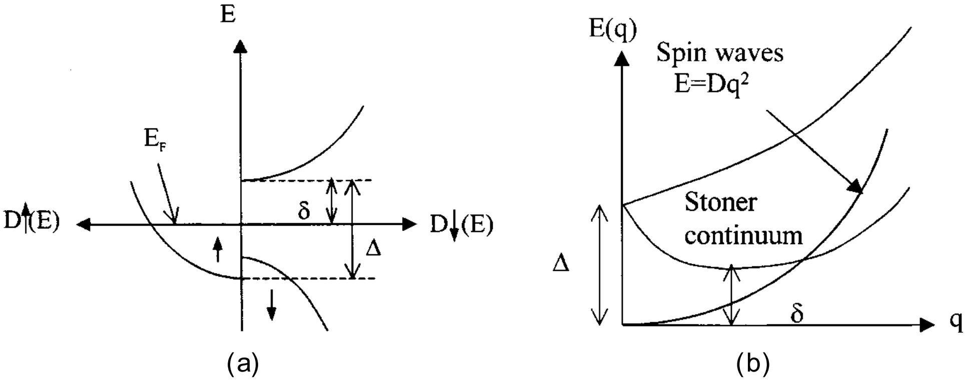

Figure 6.9: Illustrations of the band structure (a) and spin-wave dispersion (b) for a half-metallic ferromagnet. Reproduced from the work of Hordequin *et al.*[111].

Stoner-like, ferromagnetism, in accordance with several theoretical predictions[107–110]. Below 200 K, Gardelis *et al.*'s data was consistent with Bloch's $T^{3/2}$ law. Thus, in that work, it was claimed that NiMnSb underwent a transition from a Heisenberg ferromagnet to an itinerant ferromagnet at 200 K. Gardelis *et al.* also stated that Bloch's law should hold only up to $T \sim T_C/3$, which for NiMnSb would be $\sim$ 240 K.

A Heisenberg-to-Stoner picture for NiMnSb was also put forward by Hordequin *et al.*, who saw the same $T^{3/2} - T^2$ transition in their $M\text{v}T$, only at a lower temperature of 70 K[105]. They argued that this transition was indicative of a crossover from half-metallicity to normal ferromagnetism[111], justifying their claim in this way: At low temperatures, only the classical transverse spin-waves, with the associated $T^{3/2}$ magnetisation dependence, can exist. With increasing temperature, access to a Stoner mode is achieved, where spin-up electrons may be scattered into spin-down states. This is the mechanism that provides the T^2 magnetisation dependence in normal itinerant ferromagnets, but it is clearly incompatible with the description of the ground state of an ideal half-metal because there are no available spin-down states at the Fermi energy - see figure 6.9. Access to the Stoner mode in a half-metal ought to be impossible without providing energy of at least δ, the gap between the Fermi energy and the bottom of the unpopulated spin-minority conduction band. Hordequin *et al.* estimated the required temperature for this to be around 800 K in NiMnSb and stated that, "the relation between the crossover temperature observed in the magnetization [...] and the value of this gap is not yet clearly understood." They suggested that δ may be reduced due to atomic disorder, specifically of the Mn atoms, therefore allowing access to the Stoner mode at a lower temperature. This theory is supported by Brown *et al.*, who explicitly stated that disorder introduced additional minority spin states within the energy range of the band gap[112].

With respect to the previously reported transitions in NiMnSb magnetic behaviour, in this work the $M\mathrm{v}T$ data were differentiated in order to expose any difference in the T power law over the measured temperature range. There were no turning points in $\mathrm{d}M/\mathrm{d}T$ for 0.75 or 2.5 T and the $\mathrm{d}^2M/\mathrm{d}T^2$ plots were essentially zero - see figure 6.7. Therefore no transitions are believed to occur.

Modified Bloch's law

In their later work, Hordequin *et al.* suggested a modified form of Bloch's law for low temperature NiMnSb $M\mathrm{v}T$ data, where the magnetisation is dependent on $T^{3/2}\ \mathrm{e}^{-\beta/k_BT}$. This is due to the existence of a low wavevector gap, β, in the classical spin-wave dispersion. Bloch's law assumes β to be zero, but a more complete description, with a non-zero gap, requires an additional term of the form[113]

$$f_{3/2}(y) = \sum_{m=1}^{\infty} \frac{\mathrm{e}^{-my}}{m^{3/2}}, \tag{6.3}$$

where y is equal to β/k_BT. Thus, the first term is $\mathrm{e}^{-\beta/k_BT}$, and the importance of subsequent terms diminishes rapidly with m.

Compared to T^n free fitting, this modified function provided a significantly worse fit over the full $M\mathrm{v}T$ region for both fields examined in this work (reduced-$\chi^2_{0.75} = 4.40$ and reduced-$\chi^2_{2.5} = 2.12$), and residual plots showed it was quite deficient in describing the $M\mathrm{v}T$ shapes. It was therefore rejected. However, it *did* provide an improvement over the simpler $T^{3/2}$ model. The value of β was 19 ± 2 meV, far larger than the value of 1.0 ± 0.2 meV previously found by Hordequin *et al.* with inelastic neutron scattering; this is discussed further in the concluding section of this chapter. Hordequin *et al.* themselves found that this modified law provided no advantage over the usual $T^{3/2}$ law in their low temperature magnetometry along the three principal crystallographic axes.

T^n exponents in this work

Previous work on NiMnSb, most notably the fairly extensive work of Hordequin *et al.*, suggests that the $T^{2.26}$ and $T^{2.06}$ magnetisation dependence observed in our work is most likely a result of itinerant Stoner-like magnetism. Once again, this theory is incompatible with the idea that NiMnSb is an ideal half-metal, because it requires a non-zero minority DoS close to the Fermi energy. In Hordequin *et al.*'s work, Stoner-like magnetism observed only above a transition temperature of 70 K, so the magnetisation data was still consistent with a half-metallic ground state, even if the mechanism that allowed Stoner excitations at such a low temperature was not understood. In this work, the approximately T^2 magnetisation dependence existed from 5 K up to 350 K, suggesting the presence of a non-zero density of states in the spin-minority channel for the full temperature range. The implications of this result are discussed in more detail in the conclusion to this chapter.

Finally, the issue of the n value disagreement between 0.75 and 2.5 T data is addressed. As already mentioned, Bloch's law assumes a classical spin-wave dispersion of the form $E(\boldsymbol{q}) = D\boldsymbol{q}^2$. A spin-wave gap would modify this to $E(\boldsymbol{q}) = \beta + D\boldsymbol{q}^2$. Smolyaninova *et al.* pointed out that the size of the spin-wave energy gap is determined by the applied field[113]:

$$\beta = \beta_0 + g\mu_\mathrm{B}(H - NM), \tag{6.4}$$

where β_0 is an intrinsic gap, $g = 2$ is the Landé factor, μ_B is the Bohr magneton, H is the applied field, N is the demagnetisation factor and M is the magnetisation. Thus, the size of the 'effective' gap linearly increases with the applied field. Smolyaninova *et al.* showed that when a T^n approximation is used for Bloch's law, the n value increases with H. In this work, because the same NiMnSb sample was used for all measurements, N stayed the same. Therefore, the n value difference between 0.75 and 2.5 T can be solely attributed to the increase in β, due to the increase in H. Smolyaninova *et al.* made the same argument, showing that the T^n exponent for $La_{0.7}Sr_{0.3}MnO_3$ varied from 1.4 ± 0.1 to 1.7 ± 0.1 on increasing H from 1 to 3 T. Their result was supported by the work of Ai-Yuan *et al.* who studied the $La_{1-x}Sr_xMnO_3$ system theoretically, modelling its magnetisation and spin-wave dispersion as a function of temperature and magnetic field[114]. The value of n obtained in the lowest field is more representative of the ground state of the system because the spin-wave gap, β, is closer to β_0, which may actually be zero. In the case of NiMnSb, we can say that the lowest value of n, which was obtained with a field sufficient to be assured of magnetic saturation, while modifying β the least, suggests that a T^2 law is far more appropriate than Bloch's $T^{3/2}$ law.

6.4 SPR-KKR calculations

To complement the experimental work, DFT calculations were performed on NiMnSb. These used the Munich spin-polarised relativistic - Korringa-Kohn-Rostocker package (SPR-KKR)[73,74]. A basic description of SPR-KKR's operation can be found in section 5.4.

Calculation details

The calculations called for a $52 \times 52 \times 52$ k-space grid to sample the full NiMnSb Brillouin zone (BZ). The SPR-KKR program limited the calculation to an irreducible wedge of the BZ, where $\sim$18000 k-points were used. A series of trial calculations were performed with larger numbers of k-points, but provided the same results for total energy, spin and orbital moments. Therefore, this k-mesh was deemed satisfactory. These calculations used the PBE exchange-correlation approximation[71], and employed Lloyd's formula, which provides an improved determination of the DoS and Fermi level[115,116]. Lloyd's formula, which is accessible via a switch in the SPR-KKR program, was derived under the assumption that the DoS of ordered or random alloys is solely a function of the positions of the electron scattering potentials (the atoms) and their associated phase shifts. Lloyd showed that, for a regular lattice, the DoS is a generalisation of the Green function, which is calculated as part of the KKR band structure determination[115].

Lattice optimisation

First, a lattice optimisation was conducted. Multiple calculations with varying lattice parameters were performed, and the resulting total energies, spin moments and Fermi level spin polarisations were examined - see figure 6.10. The spin polarisation values were obtained directly from the DoS for each calculation, using equation 6.1. The minimum total energy occurs at the optimum lattice parameter, or cell volume. The total energies, $E(V)$, were fitted

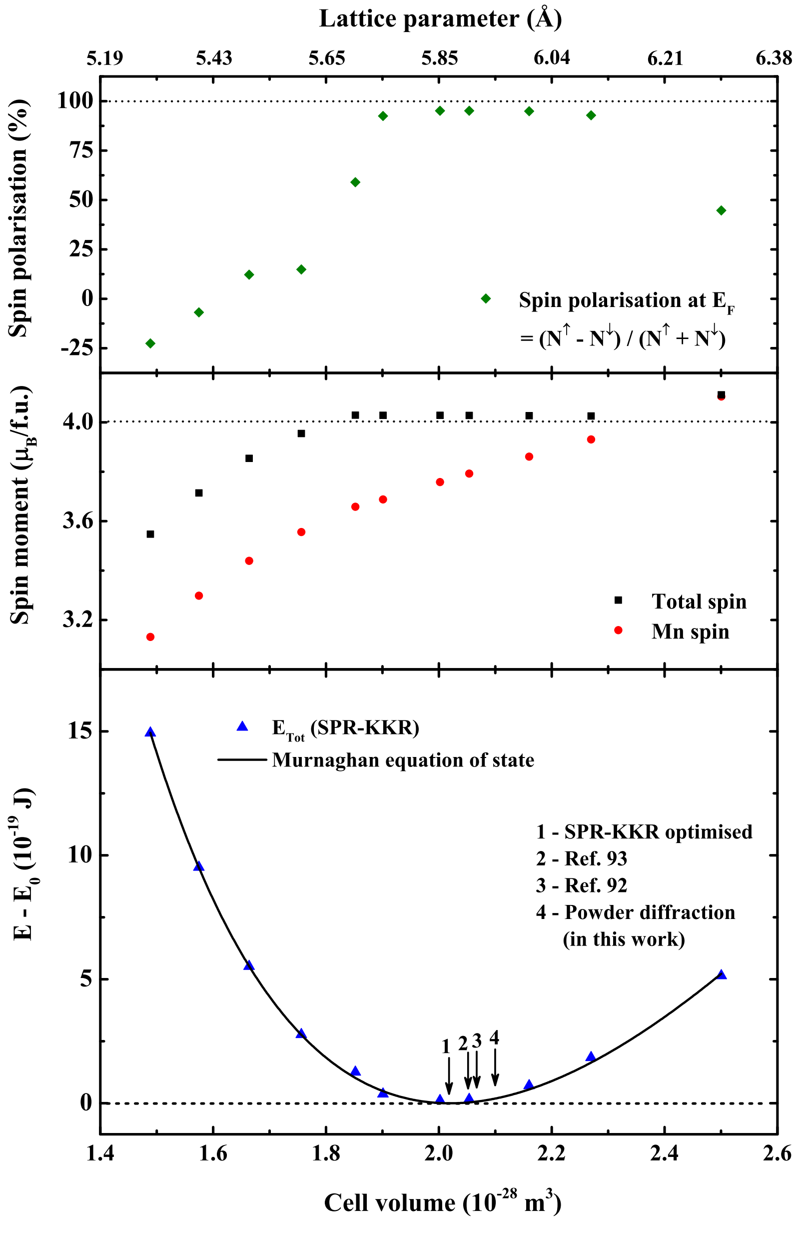

Figure 6.10: Cell optimisation of NiMnSb. Total energies, total spin moments, Mn spin moments and spin polarisation values are from SPR-KKR calculations. The black line is a fitted Murnaghan equation of state, as in equation 6.5.

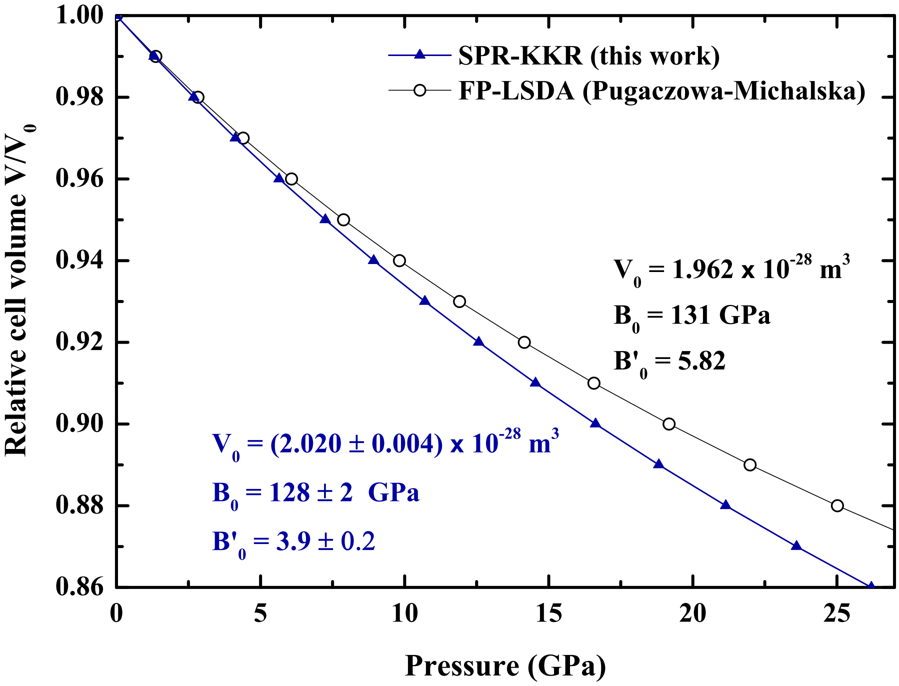

Figure 6.11: The volume-pressure response of NiMnSb, from equation 6.6, using values determined by by the Murnaghan equation of state. Results from this work (blue line, triangles) are compared with work by Pugaczowa-Michalska (black line, circles).

with the second-order Murnaghan equation of state[117],

$$E(V) = E_0 + \frac{B_0 V}{B_0'} \left(\frac{\left(\frac{V_0}{V}\right)^{B_0'}}{B_0' - 1} + 1 \right) - \frac{B_0 V_0}{B_0' - 1}, \tag{6.5}$$

where E_0 is the energy associated with the optimum cell volume V_0, and B_0 and B_0' are the bulk modulus and its pressure derivative, respectively.

The SPR-KKR optimised lattice parameter was found to be 5.867 ± 0.004 Å, which is 1.3% smaller than the experimental value determined in this work, and between 0.6 and 0.9% smaller than previously reported values[96–98]. However, discrepancies of this order between DFT and experimental results for the lattice parameter are well documented[118,119]. The total spin moment is stabilised at $\sim 4\ \mu_\mathrm{B}$ over a small range of cell volumes around the optimum value. This is a good indication that the calculations have converged at the electronic structure expected from the 18 electron rule discussed in section 6.1. The behaviour of the total spin and Mn spin with lattice parameter is in reasonable agreement with a previous theoretical result from Pugaczowa-Michalska[120].

Regarding the values of spin polarisation provided in the top cell of figure 6.10, there are three points to discuss. First, the maximum values are around 96%, which is clearly smaller than the predicted 100%. This discrepancy is likely an artefact associated with calculating the DoS values. It seems that a small but non-zero minority DoS always exists at the Fermi level, even when it is situated well inside the band gap. This effect persisted when the calculations were performed with higher k-point sampling and higher energy resolution in the DoS plotting. Second, the effect of altering the lattice parameter was similar to shifting the position of E_F with respect to the minority channel band gap. Thus, the spin polarisation was not reduced from its maximum value until E_F encountered minority states, which happened at around $a \pm 2.5\%$, where a is the optimised lattice parameter. Lastly, the spin polarisation and total spin moment at the experimental lattice parameter were the same as those at the SPR-KKR optimised parameter, suggesting that the electronic structures are effectively the same.

Returning to structural information, fitting the theoretical total energies with the Murnaghan equation of state yielded values for B_0 and B_0'. Inputting these values into another form of the equation of state,

$$V(P) = V_0 \left(1 + B_0' \frac{P}{B_0}\right)^{-1/B_0'}, \tag{6.6}$$

provided the response of the cell volume to hydrostatic pressure, P. Figure 6.11 shows this pressure-volume relationship for NiMnSb, and gives the values for V_0, B_0 and B_0'. Also presented is the same curve produced with theoretical values from the work of Pugaczowa-Michalska, where the LSDA was applied[120]. Even at 25 GPa, the disagreement is in the region of 1.5%, suggesting that the LSDA and GGA exchange-correlation approximations are in good agreement. No experimental measurement of the bulk modulus for NiMnSb exists for comparison. Theoretical reports of bulk moduli for full Heusler alloys Ni_2MnIn, Ni_2MnSn and similar materials, are in the range 138 to 170 GPa[121,122]. Owing to the extra vacant site, the half-Heusler NiMnSb ought to be more compressible than this, so the value of 128 ± 2 GPa from SPR-KKR seems reasonable. Recent GGA work by Özişik *et al.* put the bulk moduli of half-Heuslers NiZrSn and NiHfSn at 119.4 and 125.3 GPa, respectively[123].

	Spin (μ_B/f.u.)				Orbital (μ_B/f.u.)			
	s	p	d	Sum	s	p	d	Sum
Total	0.066	-0.070	4.033	4.029	0.000	-0.001	0.046	0.045
Ni	-0.013	-0.039	0.345	0.292	0.000	0.001	0.017	0.018
Mn	0.052	0.044	3.673	3.770	0.000	0.000	0.029	0.029
Sb	0.015	-0.096	0.010	-0.071	0.000	-0.001	-0.001	-0.002
Vacancy	0.012	0.029	0.006	0.037	0.000	0.000	0.000	0.000

Table 6.1: NiMnSb spin and orbital moments from a SPR-KKR calculation at the optimised lattice parameter of 5.867 Å. Contributions are provided for individual sites and electronic bands (i.e. s-, p- and d-type).

Electronic and magnetic structure

The site-specific DoS for NiMnSb with the optimised lattice parameter is shown in figure 6.12. It is in good agreement with previous results. There are many sources for comparison, but one of the most comprehensive, and most frequently referenced, is the work of Galanakis *et al.*[101]. The most interesting feature of the total DoS is the band gap in the minority channel, which, in agreement with the work of Galanakis *et al.*, is around 0.55 eV wide. This, along with the total spin moment of $\sim 4\ \mu_B$/f.u., means that this calculation conforms to expectations; it is a half-metallic-ferromagnet. It should be noted that, according to DFT work by Kulatov and Mazin, the exact position of the Fermi level with respect to the minority band gap can not be reliably determined from LDA calculations[124]. Therefore, the position of E_F roughly in the centre of the band gap should not be taken as the definitive situation.

The general features of the Ni, Mn and Sb DoS are as described in section 6.1. The $5s$ states of Sb are seen around -12 to -10 eV. The Sb $5p$ band, which plays the crucial role of accommodating 3 extra electrons donated by the transition metals, spans from -6 eV up to the Fermi level, but only small contributions exist above $\sim$ -2 eV. The Ni $3d$ majority states are fully occupied, and the minority states are nearly fully occupied, except for a small contribution above the Fermi level. This is due to d-d hybridisation with Mn states, and leads to a Ni spin moment of $\sim 0.3\ \mu_B$. Finally, we see the bonding and antibonding states of Mn, below and above the Fermi level, respectively. Some Mn minority states exist below the Fermi level, again due to d-d hybridisation with Ni, which means that the Mn spin moment

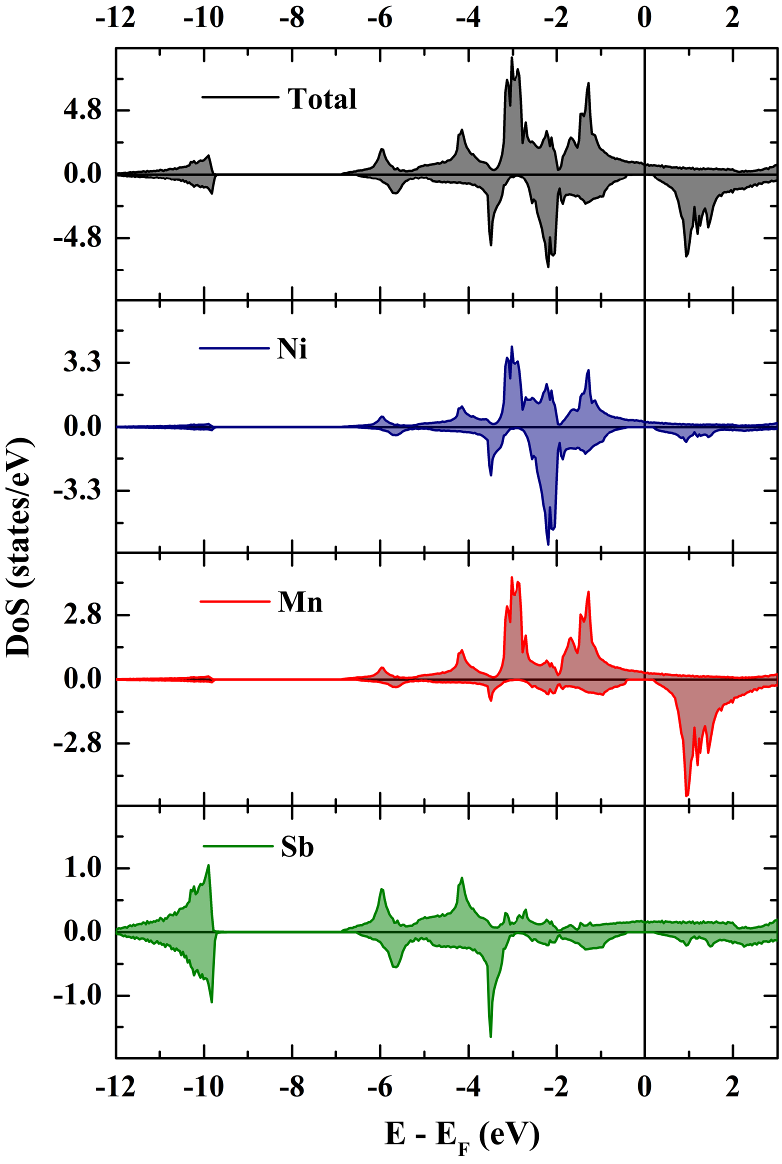

Figure 6.12: NiMnSb site-specific density-of-states obtained from SPR-KKR. The calculation details are given in section 6.4.

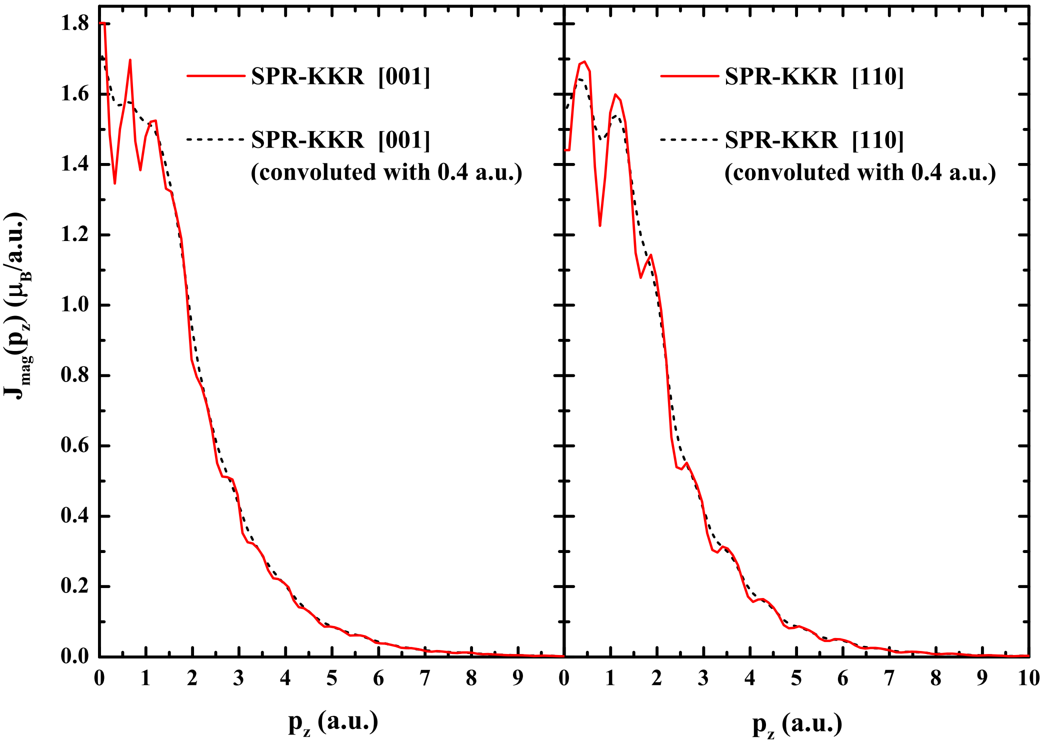

Figure 6.13: Theoretical [001] (left) and [110] (right) MCPs for NiMnSb obtained using SPR-KKR. The 'raw' profiles, obtained directly from the DFT package, are shown as solid red lines, whilst dashed black lines represent the profiles convoluted with a resolution of 0.4 a.u.

is slightly reduced from the 4 μ_B predicted by the entirely ionic model. The spin and orbital moments for each element in the calculation are given in table 6.1.

Theoretical magnetic Compton profiles

Theoretical MCPs from SPR-KKR are shown in figures 6.13 and 6.14. The former shows the 'raw' [001] and [110] MCPs that were obtained directly from the calculations, as well the same profiles convoluted with a momentum resolution of 0.4 a.u. to simulate the level of precision available through experiment. An important feature to note is the presence of periodic fluctuations in the MCP tails. These umklapp features are caused by the Fermi surface topology and stem from the fact that, as described by Bloch theory, electrons with momentum $\boldsymbol{k}$ inside the first Brillouin zone also contribute at $\boldsymbol{p} = \boldsymbol{k} \pm n\boldsymbol{G}$, where $\boldsymbol{G}$ is the reciprocal lattice vector and n is an integer[125]. The importance of a good theoretical description of experimentally observed umklapp features is underlined in the magnetic Compton scattering study of Ni by Dixon *et al.*, who also provide a more advanced discussion of their origins[125].

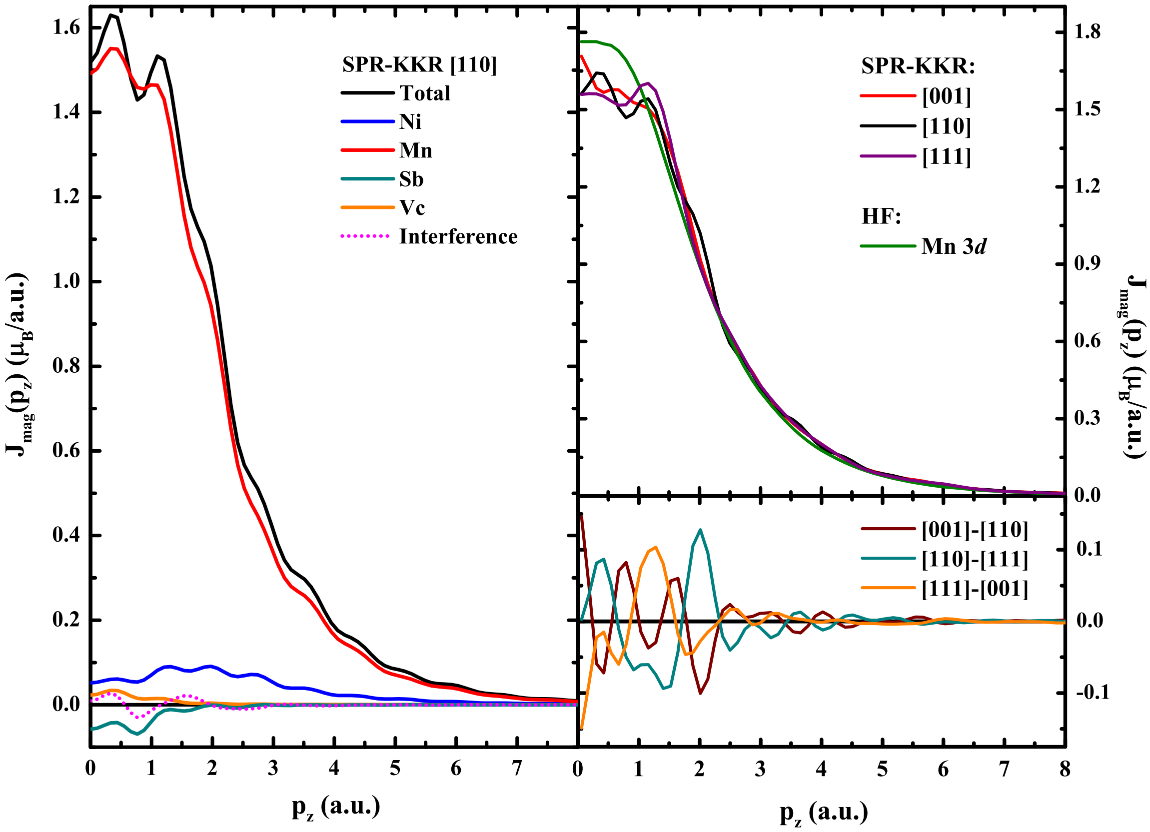

Figure 6.14: Theoretical MCPs for NiMnSb obtained using SPR-KKR. All MCPs here have been convoluted with the experimental momentum resolution of 0.4 a.u. (Left) The total [110] MCP, along with site-specific contributions weighted by their respective spin moments. (Right, top) Projections along the [001], [110] and [111] crystallographic directions. The Compton profile due to a Mn 3d relativistic Hartree-Fock calculation is shown as a green line. (Right, bottom) Directional difference MCPs.

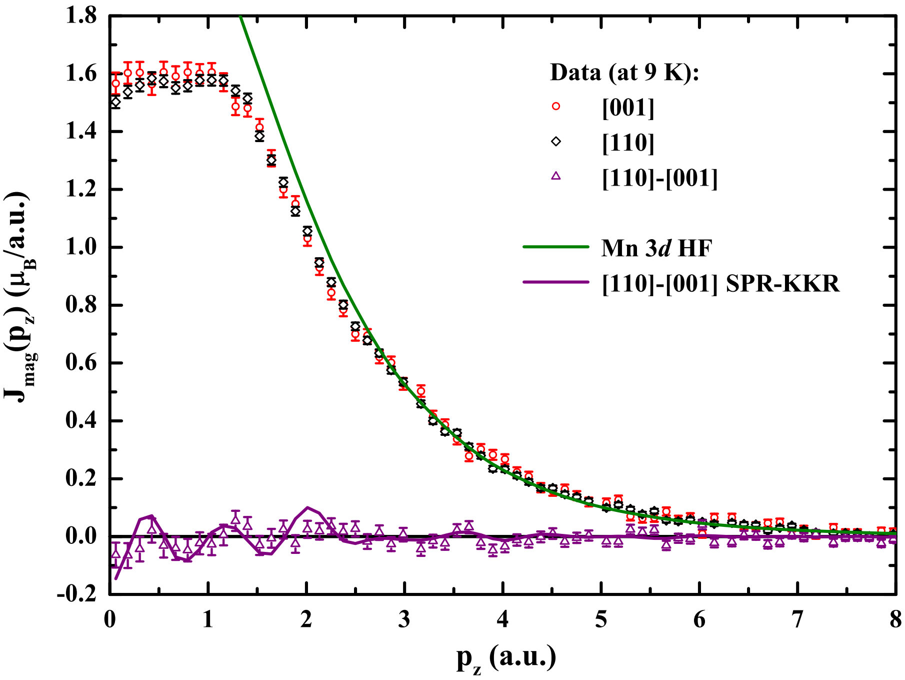

Figure 6.15: Experimental magnetic Compton profiles for NiMnSb obtained at 9 K and 2.5 T. Measurements along the [001] and [110] crystallographic directions are shown as red circles and black diamonds, respectively. Also shown is the resulting experimental difference profile (purple triangles), the difference profile according to SPR-KKR calculations (purple line) and the Mn 3d HF profile (green line).

In figure 6.14, the site-specific [110] MCPs are weighted according to the spins associated with each species, as provided in table 6.1, therefore the Mn contribution is the largest and is close to the total. The umklapp features are apparent in the total [110] MCP even after the 0.4 a.u. momentum resolution was applied. In the right top cell, a free-atom Hartree-Fock (HF) Mn 3d profile is shown for comparison. There is good agreement between the SPR-KKR results and the HF profile from high momentum above 1.5 a.u., below which contributions from more itinerant s and p bands determine the total SPR-KKR profile shape.

6.5 Magnetic Compton profiles and analysis

NiMnSb magnetic Compton profiles were collected in a magnetic field of 2.5 T at 9 K and 300 K on the BL08W beamline at SPring-8. It was intended that MCPs along three high symmetry directions, the [001], [111] and [110], would be collected for both temperatures, and these directions were aligned using the back-reflection Laue method prior to the experiment. Complications with the rotating sample stage on the BL08W magnet meant that, at 9 K, we

	Spin (μ_B/f.u.)	
	9 K	300 K
[001]	4.15 ± 0.04	3.89 ± 0.03
[111]	-	3.87 ± 0.03
[110]	4.16 ± 0.04	3.88 ± 0.03

Table 6.2: NiMnSb spin moments obtained from magnetic Compton profiles at ±2.5 T.

could only have confidence in the [001] and [110] data.

Figures 6.15 and 6.16 show the experimental MCPs at 9 K in addition to profiles from HF theory and SPR-KKR calculations. The 300 K MCPs are not shown, but share the shapes of those from 9 K when normalised to the same spin moment. There is no indication from temperature-difference MCPs in equivalent crystallographic directions that the spin density is significantly different between 9 K and 300 K. The experimental spin moments are given in table 6.2; at 9 K, closest to the theoretical ground state, they are around 4% larger than the predicted value of 4 μ_B/f.u. The mean spin moment at 300 K is (93.4 ± 0.3)% of that at 9 K, in good agreement with the relationship between the total moments at the same temperatures, as obtained from SQuID magnetometry.

Magnetic Compton profile analysis

There is clearly some disagreement between the experimental NiMnSb profiles and those from free-atom Mn $3d$ HF and SPR-KKR calculations. Agreement between the free-atom Mn $3d$ HF profile and the experimental MCP tails is expected since Mn is predicted to provide around 94% of the total spin (according to the SPR-KKR calculations above), a value which has been confirmed by polarised neutron diffraction work[112]. The Mn $3d$ HF profile describes the 9 K MCPs well above a momentum of around 2.7 a.u. only.

The SPR-KKR profiles, when normalised to the theoretical spin moment of 4.029 μ_B/f.u., consistently underestimate the experimental MCPs for momenta over around 1.5 a.u. Normalising the SPR-KKR profiles to the experimental moments does little to improve the discrepancy. This is partly because, in addition to the difference in the theoretical and experimental MCP

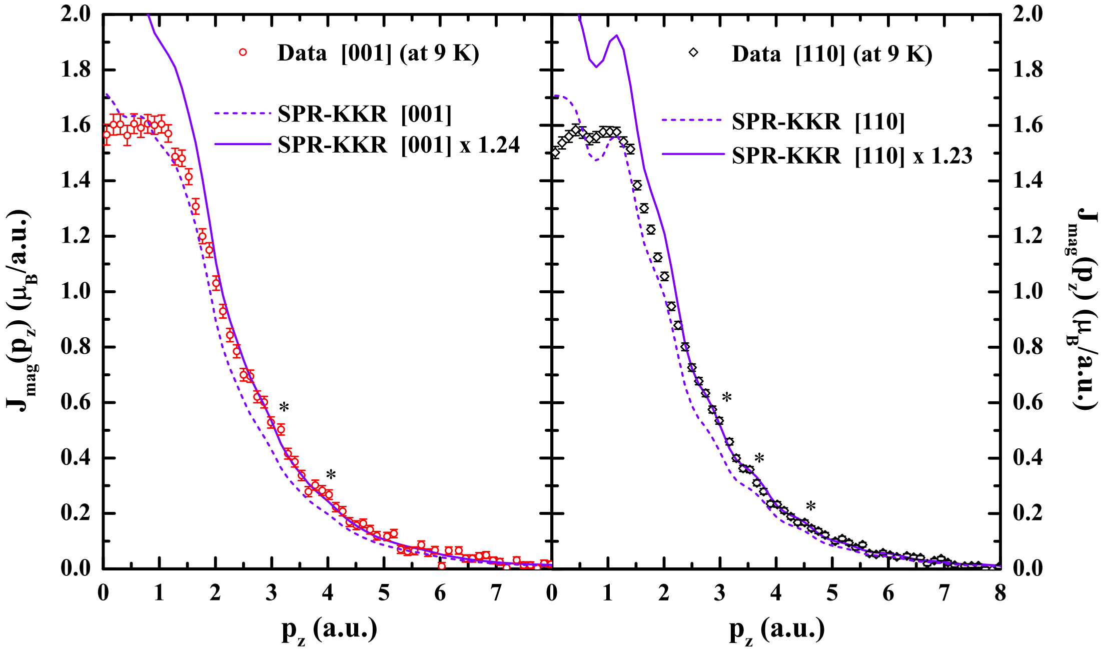

Figure 6.16: Experimental and theoretical (SPR-KKR) [001] and [110] magnetic Compton profiles for NiMnSb. Data collected at 9 K and 2.5 T. The * symbols indicate umklapp features present in both the experimental and theoretical MCPs - refer to the text.

tail shapes, the low momentum features, which are generally attributable to more itinerant spin-polarised electrons, are quite dissimilar; the experimental MCPs 'flatten out' below ~1.2 a.u., whereas the theoretical profiles tend to increase all the way to zero momentum, with the exception of a small dip in the [110] profile at 0.7 a.u. On the other hand, the experimental spin density anisotropy, as reflected by the [110]-[001] difference MCP in figure 6.15, is reproduced relatively well by the SPR-KKR calculations, though this agreement may simply be random in origin.

Applying scaling factors of 1.24 and 1.23 to the [001] and [110] SPR-KKR profiles, obtained by normalising their areas to the experimental spin moments in the region 3 to 10 a.u., resulted in good descriptions of the experimental MCPs above 2.5 and 2.3 a.u. for the [001] and [110] directions, respectively. Significantly, and especially observable for the [110] direction, these scaled theoretical profiles were able to describe the experimental umklapp features in the region of 2.8 to 4.5 a.u. quite well. The umklapp features are indicated in figure 6.16 with * symbols and, as mentioned previously, are reflective of the material's Fermi surface topology. Despite this, the scaled profiles were far less able to describe the experimental MCPs at lower momentum, even down to 1.5 a.u. where the transition metal $3d$ contributions should still be dominant in determining the MCP shapes. This raises the possibility that the respective spin moments of the transition metals in this system are different from those predicted by theory and reflected in the SPR-KKR profiles. The predicted Mn:Ni spin moment ratio, for ideal half-metallic NiMnSb, is 12.9:1. Variations in this ratio are now explored.

Possible larger Ni spin contribution

A series of modified theoretical profiles were obtained by adding the site-specific SPR-KKR profile for Ni to the total [001] NiMnSb profile. The extra Ni spin contribution was added in quantities from 2 to 4.5 times the amount predicted by the *ab initio* SPR-KKR calculation. This resulted in final Mn:Ni spin moment ratios between 4.3:1 and 2.3:1 for the modified profiles. The profiles were fitted to the experimental data using only the momentum region from 3 to 10 a.u. The results are shown in figure 6.17. It should be noted that these modified profiles no longer represent self-consistent electronic band structures. They serve as experiment-informed approximations to the total spin density where the Mn and Ni spin moments are different from those predicted by *ab initio* calculations. More progress with this approach could possibly be made with fixed-spin or rigid band shifting calculations in the linear muffin-tin orbitals (LMTO) regime of DFT. The rigid band shifting method was previously employed in the study of $Co_{1-x}Fe_xS_2$, in which the material's Fermi level spin polarisation was deduced[126].

The theoretical profile in which the Mn:Ni spin moment ratio was manually altered to 3.2:1 provided a far better description of the experimental [001] MCP than the unmodified profile (the reduced-χ^2 was diminished from 9.2 to 6.1). The MCP shape between 1.5 and 2.5 a.u. was replicated well, in way in which the unmodified total SPR-KKR profile was incapable even with an applied scaling factor. Additionally, the region below 1 a.u. of this modified profile was flatter, reproducing the general shape of the experimental MCP in the low momentum range. The theoretical profile had 4 times the originally predicted Ni spin moment. Its area was 4.03 μ_B/f.u., which would indicate spin moments of 3.07 and 0.96 μ_B/f.u. attributable to Mn and Ni, respectively (temporarily ignoring the small negative moment predicted for Sb). These clearly deviate from the 3.77 and 0.292 μ_B/f.u. predicted for the Mn and Ni in half-metallic NiMnSb. They are also different from the values obtained experimentally

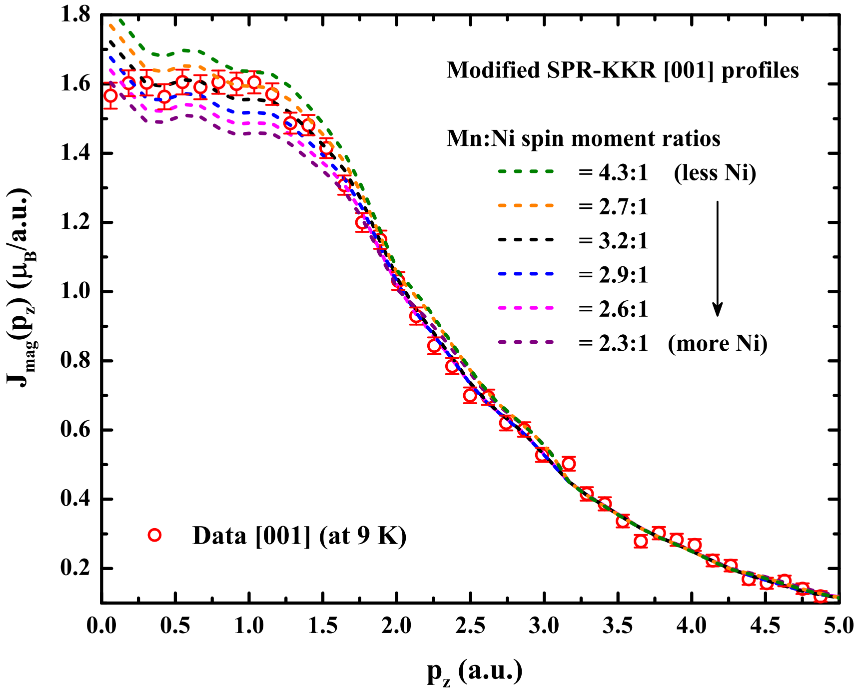

Figure 6.17: The possibility of a larger Ni spin contribution in NiMnSb is explored by varying the relative spin contributions from Mn and Ni. The experimental [001] MCP is shown as red circles, while the dashed lines represent profiles with varying Mn:Ni spin moment ratios.

by Brown *et al.* using polarised neutron diffraction[112]. The magnetisation values obtained by Brown *et al.* for the Mn and Ni sites were 3.90(2) μ_B and 0.147(11) μ_B, respectively, in reasonable agreement with predictions from DFT. The implications of such a deviation of the transition metal spin moments from the predicted values for NiMnSb are discussed in the concluding section of this chapter.

Fermi level shift

Further to the Mn/Ni spin moment variation approach, several calculations were performed to determine whether a shift in the position of the Fermi energy, or rather a shift in all electronic bands relative to the Fermi energy, could account for the experimental-theoretical disparity in the NiMnSb MCPs. The position of the Fermi energy was manually shifted by -0.6, -0.3, +0.3 and +0.6 eV from the value given in the self-consistent converged potential. Note that the theoretical size of the minority channel band gap is 0.55 eV. The result was to introduce or remove occupied majority- and minority-spin states from the region around the Fermi energy. Whilst shifting electronic bands by these energies might be considered unphysical,

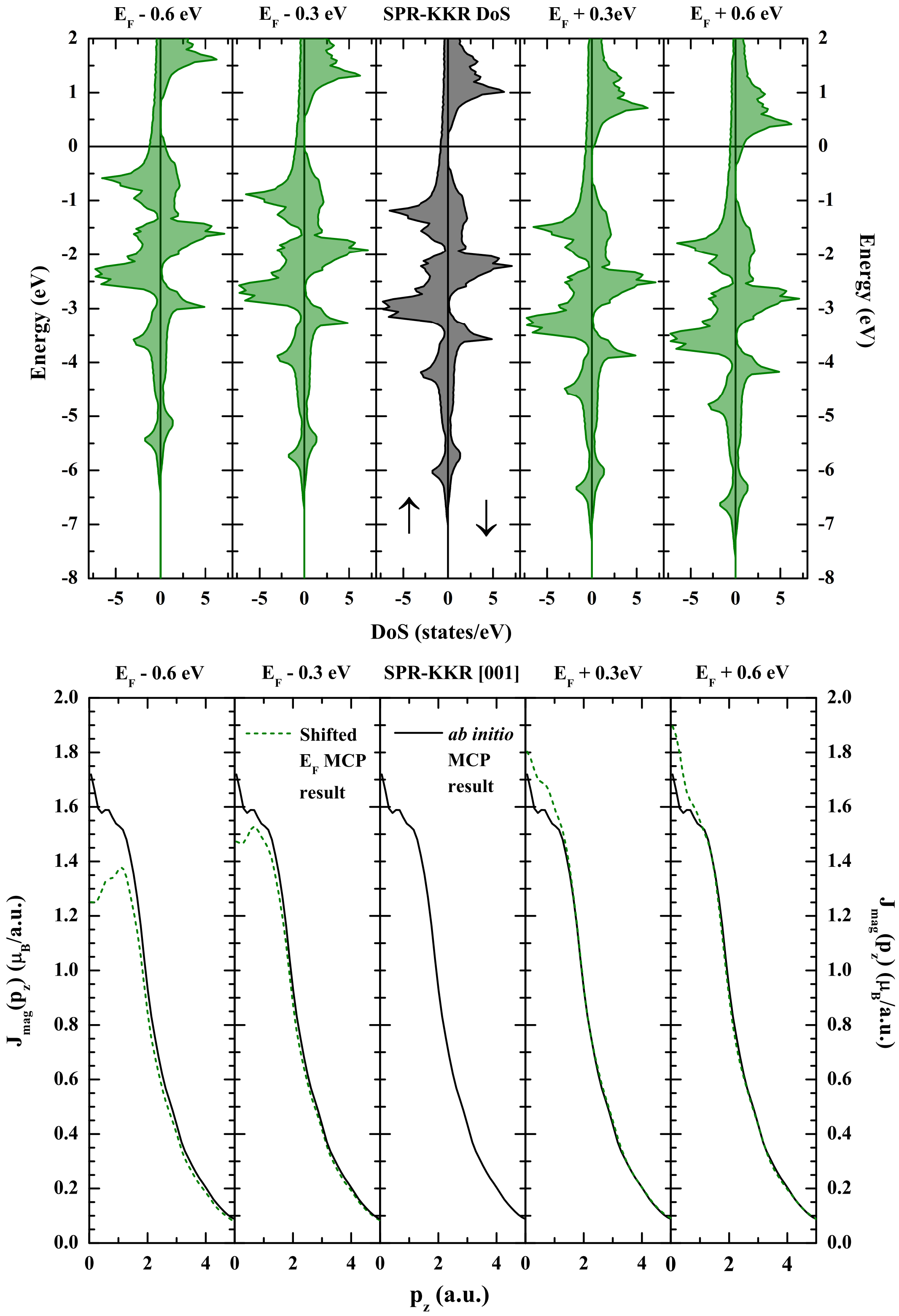

Figure 6.18: (Top) DoS diagrams corresponding to NiMnSb calculations with manually shifted Fermi levels. (Bottom) [001] MCPs for the same calculations highlight the changes in the total moment, as well as shape differences due to the varying contributions of different electronic bands. In each MCP, the dashed green line represents the shifted band structure and the black line represents the unmodified case.

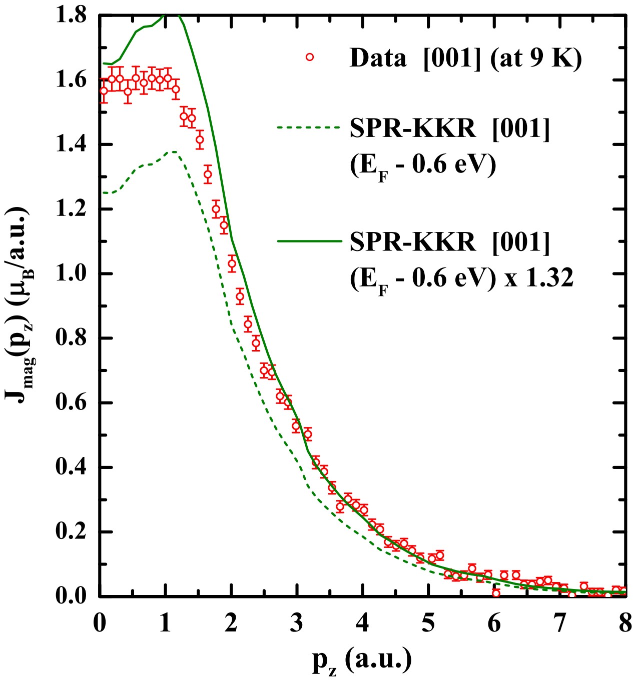

Figure 6.19: Experimental [001] NiMnSb MCP at 9 K (red circles) and the SPR-KKR profile in which the Fermi energy was manually shifted by -0.6 eV. The dashed green line represents the profile normalised to 3.515 μ_{B} and the solid green line has a scaling factor of 1.32.

this method serves as a useful approximative tool because the states around the Fermi energy are of the types most likely to be populated if significant atomic disorder exists in the system, or if the minority band gap is smaller than predicted. DoS diagrams and the corresponding MCPs for these calculations are shown in figure 6.18.

When the Fermi level was reduced by 0.3 then 0.6 eV, the Ni and Mn spin moments became smaller, first by reducing the number of occupied majority states, then, once E_{F} passed out of the minority band gap, by reducing the total majority *and* minority occupation. At E_{F} - 0.6 eV the total spin moment was 3.515 μ_{B} (*cf.* 4.029 μ_{B} in the normal calculation); the Ni moment was reduced by over 50% and the Mn spin was reduced by ~6%. This is reflected in the MCP, which is fractionally narrower than the normal result above ~ 2 a.u., indicating a smaller 3d contribution. When the Fermi level was increased by 0.6 eV, the total spin moment increased, though only by 0.1 μ_{B}. The Ni and Mn moments stayed roughly the same; the additional moment was due to Sb majority s and p states. The inclusion of these more itinerant states is again reflected in the shape of the resulting MCP - an additional very narrow peak (HWHM ~ 0.5 a.u.) is present at low momentum. Although extra Ni and Mn states are occupied if the Fermi level is increased, it seems that the numbers of extra majority and minority states cancel fairly well, resulting in no additional $3d$ moment.

Figure 6.19 shows the SPR-KKR profile with the Fermi energy shifted by -0.6 eV and the experimental NiMnSb [001] MCP at 9 K. Comparison was made with the E_F - 0.6 eV result because its profile was narrower than the *ab initio* result, a feature which ought to improve the agreement with experiment. However, the modified theoretical profile was unable to describe the experimental MCP when it was normalised to its spin moment of 3.515 μ_B or when a scaling factor of 1.32, obtained from fitting between 3 and 10 a.u., was applied. What these results show most clearly is that a simple electronic band shift, which introduces or removes states from the region around the Fermi energy, is not sufficient to reproduce the spin momentum density seen experimentally.

Atomic disorder

A final series of calculations was performed in which the coherent potential approximation (CPA)[76] was used to approximate atomic disorder in NiMnSb. Two types of disorder were investigated. In the first, substitutional disorder, certain fractions of each atom (2, 5 and 10%) were removed from their own crystallographic sites and interchanged with other atoms. In the second, non-stoichiometric disorder, the fractional content of Ni, Mn and Sb were reduced, effectively leaving additional vacant sites in the crystal. A host of these calculations were performed, but only minor variations in the theroretical profile widths were observed. The largest changes were in the region 0 to 2 a.u., generally relating to increases or decreases in the spin moment of itinerant s and p bands.

6.6 Surface preparation of MnSb, NiSb and NiMnSb

XPS was performed on polycrystalline samples of MnSb and NiSb, as well as a single crystal of NiMnSb. The purpose of the experiments was to determine whether the surfaces of bulk samples, which understandably become oxidised by exposure to atmosphere, could be restored to clean, stoichiometric ideals by means of relatively simple preparation techniques. To date, there exists no rigorous and dependable methodology documented in the literature for achieving this result. The surface preparation methods investigated here were hydrochloric acid (HCl) etching, Ar^+ sputtering and vacuum annealing.

Motivation

The primary motivation for this work was the desire to perform experiments such as X-ray magnetic circular dichroism (XMCD) and spin-polarised angle-resolved photoelectron spectroscopy (SPARPES) on clean, stoichiometric surfaces, having prepared the samples *in situ* or, in the case of HCl etching, as soon as possible before introduction into vacuum. XMCD is an element-specific probe of magnetisation, while SPARPES, another X-ray technique, allows the spin-polarised band structure of a material to be reconstructed. By measuring clean, stoichiometric surfaces, experimental results may be compared to theoretical predictions regarding the electronic structure of a particular system. Significantly, the development of a simple and reliable surface preparation method would raise the inviting possibility of performing several electronic structure-sensitive measurements (e.g. magnetic Compton scattering, XMCD *and* SPARPES) on the same sample during the same synchrotron-based experiment.

Although the ultimate interest in Heusler alloys and related binary compounds lies in the realm of thin films, the development of bulk-sample surface preparation methods is important for several reasons. Firstly, in many instances, stoichiometric bulk crystals are easier to produce, and are therefore more easily obtained, than their thin film counterparts. This is especially true of ternary alloys like NiMnSb, where growth by molecular beam epitaxy (MBE), pulsed laser deposition (PLD), or other thin film growth methods is relatively time-intensive and requires a great deal of prior investigative work. If bulk-sample surfaces can be prepared adequately and easily, they may be subject to a wide range of informative techniques with considerably less effort than that associated with thin film samples. Secondly, because thin films tend to be *very* thin films, ranging from a few atomic monolayers up to a few tens of nanometers, the materials under investigation are likely to be irreversibly damaged by any series of preparation methods. Whereas, following repeated wet chemical etching and/or ion bombardment processes a bulk crystal can simply be repolished and used again, an equivalent thin film sample would likely be destroyed and a new one would be required.

MnSb and NiSb samples

MnSb and NiSb polycrystal samples were produced in the same manner as the NiMnSb starting ingot discussed previously; repeated tri-arc melting followed by vacuum annealing. The ingots were annealed at 800 °C for 150 hours. EDX analysis put the TM:Sb ratios at 1:1 for both the MnSb and NiSb, while powder X-ray diffraction confirmed their expected crystal structures (space group $P6_3/mmc$).

Samples approximately 5 mm × 5 mm × 2 mm were cut from the polycrystal ingots using a rotating diamond blade and subsequently polished with increasingly fine grades of lapping paper. In the final polishing phase, a diamond suspension with fragments $\sim$0.25 μm was employed. The polished surfaces possessed the metallic lustre expected of these materials. Atomic force microscopy (AFM) of regions 25 μm × 25 μm revealed an overall root-mean-squared surface roughness of 26 nm, with a few large trench-like features, left by the final polishing stages, up to 150 nm wide.

Experimental procedure - HCl etching and vacuum annealing

The polished MnSb and NiSb samples were subject to XPS in three states; as-loaded, after a HCl etch, and after an *in situ* vacuum anneal. The HCl etch process comprised a 10 second submersion in a solution of 36% hydrochloric acid, followed by rinsing with de-ionised water and drying with pressurised nitrogen. The vacuum anneal was 1 hour at 300 °C. The XPS regions of interest were the Ni $2p$ (binding energies between 850 and 875 eV), Mn $2p$ (635 to 660 eV), Sb $3d$ and oxygen $1s$ (525 to 545 eV), and Sb $4d$ (28 to 40 eV). Results for MnSb and NiSb are shown in figures 6.20 and 6.21, respectively.

XPS analysis - HCl etching and vacuum annealing

One of the first features of note is the reduction to background of the oxygen $1s$ peak (binding energy 530.4 eV) for both MnSb and NiSb after the complete surface treatment. This is a good indicator that the preparation methods successfully removed a lot of oxide contamination. Often the area of the $1s$ peak can be used as a good measure of the oxygen concentration of the surface. In this case however, the peak appears in the same region as that of Sb $2p_{3/2}$ and its associated oxide. Proper fitting to the XPS peaks in this region was impossible, so

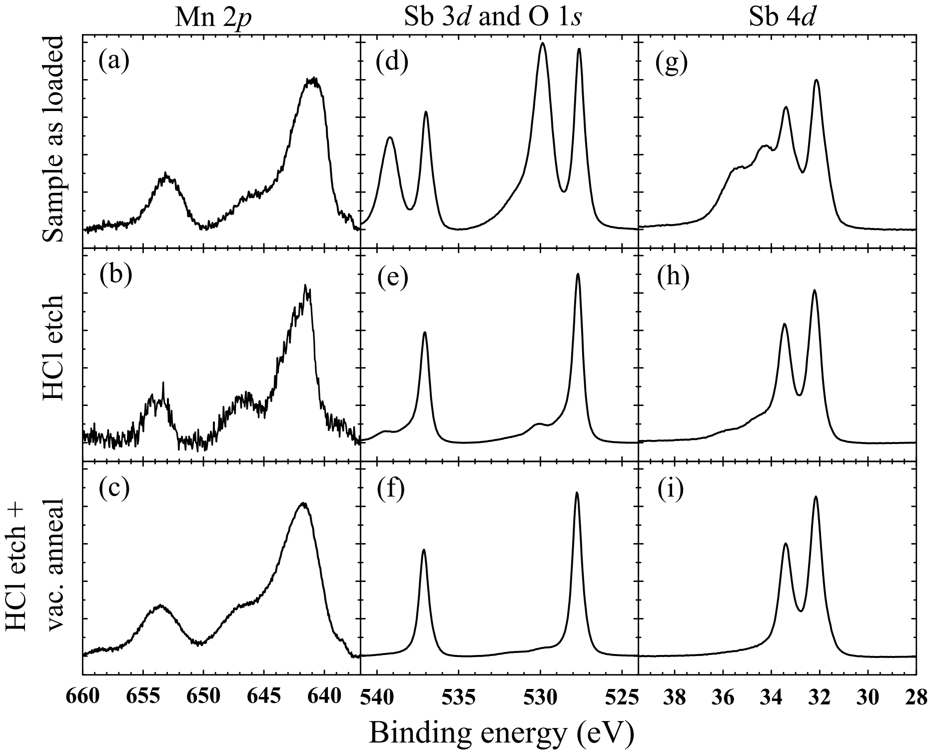

Figure 6.20: The Mn 2p, Sb 3d and Sb 4d core level regions of a MnSb polycrystal XPS, showing the effects of a HCl etch and annealing under vacuum.

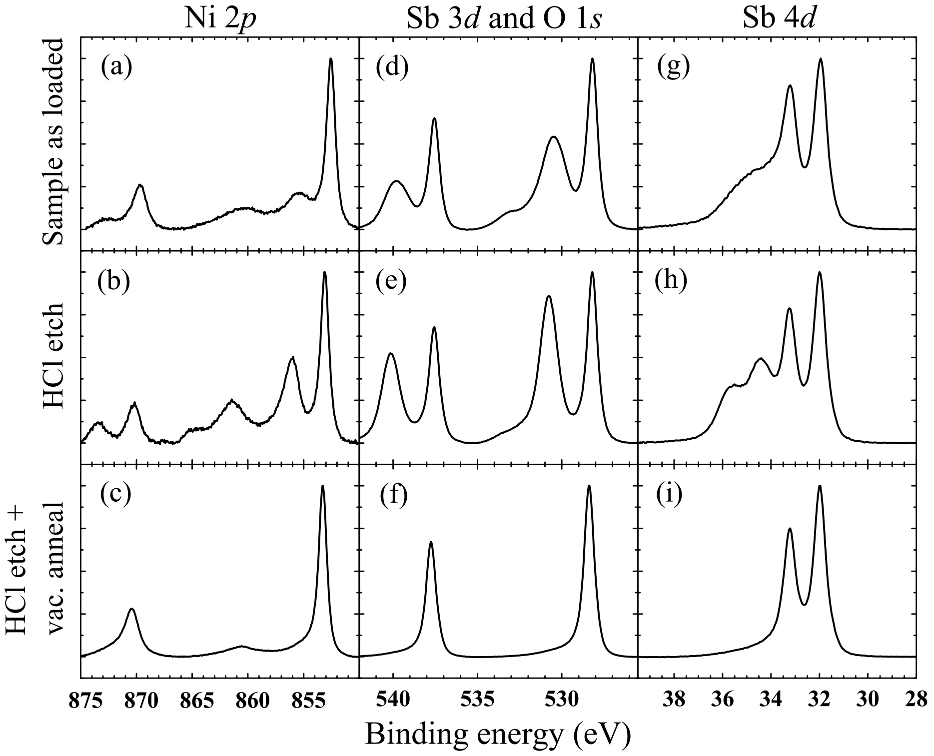

Figure 6.21: The Ni 2p, Sb 3d and Sb 4d core level regions of a NiSb polycrystal XPS, showing the effects of a HCl etch and annealing under vacuum.

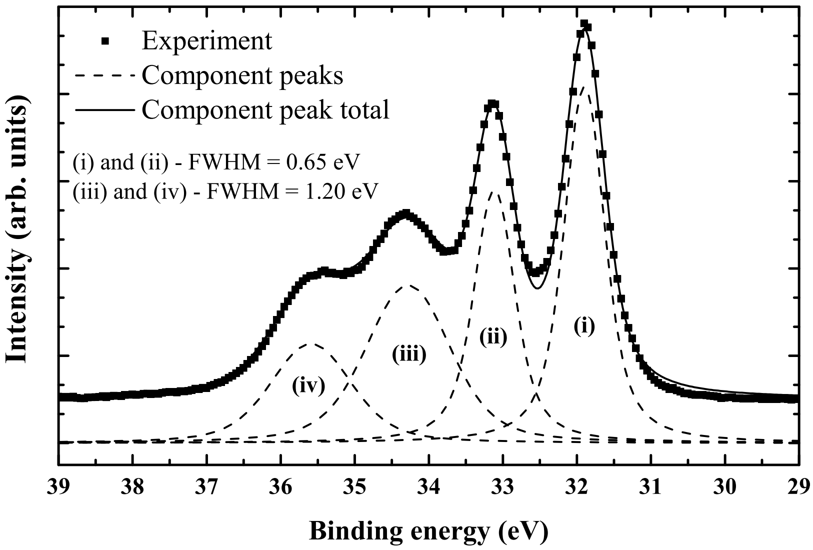

Figure 6.22: Illustration of the XPS peak fitting procedure for the Sb 4d core level region.

the oxygen concentration trend was determined from the Sb 4d region instead.

Note that the peak fitting procedure used here was less complex than seen in some XPS work. Full identification and treatment of all the bonding environments contributing to the XPS spectra (metal-metal, metal-Sb, various oxides, satellite features, etc.) was deemed unnecessary. Instead, a more qualitative analysis was used to obtain the important information.

Figure 6.22 illustrates how the Sb 4d fitting was performed. Each peak was assumed to have a Voigt lineshape, with both Gaussian and Lorentzian broadening contributing to the full-width at half-maximum (FWHM). Fitting was first performed on the spectra from fully treated samples, to obtain reasonable peak positions and FWHM values for almost oxide-free peaks. These values were kept constant while fitting to the other spectra, in order to identify the oxide contributions. After shifting the binding energies by a small amount ($|\text{mean shift}| =$ 0.17 eV) so that the C 1s peaks of each sample aligned at 285 eV[127], the Sb 4$d_{5/2}$ binding energies were found to be 31.93 and 32.17 eV for NiSb and MnSb, respectively. The 4$d_{3/2}$ energies were 33.17 and 33.28 eV. The average spin-orbit splitting of the Sb 4d peaks was 1.18 eV and the FWHM for these peaks was 0.65 eV; both of these values are in decent agreement with XPS work on MnSb thin films[128]. The FWHM of the higher binding energy peaks in as-loaded and HCl-etched spectra were allowed to be larger, so as to represent a

	Surface preparation		
	As loaded	HCl etch	Etch and anneal
MnSb	66 %	18 %	3 %
NiSb	36 %	56 %	6 %

Table 6.3: Behaviour of surface Sb oxide concentrations for MnSb and NiSb with surface preparation - as determined by fitting peak areas in the Sb 4*d* region. The % values represent the fraction of each Sb 4*d* region which is attributed to oxides.

range of bonding environments, though the spin-orbit separation was kept at the same value of 1.18 eV. This is a reasonable approach since a number of antimony oxides, such as Sb_2O_3, Sb_2O_4 and Sb_2O_5, are known to exist, each having different Sb 4*d* binding energies[49]. With respect to the Voigt lineshapes, a single FWHM value is estimated from the Gaussian and Lorentzian widths using the approximation of Olivero and Longbothum[129].

Sb oxide concentrations

Table 6.3 provides the percentage of each Sb 4*d* XPS region that is attributed to Sb-oxygen bonding. For both NiSb and MnSb the oxide content is severely diminished after the full surface treatment. However, the effect of the HCl etch alone seems to be quite different for each sample. The oxide content of the NiSb surface increases after the HCl etch, and this is reflected in the size of the oxygen 1*s* peak - see figure 6.21, cells (d), (e) and (f). It is possible that, though great taken was taken during the surface preparation procedure, the increased oxide content of NiSb in the intermediate stage was a consequence of prolonged exposure to atmosphere after the HCl etch but before the sample's insertion into vacuum.

Focussing now on the Sb 3*d* spectra, the binding energy separation between the Sb $3d_{3/2}$ peaks and their oxide features is in the region of 2.3 ± 0.1 eV. Peak separations of this size have previously been attributed to an oxide[130], and in particular Sb_2O_3[49]. However, the oxide features seen here are quite broad and are probably composed of contributions from all three of the previously mentioned Sb-oxides.

Sample stoichiometry

In the final stage of the MnSb and NiSb XPS analysis, the stoichiometry, i.e. TM:Sb ratio,

	Surface preparation		
	As loaded	HCl etch	Etch and anneal
MnSb	1:1	0.1:1	0.7:1
NiSb	0.7:1	0.4:1	0.8:1

Table 6.4: Sample surface stoichiometry before and after treatments. Values represent the proportions of TM:Sb and are obtained from analysis of XPS spectra normalised with the relevant atomic sensitivity factors and inelastic mean free paths.

was determined for each stage of the surface preparation process - the results are given in table 6.4. The TM $2p$ and Sb $4d$ regions were examined. The peak areas were normalised with the relevant atomic sensitivity factors (ASF)[131] and inelastic mean free paths (IMFP) so that the compositions could be deduced. IMFPs are the mean lengths through which electrons can travel through a material without undergoing inelastic scattering and losing some of their characteristic energy. These were obtained using the TPP-2M equation of Tanuma *et al.*[132], implemented in the NIST Electron Inelastic Mean Free Path program[133].

The starting stoichiometries for each sample's surface were different, but in both cases the HCl etch resulted in a more Sb-rich surface. The effect was particularly large for the MnSb sample, where the Mn concentration at the surface was reduced by a factor of ten. The smaller effect observed for Ni may possibly be explained by the fact that only one Ni oxide (NiO) is known to exist, compared to large number of oxides (MnO, Mn_2O_3, Mn_3O_4, etc.) that exist for Mn. After the vacuum anneal at 300 °C for 1 hour, the surfaces of both samples were partially restored to bulk-like stoichiometry, suggesting that some refinement of this final process, using a different temperature and/or anneal time, might provide the desired TM:Sb ratio of 1:1.

Experimental procedure - *in situ* Ar^+ bombardment

XPS measurements were made on the single crystal NiMnSb sample, which was treated with an entirely *in situ* surface preparation procedure. The four states were; as-loaded, after a 0.5 keV Ar^+ bombardment, vacuum annealed, and after a final 1 keV Ar^+ bombardment. As before, the main objectives were the removal of surface oxidation and the restoration of the surface to bulk-like stoichiometry. Both ion bombardment intervals were 30 minutes, while the vacuum anneal was at 250 °C and lasted 1 hour. All of these procedures took place within

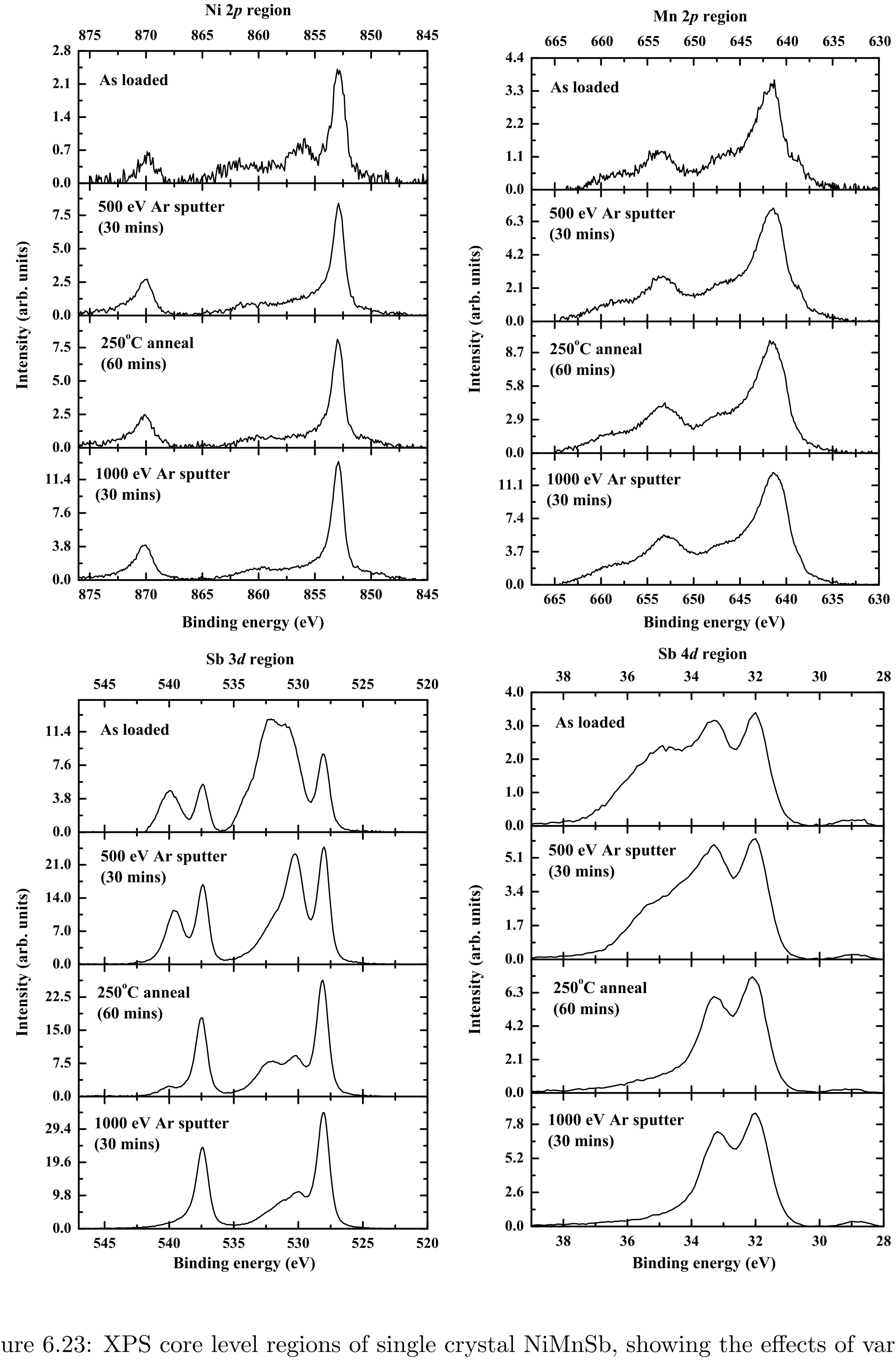

Figure 6.23: XPS core level regions of single crystal NiMnSb, showing the effects of various Ar^+ sputtering and annealing procedures.

the same vacuum system used for the XPS measurements.

XPS analysis - *in situ* Ar$^+$ bombardment

The NiMnSb XPS results are shown in figure 6.23. Looking at the Sb $3d$ and $4d$ regions, the incremental reduction of the surface oxide is clear, but it is not as complete as seen in the HCl treatment of MnSb and NiSb. In the final treated state, the oxide contribution to the Sb $4d$ region (determined from the same fitting procedure as used previously) was found to be $\sim$ 12%, significantly higher than seen after the complete HCl treatment. Also, the oxygen $1s$ peak was still quite apparent at around 530 eV. The ratio of Ni:Mn:Sb for the final treated state was found to be 17:67:16, which deviates significantly from the stoichiometric ideal.

6.7 Conclusions

Single crystal production

The objective of producing a single crystal of NiMnSb was achieved. This is evidenced by results from EDX, Laue diffraction and, most significantly, X-ray powder diffraction. The latter confirmed that the crystal possessed the correct crystal structure (see figure 6.1) and had a lattice parameter consistent with values previously reported in the literature. The lattice parameter was found to be 5.945 ± 0.001 Å.

Magnetometry

$M\mathrm{v}H$ and $M\mathrm{v}T$ magnetometry yielded a total moment for NiMnSb of 3.98 μ_{B}/f.u., in good agreement with other work and predictions. Although this was not sufficient by itself to confirm the half-metallicity of the material, it was a further indicator of the high quality of the crystal and suggested that the electronic structure was close to that expected for half-metallic NiMnSb. The saturating field of $\sim$ 0.25 T was in good agreement with previous work.

With respect to the $M\mathrm{v}T$ magnetometry, two main pieces of information can be extracted from the data and fitting. First, from 5 to 380 K, and in fields of 0.75 and 2.5 T, there is no evidence for a T^n power law transition of the kind previously reported by Gardelis *et al.* and Hordequin *et al.* We can conclude that a changeover form one form of magnetism to another, e.g. well-localised to itinerant, does not occur in our sample, and that if some other change exists in the electronic structure it is not reflected in the magnetisation data. Second, the fact that the appropriate T^n exponent was found to be around 2, rather than the 3/2 suggested by Bloch theory, suggests that the magnetism may be delocalised, or Stoner-like. This is a surprising result. Stoner excitations are those which scatter one spin type (majority or minority) into the other. Since NiMnSb is predicted to have zero available states in the minority channel near the Fermi energy, it should be impossible for Stoner excitations to exist, leaving only the classical transverse spin-waves to disrupt the magnetic order. The determined T^2 dependence raises the possibility that the predicted minority-spin band gap is either non-existent or compromised in the studied NiMnSb sample.

An alternate interpretation of the observed T^2 magnetisation dependence is that it is due to the presence of a low wavevector gap in the classical spin-wave dispersion. Smolyaninova *et al.* argued that such a gap is created with the application of a magnetic field. Fitting $M\mathrm{v}T$ data with a law of the form T^n then results in modified n values that depend on the applied field and can be 2 or higher. The factor that detracts from this interpretation is that the gap, β, deduced from fitting our NiMnSb $M\mathrm{v}T$ data with Smolyaninova *et al.*'s modified power law is found to be 19 ± 2 meV, far larger than the value of 1.0 ± 0.2 meV previously found by Hordequin *et al.* with inelastic neutron scattering.

A final result from the NiMnSb magnetometry work, one that was not mentioned in the relevant section but is still of some interest, relates to the DLM-DFT calculations discussed in the introductory section. These calculations predicted a vastly reduced spin polarisation for NiMnSb at a T^* of 100 or 180 K. The interpretation of reduced magnetisation from the DLM-DFT calculations into T^* values was achieved with a Brillouin function describing magnetisation as a function of temperature. In this chapter is presented magnetisation data for NiMnSb, in agreement with other work from Otto *et al.*[106], which shows that the saturated moment reduces more slowly with temperature than estimated in the DLM-DFT work. If the experimental behaviour of $M(T)$ is considered instead, T^* for NiMnSb may actually be closer to room temperature, at around 250 K, indicating that its spin polarisation is more robust than the DLM-DFT work suggests.

Density-functional theory calculations

The NiMnSb DFT calculations conformed to expectations and previous results, inasmuch as they generated a half-metallic electronic structure, an integer spin moment of 4 μ_B, and put the optimum lattice parameter at just under the experimental value, at 5.867 ± 0.004 Å. The lattice optimisation work showed that the system followed well the pressure-volume-energy relationships given by the Murnaghan equation of state, and the derived bulk modulus of 128 ± 2 GPa is consistent with other work.

No new information was likely to be gleaned from an analysis of the NiMnSb DoS given here, since the electronic structure has been understood for some time. However, the equivalence of the DoS with other work adds to the veracity of all aspects of the calculations, most importantly the theoretical magnetic Compton profiles. The site-projection of the DoS and MCPs, as well as the site- and band-specific spin moments, puts forward a rounded picture of the magnetic contributions in NiMnSb which can serve as a useful reference in future work.

Magnetic Compton scattering

The spin moments obtained from magnetic Compton scattering at 9 K were slightly (∼4%) larger than the expected 4 μ_B/f.u. for NiMnSb. The relative sizes of the spin moments at 9 K and 300 K were in good agreement with the equivalent total moments obtained from SQuID magnetometry. In addition, there was little directional variation in the size of the measured spin moment (magnetic anisotropy), agreeing with magnetometry results from other work.

The Mn 3*d* HF Compton profile and the total NiMnSb SPR-KKR profile were unable to describe the experimental MCPs. This is a fairly strong indication that the spin density, and therefore electronic band structure, of the measured sample is different from that predicted for half-metallic NiMnSb. Attempts to identify and resolve the experimental-theoretical discrepancy led to modifications of the *ab initio* DFT results; scaling the SPR-KKR MCPs, changing the Mn/Ni spin moment contributions, manually shifting the conduction bands with respect to the Fermi level, and introducing varying levels of atomic disorder. Of these approaches, only significantly increasing the fractional Ni spin moment resulted in a theoretical profile capable of describing the experimental MCP well. When the total spin moment was given by the ratio Mn:Ni = 3.2:1 (3.07 μ_{B}/f.u. and 0.96 μ_{B}/f.u. on the Mn and Ni sites, respectively) the agreement over the full MCP was vastly improved compared to the unmodified profile. This result, in addition to the deviation from Bloch's $T^{3/2}$ law for the temperature-dependent magnetisation, suggests that the NiMnSb crystals studied here are probably not half-metallic. On the other hand, an encouraging facet of the magnetic Compton scattering work comes from the fact that the experimental MCPs possess umklapp features, related to the material's Fermi surface topology, that are well replicated by the theoretical MCPs from SPR-KKR.

Surface preparation of MnSb, NiSb and NiMnSb

Looking now at the surface preparation work, the HCl etch and anneal given to MnSb and NiSb was quite effective; surface oxides were removed and, in the final stage, the stoichiometries were *almost* restored to a 1:1 ratio of TM:Sb. With some future refinement, most likely focussing on the details of the annealing process, it ought to be possible to achieve the desired stoichiometry.

The ion bombardment and annealing process used here was less effective than the HCl etch, with the full treatment resulting in a Mn-rich surface (Ni:Mn:Sb = 17:67:16). However, the Ar^{+} ion treatment offers advantages over the wet chemical method; since it is entirely *in situ*, the likelihood of sample contamination and oxidation between preparation stages is negligible, and XPS spectra can be recorded quickly after each preparation process. In the simplest terms, an entirely *in situ* cleaning process is desirable because it is easier and less messy.

Future work

An area which could benefit from more work is the investigation of NiMnSb's $M \mathrm{v} T$ behaviour. A future study, including wider temperature ranges and multiple applied field strengths, could reveal the zero field temperature-dependence, where the spin-wave dispersion relation is unmodified by an applied field, and the relationship of the T power exponent with the applied field. In addition, the necessity of extra modifying terms in Bloch's power law could be addressed. Since the electronic structure of NiMnSb is intimately linked to its magnetic behaviour, all of this information could be useful, most likely in combination with results from other experimental techniques, in determining the extent of its half-metallicity.

Similar magnetometry work, in addition to magnetic Compton scattering experiments, could be carried out on other half-metal candidates from within and without the half-Heusler family of alloys. This could determine whether NiMnSb is unique in its non-Bloch-magnetism/predicted-half-metal disparity, or if it is a feature of the half-Heuslers or, more generally, all of the predicted half-metals. The results of such a study could certainly be of key importance in the field. A good first choice for this work might be the simpler binary pnictide systems, wurtzite-MnSb and zincblende-MnSb. These systems are closely related to NiMnSb, but have an advantage, from the standpoint of experimental interpretation, of possessing a single magnetic ion only; on the other hand, the production of these materials, which is by MBE, is in its very early stages and may not be capable of yielding samples for immediate study.

It would be advisable to repeat the magnetic Compton scattering experiment on NiMnSb, ideally using a crystal sample other than the one studied here. In this way, the validity of the MCPs can be established, as well as examining the unlikely possibility that the sample studied in this work possessed a spin momentum density different from other parts of the synthesised boule. An investigation of the temperature-dependent MCP shapes might reveal some change in the spin density, or even a clear transition, related to the predicted drop-off in spin polarisation with temperature.

Considering further density-functional theory calculations, the LMTO package, primarily used by members of the Compton scattering group based in Bristol, might be useful in deducing the band structure of the measured NiMnSb sample. This package has a capability that SPR-KKR does not; it allows for individual electronic bands to be shifted within the converged potential. Using iterative steps, the LMTO magnetic Compton profiles are compared to those obtained experimentally and the band structure is altered in order to minimise the theoretical-experimental disagreement.

Finally, the NiMnSb surface could be studied in more detail. There was a previous report on the nanostructuring of a NiMnSb (110) surface as a consequence of Ar^+ bombarding and vacuum annealing[95]. In that work, the nanostructuring affected the surface magnetisation. A full investigation would look at the structural effects of both Ar^+ and Ne^+ bombardment using scanning electron microscopy (SEM) and atomic force microscopy (AFM). Information about the electronic structure at the surface could then be inferred from spin-polarised angle-resolved photoemission (SPARPES), and magnetisation data could come from a magneto-optic Kerr effect magnetometer, which is currently in development. There is also the possibility of a hard X-ray photoemission (HAXPES) study of the bulk NiMnSb crystal. This will use X-rays of energy ~ 8 keV to examine the total density-of-states around the Fermi energy, and will hopefully allow, through comparison with theoretical work of the kind provided here, a determination of the extent of the predicted minority-spin band gap.

Chapter 7

The 4*f* orbital occupation and magnetic structure of $TbMnO_3$

For the purpose of this work on $TbMnO_3$, magnetic Compton scattering was employed as an atomic orbital-specific probe of the magnetism, providing information about the system's magnetic structure and electronic configuration. Experimental results, coupled with theoretical work from the GAMESS linear combination of atomic orbitals (LCAO) code, provided a useful tool for the study of this $4f$-$3d$ system, allowing the determination of the Tb spin structure and the first confirmation of the predicted arrangement of Tb moments using separate spin and orbital contributions.

7.1 Introduction

$TbMnO_3$ is part of the class of *magnetoelectric multiferroics*, exhibiting electric polarisation in an applied magnetic field and magnetisation in an applied electric field[134,135]. Such materials, many of the form RMnO$_3$, where R is a rare-earth ion, have attracted attention in recent years because of their interesting and potentially useful properties; magnetoresistance[136], magnetocapacitance[137], half-metallicity[138,139], orbital ordering[140,141], and a range of metallic and magnetic transitions. Underlying these properties is a coupling between the magnetic order and lattice distortions[142], the understanding of which provides the motivation for much of the ongoing research.

Predicted magnetic and electronic structure

There has so far been relatively little published work regarding the electronic structure of

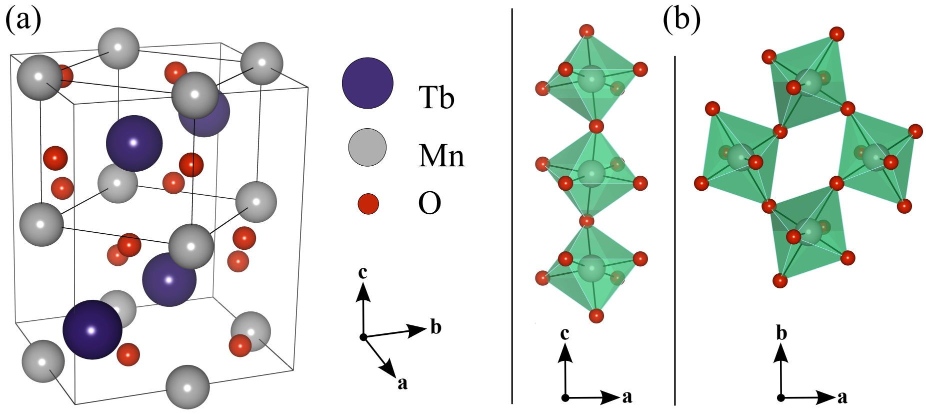

Figure 7.1: The *Pbnm* unit cell (grey line) of $TbMnO_3$ is shown in (a), where the near-cubic environment around each Tb ion is highlighted (black line). (b) shows the distortion of the MnO_6 octahedra which leads to the staggered orbital ordering described in the text.

$TbMnO_3$ beyond comparison with similar materials. The Tb ion is thought to have a simple Hund's rule spin structure, $4f^{7\uparrow+1\downarrow}$, while the Mn possesses a $3d$ $t_{2g}{}^3$ $e_g{}^1$ configuration with staggered $3d_{x^2-r^2}$ and $3d_{y^2-r^2}$ orbitals in the $\boldsymbol{a}$-$\boldsymbol{b}$ plane[141,143]. This type of Mn orbital ordering is known to exist in the 'parent' compound $LaMnO_3$[144], and is a result of the Jahn-Teller distortion described in section 2.3, albeit with the cell elongation along the y-axis rather than the z-axis. The structure of $TbMnO_3$, and the arrangement of the Jahn-Teller-distorted MnO_6 octahedra, are illustrated in figure 7.1.

Theoretical studies on $TbMnO_3$ have focussed on the complex ground-state magnetic ordering of the Tb and Mn sublattices. Both are predicted to order with cycloidal structures at low temperatures, which is consistent with evidence from neutron and X-ray scattering studies[144–146]. Other experimental work has characterised the macroscopic dielectric and magnetic properties, resulting in fairly comprehensive phase diagrams[147,148].

Independent DFT calculations by Xiang *et al.*, Yamauchi *et al.* and Chen *et al.* have predicted the system to be an insulator, with a gap between majority spin Mn e_g states[141–143]. Xiang *et al.* put the insulating gap at about 0.5 eV, which has been confirmed by resistivity measurements of thin film and bulk samples[149]. Of these DFT studies, the most relevant to this work is that of Xiang *et al.*, who also examined the electronic structure of the Tb. They found that the majority $4f$ states were fully occupied, lying between -7.5 and -6 eV relative

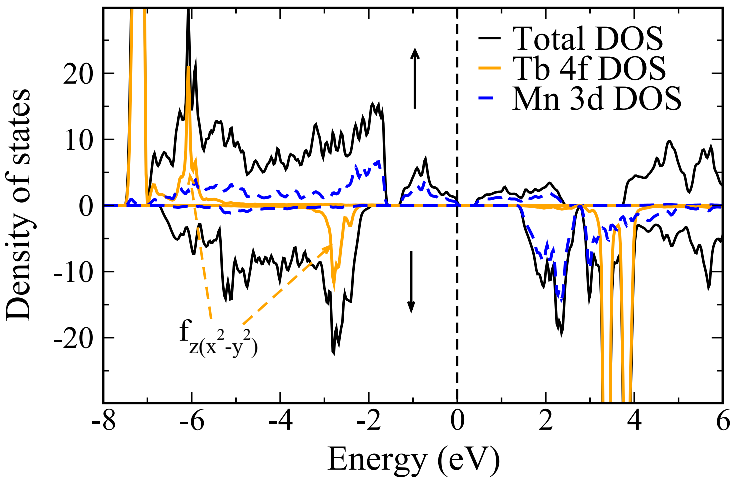

Figure 7.2: Tb $4f$ and Mn $3d$ components of the TbMnO$_3$ DoS (from DFT + U + SOC calculations). Reproduced from the work of Xiang *et al.*[143].

to the Fermi energy. Of the minority states, most were clustered around 3.5 eV, with a single occupied band, identified as the $4f_{z(x^2-y^2)}$, being found at about -3 eV. There was also a small $4f_{xyz}$ contribution to the minority states. The $4f$ bands possessed a very narrow energy range in the DoS, indicating that the electron distribution is well-localised. The DoS from Xiang *et al.* is provided in figure 7.2.

7.2 Magnetic and electric properties

Magnetoelectric effect and magnetic ordering temperatures

Kimura *et al.* were the first to observe the magnetoelectric effect in TbMnO$_3$[134]. Magnetisation, transport and heat capacity measurements revealed three distinct phases in the system and showed that the onset of spontaneous electric polarisation along the c-axis occurred at one of the magnetic ordering temperatures - see figure 7.3. Neutron diffraction work by Kenzelmann *et al.* confirmed the critical temperatures previously reported and provided information for a more complete description of the magnetic ordering in the system[144]. According to Kenzelmann *et al.*, below a Néel temperature, $T_{\mathrm{N}}^{\mathrm{Mn}} = 42$ K, the Mn moments order with a collinear sinusoidal antiferromagnetic arrangement in the $\boldsymbol{b}$ direction - see figure 7.4(a). Below a second critical temperature of 28 K, the Mn moments order with a cycloidal structure in the $\boldsymbol{b}$-$\boldsymbol{c}$ plane - figure 7.4(b). Evidence for the long-range ordering of the Tb moments below 28 K has come from resonant X-ray scattering[145,147] and circularly polarised nonresonant

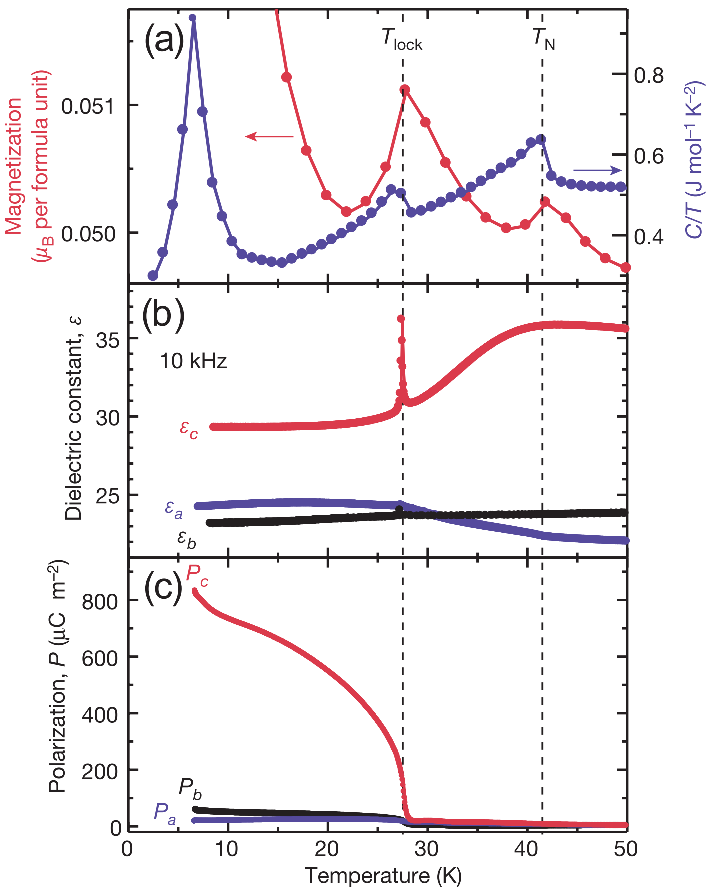

Figure 7.3: The magnetoelectric effect is apparent from the coincidence of electric polaristion (c) with a peak in the magnetisation (a). Reproduced from the work of Kimura *et al.*[134].

X-ray scattering[146], though the nature of this ordering, and how it relates to that of the Mn sublattice, is still debated. Finally, at $T_{\mathrm{N}}^{\mathrm{Tb}} = 7$ K, the Tb moments experience an ordering which is generally accepted to be independent of the Mn magnetism.

Phase diagram

Figure 7.5, from the work of Strempfer *et al.*, shows magnetic phase diagrams for $\mathrm{TbMnO_3}$ along the crystallographic a and b directions based on resonant and non-resonant X-ray diffraction[147]. The b direction phase diagram is in agreement with that put forward in one of the first $\mathrm{TbMnO_3}$ studies, the 2003 work of Kimura *et al.*[134].

Magnetoelectric mechanism

Katsura *et al.* put forward a mechanism for non-collinear magnets whereby the direction of the spontaneous electric polarisation, $\boldsymbol{P}_{ij}$, relates to the neighbouring spins, $\boldsymbol{S}_i$ and $\boldsymbol{S}_j$, and

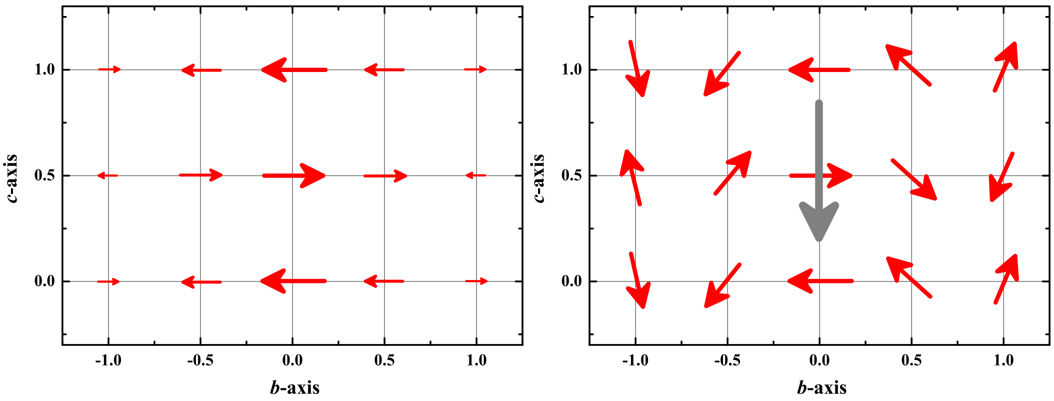

(a) (b)

Figure 7.4: Magnetic structure of the Mn moments in $TbMnO_3$ below (a) 42 K and (b) 28 K. Red arrows represent the relative size and direction of Mn moments, while the grey arrow in (b) shows the direction of electric polarisation.

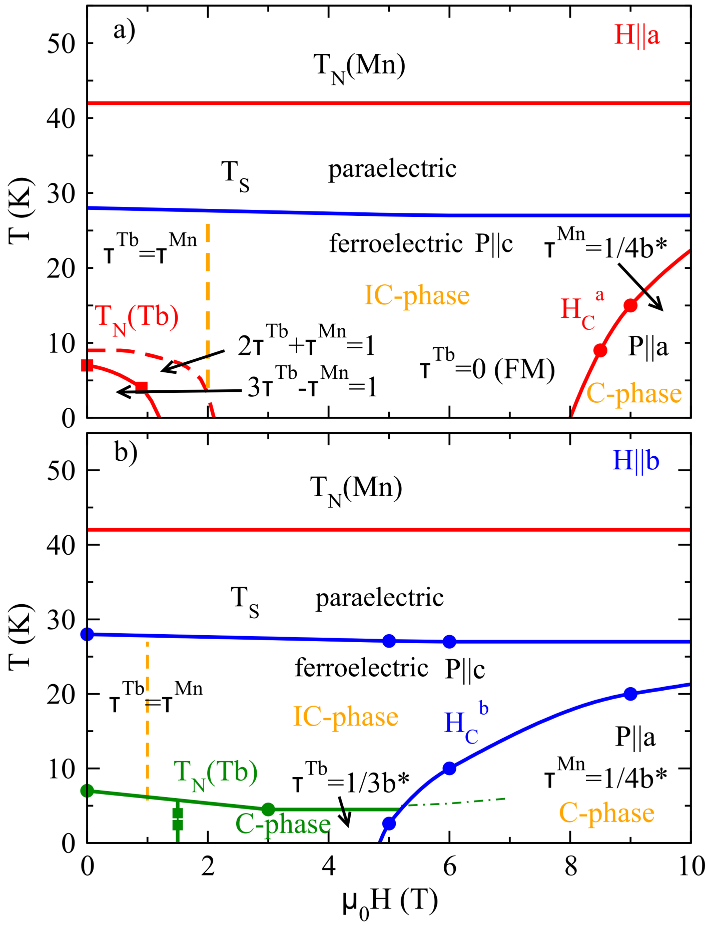

Figure 7.5: $TbMnO_3$ phase diagram along the crystallographic a and b directions from resonant and non-resonant X-ray diffraction measurements. 'IC-phase' and 'C-phase' refer to the incommensurate (cycloid) and commensurate (spin density wave) ordering of the Mn spins. Reproduced from the work of Strempfer *et al.*[147].

the vector between them, $\boldsymbol{r}_{ij}$. We have that[150]

$$\boldsymbol{P}_{ij} \propto \boldsymbol{r}_{ij} \times (\boldsymbol{S}_i \times \boldsymbol{S}_j). \tag{7.1}$$

If the Mn moments possess a cycloidal structure in the $\boldsymbol{b}$-$\boldsymbol{c}$ plane, then $\boldsymbol{S}_i \times \boldsymbol{S}_j$ is parallel to $\boldsymbol{a}$. Equation 7.1 tells us that the resulting polarisation is proportional to $\boldsymbol{b} \times \boldsymbol{a}$, therefore pointing along $\boldsymbol{c}$, as confirmed by Kimura *et al.*'s initial work. Equation 7.1 offers a similarly straightforward explanation for the fact that the polarisation direction is switched from $\boldsymbol{c}$ to $\boldsymbol{a}$ with the application of a magnetic field along $\boldsymbol{b}$; this is the polarisation 'flop' as observed by Hur *et al.*[151]. In that case, only a cycloid in the $\boldsymbol{a}$-$\boldsymbol{b}$ plane could be responsible, and this was confirmed experimentally by Aliouane *et al.* using single crystal neutron diffraction[152].

The Dzyaloshinsky-Moriya interaction

Another contribution to the description of electric polarisation in multiferroics came from Sergienko *et al.*, who argued that the Dzyaloshinsky-Moriya interaction (DMI) provided the mechanism for the strong coupling between ferroelectricity and magnetism[153,154]. The DMI is a form of anisotropic superexchange which includes the effect of spin-orbit coupling[155]. The result is that an excited state of a particular magnetic ion may interact with the ground state of its neighbour. Though the derivation is fairly involved[155–157], the Hamiltonian associated with the DMI is simply given by

$$\widehat{\mathrm{H}}_{ij} = \boldsymbol{D}_{ij} \cdot (\boldsymbol{S}_i \times \boldsymbol{S}_j), \tag{7.2}$$

where $\boldsymbol{D}_{ij}$ is a constant vector. This energy term often means that a canted alignment of moments is preferred over true antiferromagnetism; Dzyaloshinskii and Moriya referred to this as 'weak' ferromagnetism. The vector $\boldsymbol{D}_{ij}$ differs according to the symmetry of the crystal in question, but in the case of $\mathrm{TbMnO_3}$ it is proportional to $\boldsymbol{x} \times \boldsymbol{r}_{ij}$, where $\boldsymbol{x}$ is the displacement of the oxygen ion from its ideal position and, as before, $\boldsymbol{r}_{ij}$ is the vector between the spins $\boldsymbol{S}_i$ and $\boldsymbol{S}_j$ - see figure 7.6. With this in mind, it is easy to see that the DMI energy increases with the displacement of the oxygen ions, and since these are negatively charged and the Mn ions are positive, the result is an electric polarisation perpendicular to the direction of magnetic propagation. This effect is seen for all incommensurate multiferroics.

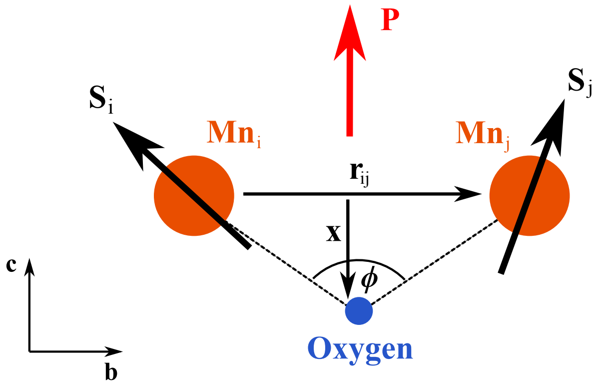

Figure 7.6: The electric polarisation mechanism in $TbMnO_3$, as proposed by Katsura *et al.*[150] (see equation 7.1). $\phi = 146°$.

Magnetic ordering of the rare-earth ions

It was proposed by Feyerherm *et al.* that the rare-earth ions play an important role in determining the ferroelectric properties of rare-earth perovskites[158]. They studied $DyMnO_3$ and $GdMnO_3$ with resonant X-ray magnetic scattering, showing that the Mn cycloidal ordering and the ferroelectric polarisation were affected, and possibly stabilised, by the ordering of the rare-earth moments. They concluded that, “for a full understanding of the ferroelectricity in rare-earth manganites an understanding of the rare-earth magnetism is very important.”

Tb moments in $TbMnO_3$

Magnetometry for single crystals of $TbMnO_3$ along three principal crystallographic directions is shown in figure 7.7. These results are from the Ph.D. thesis of Daniel O’Flynn[159], formerly of the Warwick Superconductivity and Magnetism group, and were recorded using a vibrating sample magnetometer (VSM). The data reveal metamagnetic transitions which are consistent with the “Ising-like”[160] model for the Tb moments that was used in the late 1960’s and 1970’s to explain very similar behaviour in $TbAlO_3$[160], $TbFeO_3$[161] and other Tb perovskites[162]. In $TbMnO_3$ the total moment in the $\boldsymbol{a}$ direction experiences a sharp increase at ~ 1.5 T, before saturating at ~ 2 T. In the $\boldsymbol{b}$ direction there are two transitions; one at ~ 1 T and one at ~ 4.5 T. It is important to note that the ‘saturation’ mentioned here applies specifically to this Ising-like model and does not indicate that the Tb spins become fully oriented along the direction of applied magnetisation - this would result in the 9 μ_B/f.u. classically associated with the Tb^{3+} ion. Rather, due to Tb-Tb dipole interactions and the exchange and dipole

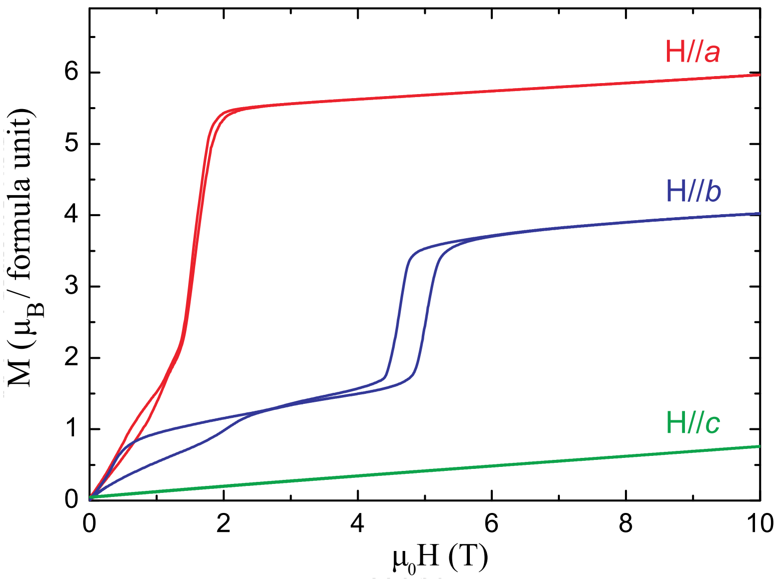

Figure 7.7: Magnetometry of $TbMnO_3$ recorded at 1.45 K for the crystallographic $\boldsymbol{a}$, $\boldsymbol{b}$ and $\boldsymbol{c}$ directions. Reproduced from the Ph.D. thesis of Daniel O'Flynn[159].

fields exerted by the transition metal ions, they have energetically favourable orientations with an angle in the region of 57° to the b-axis[163,164]. According to Belov *et al.*, the observed metamagnetic transitions are the reversal of those ions whose magnetic moments are directed opposite to the external field[163].

Figure 7.8 illustrates the Ising-like model whereby, in zero field, the moments of the four Tb sites of the orthorhombic cell order in the $\boldsymbol{a}$-$\boldsymbol{b}$ plane with no net magnetisation. With a field applied in the $\boldsymbol{a}$ direction, the moments on two sites are flipped, giving two pairs of aligned moments making an angle, θ, with the b-axis. Applying a field in the $\boldsymbol{b}$ direction causes one Tb moment to flip at ~ 1 T and a second to flip at ~ 4.5 T. Belov *et al.*, who theoretically examined the energetics of the closely related $TbFeO_3$ system, described the $H \parallel a$ and $H \parallel b$ metamagnetic transitions as $A'_xG'_y \rightarrow F'_xC'_y$ and $A'_xG'_y \rightarrow A'_{xy}G'_{yx}F'_{xy}C'_{yx} \rightarrow F'_yC'_x$ for the Tb ions[163]. θ has been reported as between 50° and 56° for various Tb perovskites[160–163], with the angle of 57° given for $TbMnO_3$ by Quezel *et al.*[164].

Quezel *et al.* seemingly obtained their θ value from a comparison of the total magnetic moments along the $\boldsymbol{a}$ and $\boldsymbol{b}$ directions. This approach assumes that all of the moment can be attributed to Tb. In contrast, an important outcome of the work described here is the

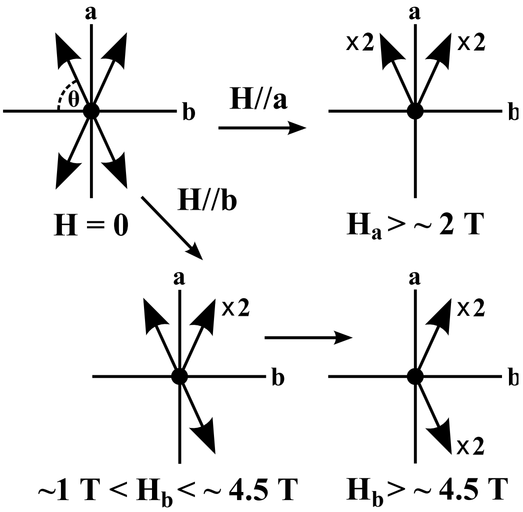

Figure 7.8: Ising-like model for the Tb spins in $TbMnO_3$. Refer to the text for a full description.

assignment of spin and orbital contributions separately to Tb and Mn. This allowed for a more meaningful investigation of the Ising model and the determination of θ values based solely on the spin moments *or* the orbital moments.

7.3 GAMESS theoretical work

GAMESS LCAO calculations were performed on $TbMnO_3$ in order to obtain species- and atomic orbital-specific Compton profiles to fit to experimental MCPs. Of primary interest were the seven $4f$ orbitals of the Tb ion, and the five hybridised d-like orbitals of the MnO_6 octahedra. For a rare-earth/transition metal system such as this, it is reasonable to assume that the $4f$ and $3d$ electrons contribute most significantly to the magnetism and therefore determine the shape of the MCPs. The possibility of magnetic contributions from other electrons is not excluded; polarised *sp* bands are known to exist in many rare-earth and transition metal systems[165–167]. This issue is discussed further in the following sections.

Calculation details - the Tb ion

Calculations were first performed on a Tb^{3+} ion surrounded by a cubic perovskite-like distribution of point charges; $+3e$ and $-2e$ for Mn and oxygen, respectively - the formal ionicity is $Tb^{3+}Mn^{3+}(O_3)^{6-}$. The environment closely emulated the near-cubic positioning of the neighbouring ions (see the $TbMnO_3$ unit cell in figure 7.1(a)), with the largest discrepancy

			$Pbnm$ (distorted)				$Pm\bar{3}m$ (cubic)	
Space group			62				221	
Lattice parameters (Å)	a		5.293					
	b		5.838		a		3.940	
	c		7.403					
		x	y	z		x	y	z
Tb	$4c$	0.983	0.082	1/4	$1a$	0	0	0
Mn	$4b$	1/2	0	0	$1b$	1/2	1/2	1/2
O_1	$4c$	0.104	0.467	1/4	$3c$	0	1/2	1/2
O_2	$8d$	0.704	0.326	0.051				

Table 7.1: Structural information for $TbMnO_3$ in its distorted perovskite phase ($Pbnm$). Lattice parameters and Wyckoff positions are from work by Alonso *et al.*[168]. Also given are the corresponding atom positions for a cubic perovskite approximation to the real structure. The cubic lattice parameter is taken from an average of the distorted parameters, using $a^2 = (5.293/2\ \text{Å})^2 + (5.838/2\ \text{Å})^2$ - see figure 7.1.

existing for the placement of the oxygen ions. The interatomic distances were 3.41 Å for Tb-Mn and 2.79 Å for Tb-O. Structural information for the orthorhombic distorted cell and the cubic perovskite cell is given in table 7.1. Lattice parameters and Wyckoff positions are from neutron powder diffraction by Alonso *et al.*[168].

The spatially localised nature of the Tb $4f$ wavefunctions means they were not expected to strongly hybridise with those of the other atoms, and indeed this was the case when several calculations were performed which included all of the atoms in the perovskite and orthorhombic cells. These calculations were computationally intensive, so thereafter, point-charges were used, providing a sufficient approximation for the potentials from nearby atoms. The same method was used by Qureshi *et al.*[59] and Koizumi *et al.*[55–58], and may be considered a standard approach. The Tb wavefunctions were described by the CRENBL basis set of Ross *et al.*[169], which removed some low-lying electrons from the calculation, replacing them with an effective core potential (ECP). This further reduced the complexity of the calculation, whilst retaining the validity of the $4f$ wavefunctions and their momentum densities. As a final note about these orbitals, which are shown in figure 7.9, the GAMESS calculations provided what are referred to as the 'cubic set' of $4f$ orbitals. These are known to be appropriate when the $4f$ ion is in a crystal environment with cubic symmetry. The other 'general set'

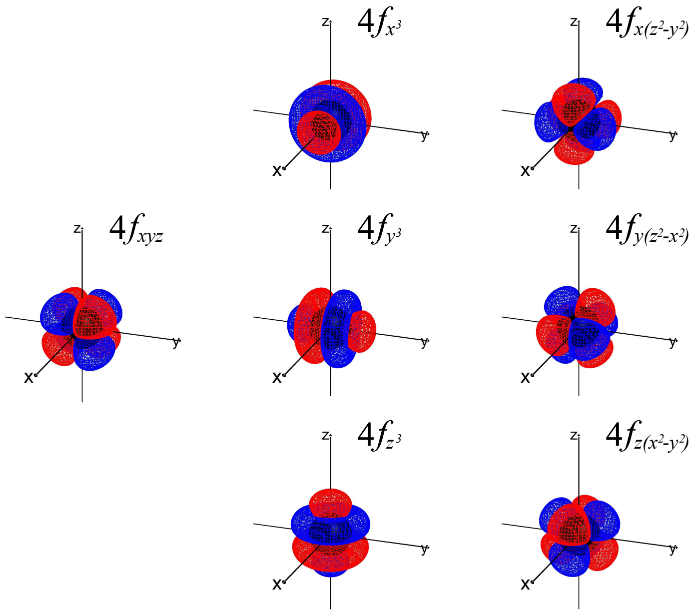

Figure 7.9: Real-space electronic wavefunctions of the Tb $4f$ orbitals from GAMESS calculations.

are used when such symmetry is absent. The $4f$ general set were provided by GAMESS when calculations were performed on a single Tb free atom, and investigations showed that the electron momentum densities for the two sets were different. This highlights the importance of defining the immediate environment correctly in this kind of LCAO work.

The Tb $4f$ wavefunctions were treated according to the procedure given in section 5.2 to obtain 3-D electron momentum densities and, by integrating along directions perpendicular to the scattering direction, the corresponding Compton profiles. Before the Compton profiles are discussed, brief attention is paid to an intermediate step, the plane-projections that result when just one of the integrations is performed. These are the 2-D electron momentum densities (2-D EMD). A half-filled f shell ($S = 7/2$, $L = 0$) is understood to have an isotropic charge distribution, virtually unaffected by crystal field effects from the electrically polarised crystal environment. The 2-D EMD for such a charge distribution is also isotropic, and this was seen to be true for the GAMESS calculations presented here when the 2-D EMDs of all seven $4f$ orbitals were summed - essentially modelling a Tb^{4+} ion with $4f^{7\uparrow}$ configuration. Thus, this aspect of the calculation agrees with expectations. The shape isotropy is lifted when any orbital is added or subtracted from the full set. Figure 7.10 shows the 2-D EMDs and

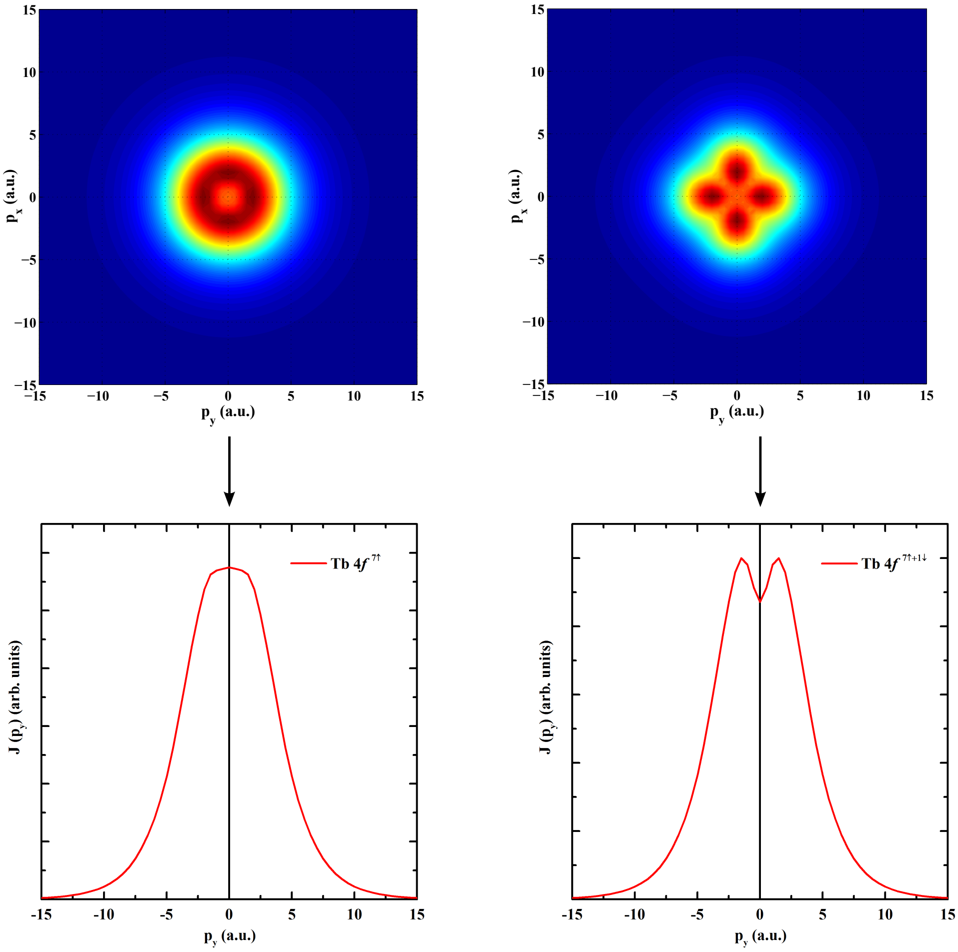

Figure 7.10: (Top) Theoretical 2-D electron momentum densities, in the $\boldsymbol{p}_x$-$\boldsymbol{p}_y$ plane, of Tb $4f$ orbitals in TbMnO$_3$. (Bottom) Compton profiles along the $\boldsymbol{p}_y$ direction corresponding to the above 2-D EMDs. The examples shown represent spin configurations of $4f^{7\uparrow}$ (left) and $4f^{7\uparrow+1\downarrow}$ (right). In the latter, the doubly occupied orbital is the $4f_{z(x^2-y^2)}$.

Compton profiles for a Tb $4f^{7\uparrow}$ and a $4f^{7\uparrow+1\downarrow}$ spin configuration where, in the latter, the doubly occupied orbital is the $4f_{z(x^2-y^2)}$. The 2D-EMDs, showing momentum density in the $\boldsymbol{p}_x$-$\boldsymbol{p}_y$ plane, were obtained by integrating the 3D-EMDs along $\boldsymbol{p}_z$.

Calculation details - the MnO$_6$ cluster

Calculations were next performed on the distorted $(MnO_6)^{9-}$ octahedra in $TbMnO_3$. There are two configurations for these octahedra; each may be considered a tilted and rotated version of the other, and each has an O-Mn-O bond which is longer in the $\boldsymbol{b}$ direction than in the $\boldsymbol{a}$ direction. According to DFT work by Chen *et al.* (GGA + U)[141] and Xiang *et al.* (DFT + U + SOC)[143], these two types of octahedra are electronically unique, possessing distinct e_g orbitals of type $3d_{x^2-r^2}$ and $3d_{y^2-r^2}$. For this reason, both types of MnO_6 cluster were modelled and the proper orthorhombic atomic positions were used. In contrast to the Tb calculations described above, because strong *sp*-*d* hybridisation was expected, it was necessary to include the atomic wavefunctions of both Mn and oxygen. The octahedra were embedded in a large number of point charges, representing the potentials of Tb, Mn and oxygen out to several unit cells from the central Mn ion. The triple zeta valence (TZV) basis set of Schaefer *et al.*[170] was used, as it has been previously demonstrated to describe well the electron densities of MnO_6 octahedra[55–57].

The GAMESS calculations predicted the same orbital occupation as determined by Chen *et al.* and Xiang *et al.* For both MnO_6 octahedra types, the spin configuration was given as $3d^{4\uparrow}$, with all three majority t_{2g} orbitals, the $3d_{xy}$, $3d_{xz}$ and $3d_{yz}$, being occupied. In each MnO_6 cluster, a different e_g orbital was occupied; these were the $3d_{x^2-r^2}$ and $3d_{y^2-r^2}$ which stagger along the $\boldsymbol{b}$ direction. Thus, for the purpose of fitting to experimental data, the Mn e_g band was represented by $1/2\ (3d_{x^2-r^2} + 3d_{y^2-r^2})$, reflecting an average over the whole measured crystal. For clarity, note that although the orthorhombic distortion of the MnO_6 cluster results in *two* orbitals which might equally be identified as $y^2 - r^2$, because the angles they make with the y-axis are equal, the convention in the literature is to label one as $x^2 - r^2$.

The MnO_6 $3d$ energy levels according to GAMESS are represented in figure 7.11, the ordering of which is in fair agreement with Xiang *et al.*, except for the placement of a single t_{2g} orbital. In

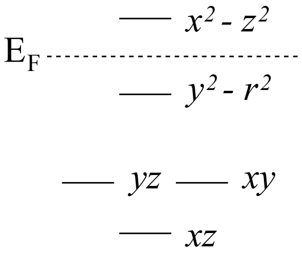

Figure 7.11: The Mn $3d$ energy levels according to GAMESS.

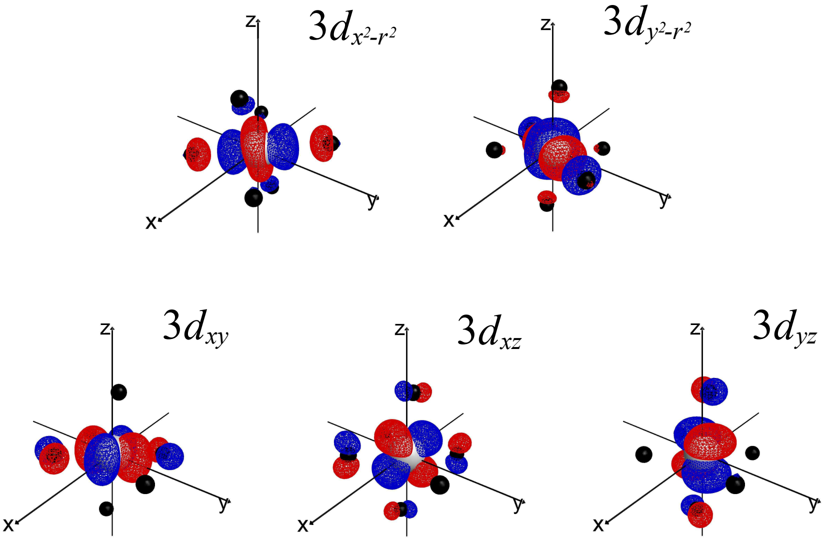

Figure 7.12: Real-space electronic wavefunctions of the MnO_6 octahedra from GAMESS calculations. They are composed primarily of hybridised Mn $3d$, oxygen $2s$ and oxygen $2p$ orbitals. Black spheres represent the oxygen ions and the central white sphere is the Mn ion.

this matter, since the LCAO method is not as sophisticated as DFT in determining energies, and does not actually include all of the electrons, we can accept the discrepancy.

The MnO_6 hybridised orbitals are shown in figure 7.12 and the 2-D EMDs for the summed t_{2g} and e_g bands are given in figure 7.13. The first feature of note is that the Mn $3d$ 2-D EMDs do not extend as far in momentum space as those seen for Tb $4f$. This, of course, is expected, since the $3d$ electrons have the larger real-space distribution. The t_{2g} band shows some anisotropy, most significantly between $\langle 100\rangle$ and $\langle 110\rangle$ directions, while the e_g band exhibits far more, reflecting the strong directionality of the e_g orbitals along the $\boldsymbol{b}$ direction.

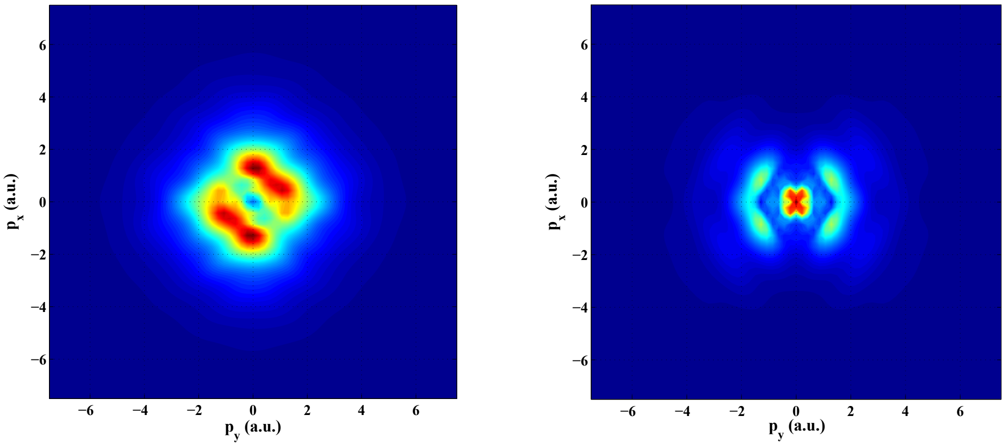

Figure 7.13: Theoretical 2-D electron momentum densities, in the $\boldsymbol{p}_x$-$\boldsymbol{p}_y$ plane, for the t_{2g} (left) and e_g (right) bands of Mn in $TbMnO_3$.

The LCAO Compton profiles

The Compton profiles associated with the LCAO wavefunctions for Tb and MnO_6 are shown in figures 7.14 and 7.15, respectively, where the profile of each orbital has an area representing 1 μ_B. It is important to note that, within the cubic approximation used for the Tb calculations, the relevant $4f$ Compton profiles are actually those along the cubic $\langle 110 \rangle$ directions. Due to the ~45° rotation needed to describe the larger orthorhombic cell, these are roughly equivalent to the $\boldsymbol{a}$ and $\boldsymbol{b}$ directions that were actually measured for the $TbMnO_3$ crystal. The small difference between $\boldsymbol{a}$ and $\boldsymbol{b}$ lattice parameters means that the exact rotations necessary are 45 ± 2°, but the Compton profiles varied insignificantly when this extra precision was considered. Two pairs of Tb $4f$ orbitals, the f_{x^3} and f_{y^3}, and the $f_{x(z^2-y^2)}$ and $f_{y(z^2-x^2)}$, have identical Compton profile shapes. This is consistent with the shapes of the real-space wavefunctions shown in figure 7.9. Those orbitals are symmetric pairs about a plane half way between the cubic x- and y-axes; therefore, a Compton scattering measurement along [110] will be unable to distinguish between them.

With respect to the MnO_6 results, the veracity of the GAMESS calculations is attested by the agreement of the total Compton profiles (t_{2g} + e_g) with HF theory over the profile tails. The disagreement at low momentum is associated with contributions from more itinerant s and p orbitals, which obviously are not present in the pure Mn $3d$ HF profile, as well as the directionality of the GAMESS profiles compared to the spherical average of the HF

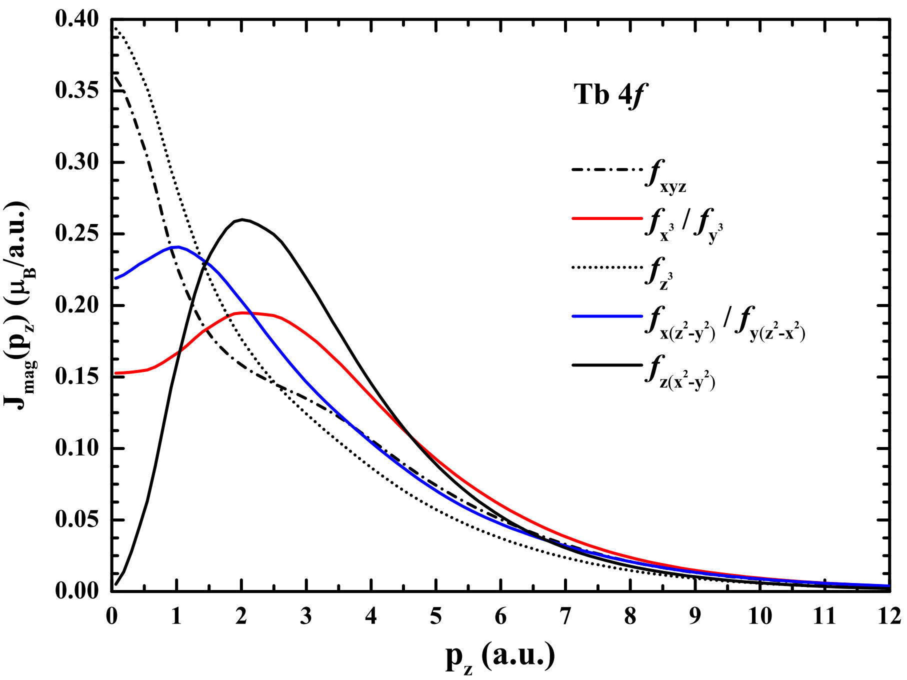

Figure 7.14: Theoretical Compton profiles originating from the Tb 4f orbitals illustrated in figure 7.9. These profiles are projections along the crystallographic [110] direction of the cubic perovskite system, which is roughly equivalent to the ***a*** and ***b*** directions of the distorted perovskite - see figure 7.1.

approximation. As described in section 5.2, the full molecular orbitals are made from a combination of atomic orbitals; in this case, the s, p and d wavefunctions of both species contributed to varying extents. The largest contributions were from Mn d orbitals; these dominated the t_{2g} types, comprising about 85% of their total. In comparison, the e_g molecular orbitals had large oxygen s and p contributions, in the region of 43%. This is consistent with the idea that a larger degree of hybridisation should occur in the e_g orbitals because the 'lobes' of the TM and oxygen electron densities point towards each other and necessarily overlap.

7.4 Magnetic Compton profiles and analysis

TbMnO$_3$ samples

Crystals of TbMnO$_3$ were obtained from the Superconductivity and Magnetism group, where they were originally grown by Daniel O'Flynn[159]. They were produced by the floating zone method, using stoichiometric polycrystals synthesised by the reaction of Tb$_4$O$_7$ and MnO$_2$.

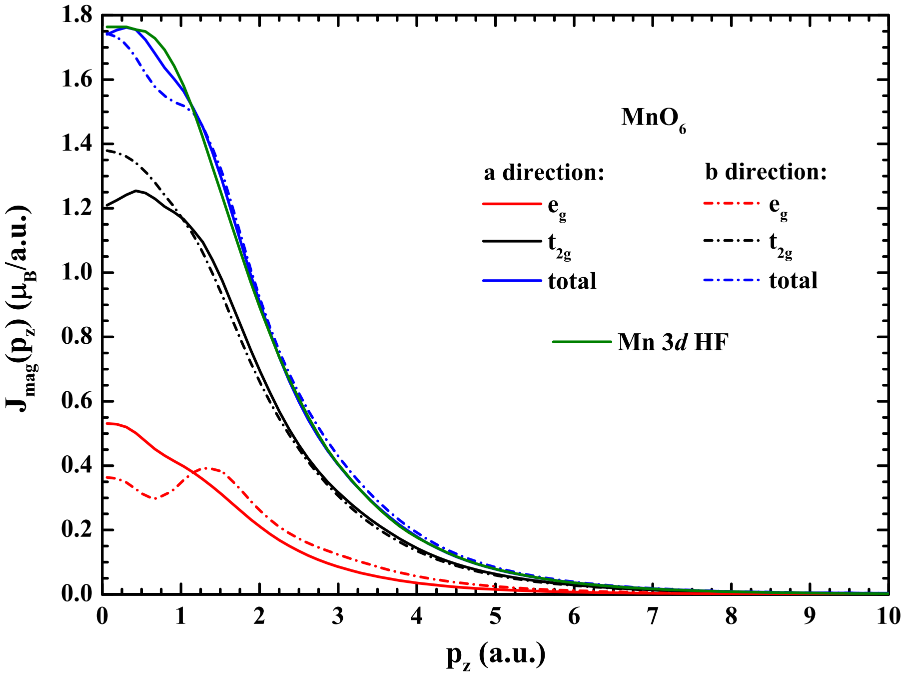

Figure 7.15: Theoretical Compton profiles originating from the MnO$_6$ octahedra along the orthorhobic $\boldsymbol{a}$ and $\boldsymbol{b}$ directions.

Data collection

TbMnO$_3$ magnetic Compton profiles were collected on three separate experimental runs. The first and third took place on the BL08W beamline at SPring-8, the second used the ID15A beamline at the ESRF. The first experiment (November 2011) provided data of high statistical quality for both the $\boldsymbol{a}$ and $\boldsymbol{b}$ directions, but the maximum applied field was limited to ±2.5 T. The second experiment (July 2012) used the Oxford Instruments Spectromag magnet to provide access to the high field region of the TbMnO$_3$ $\boldsymbol{b}$ direction magnetisation and allowed measurements to be made at 1.45 K, in contrast to the 7 K available on BL08W. The third experiment (January 2013) also used the Oxford Instruments magnet, which was recently transported from the ESRF to SPring-8 as part of a long-term project, and was performed primarily to ensure the reproducibility of the MCPs. In addition to the different synchrotrons and magnets, some of the numerical results and MCPs given here were obtained from work on two different samples, though both were fragments from the same large TbMnO$_3$ crystal. Therefore, before more specific information is given, it is important to demonstrate the extent of the agreement between the datasets.

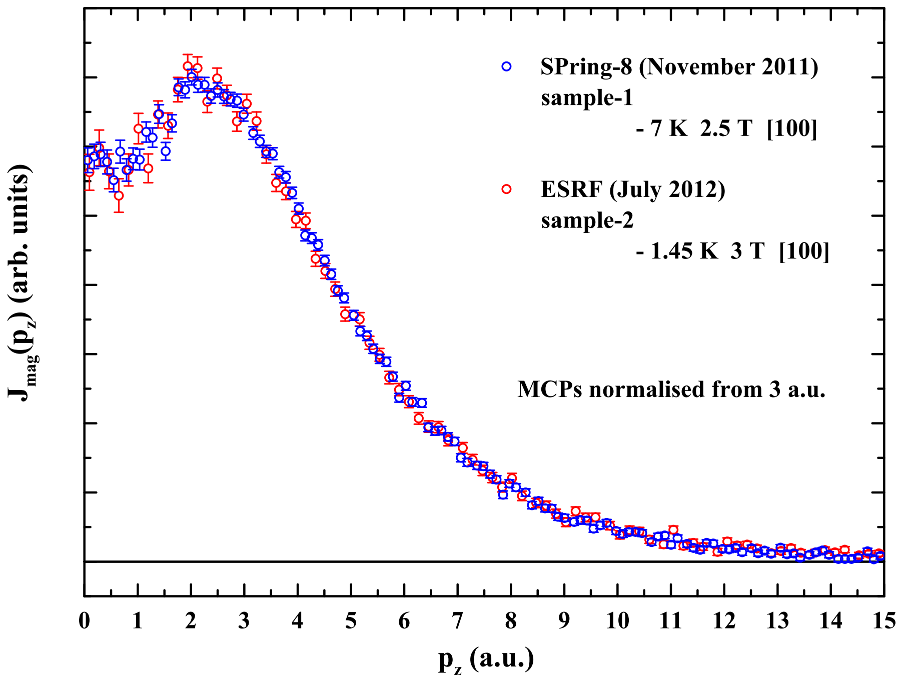

Figure 7.16: $TbMnO_3$ [100] MCPs from two samples and synchrotron beamlines. The excellent correspondence in shape means we can have confidence in these MCPs.

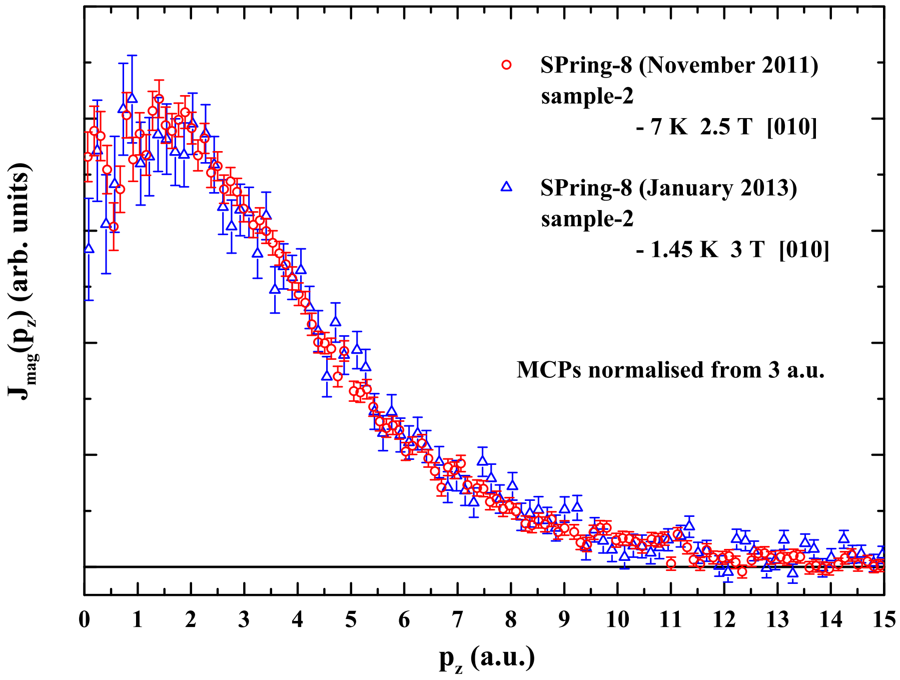

Figure 7.17: $TbMnO_3$ [010] MCPs from two samples. The excellent correspondence in shape means we can have confidence in these MCPs.

Direction	Field (T)	Total moment (μ_B/f.u.)	Spin (μ_B/f.u.)	Orbital (μ_B/f.u.)
$\boldsymbol{a}$	2.5	5.52	3.80 ± 0.06	1.72 ± 0.06
$\boldsymbol{b}$	2.5	1.36	0.89 ± 0.01	0.47 ± 0.01
	6	3.71	2.74 ± 0.05	0.97 ± 0.05

Table 7.2: Total moments from VSM magnetometry, as well as spin and orbital contributions for the $\boldsymbol{a}$ and $\boldsymbol{b}$ directions.

Figures 7.16 and 7.17 show MCPs along the $\boldsymbol{a}$ and $\boldsymbol{b}$ directions, respectively, for two $TbMnO_3$ samples, labelled 'sample-1' and 'sample-2', collected during different experiments. The MCPs were of different sizes (their spin moments differed according to the temperatures and applied fields), so they were normalised by setting their integrals from 3 to 15 a.u. to unity. Normalising over the MCP tail in this way avoids sensitivity to the low momentum region, where larger deviations between datasets might be expected. Even so, the MCPs from different samples and experimental runs shared the same shapes. We can therefore have confidence that the MCPs collected during different experiments reflect the same spin density distribution.

Spin moments

The experimental spin moments for $TbMnO_3$ are given in table 7.2, where the total moments from VSM measurements are also provided. The difference between the total and spin moment is the orbital moment. If we assume that the Mn $3d$ orbital moment is fully quenched, which is usually true for transition metals (see section 2.4), the orbital moment in $TbMnO_3$ can be attributed to the Tb only. The significance of the magnitudes of the orbital moments is examined later. First, the fitting procedure which led to the determination of site-specific spin moments is described.

Fitting to the experimental MCPs

Fitting to the experimental MCPs was performed by varying the contributions from two theoretical profiles, one representing the Tb spin, the other originating from hybridised Mn and oxygen orbitals. The goodness of each fit was quantified by reduced-χ^2 values. Due to the shape-degeneracy of two pairs of Tb $4f$ profiles, there existed only five possible Tb models; in each, a single $4f$ orbital profile was subtracted from a sum of all seven, according to the

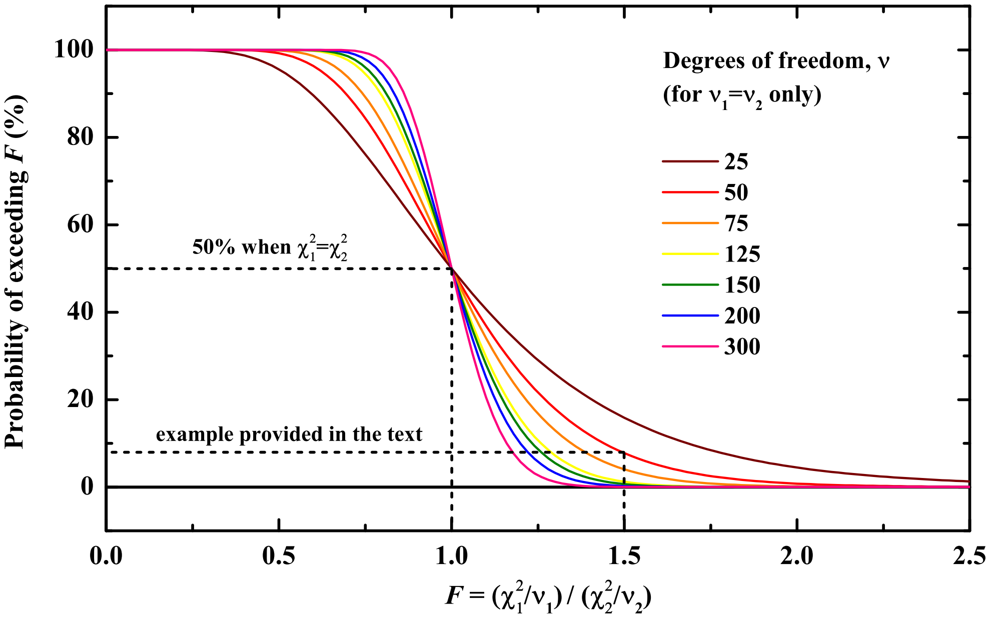

Figure 7.18: The statistical F distribution for comparing two fits with χ^2 values of χ_1^2 and χ_2^2, and ν_1 and ν_2 degrees of freedom. The value of F is given by the ratio of reduced-χ^2 values, i.e. $F = \frac{\chi_1^2}{\nu_1} / \frac{\chi_2^2}{\nu_2}$. The probability of exceeding a particular F value is provided by an integral over the associated probability density function - refer to section 11.4 of of *Data Reduction and Error Analysis* by Bevington and Robinson[171]. Refer to the text for more information.

Hund's rule spin configuration $4f^{7\uparrow+1\downarrow}$. As discussed above, the profiles representing the MnO_6 octahedra were from a $3d$ t_{2g}^3 e_g^1 configuration. Fitting was performed over the whole momentum range of the MCPs, excluding the region below 2 a.u., where contributions from largely hybridised and itinerant electronic bands are not well represented by combinations of atomic orbitals.

Reduced-χ^2 values and the F distribution

Table 7.3 provides reduced-χ^2 fitting values for the $\boldsymbol{a}$ and $\boldsymbol{b}$ direction MCPs obtained at 2.5 T from SPring-8. In both cases, the model in which the $4f$ minority orbital was the $f_{z(x^2-y^2)}$ provided the lowest reduced-χ^2 value, indicating that it was most likely to be correct. To frame these values more meaningfully, and to investigate the relationships between reduced-χ^2 values, the F distribution, also known as the Fisher-Snedecor distribution, was employed. A full description of the F distribution can be found in section 11.4 of *Data Reduction and Error Analysis* by Bevington and Robinson[171]. Its primary use is to compare two statistics, in this case reduced-χ^2 values, and determine the probability of exceeding F, which is simply their ratio, with a random set of data compared to the correct fitting function.

Figure 7.18 shows the probability of exceeding a range of F values when there are various degrees of freedom involved in the fit. When the reduced-χ^2 values of two competing models, model 1 and model 2, are equal (the ratio χ_1^2/χ_2^2=1), they can be thought of as providing an equally valid description of the data, and the probability of F being exceeded is 50%. As χ_1^2 becomes increasingly large with respect to χ_2^2, i.e. as model 1 becomes increasingly poor with respect to model 2, then the probability of exceeding their reduced-χ^2 ratio becomes smaller. This means that model 2 becomes the preferred fit of the two options, and the 'probability of exceeding F' can be interpreted as a level of confidence that model 2 is better than model 1. To provide an example; if there are fifty degrees of freedom in a fitting procedure, and the ratio χ_1^2/χ_2^2=1.5, then the probability of exceeding F is 8% (as illustrated in figure 7.18). We can then say, with a confidence level of 92%, that model 2 is better than model 1.

The question being posed with such an evaluation as implemented here, is this: with what level of confidence can we say that any model is better than the $f_{z(x^2-y^2)}$ model? The number of degrees of freedom in this analysis was 107, that is 109 data points minus two fitting variables (the sizes of the theoretical Tb and Mn profiles). The penultimate column of table 7.3 tells us that, for the $\boldsymbol{a}$ direction at 2.5 T, we have to accept only a 2% likelihood that model 2 is better than the $f_{z(x^2-y^2)}$ model, which is sufficient to disregard it, and the others which have even lower probabilities. The situation is less clear-cut for the $\boldsymbol{b}$ direction at 2.5 T, due primarily to the poorer statistical quality of the data. The $f_{z(x^2-y^2)}$ model was still preferred, but there is a chance that it might be exceeded by another. In the case of the $\boldsymbol{b}$ direction data measured at 6 T, it was found that no particular model was preferred.

Fit results

The experimental data and fits are shown in figure 7.19, and residual plots for the $\boldsymbol{a}$ direction, showing the fit residuals for several Tb 4f models, are shown in figure 7.20. Upon examining figure 7.19 it must be understood that the $f_{z(x^2-y^2)}$ minority spin model is explicitly preferred in fitting to *two* of the presented MCPs only; these are the 'low-field' $\boldsymbol{a}$ and $\boldsymbol{b}$ direction datasets shown in the upper two cells. For the 6 T $\boldsymbol{b}$ direction dataset, all of the Tb minority orbital models were almost equally valid, providing very similar reduced-χ^2 values. The

	Minority spin	Reduced-χ^2		F		Probability of exceeding F (%)	
		$\boldsymbol{a}$	$\boldsymbol{b}$	$\boldsymbol{a}$	$\boldsymbol{b}$	$\boldsymbol{a}$	$\boldsymbol{b}$
Model 1	f_{xyz}	2.29	1.26	1.91	1.21	0.1	16
Model 2	f_{x^3} or f_{y^3}	1.79	1.17	1.49	1.13	1.9	27
Model 3	f_{z^3}	2.09	1.23	1.74	1.18	0.2	19
Model 4	$f_{x(z^2-y^2)}$ or $f_{y(z^2-x^2)}$	2.53	1.32	2.11	1.27	0.0	11
Model 5	$f_{z(x^2-y^2)}$	1.20	1.04	-	-	-	-

Table 7.3: Fitting results for the five models available to describe the Tb spin configuration. Only the results for the $\boldsymbol{a}$ and $\boldsymbol{b}$ direction datasets measured at 2.5 T are included. In the final column, probabilities of exceeding the $f_{z(x^2-y^2)}$ fit are provided - see text.

$f_{z(x^2-y^2)}$ model fit is shown for this dataset anyway because it is capable of describing the MCP well and provides the site-specific spin moments which are later used to infer information about the Tb and Mn magnetic structures.

With respect to figure 7.20, the residuals for models in which the $4f$ minority orbital was the f_{x^3} or f_{y^3} (next-best fit according to reduced-χ^2), or the $f_{x(z^2-y^2)}$ or $f_{y(z^2-x^2)}$ (worst fit according to reduced-χ^2), deviated significantly and consistently from zero. This was true over the full momentum range. The model with the lowest reduced-χ^2, where the $4f$ minority orbital was the $f_{z(x^2-y^2)}$, resulted in a residual plot with far less additional structure compared to the others. While the $f_{z(x^2-y^2)}$ residual plot possessed *some* structure, analysis of the normalised residual plot revealed that 66% and 95% of the data points were within $\pm\sigma$ and $\pm 2\sigma$, respectively, of zero. This is in agreement with the values 68% and 95% expected for a Gaussian distribution around a good fit, and any resdidual structure need not necessarily be significant for the number of data points used.

7.5 The magnetic structure

In all, when putting forward a particular model for the arrangement of the moments in $TbMnO_3$, we have to consider not only the statistical methods deployed above, which necessarily possess a degree of ambiguity, but also the extent to which it is consistent with other information. It will now be demonstrated that the minority $f_{z(x^2-y^2)}$ model, in conjunction with the Ising-like

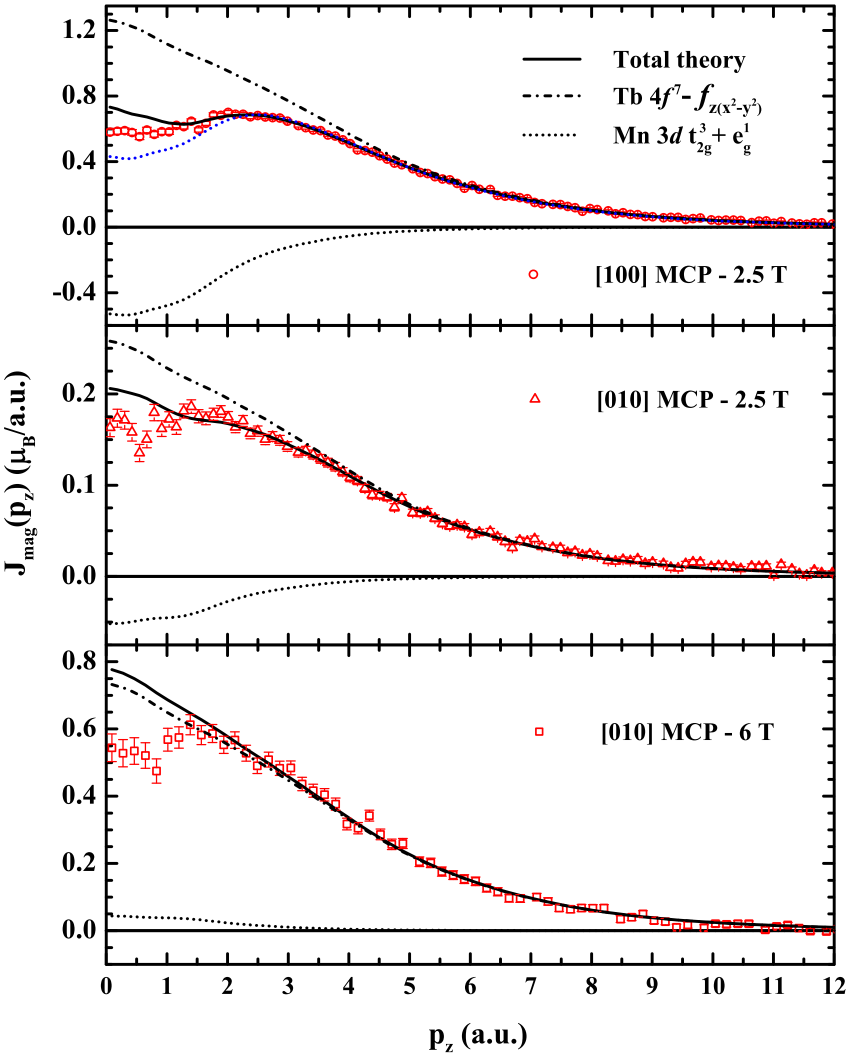

$4f^7$- $f_{z(x^2-y^2)}$ model preferred by fitting.

$4f^7$- $f_{z(x^2-y^2)}$ model preferred by fitting.

All Tb models provide similar quality of fit.

Figure 7.19: $TbMnO_3$ experimental MCPs and theoretical fits for the $\boldsymbol{a}$ and $\boldsymbol{b}$ directions. The total fit is shown as a solid black line, while the Tb and Mn components are shown as dash-dots and simple dots, respectively. The blue dotted line in the top panel represents the $\boldsymbol{a}$ direction fit from either the f_{x^3} or f_{y^3} models, the next-best according to reduced-χ^2 fitting.

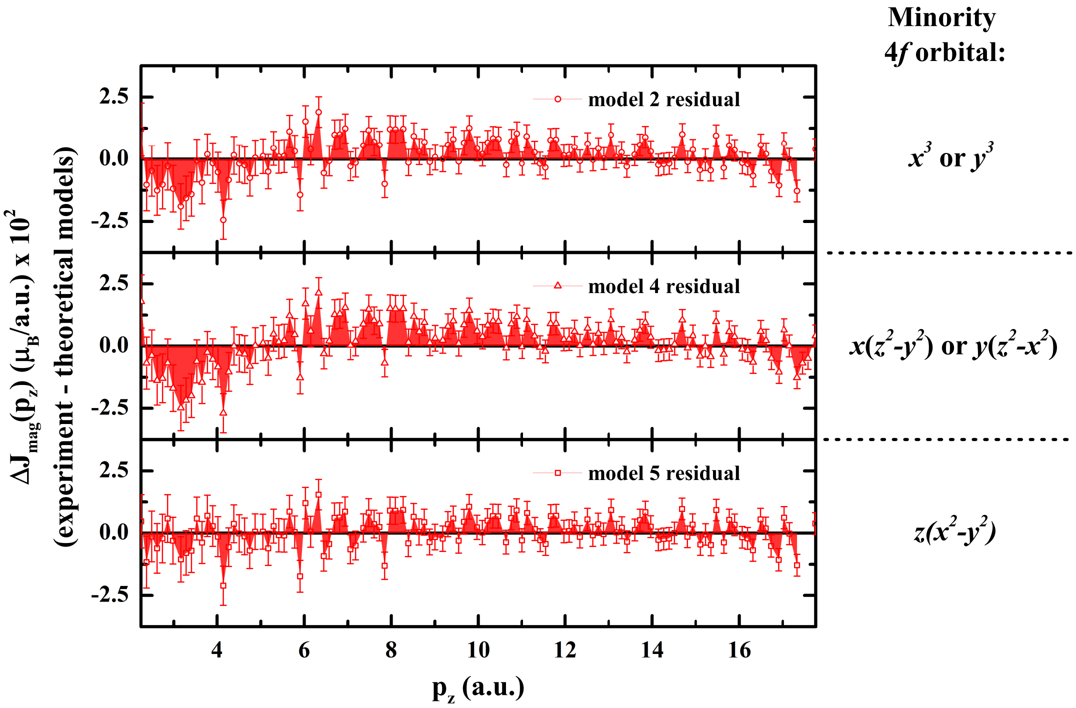

Figure 7.20: TbMnO$_3$ ***a***-direction MCP fit residuals for three minority orbital models; the f_{x^3} or f_{y^3} (next-best fit according to reduced-χ^2), the $f_{x(z^2-y^2)}$ or $f_{y(z^2-x^2)}$ (worst fit according to reduced-χ^2), and the $f_{z(x^2-y^2)}$ (best fit, and suggested by DFT results[143]).

configuration discussed previously, is best capable of describing the Tb moments in TbMnO$_3$. The Tb spin moments, as derived from the MCP fits, are given in table 7.4, as are the differences between the Tb spin and total measured spin. These are discussed shortly.

Orientation of the Tb spin moments

Using the Tb spin moments projected along the ***a*** and ***b*** directions, the magnitude of the Tb spin is found to be 5.77 ± 0.05 μ_B, by the simple application of the Pythagorean theorem. We can also deduce the angle, θ_{spin}, that the Tb spins make with the b-axis (refer to figures 7.8

Direction	Field (T)	Tb spin (μ_B/f.u.)	Total spin - Tb spin (μ_B/f.u.)
a	2.5	4.97 ± 0.05	-1.17 ± 0.08
b	2.5	1.03 ± 0.05	-0.14 ± 0.05
	6	2.94 ± 0.06	-0.20 ± 0.08

Table 7.4: Tb spin moments, and the difference between total spin and Tb spin, for the ***a*** and ***b*** directions at 1.45 K.

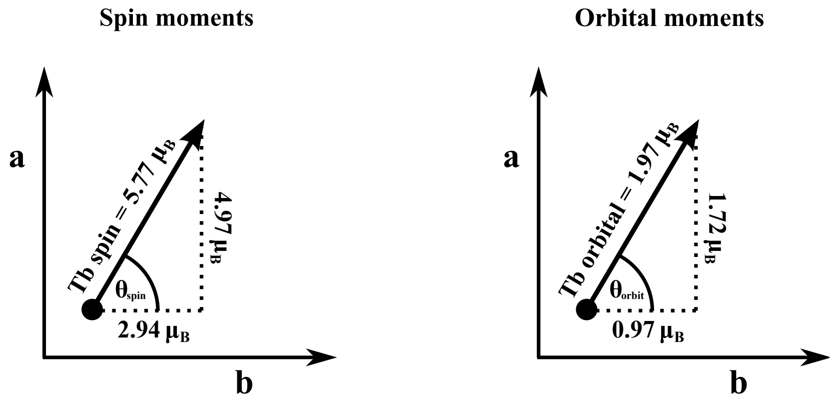

Figure 7.21: Tb moment direction as deduced from the derived spin and orbital contributions.

and 7.21). We have that

$$\theta_{\text{spin}} = \tan^{-1}\left(\frac{4.97 \pm 0.05\ \mu_{\text{B}}}{2.94 \pm 0.06\ \mu_{\text{B}}}\right) = 59.4\ \pm\ 0.8^{\circ}, \tag{7.3}$$

which is consistent with the $4f^{7\uparrow+1\downarrow}$ model because the Tb spins would be 6 μ_{B} $\sin(59.4^{\circ}) = 5.16$ μ_{B} and 6 μ_{B} $\cos(59.4^{\circ}) = 3.05$ μ_{B} along $\boldsymbol{a}$ and $\boldsymbol{b}$, respectively. These are close to the values determined by fitting; in fact, our values are ∼96% of the ideal values in both cases.

Orientation of the Tb orbital moments

Similarly, using the orbital moments from table 7.2, which are entirely attributed to Tb, gives a total Tb orbital moment of 1.97 ± 0.06 μ_{B}. θ_{orbit} is then given by,

$$\theta_{\text{orbit}} = \tan^{-1}\left(\frac{1.72 \pm 0.06\ \mu_{\text{B}}}{0.97 \pm 0.05\ \mu_{\text{B}}}\right) = 61\ {}^{+\,1}_{-\,2}{}^{\circ}, \tag{7.4}$$

which again is consistent with the Ising-like model discussed previously and the population of the $4f_{z(x^2-y^2)}$ minority state. This atomic orbital has the magnetic quantum number $m_l = 2$. Therefore, orbital moment contributions in the $\boldsymbol{a}$ and $\boldsymbol{b}$ directions should be 2 μ_{B} $\sin(61^{\circ}) = 1.75$ μ_{B} and 2 μ_{B} $\cos(61^{\circ}) = 0.97$ μ_{B}, which are in good agreement with our measured orbital moments. The angles θ_{spin} and θ_{orbit} agree within error.

The Mn and oxygen spin moments

Attention is now paid to the Mn/oxygen spin moments. The values may be taken directly from fitting, from the sizes of the MnO_6 contributions to the MCPs, or perhaps more meaningfully from the last column of table 7.4. The latter values are those remaining after assigning some of the total spin to Tb through fitting, and are more appropriate since they also include spin from the low momentum regions of the MCPs, around 0 to 1 a.u., that the total fits were unable to describe well.

Mn spin moment in the $\boldsymbol{a}$ direction

In the $\boldsymbol{a}$ direction the remaining spin is -1.17 ± 0.08 μ_B/f.u., antiparallel to the Tb moments and the applied field. Antiparallel TM/rare-earth moments have been seen experimentally in $SmMn_2Ge_2$[50] (in which the moments were determined with magnetic Compton scattering), $DyFe_2$[172], RCrSb$_3$[173] and a range of perovskites; $Gd_{0.67}Ca_{0.33}MnO_3$[174], $Nd_2CoMnO_{6+\delta}$[175], RTiO$_3$[176] and $SmMnO_3$[177].

The ground state cycloidal ordering of the Mn moments, which ought to produce no net spin moment, may have been disrupted by the ordering of the Tb moments in the applied field. This might be evidence for Feyerherm *et al.*'s suggestion, mentioned previously, that the rare-earth moments in these systems play a role in stabilising the Mn cycloidal ordering[158]. Additional relevant evidence comes from the work of Kimura *et al.*, who saw a drop-off in the spontaneous electric polarisation when the applied magnetic field in the $\boldsymbol{a}$ direction passed through $\sim$ 1.5 to 2 T, the field required to align the Tb moments[134,148]. We are left with the following possible model: when the Tb moments are reconfigured from their zero field orientation, the Mn ordering is destabilised, leading to a net negative spin moment and a reduction in the polarisation which, as has been established, is intimately linked to the cycloidal order. The fact that the observed Mn moment is just -1.17 ± 0.08 μ_B/f.u., compared to the 4 μ_B/f.u. that is theoretically possible for a Mn^{3+} ion, might mean that the antiferromagnetic ordering is still relatively intact; the Mn spins may only be canted from their cycloidally ordered directions. Again, this seems consistent with Kimura *et al.*'s observation that the electric polarisation was diminished at 2.5 T, but far from fully destroyed.

Mn spin moment in the $\boldsymbol{b}$ direction

In the $\boldsymbol{b}$ direction, at 2.5 T there exists a moment of -0.14 ± 0.05 μ_B/f.u. attributable primarily to Mn. At 6 T this value is -0.20 ± 0.08 μ_B/f.u., but the Mn contribution used in the MCP fitting was negligible. The bottom cell of figure 7.19 shows that only a very narrow MCP (HWHM $\sim$ 1 a.u.) is required to describe the non-Tb spin. This may be due to the inadequacy of LCAO methods in describing the most itinerant spin contributions, but other possibilities include the presence of O $2p$-, Mn $4sp$-, and Tb $5d$- and $6sp$-like magnetic bands. The same argument might explain the low momentum deviation between theory and experiment that was seen for the $\boldsymbol{a}$ direction. For good low momentum agreement these itinerant spin contributions would need to be antiparallel to the Tb spins for both $\boldsymbol{a}$ *and* $\boldsymbol{b}$ direction MCPs. It is acknowledged however, that with the LCAO method and fitting procedure used here, it would be unwise to place too much significance on this result.

The important detail is that the Mn spin in the $\boldsymbol{b}$ direction is far smaller than that in $\boldsymbol{a}$; in fact, it is close to zero. Above the metamagnetic transition in the $\boldsymbol{b}$ direction the Mn cycloid persists, but is shifted into the $\boldsymbol{a}$-$\boldsymbol{b}$ plane rather than the $\boldsymbol{b}$-$\boldsymbol{c}$ plane. The magnitude of the electric polarisation for the high field configuration is about half of that at low field; this may be a reflection of the extent, or *completeness*, of the cycloidal ordering, but could equally be attributable to other effects, such as an altered $\boldsymbol{S}_i - \boldsymbol{S}_j$ coupling or DMI. It is therefore compatible with other data that in the $\boldsymbol{b}$ direction, irrespective of the Tb arrangement at high field, no Mn moment would be present.

7.6 Conclusions

$TbMnO_3$ has been investigated with magnetic Compton scattering, and information about the Tb $4f$ orbital occupation and general magnetic structure has been deduced and discussed. The spin moments, orbital moments, and site-specific MCP contributions from fitting are consistent with the pre-existing theoretical descriptions of the system and experimental data. Additionally, in obtaining species- and orbital-specific MCPs for fitting to experimental data, the usefulness of the GAMESS LCAO method for future magnetic Compton scattering studies has been well demonstrated.

The Tb $4f^{7\uparrow+1\downarrow}$ spin configuration

Fitting to the $\boldsymbol{a}$ direction MCP provided strong evidence for the description of the Tb ion with a $4f^{7\uparrow+1\downarrow}$ Hund's rule spin configuration. The doubly occupied $4f$ orbital was found to be the $f_{z(x^2-y^2)}$ through analysis of reduced-χ^2 values and consideration of the F distribution, a mathematical tool used to quantify the quality of competing models. This agrees with DFT results from Xiang *et al.*[143]. The same model was also indicated in fitting to the low field $\boldsymbol{b}$ direction MCP. The $f_{z(x^2-y^2)}$ model was capable of describing the high field $\boldsymbol{b}$ direction data well, but it was not explicitly determined from fitting.

Ising-like model for the Tb moments

It was shown that the Ising-like model, originally suggested for $TbMnO_3$ almost 40 years ago and illustrated in figure 7.8, was capable of describing the total Tb spin and orbital moments with a good level of accuracy when the spin configuration was $4f^{7\uparrow+1\downarrow}$ with the minority $f_{z(x^2-y^2)}$ orbital. The maximum spin and orbital moments per Tb ion allowed with this arrangement are 6 μ_B and 2 μ_B, respectively, while the deduced experimental moments were 5.77 ± 0.05 μ_B and 1.97 ± 0.06 μ_B. Furthermore, the angle that the Tb moments make with the b-axis was found to be either $59.4 \pm 0.8^\circ$ or $61\,^{+1}_{-2}{}^\circ$, depending on whether the spin or the orbital moments were considered. These are slightly larger than the value of 57° put forward by Quezel *et al.*[164], but are believed to be more reliable because Quezel *et al.* looked only at the *total* moments and did not attribute any fraction to Mn.

Additional supporting evidence for the Ising-like model comes from the relative sizes of the orbital moments in the $\boldsymbol{b}$ direction at 2.5 and 6 T; these were 0.47 ± 0.01 μ_B/f.u. and 0.97 ± 0.05 μ_B/f.u., respectively. That the low field value is around half of that seen at high field is in agreement with the theory that effectively half of the Tb moments are aligned with the external field below a critical field of ~4.5 T.

Mn spin moments

Regarding the Mn magnetism, it was seen that a significant negative Mn moment accompanied the Tb spins in the $\boldsymbol{a}$ direction. In the $\boldsymbol{b}$ direction, a relatively small Mn moment was found, with large associated errors. This is seen as being consistent with the work of Kimura *et al.*[134,148]. With an applied field along $\boldsymbol{a}$, the Mn cycloidal ordering is destabilised, resulting in a reduced electric polarisation and a non-zero spin moment. This complies with Feyerherm *et al.*'s conclusion that the rare-earth moments play a role in stabilising the Mn cycloidal ordering[158]. With the field along ***b***, the Mn cycloid is known to shift from the ***b***-***c*** plane to the ***a***-***b*** plane[151,152], with the magnitude of electric polarisation being reduced above this transition. No Mn moment was seen here at 6 T, so the destabilised cycloid argument seems not to apply, but since the Mn ordering mechanism in the ***b*** direction is clearly very different from the ***a*** direction, the reduced polarisation could easily have another, more complex cause - possibly relating to the coupling of Mn spins and/or the Dzyaloshinskii-Moriya interaction.

Future work

In considering future work, one suggestion is that the ***b*** direction MCPs are remeasured as a function of applied field. A more complete study, which also looked at the ***a*** direction with the same applied fields, might be useful in tracking the development of the Tb and Mn moments from their ground state arrangements. Performing a magnetic Compton scattering experiment along the ***c*** direction could determine whether the Tb $4f$ moments are entirely constrained within the ***a***-***b*** plane, as described by the Ising-like model. The ***c*** direction measurements would also examine the behaviour of the $3d$ moments and determine if there exists an out-of-plane component, as in the model originally put forward for $TbFeO_3$ by Bidaux *et al.*[161] and resubmitted by Kimura *et al.*[148].

A more adventurous study, one that would require considerable planning and modification of the experimental arrangements currently used to collect MCPs at SPring-8 and the ESRF, would exploit the multiferroic property of $TbMnO_3$ by using an applied electric field to modify the magnetisation. MCPs could be collected as a function of applied electric field along different crystallographic directions. The key issue would be determining whether this method of controlling the magnetisation, as opposed to applying a magnetic field, affected solely the $3d$ moments of the Mn ions, or the spin density of the whole system. The control of $TbMnO_3$'s magnetisation with an electric field has attracted far less attention than the vice versa situation, but has potentially greater implications, for example in technologies such as magnetoelectric random access memory (MERAM)[178].

Efforts should also be made to obtain theoretical $TbMnO_3$ MCPs from a DFT calculation. The SPR-KKR package is incapable of dealing with $TbMnO_3$ because the $4f$ states of Tb require an on-site Coulomb repulsion term, U, in order to be split appropriately in energy. Therefore, future theoretical work will be conducted with the ELK full-potential linearised augmented-plane wave (FP-LAPW) code[179], which has the capability of adding U terms and is currently the subject of work by the Compton scattering group at Bristol that will enable it to calculate MCPs.

In a final suggestion for future experimental work, time could be usefully spent examining the relationship between rare-earth $4f$ MCP shape and the applied field, though a system free of all other spin contributions might prove a better test-bed than $TbMnO_3$. The experiment would look for shape differences that result from the rotation of the $4f$ charge density to align with the magnetisation direction[180]. This effect, unique to the well-localised $4f$ electrons which are relatively unaffected by the crystal field, has not been considered previously by the magnetic Compton scattering group, even though studies of several rare-earth systems have been performed. The MCP shape change might be insignificant, or considerable, and therefore should be investigated in future studies.

Chapter 8

The spin density of $EuFe_{2-x}Co_xAs_2$

This chapter details an investigation, using SQuID magnetometry and magnetic Compton scattering, into the much-studied ferromagnetic superconductor $EuFe_{2-x}Co_xAs_2$. This system is part of a large family of FeAs-layered superconductors in which significant superconducting temperatures have been achieved. It is also related to the layered cuprate systems, which exhibit the highest superconducting temperatures observed to date.

In this work magnetic Compton scattering was used in a similar approach as detailed for $TbMnO_3$, as an atomic orbital-specific probe of the magnetism. Comparison and fitting of experimental MCPs with theoretical Hartree-Fock and relativistic Dirac-Hartree-Fock Compton profiles provides information about the origin of the spin moment in this system. The key issues being addressed are these; is the magnetic moment due entirely to the Eu ion, as most work has suggested, or are the transition metal ions also magnetic? If only the Eu is magnetic, which atomic orbitals are actually responsible for the magnetism? The $4f$ electrons provide most of the moment for most of the lanthanide series, but contributions from other orbital types are known to exist, with the $5d$ magnetism in pure Gd being one example[165].

8.1 Introduction

The general incompatibility of superconductivity and magnetic order is well established; materials which exhibit both phenomena, concurrently or otherwise, are of great interest in the condensed matter community. Among these materials, the FeAs-layered systems with formula $X Fe_2As_2$ (X = Ba, Sr, K, etc.) have been studied in some detail recently[181–189]. Superconducting critical temperatures, T_{SC}, of 38 K have been reported for optimally doped variants of these group 1- and 2-based compounds. X may also be a rare-earth ion, with one of the most commonly used being Eu.

Previous work

$EuFe_{2-x}Co_xAs_2$ displays superconductivity, as well as reentrant resistivity, at optimal levels of Co doping (x between 0.22 and 0.37)[190–192]. Most significantly, $EuFe_{2-x}Co_xAs_2$ exhibits the coexistence of superconducting and ferromagnetic states[191]. A lot of the experimental and theoretical work regarding these Eu-based systems has examined the superconductivity as a function of temperature, applied field and pressure. In addition, their magnetic structure has been studied with a range of techniques, including neutron diffraction, resonant X-ray scattering and conventional SQuID magnetometry[193–196]. The general result is that all of the moment observed in an applied field is due to the Eu, with no evidence for magnetic contributions from the Fe, which has robust antiferromagnetic ordering. However, there is at least one piece of evidence suggesting the existence of a Fe moment in the Eu-Fe-pnictide systems. It comes from a magnetic Compton scattering study by Ahmed *et al.*[197] of the compound $EuFe_2As_{1.46}P_{0.54}$, and is discussed in more detail shortly.

Interest in FeAs-layered systems

Major interest in transition metal-pnictide superconductors began when, in 2006 and 2007, T_{SC} of 3.5 K and 4.5 K were reported for the systems LaFePO and LaNiPO, respectively[198,199]. It was soon realised that much higher T_{SC} could be achieved by doping the various sites. In 2008, a T_{SC} of 26 K was reported in the F-doped compound $LaFeAsO_{1-x}F_x$ and by the end of that year, in which a great deal of FeAs research was published, the highest T_{SC} for a FeAs system so far was given as 56 K in $Gd_{1-x}Th_xFeAsO$[200]. Since then, a large number of TM-pnictide systems have been studied, often with a strong emphasis on the relationship between their superconductivity and magnetic order.

The ternary and quaternary compounds mentioned above are closely related. They share similar physical and electronic properties, owing to the presence in both of separated nearly two-dimensional TM-pnictide layers. Several good reviews for a large range of these systems can be found in the work of Stewart[201], Paglione and Greene[202], and Izyumov and

Kurmaev[203], including descriptions of their electronic structures and summaries of superconducting temperatures observed to date. With respect to the nature of the superconducting pairing mechanism in the FeAs systems, which, as discussed in section 2.6, provides much of the motivation for their continued study, Maitai *et al.* and Hirschfeld *et al.* provide reviews which encompass current theories and experimental results[27,28]. Some of the key points are these:

- Like the much-studied cuprate superconducting systems with CuO_2 layers, the electronic structure of FeAs systems is quasi-two-dimensional - the electronic properties are determined almost solely by the FeAs sheets.
- Unlike the cuprates, superconductivity tends to be *induced* by the partial substitution of atoms from the active layer, rather than destroyed, e.g. by the substitution of Fe atoms with Co atoms, or As atoms with P atoms.
- The Fermi surfaces (FS) of various FeAs systems are very similar. They comprise nested cylindrical sheets at the Γ (center) and $\mathbf{M}$ (corner) points of the Brillouin zone; these are the hole and electron pockets, respectively. Chemical doping has the effect of changing the sizes of these FS features.
- As mentioned briefly in section 2.6, there exists evidence for both *s*- and *d*-wave superconducting gap symmetry in the FeAs systems. Indeed, Paglione and Greene conclude their review with, "a generic representative OP [order parameter] symmetry will involve a sign-changing structure with one fairly isotropic gap and another gap with at least deep minima," and, "the presence of anisotropic and multiband scattering, and strong *c*-axis dispersion of at least parts of the FS structure, will make it difficult to conclude on any particular universal gap structure."

8.2 Structural, electronic and magnetic properties.

Types of FeAs systems

In terms of chemical stoichiometry, the FeAs systems can be arranged into four main categories; they are the 1111, 122, 111 and 11 types. 1111 refers to compounds of RFeAsO, where R is a rare-earth element, usually La. 122 systems have formula XFe_2As_2, where X may again be a

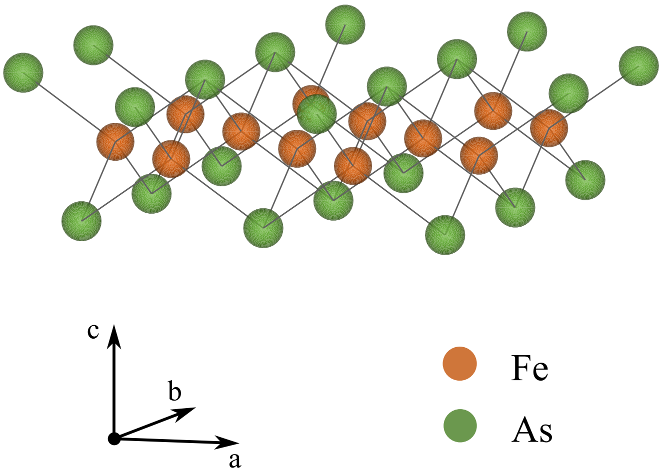

Figure 8.1: A tetragonally coordinated $FeAs_4$ layer, common to all of the FeAs systems.

rare-earth, or a group 1 or 2 element. 111 systems share the formula XFeAs, where X is a group 1 element - to date most experimental work has focussed on the X = Li compound, but theoretical work has shown that other compounds are also stable[204]. Finally, the 11 system is, as expected, the simple binary compound. Other binary compounds, such as FeS, FeSe and FeTe, are also of great interest; they share the structure of FeAs and are usually considered in the same framework as the other systems listed above. Naturally, for each of these FeAs system types, there is great scope for altering the structural, electronic and magnetic properties by doping the various sites with heterovalent or isovalent atoms, resulting in electron/hole doping and chemical pressure, respectively.

Crystal structure

As in the superconducting cuprates, FeAs-based systems possess a layered structure. The FeAs layers are almost entirely responsible for the superconductivity. Figure 8.1 illustrates the FeAs sheets common to all of the systems, while figure 8.2 displays the crystal structure of $EuFe_2As_2$ specifically. The main structural feature that differs between the systems is the composition of the 'blocking layer' separating the sheets, though the atomic spacings and bond angles between the Fe and As ions also varies.

The room temperature crystal structure of $EuFe_2As_2$ is tetragonal, as shown in figure 8.2(a). The space group is $I4/mmm$, often referred to as as $ThCr_2Si_2$-type. The lattice parameters

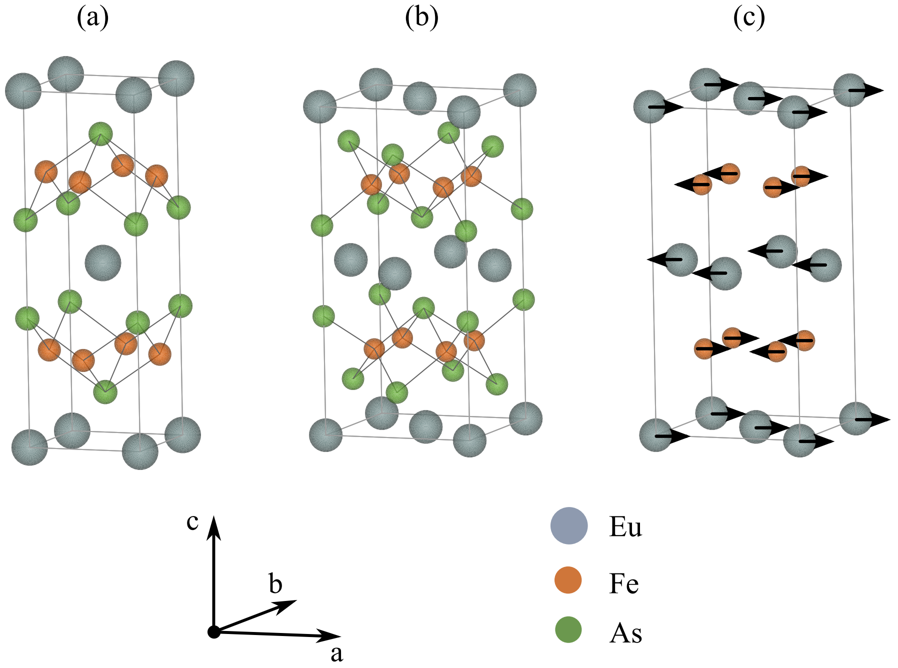

Figure 8.2: The $I4/mmm$ (a) and $Fmmm$ (b) crystal structures of $EuFe_2As_2$. Eu, Fe, and As atoms are represented by grey, red and green spheres, respectively. (c) shows the ground state spin structure. Note that these representations are not the crystallographic unit cell, but serve as a better illustration of the Fe-As coordination and magnetic alignment.

in this phase are $a = b = 3.9062$ Å and $c = 12.1247$ Å, according to powder X-ray diffraction by Tegel *et al.*[205]. The orthorhombic space group, $Fmmm$, has been shown to exist below a temperature, $T_{\text{SDW}}^{\text{Fe}}$, also associated with a spin-density wave (SDW) transition. This low temperature crystal structure is shown in 8.2(b) and has lattice parameters $a = 5.5546$ Å, $b = 5.4983$ Å and $c = 12.0590$ Å, again from the work of Tegel *et al.*

Fe magnetic order

Below $T_{\text{SDW}}^{\text{Fe}}$, which is ~ 189 K for $EuFe_2As_2$[205,206], there exists a three-dimensional antiferromagnetic ordering of the Fe moments (figure 8.2(c)), evidenced by numerous neutron diffraction measurements[206–211]. This ordering is thought to remain intact even in very high fields. MvH measurements up to 55 T performed by Tokunaga *et al.* revealed no sign of ferromagnetic Fe ordering[212], though the authors admitted that the small change in susceptibility predicted for T_{N}^{Fe} might be difficult to detect with their pulsed-field method. Their results are compatible with theoretical work from McQueeney *et al.*[213] and Han *et al.*[214], who found very strong antiferromagnetic coupling, of the order 40 meV, between Fe moments in several FeAs systems. From MvT measurements, Tokunaga *et al.* suggested that

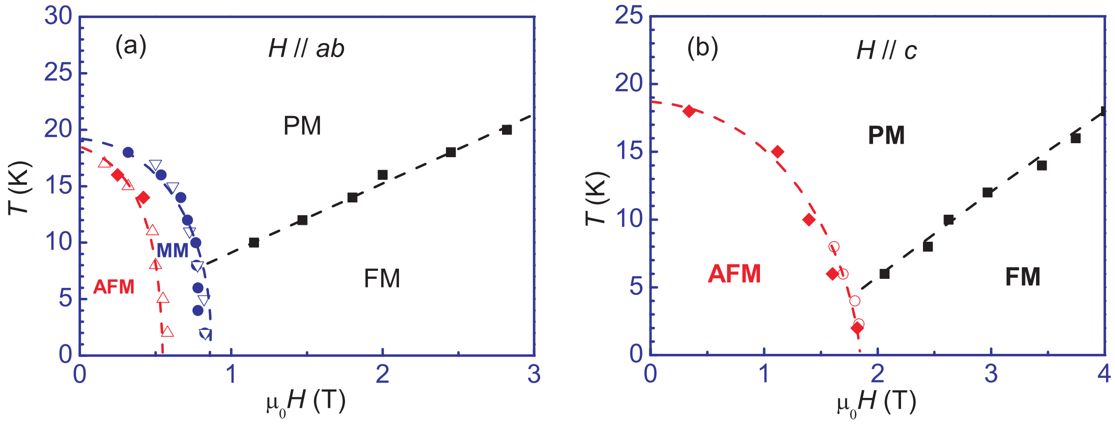

Figure 8.3: $EuFe_2As_2$ *ab*-plane (left) and *c*-axis (right) magnetic phase diagrams. The open and filled symbols are from *M(H)* and *R(H)* measurements, respectively. The dashed lines are guides to the eyes. AFM, PM, FM and MM refer to antiferromagnetic, paramagnetic ferromagnetic and metamagnetic phases, respectively. Reproduced from the work of Jiang *et al.*[191].

a field of 500 T may be required to suppress the Fe antiferromagnetic state at low temperatures.

Eu magnetic order

Evidence from neutron diffraction[194,206] and resonant X-ray scattering[193] show that the Eu moments are aligned parallel with the *a*-axis in an *A*-type antiferromagnetic phase below a temperature of $T_N^{Eu} = 19$ K (figure 8.2(c)). Xiao *et al.* showed that the ground state Eu alignment changed to ferromagnetic above a critical field, which depended on the crystallographic direction[194]. At 2 K a field of 1.8 T was required to obtain FM ordering in the *c*-axis, while in the *a*-axis, it was closer to 0.8 T. These critical fields were in good agreement with previous findings[191,195] and support the model of *a*-axis alignment for the Eu moments. Xiao *et al.* estimated values of 6.9(4) μ_B and 6.7(4) μ_B for the Eu^{2+} moments aligned along the *c*- and *a*-axis, respectively. They also examined the Fe magnetism and concluded that the SDW order is robust, persisting in fields up to at least 3 T.

Figures 8.3 and 8.4 are the most relevant phase diagrams from Jiang *et al.*[191,215] regarding the $EuFe_{2-x}Co_xAs_2$ system. They illustrate the magnetic behaviour of the undoped compound, as well as the electronic and magnetic properties of the $x = 0.22$ compound, for fields in the *ab*-plane and *c*-axis. The relevant information for the $x = 0.3$ compound, as investigated in this chapter, was unavailable, as was a phase diagram as a function of the Co doping level.

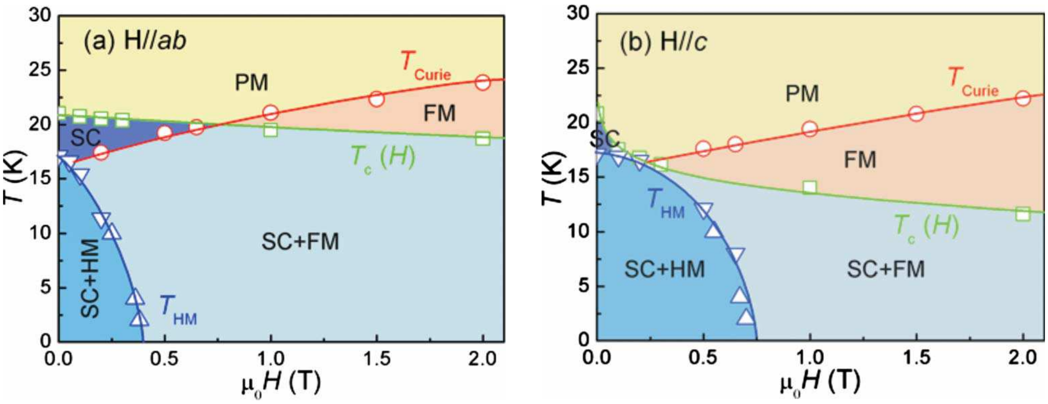

Figure 8.4: $EuFe_{1.78}Co_{0.22}As_2$ electronic phase diagram for magnetic fields applied in the *ab*-plane and along the *c*-axis. SC, HM, FM and PM refer to superconducting, heliomagnetic, ferromagnetic and paramagnetic phases.Reproduced from the work of Jiang *et al.*[215].

Electronic structure

Looking at the structure of the FeAs systems, we see that each Fe is tetrahedrally surrounded by four As ions. This leads to a large hybridisation between Fe $3d$ and As $4p$ orbitals. It has been shown in several first principles calculations that the DoS for the FeAs systems is fairly uncomplicated; nearly pure Fe $3d$ states dominate the region from -2 to 2 eV, with hybridised dp bands found around -3 eV[216–218]. Figure 8.5 shows a DoS for $BaFe_2As_2$, closely related to $EuFe_2As_2$, calculated with the SPR-KKR DFT package. The calculation employed the LSDA exchange-correlation functional of Vosko, Wilk and Nusair[65] and used $\sim$ 1200 k-points to sample the Brillouin zone. As in the work on NiMnSb, Lloyd's formula[115] was used for an improved determination of the Fermi level. The general features in figure 8.5 are in good agreement with the results of Singh[217] and Krellner *et al.*[218].

Jeevan *et al.*[219] and Li *et al.*[216] performed calculations on $EuFe_2As_2$ using the LSDA+U and GGA+U methods, respectively. The U term is an on-site Coulomb repulsion, required to split the Eu $4f$ orbitals into physically reasonable occupied and unoccupied complexes; the standard value of U for a Eu^{2+} ion is 8 eV. Both groups of authors found a localised, half-filled Eu $4f$ band at around -2.5 eV, but otherwise, the Fe-As parts of their DoS were unchanged from those of $SrFe_2As_2$ and $BaFe_2As_2$. The functionality of adding a U term is not present in the SPR-KKR code, so obtaining a realistic DoS for $EuFe_2As_2$ in this work was

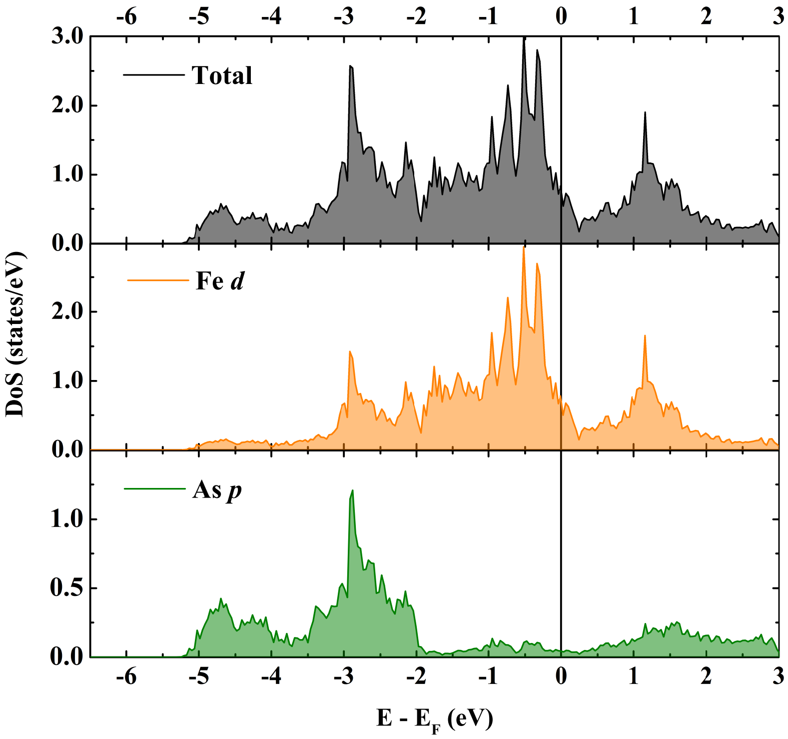

Figure 8.5: $BaFe_2As_2$ density-of-states from a SPR-KKR calculation. (Top) Total, (middle) Fe *d* and (bottom) As *p* contributions.

not possible. Calculations without a U term resulted in the placement of the Eu $4f$ orbitals around 18 eV above the Fermi energy, which is physically unrealistic.

Fe moment observed in $EuFe_2As_{1.46}P_{0.54}$

A recent study that requires special attention and discussion is that of Ahmed *et al.*[197], which was mentioned in the introduction to this chapter. The authors used magnetic Compton scattering to investigate polycrystalline samples of $EuFe_2As_{1.46}P_{0.54}$ - a material exhibiting the onset of superconductivity at around 26 K and reentrant resistivity at 18 K. Magnetic Compton profiles were recorded on the BL08W beamline at SPring-8, at a range of temperature from 5 to 31 K and in applied fields of ±2.5 T. The resulting spin moments shared the magnitude and MvT shape of the total magnetisation for these Eu-based systems.

The authors fitted their magnetic Compton profiles with theoretical orbital-specific MCPs from SPR-KKR, using the CPA[76] to deal with the partial substitution on the As site. They attributed fractions of the total spin to Eu $4f$, Fe $3d$, As $4p$ and P $3p$ electrons. Over most

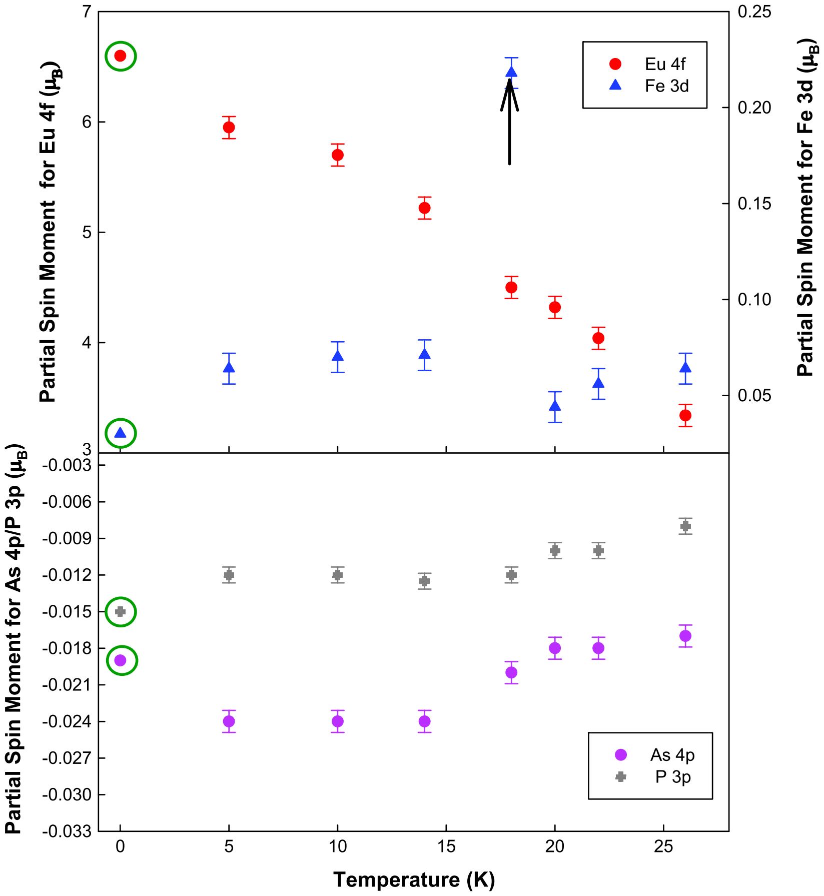

Figure 8.6: Spin moments in polycrystalline $EuFe_2As_{1.46}P_{0.54}$. The spin moments were attributed to Eu $4f$ (red circles), Fe $3d$ (blue triangles), As $4p$ (magenta circles) and P $3p$ (grey circles) electrons by fitting with orbital-specific MCPs from SPR-KKR. The black arrow indicates an increase in the Fe moment at 18 K. From the work of Ahmed *et al.*[197].

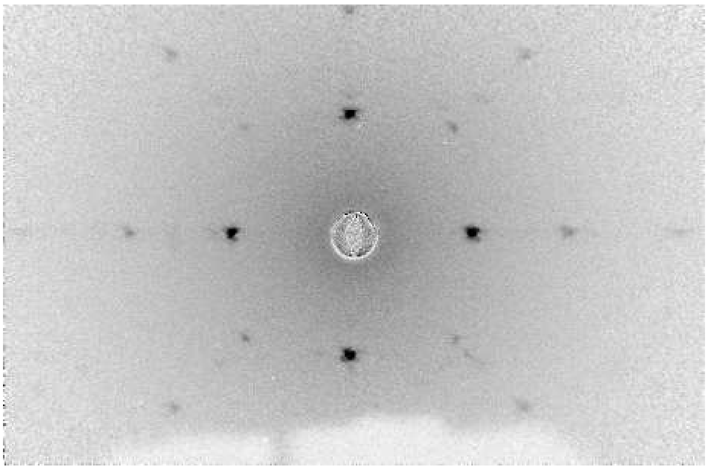

Figure 8.7: Back-reflection Laue image of $EuFe_2AS_2$ aligned along the c-axis.

of the temperature range, the Fe $3d$ spin moment was between 0.05 and 0.07 μ_B/f.u., but this increased significantly to ~ 0.22 μ_B/f.u. at 18 K, as shown in figure 8.6. Ahmed *et al.* suggested that the larger ferromagnetic Fe $3d$ response at 18 K was partly responsible for breaking down the superconductivity at the same temperature, giving rise to the reentrant resistivity seen in the transport measurements. Interestingly, the authors were able to obtain theoretical MCPs that appear consistent with LSDA/GGA + U theory, despite the lack of U terms in SPR-KKR. The Compton group at Warwick, in consultation with SPR-KKR co-creators Hubert Ebert and Jan Minar, were unable to replicate the calculations put forward by Ahmed *et al.*, and attempts to contact the authors to discuss their theoretical methods elicited no response. It is worth noting that Jeevan *et al.* believed Ahmed *et al.*'s finding, that superconductivity and Fe ferromagnetism coexist in $EuFe_2As_{1.46}P_{0.54}$, to be related to, "inhomogeneous phosphorus doping concentration in [their] polycrystalline samples[220]."

8.3 Magnetometry

The single crystal samples

Single crystal samples of $EuFe_{2-x}Co_xAs_2$, with $x = 0$ and 0.3, were produced and provided by Zbigniew Bukowski of the Laboratory for Solid State Physics, ETH Zürich, Switzerland. Transport measurements performed by Bukowski showed the expected resistivity features at 189 K and 19 K for the undoped compound. These are $T_{\rm SDW}^{\rm Fe}$ (structural transition and Fe moment ordering) and $T_{\rm N}^{\rm Eu}$ (Eu moment ordering), respectively. There was no indication of a

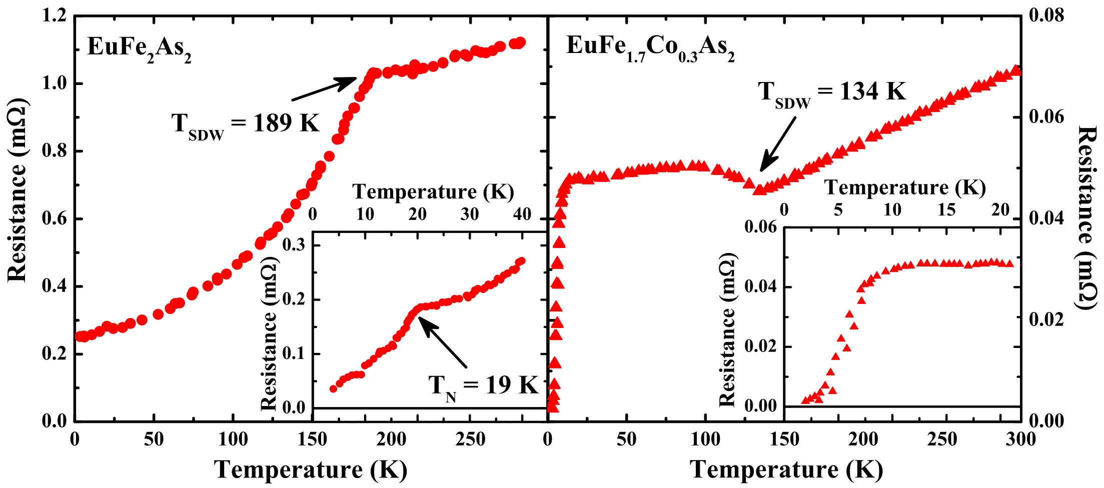

Figure 8.8: EuFe$_2$AS$_2$ (left) and EuFe$_{1.7}$Co$_{0.3}$AS$_2$ (right) resistance.

SC regime above 2 K for the undoped compound. With $x = 0.3$, $T_{\mathrm{SDW}}^{\mathrm{Fe}}$ was seen at 134 K, which is consistent with other resistivity data[221]. The resistivity at 2 K was vastly reduced, but non-zero, highlighting the development of superconductivity with optimal Co-doping. Again, this is consistent with other work[221]. At Warwick, the back-reflection Laue method confirmed that the samples were single crystals and allowed for their proper alignment for magnetometry and magnetic Compton scattering. A Laue image taken along the c-axis of the EuFe$_2$As$_2$ sample is provided in figure 8.7, and resistance data for both $x = 0$ and $x = 0.3$ samples are shown in figure 8.8. This resistance data, along with more from the EuFe$_{2-x}$Co$_x$As$_2$ doping range, appears in publication under the authorship of Błachowski, Bukowksi *et al.*[192].

MvH measurements

MvH SQuID magnetometry measurements were performed on the $x = 0$ and $x = 0.3$ samples to investigate their magnetic properties and provide total moments for comparison with the spins obtained from magnetic Compton scattering. Measurements were made along the c-axis and in the ab-plane in fields from -2.5 to 2.5 T and at temperatures of 2 and 7 K. Note that the 'ab-plane' designation used here, and throughout this chapter, refers to a direction approximately 45° between the low temperature orthorhombic a- and b-axes. This is because the Laue reflection measurements that confirmed the crystallographic directions took place at room temperature, where the tetragonal phase exists.

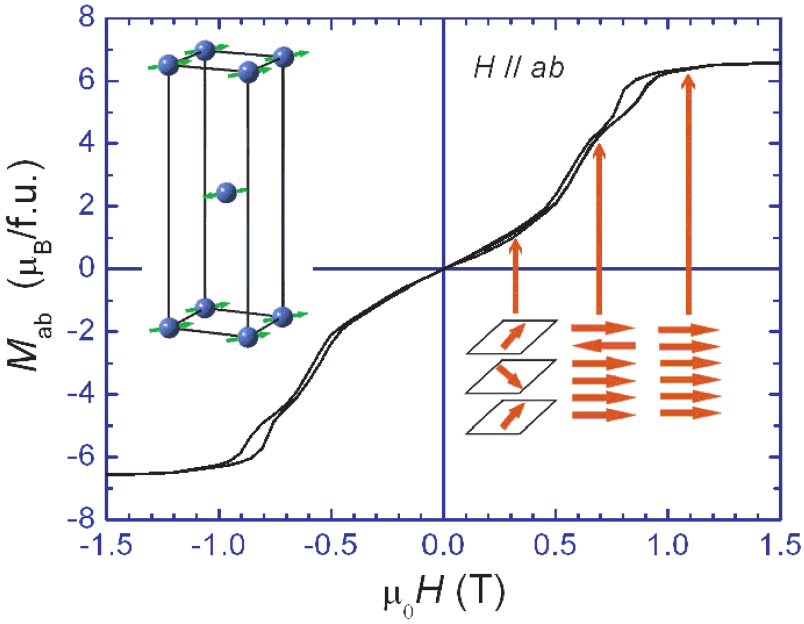

Figure 8.9: Orientation of Eu magnetic moments in $EuFe_2As_2$ *ab*-plane magnetisation, as proposed by Jiang *et al.*[191]. Reproduced from the work of those authors.

MvH analysis

The MvH data are shown in figures 8.10 to 8.13. M_{sat} values for the different samples and directions are given in table 8.1 at the end of this section. They were obtained, as in the NiMnSb work, by extrapolating the solely paramagnetic response in the region 2 to 2.5 T back to $H = 0$. The MvH shapes and saturating fields for the $EuFe_{2-x}Co_xAs_2$ samples are in good agreement with the work of Jiang *et al.*, who looked at the $x = 0$ and $x = 0.11$ systems[191,215], and of Guguchia *et al.*, who studied the $x = 0$ and 0.2 systems[196]. The features of the *ab*-plane magnetisation were described by Jiang *et al.* as being due to a combination of two hysteretic spin reorientations (below 0.45 T and between 0.7 and 1.0 T) and a metamagnetic transition (between 0.5 and 0.7 T), as illustrated in figure 8.9. The transition, they proposed, was related to the anti-alignment of one Eu^{2+} layer in every six with the applied field. The authors pointed to the case of $HoNi_2B_2C$ as an example of this kind of metamagnetic phase[222]. Jiang *et al.* and Xiao *et al.*[194] ascribed the linearity in the *c*-axis MvH shapes to the gradual canting of the Eu moments from the *ab*-plane to align with the applied field.

There is *some* disagreement between this work and others; Jiang *et al.*'s saturated moments

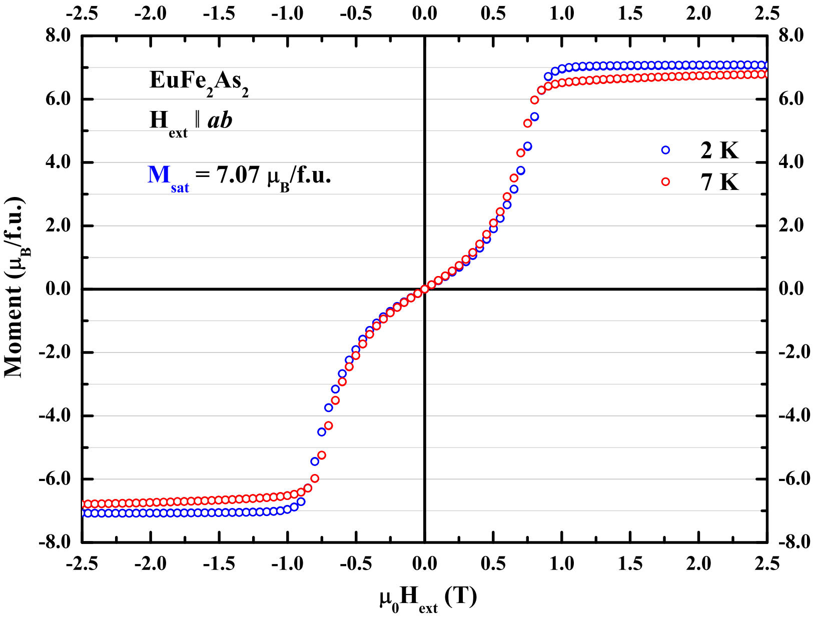

Figure 8.10: SQuID magnetometry of EuFe$_2$As$_2$ in the *ab*-plane at 2 K and 7 K.

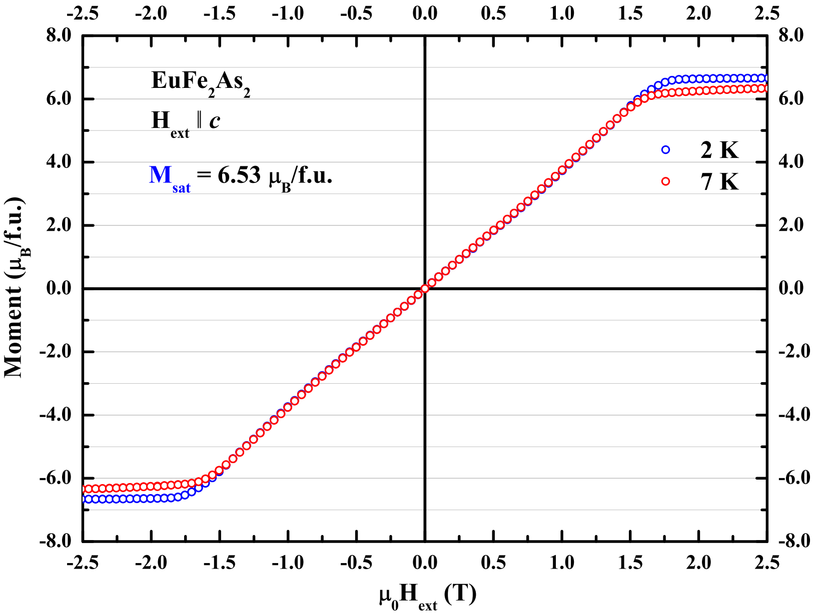

Figure 8.11: SQuID magnetometry of EuFe$_2$As$_2$ along the *c*-axis at 2 K and 7 K.

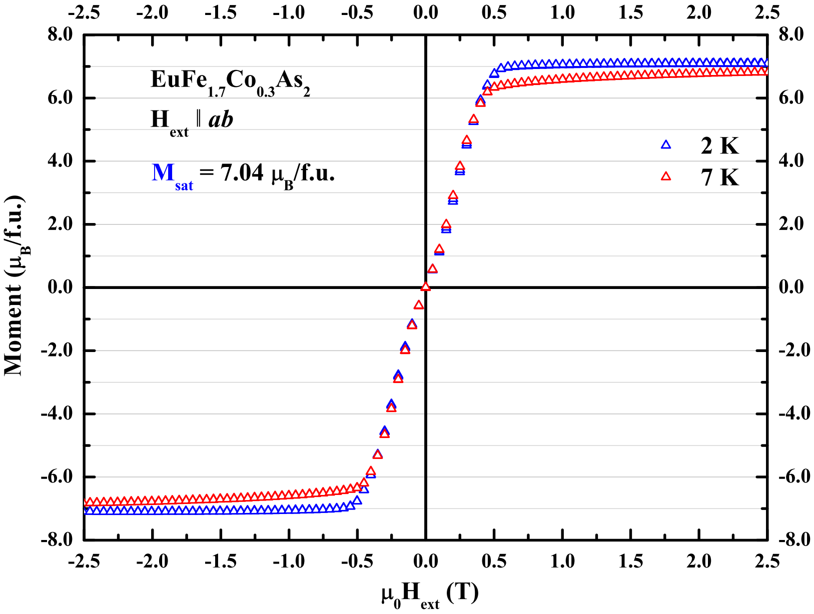

Figure 8.12: SQuID magnetometry of $EuFe_{1.7}Co_{0.3}As_2$ in the *ab*-plane at 2 K and 7 K.

for $EuFe_2AS_2$ were 6.6 and 7 μ_B/f.u. for the *ab*-plane and *c*-axis, respectively. Here, the values were found to be 7.07 and 6.53 μ_B/f.u., representing differences of around ±7%. However, work on the same compound carried out by Guguchia *et al.* put the *ab*-plane moment at 6.8 μ_B/f.u., and Ren *et al.* saw a moment of just 6 μ_B/f.u.[223], so discrepancies of this magnitude may not be significant, especially considering the general reproducibility of SQuID magnetometry measurements. It can be said that, since even the lowest value of 6.53 μ_B is still 93% of the 7 μ_B expected for the Eu^{2+} ion, the M_{sat} values presented here are consistent with other work and theory.

MvT measurements

The MvT data for $EuFe_2As_2$ and $EuFe_{1.7}Co_{0.3}As_2$ are shown in figures 8.14 and 8.15. Three types of fitting were performed on these datasets to extract useful information. First, the data from 2 to 10 K (up to ∼ $T_C/3$) were fit with a T^n law, as given in equation 6.2 and used previously for NiMnSb. Second, following Guguchia *et al.*'s approach for the MvT response of $EuFe_2As_2$ and $EuFe_{1.8}Co_{0.2}As_2$, a power law of the form

$$M(T) = M_0 \left(1 - \frac{T}{T_C}\right)^{\widetilde{\beta}} \tag{8.1}$$

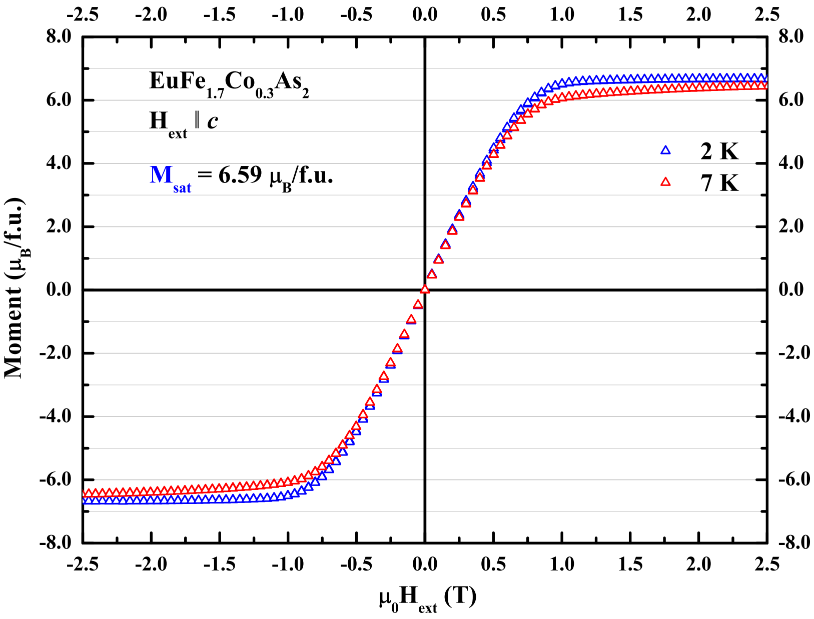

Figure 8.13: SQuID magnetometry of EuFe$_{1.7}$Co$_{0.3}$As$_2$ along the c-axis at 2 K and 7 K.

was applied from 2 to 25 K, where "$\widetilde{\beta}$ and M_0 are empirical constants[196]." This law is an empirical interpolation of the $T^{3/2}$ regime below T_C, and the $(T_C - T)^\beta$ regime near T_C, where β is the critical exponent[3]. Lastly, the Curie-Weiss law,

$$\chi^{-1}(T) = \frac{T - \theta_{CW}}{C}, \tag{8.2}$$

was used from 40 to 150 K, inside the accepted paramagnetic regime. All of the relevant parameters from these fits are given in table 8.1.

T^n fitting

The T^n law exponents range from 1.84 ± 0.01 to 2.05 ± 0.01. They deviate significantly from the value of 3/2, suggesting that the moments are not well described by Bloch's law. This might be considered unusual because the Eu^{2+} $4f$ moments, which provide all of (or possibly just *most* of) the magnetism in this system, are well-localised, and ought to adhere to Bloch's $T^{3/2}$ law for classical Heisenberg spins. The effective T exponents at zero field might be smaller than the values in table 8.1 if they follow the same field-dependence shown for NiMnSb and, in other work, for La$_{0.7}$Sr$_{0.3}$MnO$_3$[113]. With this in mind, it is important to note that the validity of this T^n fitting approach, and the resulting inferences about the localisation/itinerancy

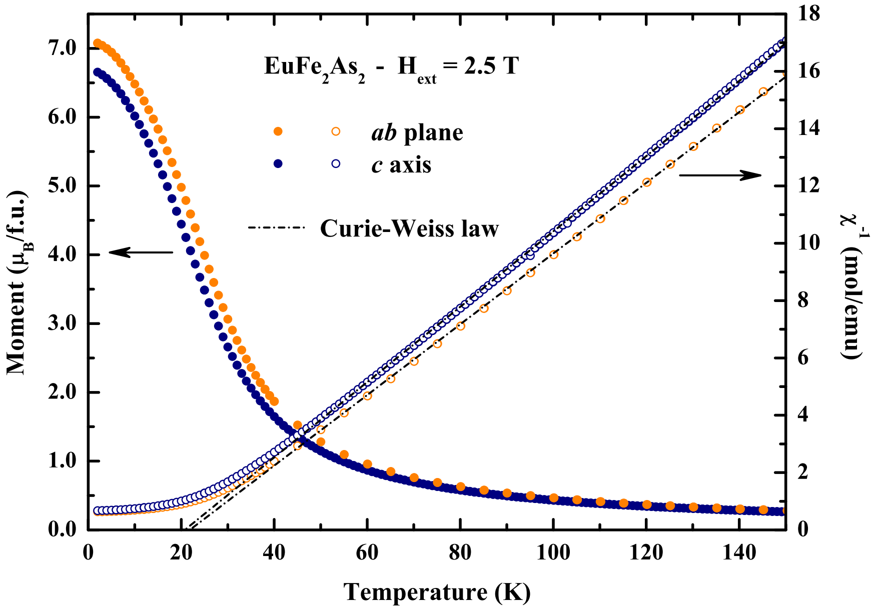

Figure 8.14: Temperature-dependent SQuID magnetometry of $EuFe_2As_2$ in the c-axis and ab-plane in a field of 2.5 T. Magnetisation and inverse susceptibility are shown as filled and open symbols, respectively. The dashed black line is a fitted Curie-Weiss law.

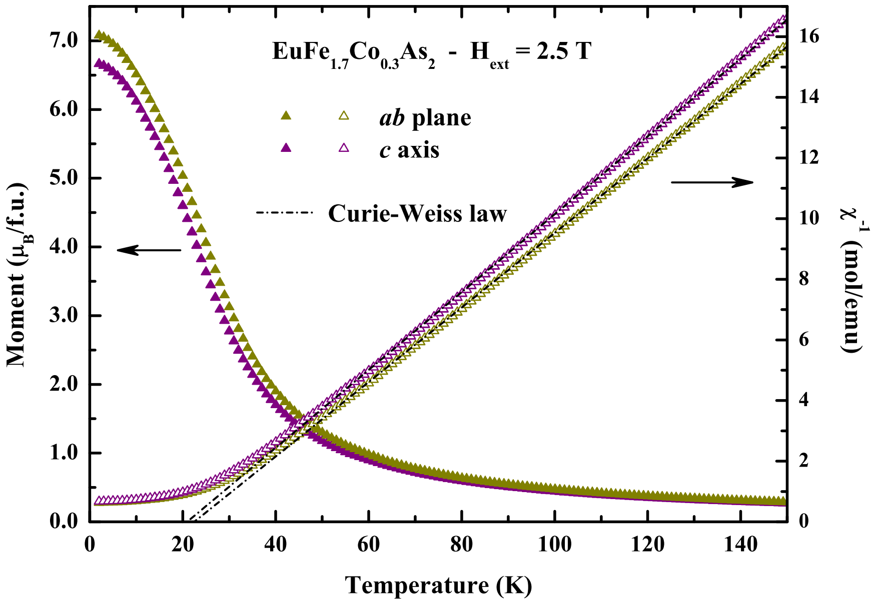

Figure 8.15: Temperature-dependent SQuID magnetometry of $EuFe_{1.7}Co_{0.3}As_2$ in the c-axis and ab-plane in a field of 2.5 T. Magnetisation and inverse susceptibility are shown as filled and open symbols, respectively. The dashed black line is a fitted Curie-Weiss law.

of the Eu moments, is uncertain. This is because, unlike NiMnSb where the ground state ferromagnetic alignment was simply *enhanced* by an applied field, in $\mathrm{EuFe_{2-x}Co_xAs_2}$ the zero field (antiferromagnetic) and high field (ferromagnetic) states are different. In particular, the low wavevector spin-wave dispersion relation, $E(\boldsymbol{q}) = D\boldsymbol{q}^2$, which results in Bloch's $T^{3/2}$ law for Heisenberg ferromagnets, is known to be replaced with a linear relationship of the form $E(\boldsymbol{q}) \propto \boldsymbol{q}$ for antiferromagnets[224]. A more extensive MvH investigation, with a range of applied fields above and below the metamagnetic transition, would explore this issue further.

Modified power law

Applying equation 8.1 from 2 to 25 K provided $\widetilde{\beta}$ values from 0.33 ± 0.01 to 0.39 ± 0.01 for both compounds and directions, with only the latter value not strictly agreeing with the others within error. They compare well to the value of 0.39 provided by Guguchia *et al.*, once again indicating good correspondence in the magnetic behaviour of our samples and those studied by others. It is important to state clearly that the $\widetilde{\beta}$ values determined here, and in the work of Guguchia *et al.*, are *not* explicitly the critical exponents of the $\mathrm{EuFe_{2-x}Co_xAs_2}$ magnetisation. Those values, denoted β, are usually determined by rigorously examining the magnetic susceptibility in the region very close to the Curie temperature ($\sim T_\mathrm{C} \pm 1$ K). However, critical exponents in this range have previously been associated with 3-D Ising or 3-D Heisenberg behaviour[225–229]; in either case deviating from the value of 0.5 predicted by mean field theory[3] and the value of 0.125 for 2-D Ising behaviour (i.e. moments constrained in a 2-D plane)[230]. The values for T_C from the same fitting procedure are in the region of 29.4 K, slightly larger than the 27.2 K provided by Guguchia *et al.* They reported a linear increase in T_C with the applied field; since their measurement was performed at 1.5 T, and the results here were obtained at 2.5 T, the discrepancy seems reasonable.

Curie-Weiss law

Fitting the Curie-Weiss law above 40 K confirmed the expected paramagnetic response. It also provided Curie constants, C, and Curie-Weiss temperatures, θ_CW. The positive values of θ_CW indicate that the interaction between Eu moments is ferromagnetic. The Curie constants were found to lie between 7.61 ± 0.01 and 8.14 ± 0.01 emu K/mol. The values of C and θ_CW are consistent with previous results[191,196,223].

		M_{sat} (μ_B)	T^n	$\widetilde{\beta}$	T_C	C	θ_CW
		(μ_B/f.u.)	(exponent)	(exponent)	(K)	(emu K/mol)	(K)
$\mathrm{EuFe_2As_2}$	$H \parallel \boldsymbol{ab}$	7.07	1.91 ± 0.02	0.34 ± 0.01	29.4 ± 0.4	8.11 ± 0.02	21.8 ± 0.2
	$H \parallel \boldsymbol{c}$	6.53	1.84 ± 0.01	0.39 ± 0.01	29.6 ± 0.4	7.61 ± 0.01	20.74 ± 0.08
$\mathrm{EuFe_{1.7}Co_{0.3}As_2}$	$H \parallel \boldsymbol{ab}$	7.04	1.99 ± 0.01	0.33 ± 0.01	29.4 ± 0.4	8.14 ± 0.01	22.48 ± 0.07
	$H \parallel \boldsymbol{c}$	6.59	2.05 ± 0.01	0.35 ± 0.01	29.0 ± 0.4	7.79 ± 0.01	20.97 ± 0.08

Table 8.1: $\mathrm{EuFe_{2-x}Co_xAs_2}$ magnetometry fitted parameters. M_{sat} was determined by extrapolating the saturated 2 K MvH data down to 0 T. The T^n exponent came from fitting Bloch's law to MvT data between 2 and 10 K. β and T_C come from fitting an adapted power law (equation 8.1) up to 25 K, and the other parameters were obtained by applying the Curie-Weiss law to magnetometry above 40 K. The values from MvH fitting are only strictly valid for the field of 2.5 T in which the measurements were performed. Refer to the text for more information.

Temperature (K)	Spin moment (μ_B/f.u.) $x = 0$ c-axis	 $x = 0.3$ c-axis	 $x = 0.3$ ab-plane
7	6.66 ± 0.06	6.61 ± 0.06	-
11	-	-	6.90 ± 0.06
13	-	5.48 ± 0.05	-
17	-	4.95 ± 0.05	-
20	-	4.39 ± 0.05	5.10 ± 0.05
22	-	4.04 ± 0.04	-
30	-	-	2.83 ± 0.03

Table 8.2: Experimental $EuFe_{2-x}Co_xAs_2$ spin moments from integrated MCPs at 2.5 T.

8.4 Magnetic Compton profiles and analysis

Magnetic Compton profiles for $EuFe_2As_2$ and $EuFe_{1.7}Co_{0.3}As_2$ were obtained on the BL08W beamline at SPring-8. A single MCP for the $EuFe_2As_2$ c-axis was measured, while for $EuFe_{1.7}Co_{0.3}As_2$ the c-axis and the ab-plane were examined. Measurements were made in a field of ±2.5 T, well inside the region of ferromagnetic saturation evidenced by SQuID magnetometry, and at a range of temperatures from 7 to 30 K. The resulting spin moments, determined from the integrated MCP areas, are provided in table 8.2. The temperature-dependent spins for $EuFe_{1.7}Co_{0.3}As_2$ are shown with the total moments from SQuID magnetometry in figure 8.16.

Spin moments

Inspecting figure 8.16 it can be seen that, with the exception of a single data point for the ab-plane at 20 K, the $EuFe_{1.7}Co_{0.3}As_2$ spin moments are not in good agreement with the total moments. A strict interpretation of this disparity would be that there exists an orbital moment in the system and that its size varies with temperature. In the c-axis, this orbital moment would be -0.2 μ_B/f.u. at 7 K, then taking values of around 0.2 μ_B/f.u. at higher temperatures. In the ab-plane, the value would vary between -0.5 μ_B/f.u. at 11 K and 0.3 μ_B/f.u. at 30 K. However, it seems unlikely that these orbital moments actually exist. Firstly, the presence of *any* orbital moment in $EuFe_{2-x}Co_xAs_2$ is inconsistent with the predicted $4f^7$ (L=0) spin configuration of the Eu ion and the fact that the orbital moment for transition metals is usually fully quenched. Secondly, the variation in the size of these differences does not have a

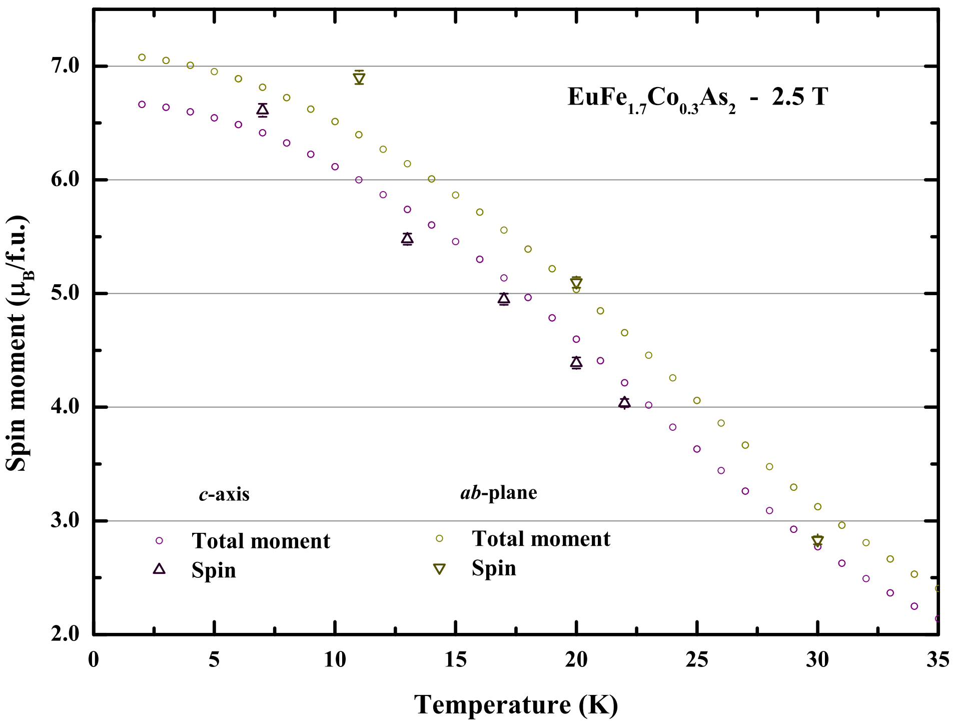

Figure 8.16: EuFe$_{1.7}$Co$_{0.3}$As$_2$ spin moments from integrated MCPs and, for comparison, the total magnetometry from SQuID measurements. The error bars on the spin moments are approximately the size of the symbols.

physical basis. Only significant changes in the electronic band structure could account for such a variation in the orbital moment with temperature, and there is no evidence to support this. It is believed that the differences between the spin and total moments are possibly due to some systematic error (the magnetic Compton scattering data were re-analysed with great care to ensure that the MCPs did not suffer normalisation problems that might affect the spin moment). It is recommended that repeat measurements are made, ideally over a greater temperature range, in order to investigate further the issue of spin moment/total moment disagreement.

MCP shape consistency

Figure 8.17 (top panel) shows three of the EuFe$_{2-x}$Co$_x$As$_2$ MCPs - those recorded at the lowest temperature for each compound and direction measured. They were normalised to unity in order to compare their shapes more easily. The agreement of the MCPs down to 0 a.u. is extremely good; this is highlighted in the bottom panel of figure 8.17, which shows the difference MCPs that result from Co doping (for the same direction) and the direction of

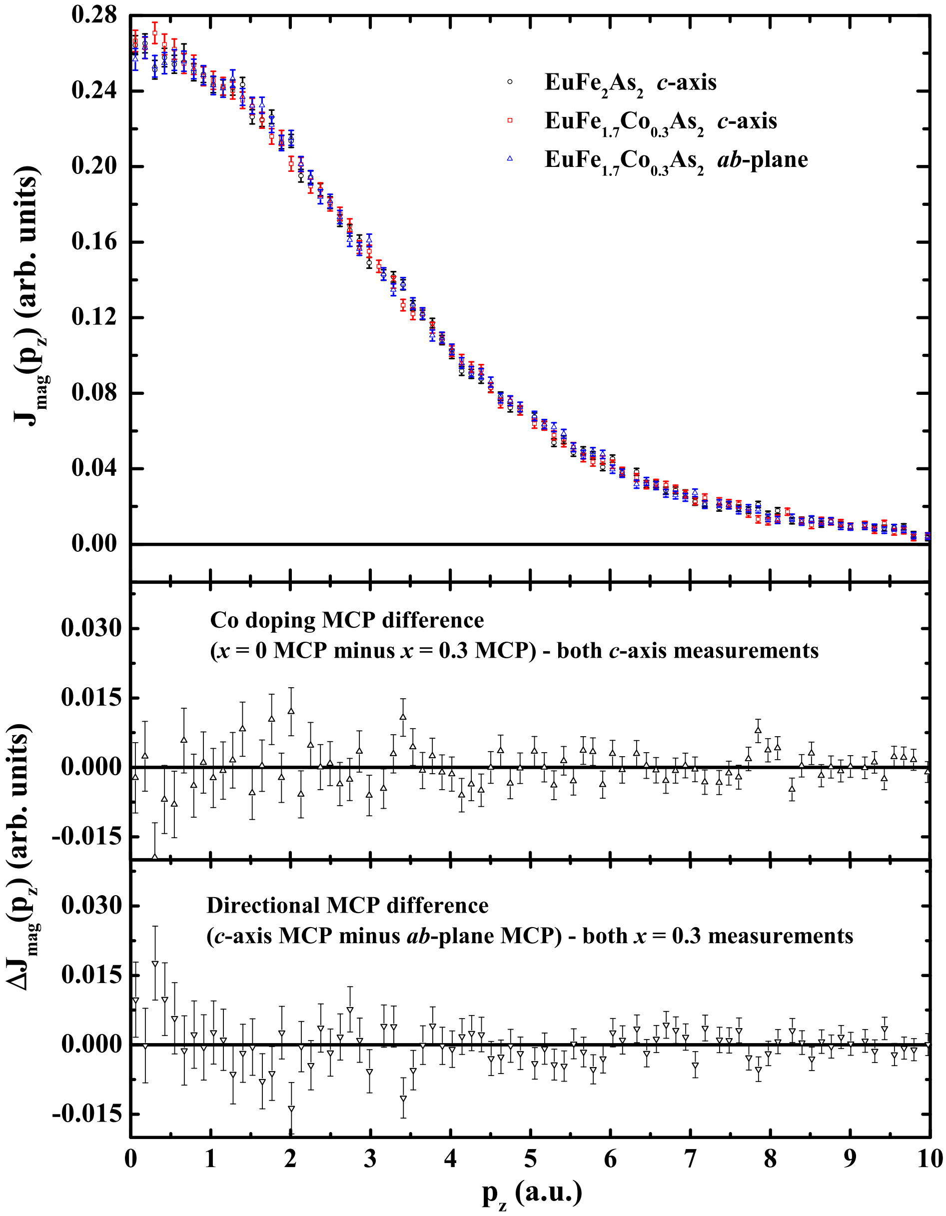

Figure 8.17: (Top) Experimental MCPs for EuFe$_2$As$_2$ (*c*-axis), EuFe$_{1.7}$Co$_{0.3}$As$_2$ (*c*-axis) and EuFe$_{1.7}$Co$_{0.3}$As$_2$ (*ab*-plane). (Bottom) Difference MCPs for EuFe$_{2-x}$Co$_x$As$_2$ showing the effect of Co doping (for the same direction) and direction (for the same doping level).

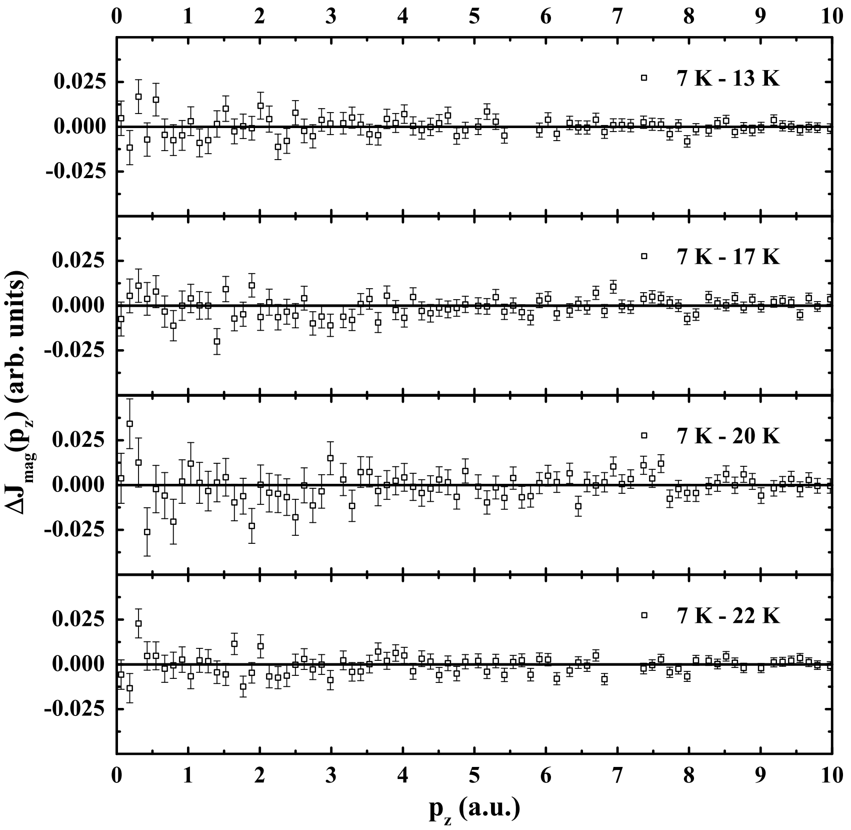

Figure 8.18: Temperature-difference $EuFe_{1.7}Co_{0.3}As_2$ c-axis MCPs. Before being subtracted from the 7 K dataset, the area of each MCP was set to unity.

measurement (for the same doping level). Two pieces of information can be gained from the agreement of these three datasets: first, the Co doping level, $x = 0$ or 0.3, has no effect on the MCP shapes along the $\boldsymbol{c}$ direction; second, since the MCPs for two orthogonal directions of $EuFe_{1.7}Co_{0.3}As_2$ are virtually identical, the spin momentum density distribution being probed is most likely isotropic. The second point is consistent with the idea that all of the spin in this system is due to the half-filled $4f$ shell of a Eu^{2+} ion, which has spherical symmetry.

Temperature-difference MCPs

Two types of temperature-difference MCPs for $EuFe_{1.7}Co_{0.3}As_2$ are presented. In the first type, the MCP at each temperature was normalised to unity before being subtracted from that at 7 K. Therefore, distributions around zero represent no change in the measured spin density. In the second type, temperature-difference MCPs of the form 13 K - 7 K, 17 K - 13 K, etc. were produced from initial MCPs that had areas equal to their spin moments. They are shown in figures 8.18 and 8.19, respectively, where the second figure also includes the data for

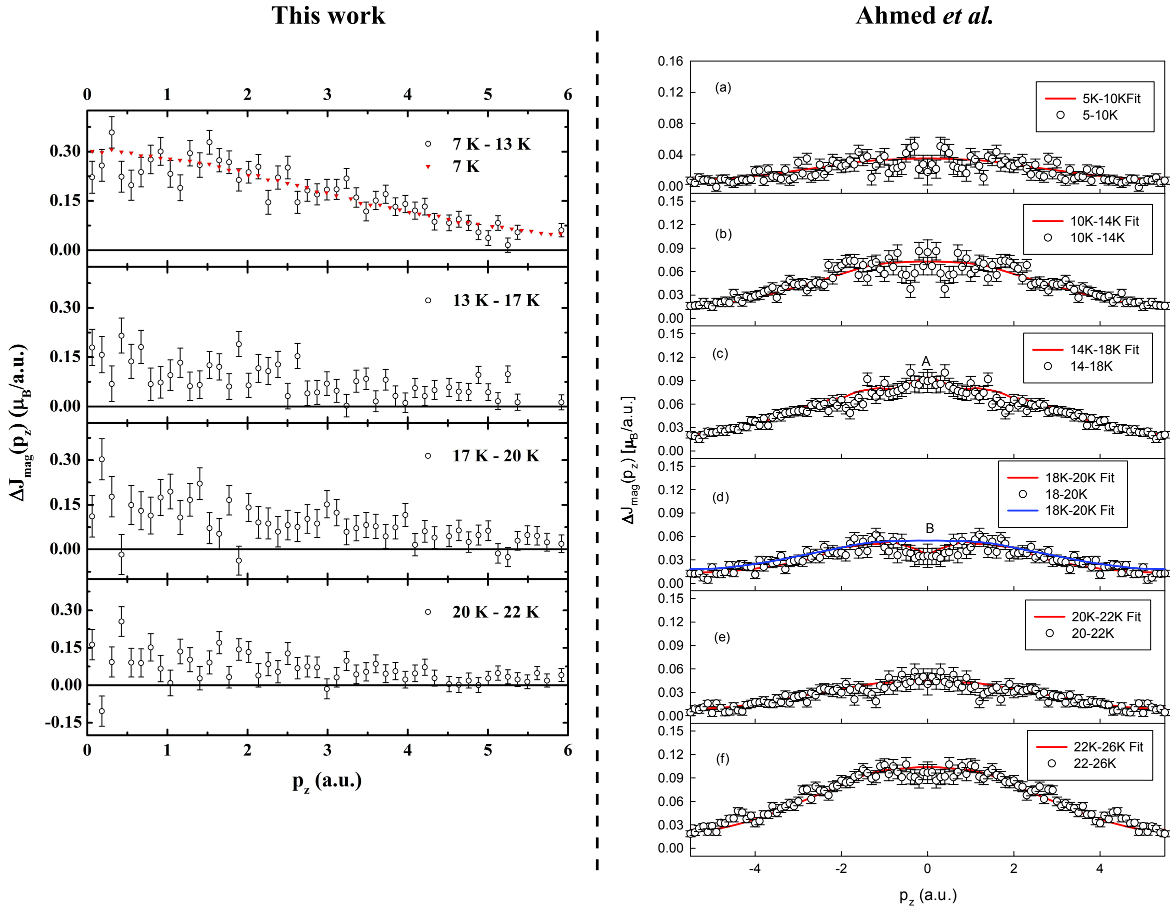

Figure 8.19: Temperature-difference MCPs for $EuFe_{1.7}Co_{0.3}As_2$ (left) and polycrystal $EuFe_2As_{1.46}P_{0.54}$ (right). The $EuFe_2As_{1.46}P_{0.54}$ data is from the work of Ahmed *et al.*[197]. Note that in these plots each MCP was initially normalised to its measured spin, as opposed to figure 8.18 in which they were normalised to unity. This was done so that the temperature-difference MCPs might be more easily compared to those of Ahmed *et al.* In the left figure, a scaled 7 K MCP is shown in addition to the 7 K - 13 K difference MCP, showing that there is no change in the MCP shape with this increase in temperature.

polycrystal $EuFe_2As_{1.46}P_{0.54}$ from Ahmed *et al.*[197]. The second type of temperature-difference MCPs were produced so that comparison could more easily be made with the data of Ahmed *et al.*, who presented their data in this way.

Both types of temperature-difference MCP show no sign of anomalous temperature effects such as that observed by Ahmed *et al.* The difference in the statistical quality of the datasets means that comparison is difficult. However, within the limit of the statistics achieved by our experiment, there is no evidence for a low momentum dip of the type seen in Ahmed *et al.*'s 20 K - 18 K difference profile. As mentioned previously, this dip was attributed to an increased Fe $3d$ spin moment at 18 K.

Fitting with Eu and Fe Hartree-Fock Compton profiles

The similarity of the $EuFe_2As_2$ c-axis, $EuFe_{1.7}Co_{0.3}As_2$ c-axis and $EuFe_{1.7}Co_{0.3}As_2$ ab-plane MCPs allowed them to be legitimately summed, providing a single dataset of high statistical quality for fitting purposes. As discussed in section 8.2, a realistically converged SPR-KKR calculation was not possible; instead, theoretical profiles for Fe and Eu came from the Hartree-Fock (HF) and relativistic Dirac-Hartree-Fock (RDHF) Compton profiles of Biggs *et al.*[51].

With respect to the issue of Fe/Co $3d$ Compton profile width, the Fe $3d$ HF profile was virtually indistinguishable from one composed of Fe and Co in the ratio 1.7:0.3. Therefore, the Fe $3d$ HF profile should be capable of describing the TM spin moment in $EuFe_{2-x}Co_xAs_2$ if it exists.

An experimental MCP from a pure Fe polycrystal sample was also employed in the fitting. This MCP deviates from the Fe $3d$ HF profile primarily in its low momentum dip, below $\sim$ 1.5 a.u. Kubo and Asano, who examined directional MCPs from crystalline Fe and performed comprehensive DFT calculations, ascribed the dip mainly to negatively polarised contributions from s- and p-like electrons[167]. The polycrystal MCP was used here to test whether the description of Fe/Co magnetism that included negatively polarised s and p contributions offered a better fit than the HF approximation alone. It therefore tests whether these contributions exist in $EuFe_{2-x}Co_xAs_2$. The Eu $4f$ RDHF profile, Fe $3d$ HF profile and

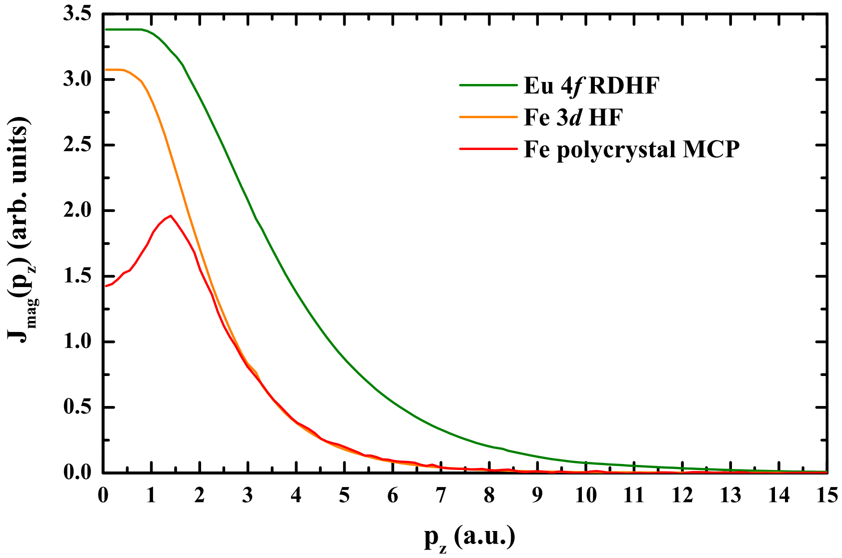

Figure 8.20: The Eu $4f$ RDHF, Fe $3d$ HF and Fe polycrystal profiles used to fit to the summed $EuFe_{2-x}Co_xAs_2$ MCP. The Fe profiles are scaled to illustrate the agreement in their high momentum tails.

experimental polycrystal Fe MCP are shown in figure 8.20.

Fitting procedure

The summed $EuFe_{2-x}Co_xAs_2$ MCP was subject to a straightforward fitting routine, whereby the contributions from the Eu and Fe profiles in figure 8.20 were varied in order to reduce the total χ^2 value. The momentum range from 0 to 15 a.u. was included in the initial fitting. Three models were trialled: in the first, all of the spin density was due to the $4f$ electrons of Eu; in the second and third, an Fe/Co spin moment was allowed, with this being represented by the pure Fe $3d$ profile and the experimental Fe polycrystal MCP, respectively. The MCP fits and their residuals are shown in figure 8.21, while the reduced-χ^2 values are provided in table 8.3, along with results from an F distribution analysis.

Fitting with the Eu $4f$ RDHF profile only

On inspecting the fit residuals in figure 8.21, the first feature of note is that the model consisting of Eu $4f$ alone provides a relatively poor description of the summed MCP, even in the high momentum region where good agreement is expected. This information must be interpreted carefully, or it may seem that the high momentum tail of the experimental data can not be well replicated by free-atom theory at all. Crucially, the fitting routine simply

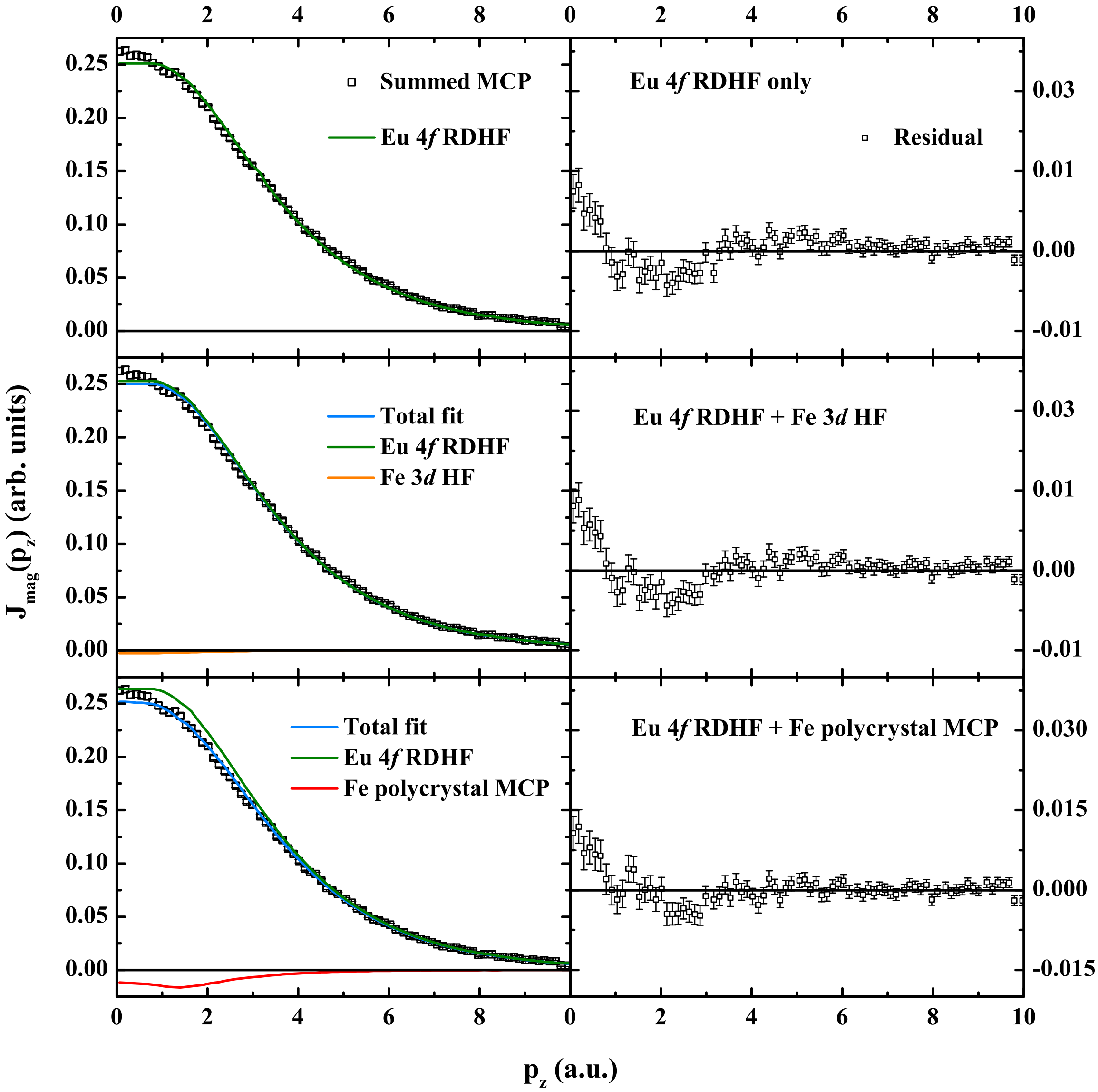

Figure 8.21: $EuFe_{2-x}Co_xAs_2$ MCP fits (left) and residuals (right) for three models: Eu 4f RDHF only, Eu 4f RDHF + Fe 3d HF and Eu 4f RDHF + Fe polycrystal MCP.

	Reduced-χ^2	F	Probability of exceeding F (%)
Eu 4f RDHF only	2.316	-	-
Eu 4f RDHF + Fe 3d HF	2.314	0.999	49.8
Eu 4f RDHF + Fe polycrystal MCP	1.785	0.774	8.1

Table 8.3: Statistical fitting results for the $EuFe_{2-x}Co_xAs_2$ MCP composed of three summed profiles - refer to the text. Reduced-χ^2 and F values are provided, as well as the probability of exceeding F. In this case, the 'reference' model, the one to which the others' F values are compared, is the one using a Eu 4f RDHF profile only.

minimises the total deviation of each experimental data point from the fit line; it does not prioritise fitting in a certain region. Therefore, the quality of the fit at higher momentum is affected by the fit at low momentum, and vice versa.

The high momentum structure seen in the residual plot for Eu 4*f* alone is a consequence of the significant shape discrepancy between the data and the Eu 4*f* RDHF profile at low momentum. To ensure that the RDHF profile was capable of describing the MCP tail well, the fitting procedure was repeated, including the data from 5 to 15 a.u. only. The fit residual is shown in figure 8.22(a) and shows that, when the fit includes only the momentum region in which the Eu 4*f* profile can significantly contribute, the agreement between free-atom theory and the data is very good.

Fitting with the Eu 4*f* RDHF and Fe 3*d* HF profiles

The residual plots and fit statistics suggest that the Eu 4*f* RDHF + Fe 3*d* HF model is no better than that of Eu 4*f* alone. Of these solutions, we would tend to choose the simplest, Eu 4*f* only, as the ‘correct’ one, especially considering the paucity of evidence in the literature supporting the existence of a TM moment. In this case the argument is even simpler; since the Fe 3*d* contribution in the second model is so small, only around -0.6% of the MCP, with a large associated error, the first two solutions are actually extremely similar. On this evidence, we would say there is no Fe/Co spin moment in $\mathrm{EuFe_{2-x}Co_xAs_2}$, for our values of x.

Fitting with the Eu 4*f* RDHF and experimental Fe polycrystal profiles

The situation is quite different when the Fe/Co spin moment is represented by the experimental Fe polycrystal MCP. The reduced-χ^2 value is smaller than that of the other models. The resulting F, which again is the ratio of the reduced-χ^2 values for the model being tested and ‘reference’ model, could be exceeded by only about 8% of random observations. The improvement in the fit with the addition of the Fe polycrystal MCP is therefore significant. The Fe/Co moment is anti-aligned with that of the Eu and the applied field, and its size is $(-4.7 \pm 0.08)\%$ of the summed MCP. If the value of 6.64 ± 0.04 μ_B/f.u. were assigned to the summed MCP, which is an average of the two values obtained for $\mathrm{EuFe_2As_2}$ and $\mathrm{EuFe_{1.7}Co_{0.3}As_2}$ at 7 K, the Fe/Co moment would be -0.31 ± 0.05 μ_B/f.u. and the corresponding Eu 4*f* moment would

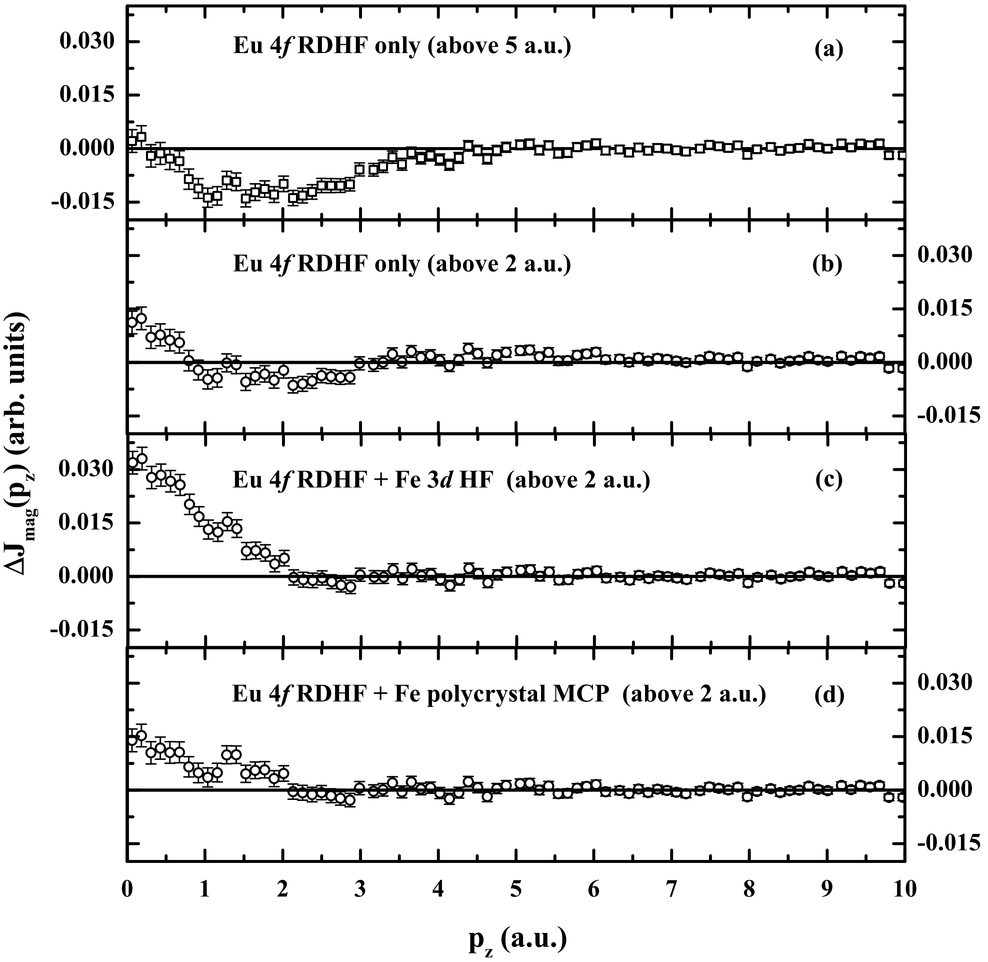

Figure 8.22: Further $\mathrm{EuFe}_{2-x}\mathrm{Co}_x\mathrm{As}_2$ fit residuals for: (a) Eu $4f$ RDHF only (above 5 a.u.), (b) Eu $4f$ RDHF only (above 2 a.u.), (c) Eu $4f$ RDHF and Fe $3d$ HF (above 2 a.u.) and (d) Eu $4f$ RDHF and Fe polycrystal MCP (above 2 a.u.)

be 6.96 ± 0.07 μ_B/f.u. The latter value is in good agreement with the 7 μ_B/f.u. possible for a half-filled $4f$ shell.

Necessity of the low momentum dip in the Fe polycrystal profile

The fit residuals in figure 8.21 reveal that the model including the polycrystal Fe MCP offers a large improvement over a broad region of momentum, clearly visible between ~ 2 and 8 a.u. The fit below 2 a.u. is also better than the alternatives, but perhaps not to the extent that might be expected, considering that it is chiefly in this region that the polycrystal MCP deviates from the HF profile. However, it is important to recognise that the improved fit above 2 a.u. is only possible because of the low momentum dip of the Fe polycrystal MCP. Without the dip, the residuals above 2 a.u. can only be improved at the expense of larger disagreement at low momentum. Evidence for this is provided in figure 8.22(b)-(d), which shows the residuals for the same fitting routines as above, performed from 2 to 15 a.u. only (*cf.* 0 to 15 a.u. used previously). These residuals show that the two models that include an Fe profile are equally capable of describing the $EuFe_{2-x}Co_xAs_2$ summed MCP from 2 a.u. Their reduced-χ^2 values are nearly identical. They differ only in the size of the low momentum discrepancy, which is minimised when the Fe polycrystal MCP is used. Therefore, the inclusion of highly itinerant, negatively polarised s and p electrons in the Fe magnetism aids in the description of the $EuFe_{2-x}Co_xAs_2$ low momentum MCP features. These magnetic s and p contributions are positively polarised with respect to the Eu $4f$ moments.

Other possible magnetic contributions

Examining the residual plots in figure 8.21 once more, it was noted that the low momentum discrepancies for all three models, i.e. the shapes of the residuals below 2 a.u., were quite similar. If a single magnetic contribution was responsible for these features, it would possess a MCP of HWHM ~ 0.5 to 1 a.u. The $5d$ RDHF and $4p$ HF profiles of Gd and As, shown in figure 8.23, fulfill this criterion and ought to be considered for different reasons.

Gd $5d$ and As $4p$ contributions

With respect to a $5d$ contribution, although band structure calculations have not yielded such in $EuFe_{2-x}Co_xAs_2$, a $5d$ moment of 0.58 μ_B is known to exist in pure Gd[165], which is

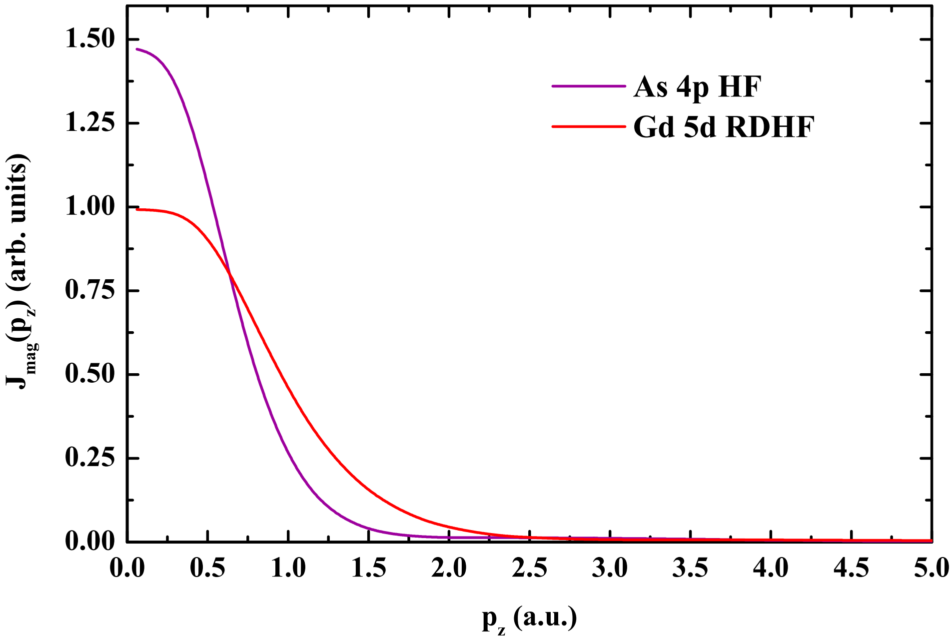

Figure 8.23: Gd 5*d* RDHF and As 4*p* HF Compton profiles.

Eu's 'neighbouring' rare-earth element. When a Gd 5*d* RDHF profile was used in conjunction with that of Eu 4*f*, the resulting fit to the summed MCP was only partially better than that offered by Eu 4*f* alone (reduced $\chi^2 = 2.079$ compared to 2.316), and provided a very similar residual plot. However, when Eu 4*f*, Gd 5*d* and Fe polycrystal profiles were combined, the fit improved significantly. The reduced-χ^2 value was 1.291, *cf.* the previous lowest of 1.785 found for Eu 4*f* RDHF + Fe polycrystal MCP. The Eu + Gd + Fe fit and residual are shown in figure 8.24. The fit residual is clearly superior to those in figure 8.21 where the Gd 5*d* RDHF profile was not included. The fit provides a good description of the data over the full momentum range. In this solution, the Eu 4*f*, 5*d* and Fe spin moments were 6.98 ± 0.05 μ_B/f.u., 0.08 ± 0.01 μ_B/f.u. and -0.39 ± 0.05 μ_B/f.u. respectively. Thus, the 4*f* and 5*d* moments were aligned (both positive), along with the *s* and *p* contributions that were included as part of the experimental Fe MCP. This is the same situation that was previously observed for pure Gd using magnetic Compton scattering[165].

The As 4*p* HF profile was employed because a moment of up to -0.024 μ_B/f.u was attributed to these electrons in the work on polycrystal $EuFe_2As_{1.46}P_{0.54}$ by Ahmed *et al.* The result of including the As 4*p* profile in the fitting was very similar to those mentioned above for the Gd 5*d* contribution. When it was paired just with the Eu 4*f* RDHF profile, there was

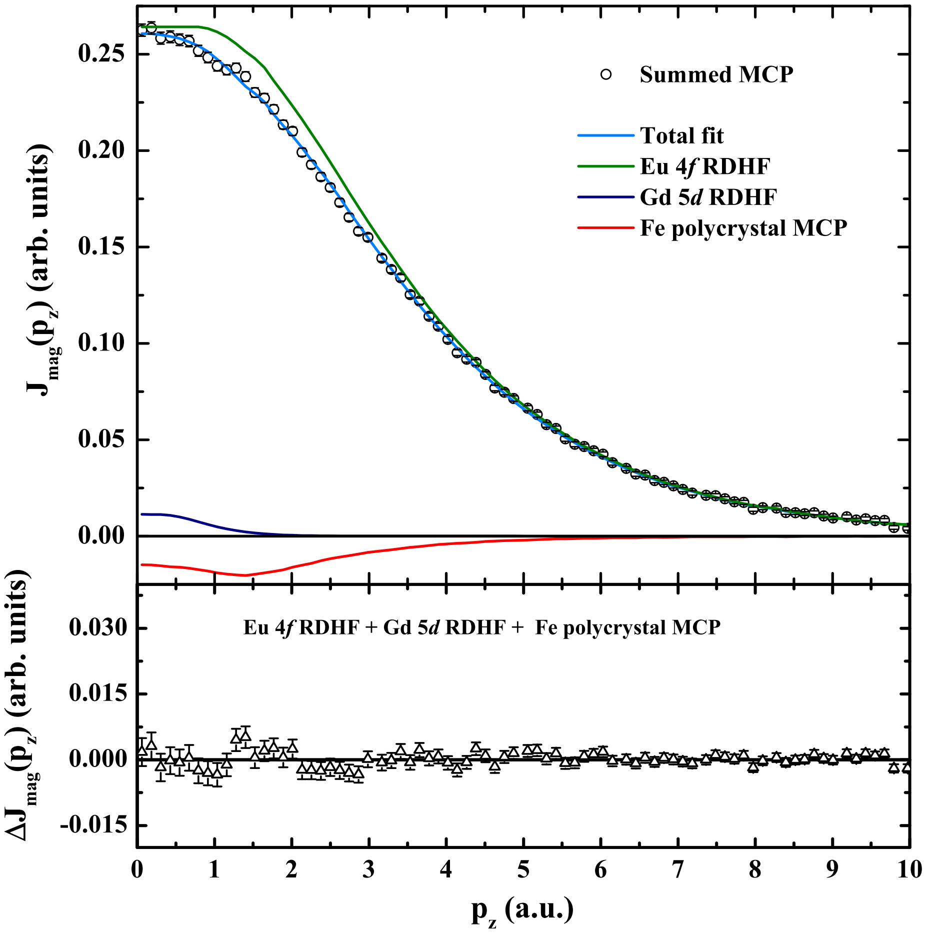

Figure 8.24: $EuFe_{2-x}Co_xAs_2$ MCP fit including Eu $4f$ (green line), Gd $5d$ (dark blue line) and Fe (red line) contributions. The total fit is shown as a light blue line. The corresponding residual for this fit is shown below.

no improvement over Eu $4f$ alone. When the Fe polycrystal MCP was added also, the reduced-χ^2 value was 1.318 and the fit residual was almost indistinguishable from that in figure 8.24. In this last fit, the Eu $4f$, As $4p$ and Fe spin moments were 6.95 ± 0.05 μ_B/f.u., 0.06 ± 0.01 μ_B/f.u. and -0.3 ± 0.05 μ_B/f.u., respectively. The implications of this last part of the MCP fitting investigation are discussed further in the following section.

8.5 Conclusions

Magnetometry

$\mathrm{EuFe_2As_2}$ and $\mathrm{EuFe_{1.7}Co_{0.3}As_2}$ crystals were subject to magnetisation vs applied field, $M\mathrm{v}H$, and magnetisation vs temperature, $M\mathrm{v}T$, measurements with a SQuID magnetometer. Magnetic behaviour along the c-axis and in the ab-plane was examined. The shapes of the $M\mathrm{v}H$ loops, as well as the associated saturated moments, were consistent with previous work and the description of the ground state arrangement of Eu moments in the ab-plane.

A range of parameters were obtained from fitting to the $M\mathrm{v}T$ data. The values that came from fitting the Curie-Weiss law in the paramagnetic regime, that is C and θ_CW, were in good agreement with previous work. Fitting with a modified power law due to Guguchia *et al.* showed an encouraging correspondence in the low temperature behaviour of our samples, whilst a T^n law applied up to $\sim T_\mathrm{C}/3$ suggested that, as for NiMnSb discussed previously, the temperature-dependent magnetisation was not described by Bloch's law. More work is needed to explore the veracity and significance of the last result.

Analysis of the magnetic Compton profiles

Analysis of the experimental MCPs for $\mathrm{EuFe_{2-x}Co_xAs_2}$ crystals, recorded at a range of temperatures and along two crystallographic directions, showed that the spin density did not vary as a function of direction, Co doping or temperature. This was demonstrated in a series of difference MCPs that possessed no structure over the full range of electron momentum. The only difference between the MCPs was the size of their associated spin moments, which were in fair agreement with the total moments from SQuID magnetometry. This indicates that there is no orbital moment in the system, which is consistent with the accepted $4f^7$ electron population of the $\mathrm{Eu^{2+}}$ ion and the fact that the orbital moment for most transition metals is fully quenched. Of the above results, the temperature-independence of the MCP shapes is the most significant since it contrasts with the findings of Ahmed *et al.*, who saw a clear change in the shape of the MCPs of the closely related compound $EuFe_2As_{1.46}P_{0.54}$ at a temperature of 18 K.

Magnetic Compton profile fitting - Eu and Fe

Fitting was performed on a $EuFe_{2-x}Co_xAs_2$ MCP of high statistical quality that was an amalgamation of three separate datasets. The summing of these datasets was deemed to be a legitimate approach because, as shown in their difference profiles, the various MCPs reflected the same spin density. The fitting employed theoretical Eu $4f$ and Fe $3d$ profiles obtained from Hartree-Fock theory, as well as an experimental MCP from polycrystal Fe. The latter was used to determine whether the inclusion of highly itinerant s- and p-like electrons, which contribute to the experimental Fe profile, was necessary to describe the $EuFe_{2-x}Co_xAs_2$ MCP.

The result of the fitting procedure was that an Fe moment should be included to describe the spin density of $EuFe_{2-x}Co_xAs_2$, but only when the Fe contribution was represented by the experimental polycrystal Fe MCP with a low momentum dip. Inclusion of this MCP provided a better description of the data over the full momentum range compared to the models that included the Eu $4f$ and Fe $3d$ HF profiles only. The improvement in the fit was reflected in the reduced-χ^2 value that was significantly lower than the corresponding values for the other models. The spin moments associated with the Eu and Fe in this model were 6.96 ± 0.07 μ_B/f.u. and -0.31 ± 0.05 μ_B/f.u., respectively. The former is in agreement with the predicted 7 μ_B available for a Eu $4f^7$ spin configuration, as well as the values of 6.9(4) μ_B and 6.7(4) μ_B from the neutron diffraction work of Xiao *et al.* The latter contrasts with previous findings that the antiferromagnetic ordering of the Fe is robust up to high fields, and with the result from Ahmed *et al.*, using magnetic Compton scattering, that the Fe spin moment in a closely related system is positive with values between 0.05 and 0.07 μ_B/f.u.

Magnetic Compton profile fitting - Gd and As

Compton profiles from Gd $5d$ and As $4p$ electrons were considered to address the low momentum features seen in all of the fit residuals involving Eu and Fe only. Inclusion of either of these profiles in addition to the experimental Fe MCP discussed above, provided a very good description of the summed MCP, with virtually no residual structure and significantly lower reduced-χ^2 values than previously achieved. Clearly, further experimental and theoretical work is required before a statement that there *is* a $5d$ or $4p$ spin contribution in $\mathrm{EuFe_{2-x}Co_xAs_2}$ can be made. Another explanation to consider is that the low momentum discrepancy is actually associated with a larger low momentum dip in the spin density of the Fe - the theoretical work of Kubo and Asano showed a very pronounced dip in the Fe [111] MCP. Future magnetic Compton scattering work will be informed by the result given here and the experiments can be designed and interpreted accordingly.

Future work

Future work with $\mathrm{EuFe_{2-x}Co_xAs_2}$ should focus on obtaining theoretical MCPs from a converged DFT calculation. These will require the addition of a self-interaction U term to properly deal with the $4f$ states of the Eu ion. Most likely, these results will come from the ELK FP-LAPW code that is is currently being modified by members of the Compton scattering group at Bristol to calculate MCPs. In particular, the issues of the Fe $3d$ moment and possible highly itinerant spin contributions from polarised s- and p-like bands should be examined in some detail. Comparison of these theoretical MCPs can then be made with those obtained experimentally, in a manner which is now becoming the standard approach within Compton scattering, as well as with those provided in other work by Ahmed *et al.*

Another area requiring more work is the re-collection and analysis of low temperature $M\mathrm{v}T$ data with SQuID magnetometry. This should take place in a range of applied fields to determine whether the T^n power law, which is a supposed indicator of the itinerancy of the magnetism, is affected by the applied field and to extrapolate a value for n at 0 T. This would require a higher data density up to T_C than presented here, and would provide a good comparison for the similar work conducted on NiMnSb. Finally, since the spin moments from the $\mathrm{EuFe_{2-x}Co_xAs_2}$ MCPs differed randomly from the total moments, another series of temperature-dependent magnetic Compton scattering experiments should be performed. This would confirm or refute the existence of a small orbital moment in the system.

Chapter 9

Conclusions and future work

The spin densities of several interesting $4f$ and $3d$ magnetic systems have been directly probed with magnetic Compton scattering. Information about their electronic configurations and magnetic structures has been deduced from comparison of their magnetic Compton profiles with those from theoretical work, further demonstrating the usefulness of this technique within condensed matter physics. In addition, experimental methods ranging from SQuID magnetometry to powder X-ray diffraction and X-ray photoelectron spectroscopy have been deployed, giving a more complete picture of each material and providing results for comparison with other work. The work on NiMnSb, $TbMnO_3$ and $EuFe_{2-x}Co_xAs_2$ presented in this thesis will be used to inform future experiments and aid in the general understanding of these materials.

9.1 Summary of important results

NiMnSb

Of the materials examined in this thesis, NiMnSb was subject to the widest range of experimental characterisation techniques and theoretical investigation. A single crystal of the predicted half-metallic ferromagnet NiMnSb was produced and subsequent analysis showed that its chemical stoichiometry, space group and lattice parameter were in agreement with expectations and previous results.

The magnetisation of a fragment of the NiMnSb crystal was investigated as a function of applied field and temperature. The saturated moment was in good agreement with previous experimental results and the value predicted by theoretical calculations for half-metallic NiMnSb.

Over the temperature range 5 to 300 K, that is up to $\sim T_{\mathrm{C}}/2.5$, the saturated magnetisation followed laws of the form $M(T) \propto (1 - AT^{2.06})$ and $M(T) \propto (1 - AT^{2.26})$ in fields of 0.75 and 2.5 T, respectively, both deviating from the $T^{3/2}$ dependence predicted by Bloch for localised, Heisenberg-like spins. The literature suggests two possible interpretations of this interesting behaviour. First, and seemingly most likely, the magnetisation is being disrupted by Stoner excitations, which scatter electrons of one spin type into the other. This process is known to exhibit a T^2 dependence in the magnetisation as a function of temperature. However, since ideal half-metallic NiMnSb is predicted to have zero available states in its minority channel at the Fermi energy, the Stoner mechanism should be inaccessible. The implication is that the NiMnSb crystal studied here did not possess a Fermi energy gap in its minority spin channel and is probably not half-metallic. The second interpretation is that the larger-than-expected T power exponents are due to the presence of a low wavevector gap in NiMnSb's spin-wave dispersion (Bloch's law assumes no such gap). The gap increases in size with the applied magnetic field, thus explaining the increased T exponent at 2.5 T compared to that at 0.75 T. The detracting factor in this interpretation is that the required spin-wave gap would be far greater than that previously measured for NiMnSb.

An investigation with the SPR-KKR density-functional theory code provided an optimised lattice geometry for further NiMnSb calculations. Fitting the theoretical total energies for a range of lattice parameters with the Murnaghan equation of state provided a value for the bulk modulus and allowed a theoretical volume-pressure relationship to be determined, both of which were in good agreement with previous results. SPR-KKR calculations then provided total and site-specific densities-of-states and magnetic Compton profiles for NiMnSb, the latter of which were compared to the experimental results.

NiMnSb magnetic Compton profiles were recorded at temperatures of 9 and 300 K. Apart from the change in the MCP areas due to their spin moments, the 9 and 300 K MCPs were essentially identical, indicating that there is no significant change in the spin momentum density over this temperature range. The spin moments at 9 K were around 4% larger than the expected 4 μ_{B}/f.u. A Mn $3d$ HF Compton profile was unable to adequately describe the experimental MCP tail shapes, as were the theoretical profiles obtained from *ab initio* SPR-KKR calculations. However, the SPR-KKR results were seen to replicate the experimental Umklapp features that reflect the shape of the Fermi surface. In addition, reasonable theoretical-experimental agreement was achieved when the fractional Ni contribution to the spin moment was ‘artificially’ increased by scaling up its site-specific SPR-KKR MCP. The resulting Mn and Ni moments in the studied crystal would then be 3.07 μ_B/f.u. and 0.96 μ_B/f.u., respectively, irreconcilable with half-metallic theory and previous experimental findings. In combination with the magnetometry results discussed above, the deviation between the *ab initio* DFT profiles and the experimental MCPs is seen as evidence that the studied NiMnSb crystal was probably not half-metallic.

The issue of most importance for future researchers of NiMnSb is the behaviour of the magnetisation as a function of temperature (on which there are several reports in the literature, but little consensus as to the mechanisms) and its relationship to the half-metalicity, which is still to be comprehensively confirmed by experiment. If the Stoner mechanism is responsible for the observed reduction in magnetisation, it places limitations on the extent of the spin polarisation and the temperature range in which it could be expected to exist.

TbMnO$_3$

The magnetoelectric multiferroic compound TbMnO$_3$ was investigated with magnetic Compton scattering along its crystallographic $\boldsymbol{a}$ and $\boldsymbol{b}$ directions. MCPs were collected above the magnetic fields in both directions required to flip the Tb moments into their available orientations lying closest to the direction of the applied field. A $\boldsymbol{b}$ direction MCP was also collected in the region between ~ 1 and ~ 4.5 T where effectively only half of the Tb moments are flipped by the field. The measurements provided the spin moments along each direction and, through comparison with SQuID magnetometry, the associated orbital moments.

In an effort to assign the experimental spin moments to the individual magnetic sites, theoretical Compton profiles were obtained from LCAO calculations performed with the GAMESS code. These calculations provided Compton profiles for each of the seven $4f$ orbitals of the Tb ion, as well as for the hybridised molecular orbitals of the MnO$_6$ octahedra. Fitting to the experimental MCPs indicated that the Tb $4f$ electron population was of the form $7\uparrow + 1\downarrow$, where the minority orbital was the $f_{z(x^2-y^2)}$. This result agrees with previous DFT calculations.

The Tb spin moment projections along the $\boldsymbol{a}$ and $\boldsymbol{b}$ directions provided a total moment of nearly 6 μ_B per Tb ion. The orbital moments, which in $\mathrm{TbMnO_3}$ can reasonably be attributed solely to the Tb ions due to quenching of the TM $3d$ moments, provided a total of almost 2 μ_B per Tb ion. Once again, these values provide strong evidence for Tb $4f^{7\uparrow+1\downarrow}$ configuration, which would in theory provide a spin of 6 μ_B and an orbital moment of 2 μ_B if the doubly occupied orbital was the $4f_{z(x^2-y^2)}$. The angle that the Tb moments make with the b-axis was found to be in the region of 60°, which is consistent with the arrangement of Tb moments as described by the pre-existing Ising-like model. This is believed to be the first instance that the model has been verified using separate spin and orbital contributions to the Tb magnetism.

With regard to the understanding of $\mathrm{TbMnO_3}$'s multiferroicity, which provides the prime motivation for the continued study of the system (as well as many related compounds), the most useful result from this work may be behaviour of the Mn $3d$ moment in an applied field and its relationship to that of the Tb. This could inform any future work which aims to investigate the roles of each magnetic ion in establishing the coupling between magnetism and ferroelectricity in any of the rare-earth/transition metal multiferroic systems.

$\mathbf{EuFe_{2-x}Co_xAs_2}$

The FeAs-layered superconductor $\mathrm{EuFe_{2-x}Co_xAs_2}$, with $x = 0$ and 0.3, was examined with SQuID magnetometry and magnetic Compton scattering. Results from the former experimental method were in good agreement with previous work and also suggested that the low temperature magnetisation, which had a T^2 dependence, might be worthy of further investigation.

With respect to the magnetic Compton scattering work, a series of difference profiles showed that the spin density of the system was unaffected by changes in temperature, Co doping level or crystallographic direction. A straightforward fitting routine for the summed experimental MCP, using profiles from Hartree-Fock theory and an experiment on pure Fe, showed that a

Eu $4f$ profile alone could not account for the spin density of $\mathrm{EuFe_{2-x}Co_xAs_2}$. An Fe spin moment of size $\sim -0.31 \pm 0.05\ \mu_{\mathrm{B}}$/f.u., that is negatively polarised with respect to the Eu moment, is required to describe the measured MCP. Further to this, the fit residuals show low momentum features that can be explained by the presence of an additional narrow MCP; possible origins include a $5d$ contribution, a $4p$ contribution (as from the As), or a larger contribution from the *sp*-like band associated with the Fe. Further work, both theoretical and experimental, is required to address this last issue.

The discovery of a significantly sized Fe moment in $\mathrm{EuFe_{2-x}Co_xAs_2}$ is the most interesting outcome of this work and could be quite significant for the understanding of this and related systems, not least because the antiferromagnetic SDW ordering of the Fe moments is well established and believed to be quite robust. However, before wide-ranging implications for the 122 and other FeAs layered superconductors can be made, it requires confirmation through further investigations; this could potentially come from more magnetic Compton scattering work examining a range of doped and undoped compounds as a function of applied field. If the existence of an Fe moment is confirmed by whatever means, a magnetic Compton scattering experiment with a very high statistical accuracy may be the best tool available to determine the orbitals/electronic bands responsible. This would be achieved by comparison of the experimental MCP shapes with theoretical MCPs from GAMESS or DFT calculations, as demonstrated throughout this thesis, and may provide evidence for a particular pairing mechanism in these unconventional superconductors.

9.2 Future work

Recommendations for future work on the three examined materials have been made in the relevant sections; they are section 6.7 for NiMnSb, section 7.6 for $\mathrm{TbMnO_3}$ and section 8.5 for $\mathrm{EuFe_{2-x}Co_xAs_2}$. Of the experimental work, it has been suggested that several magnetic Compton scattering measurements be re-performed, primarily to ensure reproducibility. Other than this, it is believed that the greatest potential for discovery lies in two areas; the low temperature $M\,\mathrm{v}\,T$ behaviour of NiMnSb and $\mathrm{EuFe_{2-x}Co_xAs_2}$, which has proved to be different from expected, and further X-ray studies (ARPES, HAXPES, etc.) of the NiMnSb crystal. In both cases, the work presented in this thesis should prove useful in designing the experiments and interpreting their results.

Theoretical work should focus on obtaining full descriptions of all three materials (site-specific spin moments, band structures, magnetic Compton profiles, etc.) with a full-potential DFT code. Work in this direction is already underway with the ELK FP-LAPW code that has been mentioned in this thesis already. Future work on NiMnSb, such as the upcoming HAXPES experiment, may also be informed by disordered local moment (DLM) DFT calculations within KKR. These aim to deal with non-zero temperature effects in magnetic systems[94].

Bibliography

[1] A. H. Compton, Phys. Rev. **21**, 483 (1923).

[2] N. Bohr, Philosophical Magazine **26**, 1 (1913).

[3] C. Kittel, *Introduction to Solid State Physics (seventh edition)*, Wiley, 1996.

[4] R. Coehoorn, C. Haas, and R. A. de Groot, Phys. Rev. B **31**, 1980 (1985).

[5] J. D. Aldous *et al.*, J. Cryst. Growth **357**, 1 (2012).

[6] K. Motizuki *et al.*, Physica B **284-288**, 1345 (2000).

[7] M. A. Ruderman and C. Kittel, Phys. Rev. **96**, 99 (1954).

[8] M. S. Dresselhaus, *Lectures on Solid State Physics, Massachusetts Institute of Technology*, 2001.

[9] W. Eerenstein, N. D. Mathur, and J. F. Scott, Nature **442**, 759 (2006).

[10] W. F. Brown, R. M. Hornreich, and S. Shtrikman, Phys. Rev. **168**, 574 (1968).

[11] J. F. Annett, *Superconductivity, Superfluids and Condensates*, Oxford, 2007.

[12] J. Bardeen, L. N. Cooper, and J. R. Schrieffer, Phys. Rev. **106**, 162 (1957).

[13] J. Bardeen, L. N. Cooper, and J. R. Schrieffer, Phys. Rev. **108**, 1175 (1957).

[14] J. B. Ketterson and S. N. Song, *Superconductivity*, Cambridge University Press, 1999.

[15] M. K. Wu *et al.*, Phys. Rev. Lett. **58**, 908 (1987).

[16] H. Maeda *et al.*, Jpn. J. Appl. Phys. **27**, L209 (1988).

[17] D. P. *et al.*, Physica C **243**, 201 (1995).

[18] W. N. Hardy *et al.*, Phys. Rev. Lett. **70**, 3999 (1993).

[19] L. Shan *et al.*, Europhys. Lett. **83**, 57004 (2008).

[20] G. Mu *et al.*, Chin. Phys. Lett **25**, 2221 (2008).

[21] H.-J. Grafe *et al.*, Phys. Rev. Lett. **101**, 047003 (2008).

[22] H. Ding *et al.*, Europhys. Lett. **83**, 47001 (2008).

[23] K. Terashima *et al.*, PNAS **106**, 7330 (2009).

[24] J. K. Dong *et al.*, Phys. Rev. Lett. **104**, 087005 (2010).

[25] K. Hashimoto *et al.*, Phys. Rev. B **81**, 220501 (2010).

[26] T. A. Maier *et al.*, Phys. Rev. B **79**, 224510 (2009).

[27] S. Maiti *et al.*, Phys. Rev. B **84** (2011).

[28] P. J. Hirschfeld, M. M. Korshunov, and I. I. Mazin, Rep. Prog. Phys. **74**, 124508 (2011).

[29] M. J. Cooper *et al.*, *X-Ray Compton Scattering*, Oxford Science Publications, 2004.

[30] R. H. Stuewer, *The Compton effect: turning point in physics*, New York: Science History Publications, 1975.

[31] J. W. M. Du Mond, Phys. Rev. **33**, 643 (1929).

[32] R. Currat, P. D. DeCicco, and R. J. Weiss, Phys. Rev. B **4**, 4256 (1971).

[33] O. Klein and Y. Nishina, Z. Physik **52**, 853 (1929).

[34] M. W. Butchers, *Magnetic Compton scattering studies of novel phases*, PhD thesis, Department of Physics, University of Warwick, 2012.

[35] F. W. Lipps and H. A. Tolhoek, Physica **20**, 395 (1954).

[36] M. Dixon, *Studies of spin and charge momentum densities using Compton scattering*, PhD thesis, Department of Physics, University of Warwick, 1998.

[37] A. Saenz, T. Asthalter, and W. Weyrich, Int. J. Quantum. Chem. **65**, 213 (1997).

[38] M. J. Cooper and J. A. Duffy, J. Phys. Chem. Solids **61**, 345 (200).

[39] J. A. Clarke, *The science and technology of undulators and wigglers.*, Oxford Science Publications, 2004.

[40] P. J. Duke, *Synchrotron radiation: production and properties.*, Oxford Science Publications, 2000.

[41] G. Rybalchenko *et al.*, Nucl. Instrum. Meth. A **467468, Part 1**, 173 (2001).

[42] X.-M. Maréchal *et al.*, J. Synchrotron Radiat. **5**, 431 (1998).

[43] *Tables of Physical & Chemical Constants. 3.10 Chemical thermodynamics*, Kaye & Laby Online. Version 1.1 (2008), http://www.kayelaby.npl.co.uk.

[44] J. Goldstein, *Scanning Electron Microscopy and X-Ray Microanalysis*, Springer, Berlin, 2003.

[45] http://www.ccp14.ac.uk/ccp/web-mirrors/lmgp-laugier bochu/.

[46] L. A. Aslanov and G. V. Fetisov, *Crystallographic Instrumentation*, Oxford University Press, 1998.

[47] W. H. Zachariasen, *Theory of Diffraction in Crystals*, Dover Phoenix, 2004.

[48] Quantum Design, 6325 Lusk Boulevard, San Diego, CA 92121, USA, 2009, SQUID VSM User's Manual.

[49] F. Garbassi, Surf. Interface Anal. **2**, 165 (1980).

[50] J. E. McCarthy *et al.*, Phys. Rev. B **62**, R6073 (2000).

[51] F. Biggs, L. B. Mendelsohn, and J. B. Mann, Atomic Data and Nuclear Data Tables **16**, 201 (1975).

[52] C. C. J. Roothaan, Rev. Mod. Phys. **23**, 69 (1951).

[53] G. G. Hall, P. Roy. Soc. Lond. A Mat. **205**, 541 (1951).

[54] M. W. Schmidt *et al.*, J. Comput. Chem. **14**, 1347 (1993).

[55] A. Koizumi *et al.*, Phys. Rev. Lett. **86**, 5589 (2001).

[56] A. Koizumi *et al.*, Phys. Rev. B **69**, 060401 (2004).

[57] A. Koizumi *et al.*, J. Phys. Chem. Solids **66**, 2183 (2005).

[58] A. Koizumi *et al.*, Phys. Rev. B **74**, 012408 (2006).

[59] N. Qureshi *et al.*, Phys. Rev. B **79**, 094417 (2009).

[60] https://bse.pnl.gov/bse/portal.

[61] http://www.scl.ameslab.gov/MacMolPlt/.

[62] P. Hohenberg and W. Kohn, Phys. Rev. **136**, B864 (1964).

[63] W. Kohn and L. J. Sham, Phys. Rev. **140**, A1133 (1965).

[64] P. A. M. Dirac, PCPS-P. Camb. Philol. S. **26**, 376 (1930).

[65] S. H. Vosko, L. Wilk, and M. Nusair, Can. J. Phys. **58**, 1200 (1980).

[66] J. P. Perdew and A. Zunger, Phys. Rev. B **23**, 5048 (1981).

[67] J. P. Perdew and Y. Wang, Phys. Rev. B **45**, 13244 (1992).

[68] L. A. Cole and J. P. Perdew, Phys. Rev. A **25**, 1265 (1982).

[69] A. D. Becke, Phys. Rev. A **33**, 3098 (1988).

[70] J. P. Perdew, K. Burke, and Y. Wang, Phys. Rev. B **54**, 16533 (1996).

[71] J. P. Perdew, K. Burke, and M. Ernzerhof, Phys. Rev. Lett. **77**, 3865 (1996).

[72] R. O. Jones, *Introduction to Density Functional Theory and Exchange-Correlation Energy Functionals*, John von Neumann Institute for Computing, Julich,, 2006.

[73] H. Ebert, *Electronic Structure and Physical Properties of Solids, Lecture Notes in Physics Vol. 535*, Springer, Berlin, 2000.

[74] T. Huhne *et al.*, Phys. Rev. B **58**, 10236 (1998).

[75] A. Bansil *et al.*, J. Phys. Chem. Solids **62**, 2191 (2001).

[76] J. S. Galsin, *Impurity Scattering in Metal Alloys*, Springer, Berlin, 2001.

[77] R. A. de Groot *et al.*, Phys. Rev. Lett. **50**, 2024 (1983).

[78] G. A. Prinz, Science **282**, 1660 (1998).

[79] S. A. Wolf *et al.*, Science **294**, 1488 (2001).

[80] A. Cho, Science **296**, 249 (2002).

[81] P. Bach *et al.*, J. Cryst. Growth **251**, 323 (2003).

[82] G. A. de Wijs and R. A. de Groot, Phys. Rev. B **64**, 020402 (2001).

[83] P. Bach *et al.*, Appl. Phys. Lett. **83**, 521 (2003).

[84] W. Van Roy, G. Borghs, and J. De Boeck, J. Magn. Magn. Mater. **242-245**, 289 (2002).

[85] W. Van Roy *et al.*, Appl. Phys. Lett. **77**, 4190 (200).

[86] D. Ristoiu *et al.*, Europhys. Lett. **49**, 624 (2000).

[87] R. J. Soulen *et al.*, Science **282**, 85 (1998).

[88] W. Branford *et al.*, J. Magn. Magn. Mater. **272**, E1399 (2004).

[89] S. K. Clowes *et al.*, Phys. Rev. B **69**, 214425 (2004).

[90] M. Sicot *et al.*, J. Magn. Magn. Mater. **303**, 54 (2006).

[91] W. Zhu *et al.*, Phys. Rev. B **64**, 060403 (2001).

[92] G. Bona *et al.*, Solid State Commun. **56**, 391 (1985).

[93] D. Orgassa *et al.*, Phys. Rev. B **60**, 13237 (1999).

[94] J. D. Aldous *et al.*, Phys. Rev. B **85**, 060403 (2012).

[95] C. Eickhoff *et al.*, Phys. Rev. B **76**, 205440 (2007).

[96] L. Castelliz, Monatsh. Chem. **82**, 1059 (1951).

[97] K. Endo, J. Phys. Soc. Jpn **29**, 643 (1970).

[98] S. Gardelis *et al.*, J. Appl. Phys. **95**, 8063 (2004).

[99] I. I. Mazin, Phys. Rev. Lett. **83**, 1427 (1999).

[100] C. Utfeld *et al.*, Phys. Rev. Lett. **103**, 226403 (2009).

[101] I. Galanakis, P. H. Dederichs, and N. Papanikolaou, Phys. Rev. B **66**, 134428 (2002).

[102] D. Jung, H.-J. Koo, and M.-H. Whangbo, J. Mol. Struct. **527**, 113 (2000).

[103] J. Tobola *et al.*, J. Phys-Condens. Mat **10**, 1013 (1998).

[104] http://www.ccp14.ac.uk/ccp/web-mirrors/powdcell/a-v/v-1/powder/e cell.html.

[105] C. Hordequin, J. Pierre, and R. Currat, J. Magn. Magn. Mater. **162**, 75 (1996).

[106] M. J. Otto *et al.*, J. Phys-Condens. Mat **1**, 2341 (1989).

[107] E. C. Stoner, P. Roy. Soc. Lond. A Mat. **165**, 372 (1938).

[108] V. Y. Irkhin and M. I. Katsnelson, J. Phys-Condens. Mat **2**, 7151 (1990).

[109] K. Makoshi and T. Moriya, J. Phys. Soc. Japan **38**, 10 (1975).

[110] T. Moriya, *Spin fluctuations in itinerant electron ferromagnetism*, Berlin: Springer, 1985.

[111] C. Hordequin *et al.*, Eur. Phys. J. B **16**, 287 (2000).

[112] P. J. Brown *et al.*, J. Phys-Condens. Mat **22**, 206004 (2010).

[113] V. N. Smolyaninova *et al.*, Phys. Rev. B **55**, 5640 (1997).

[114] A.-Y. Hu, Y. Chen, and Q. Wang, J. Appl. Phys. **108**, 093926 (2010).

[115] P. Lloyd, Proc. Phys. Soc. **90**, 207 (1967).

[116] S. Gosh *et al.*, Phys. Rev. B **73**, 085106 (2006).

[117] F. D. Murnaghan, P. Natl. Acad. Sci. USA **30**, 244 (1944).

[118] R. O. Jones and O. Gunnarsson, Rev. Mod. Phys. **61**, 689 (1989).

[119] J. P. Perdew *et al.*, Phys. Rev. B **46**, 6671 (1992).

[120] M. Pugaczowa-Michalska, Solid State Commun. **140**, 251 (2006).

[121] V. V. Godlevsky and K. M. Rabe, Phys. Rev. B **63**, 134407 (2001).

[122] A. Ayuela *et al.*, J. Phys-Condens. Mat **11**, 2017 (1999).

[123] H. Ozisik, K. Colakoglu, and H. B. Ozisik, Azerbaijan Journal of Physics: Fizika **16:2**, 154 (2010).

[124] E. Kulatov and I. I. Mazin, J. Phys-Condens. Mat **2**, 343 (1990).

[125] R. N. West, *Proc. Int. 'Enrico Fermi' School of Physics on Positron Spectroscopy of Solids*, Amsterdam: IOP Press, 1996.

[126] C. Utfeld *et al.*, Phys. Rev. Lett. **103**, 226403 (2009).

[127] B. V. Crist, *BE Lookup Table for Signals from Elements and Common Chemical Species, available at www.xpsdata.com/xpsdata*, 1999.

[128] S. Hatfield, J. Aldous, and G. Bell, Appl. Surf. Sci. **255**, 3567 (2009).

[129] J. J. Olivero and R. L. Longbothum, J. Quant. Spectrosc. Ra. **17**, 233 (1977).

[130] L. Balan *et al.*, Matter. Lett. **59**, 2898 (2005).

[131] C. D. Wagner *et al.*, Surf. Interface Anal. **3**, 211 (1981).

[132] S. Tanuma, C. J. Powell, and D. R. Penn, Surf. Interface Anal. **21**, 165 (1994).

[133] C. J. Powell, *NIST Electron Inelastic-Mean-Free-Path Database, Version 1.2, SRD 71, NIST, Gaithersburg, Md*, 2010.

[134] T. Kimura *et al.*, Nature **426**, 55 (2003).

[135] Y. Yamasaki *et al.*, Phys. Rev. Lett. **98**, 147204 (2007).

[136] Y. Tokura, Rep. Prog. Phys. **69**, 797 (2006).

[137] T. Goto *et al.*, Phys. Rev. Lett. **92**, 257201 (2004).

[138] J. Y. T. Wei, N.-C. Yeh, and R. P. Vasquez, Phys. Rev. Lett. **79**, 5150 (1997).

[139] J.-H. Park *et al.*, Nature **392**, 794 (1998).

[140] J. M. Chen *et al.*, Appl. Phys. Lett. **94**, 044105 (2009).

[141] J. M. Chen *et al.*, Phys. Rev. B **82**, 094442 (2010).

[142] K. Yamauchi and S. Picozzi, J. Phys-Condens. Mat **21**, 064203 (2009).

[143] H. J. Xiang *et al.*, Phys. Rev. Lett. **101**, 037209 (2008).

[144] M. Kenzelmann *et al.*, Phys. Rev. Lett. **95**, 087206 (2005).

[145] F. R. Forrest *et al.*, J. Phys-Condens. Mat **20**, 422205 (2008).

[146] F. Fabrizi *et al.*, Phys. Rev. Lett. **102**, 237205 (2009).

[147] J. Strempfer *et al.*, Phys. Rev. B **78**, 024429 (2008).

[148] T. Kimura *et al.*, Phys. Rev. B **71**, 224425 (2005).

[149] Y. Cui, C. Wang, and B. Cao, Solid State Commun. **133**, 641 (2005).

[150] H. Katsura, N. Hagaosa, and A. V. Balatsky, Phys. Rev. Lett. **95**, 057205 (2005).

[151] N. Hur *et al.*, Nature **429**, 392 (2004).

[152] N. Aliouane *et al.*, Phys. Rev. Lett. **102**, 207205 (2009).

[153] I. A. Sergienko, C. Şen, and E. Dagotto, Phys. Rev. Lett. **97**, 227204 (2006).

[154] I. A. Sergienko and E. Dagotto, Phys. Rev. B **73**, 094434 (2006).

[155] T. Moriya, Phys. Rev. **120**, 91 (1960).

[156] T. Moriya, Phys. Rev. **120**, 91 (1960).

[157] I. Dzyaloshinsky, J. Phys. Chem. Solids **4**, 241 (1958).

[158] R. Feyerherm *et al.*, Phys. Rev. B **79**, 134426 (2009).

[159] D. T. O'Flynn, *Multiferroic properties of rare earth manganites*, PhD thesis, Department of Physics, University of Warwick, 2010.

[160] L. Holmes, R. Sherwood, and L. G. van Uitert, J. Appl. Phys. **39**, 1373 (1968).

[161] R. Bidaux, J. E. Bouree, and J. Hammann, J. Phys. Chem. Solids **36**, 655 (1975).

[162] J. Mareschal *et al.*, J. Appl. Phys. **39**, 1365 (1968).

[163] K. P. Belov, A. K. Zvezdin, and A. M. Kadomtseva, Zh. Eksp. Theor. Fiz. **76**, 1421 (1979).

[164] S. Quezel *et al.*, Physica B & C **8688, Part 2**, 916 (1977).

[165] J. A. Duffy *et al.*, Phys. Rev. B **61**, 14331 (2000).

[166] M. A. G. Dixon *et al.*, J. Phys-Condens. Mat **10**, 2759 (1998).

[167] Y. Kubo and S. Asano, Phys. Rev. B **42**, 4431 (1990).

[168] J. A. Alonso *et al.*, Inorg. Chem. **29**, 917 (2000).

[169] R. B. Ross, W. C. Ermler, and S. Das, (Unpublished) .

[170] A. Schafer, C. Huber, and R. Ahlrichs, J. Chem. Phys. **100**, 5829 (1994).

[171] P. R. Bevington and D. K. Robinson, *Data Reduction and Error Analysis*, McGraw-Hill, 2003.

[172] E. Burzo, Solid State Commun. **14**, 1295 (1974).

[173] D. D. Jackson and Z. Fisk, Phys. Rev. B **73**, 024421 (2006).

[174] J. Kim *et al.*, Appl. Phys. Lett. **100**, 022407 (2012).

[175] A. P. Sazonov *et al.*, J. Phys-Condens. Mat **19**, 046218 (2007).

[176] H. D. Zhou and J. B. Goodenough, J. Phys-Condens. Mat **17**, 7395 (2005).

[177] J.-G. Cheng *et al.*, Phys. Rev. B **84**, 104415 (2011).

[178] M. Bibes and A. Bartélémy, Nature Materials **7**, 425 (2008).

[179] http://elk.sourceforge.net/.

[180] G. van der Laan *et al.*, Phys. Rev. Lett. **100**, 067403 (2008).

[181] M. Rotter, M. Tegel, and D. Johrendt, Phys. Rev. Lett. **101**, 107006 (2008).

[182] G.-F. Chen *et al.*, Chin. Phys. Lett **25**, 3403 (2008).

[183] K. Sasmal *et al.*, Phys. Rev. Lett. **101**, 107007 (2008).

[184] C. Liu *et al.*, Phys. Rev. Lett. **101**, 177005 (2008).

[185] M. S. Torikachvili *et al.*, Phys. Rev. Lett. **101**, 057006 (2008).

[186] Y. Jo *et al.*, Physica C **469**, 566 (2009).

[187] H. Q. Yuan *et al.*, Nature **457**, 565 (2009).

[188] N. Ni *et al.*, Phys. Rev. B **78**, 214515 (2008).

[189] M. Putti *et al.*, Supercond. Sci. Tech. **23**, 034003 (2010).

[190] Y. He *et al.*, J. Phys-Condens. Mat **22**, 235701 (2010).

[191] S. Jiang *et al.*, New J. Phys. **11**, 025007 (2009).

[192] A. Błachowski *et al.*, Phys. Rev. B **84**, 174503 (2011).

[193] J. Herrero-Martín *et al.*, Phys. Rev. B **80**, 134411 (2009).

[194] Y. Xiao *et al.*, Phys. Rev. B **81**, 220406 (2010).

[195] T. Wu *et al.*, J. Magn. Magn. Mater. **321**, 3870 (2008).

[196] Z. Guguchia *et al.*, Phys. Rev. B **84**, 144506 (2011).

[197] A. Ahmed *et al.*, Phys. Rev. Lett. **105**, 207003 (2010).

[198] Y. Kamihara *et al.*, J. Am. Chem. Soc. **128**, 10012 (2006).

[199] T. Watanabe *et al.*, Inorg. Chem. **46**, 7719 (2007).

[200] C. Wang *et al.*, Europhys. Lett. **83**, 67006 (2008).

[201] G. R. Stewart, Rev. Mod. Phys. **83**, 1589 (2011).

[202] J. Paglione and R. L. Greene, Naure Phys. **6**, 645 (2010).

[203] Y. A. Izyumov and E. Z. Kurmaev, Phys. Uspekhi **51**, 1261 (2008).

[204] Y. Li and J. Ni, Solid State Commun. **151**, 446 (2011).

[205] M. Tegel *et al.*, J. Phys-Condens. Mat **20**, 452201 (2008).

[206] Y. Xiao *et al.*, Phys. Rev. B **80**, 174424 (2009).

[207] A. I. Goldman *et al.*, Phys. Rev. B **78**, 100506 (2008).

[208] J. Zhao *et al.*, Phys. Rev. B **78**, 140504 (2008).

[209] K. Kaneko *et al.*, Phys. Rev. B **78**, 212502 (2008).

[210] Y. Su *et al.*, Phys. Rev. B **79**, 064504 (2009).

[211] Q. Huang *et al.*, Phys. Rev. Lett. **101**, 257003 (2008).

[212] M. Tokunaga *et al.*, J. Low Temp. Phys. **159**, 601 (2010).

[213] R. J. McQueeney *et al.*, Phys. Rev. Lett. **101**, 227205 (2008).

[214] M. J. Han *et al.*, Phys. Rev. Lett. **102**, 107003 (2009).

[215] S. Jiang *et al.*, Phys. Rev. B **80**, 184514 (2009).

[216] W. Li *et al.*, Phys. Rev. B **86**, 155119 (2012).

[217] D. J. Singh, Phys. Rev. B **78**, 094511 (2008).

[218] C. Krellner *et al.*, Phys. Rev. B **78**, 100504 (2008).

[219] H. S. Jeevan *et al.*, Phys. Rev. B **78**, 052502 (2008).

[220] H. S. Jeevan *et al.*, Phys. Rev. B **83**, 054511 (2011).

[221] A. Blachowski *et al.*, ArXiv e-prints (2011).

[222] C. Detlefs *et al.*, Phys. Rev. B **61**, R14916 (2000).

[223] Z. Ren *et al.*, Phys. Rev. B **78**, 052501 (2008).

[224] Z. Weihong and C. J. Hamer, Phys. Rev. B **47**, 7961 (1993).

[225] M. R. Said *et al.*, J. Magn. Magn. Mater. **195**, 679 (1999).

[226] G. D. Mukherjee *et al.*, J. Magn. Magn. Mater. **214**, 185 (2000).

[227] S. N. Kaul, J. Magn. Magn. Mater. **53**, 5 (1985).

[228] L. Zhang *et al.*, Europhys. Lett. **91**, 57001 (2010).

[229] E. Praveczki, J. Phys. C Solid State **12**, 3993 (1979).

[230] L. Onsager, Phys. Rev. **65**, 117 (1944).